

SUPRAMOLECULAR SELF-ASSEMBLY OF GOLD NANOPARTICLES

Dissertation

Zur Erlangung des akademischen Grades eines Doktors der Naturwissenschaft

-Dr. rer. Nat.-

vorgelegt von

Huibo He

geboren in Fujian, China

Fakultät für Chemie

der

Universität Duisburg-Essen

2020

DuEPublico

Duisburg-Essen Publications online

UNIVERSITÄT
DUISBURG
ESSEN

Offen im Denken

ub | universitäts
bibliothek

Diese Dissertation wird via DuEPublico, dem Dokumenten- und Publikationsserver der Universität Duisburg-Essen, zur Verfügung gestellt und liegt auch als Print-Version vor.

DOI: 10.17185/duepublico/73551

URN: urn:nbn:de:hbz:464-20220112-083358-2

Alle Rechte vorbehalten.

Declaration of authorship

I declare that I completed this work on my own and did not use any other source than stated.

Huibin He, October 2020

The work presented in this thesis was accomplished in a period between October 2016 and July 2020 under the supervision of PD Dr. Jochen Niemeyer and Prof. Dr. Carsten Schmuck at the Faculty of Chemistry (Organic Chemistry) at the University of Duisburg-Essen.

First Reviewer: PD Dr. Jochen Niemeyer

Second Reviewer: Prof. Dr. Matthias Epple

Date of oral examination: 03.12.2020

Chair: PD Dr. Bilal Gökce

In Memory of Carsten Schmuck

Acknowledgements

At the very first, I would like to express my deepest gratitude to Prof. Dr. Carsten Schmuck for his supervision and support. I thank him for giving me the opportunity to study in his group and to participate in his chemistry. He gave me great research-freedom, allowing me to choose and deal with the projects I am interested in. I appreciate his patience during the first two years of my PhD carrier when the projects were not going well. I also would like to thank him for his valuable ideas and suggestions which helped me to improve myself, not only in scientific work, but also in the presentation. He was a revered scientist, teacher, mentor, I am grateful for his respectful personality and deeply regret for his loss.

I would like to give my grateful thanks to my current supervisor, Dr. Jochen Niemeyer who took over the supervision after Prof. Dr. Carsten Schmuck passed away. Thank him for encouraging me when we lost our mentor Carsten Schmuck. With his guidance and significant contribution that I was able to continue exploring my scientific research to work out this dissertation. He has offered me a lot of suggestions in the experiment arrangement and paper writing, which are the treasure of my research life. I would also thank him for listening the new ideas and giving the comments and supports. Moreover, I am grateful for his warm concerns which made the research and life more comfortable.

I would like to thank Prof. Dr. Matthias Epple for reviewing this dissertation and allowing me to perform SEM measurement in his group.

I would like to thank my previous supervisors Prof. Dr. Hongbing Zhan and Prof. Dr. Miao Feng for their kind suggestions.

I would like to thank CSC (China Scholarship Council) for providing the fellowship and supporting me to study in Germany.

I would like to thank Dr. Thomas Mayer-Gall from DTNW for ICP measurement.

I would like to thank Tobias Bochmann from AK Epple for SEM measurement.

I would like to thank Werner Karow and Gudrun Heinrich for mass measurement.

I would like to thank my cooperative partner Jan-Erik Ostwaldt and Kevin Rudolph for TEM measurement.

I would like to thank my cooperative partner Dennis Aschmann for the synthesis of GCP building block.

I would like to give a great thanks to my colleagues in our research group for the help and support. They were so helpful and kind to me, I am grateful for their patience and tolerance. I would like to give my great thank to our acting director Jun-Prof. Dr. Michael Giese his support and helps. I would like to thank Dr. Christoph Hirschhäuser for reviewing manuscript and suggestions. Special thanks go to my subgroup members, Dr. Joydev Hatai, Toni Hättasch, Jan-Erik Ostwaldt, Maike Thiele, Robin Struth and Hongxiao Xiang for the discussions, suggestions and happy times we have had in our group meetings. Great thanks go to Mattias Killa, who is a perfect friend and colleague. He gave me lots of helpful suggestions to make research work and daily life easier. I am grateful for the great work atmosphere and conversations we have had. Great Thanks also go to my colleagues Marlen Externbrink, Pascal Naschenweng and Thies Dirksmeyer for helping me to use the instruments in the lab. I also would like to thank Elisabeth Verheggen, Ursula Nüchter, Pia Mereu, Daniel Sebena, Alexander Zimmermann, Patryciusz Piotrowski, Marcel Klein-Hitpaß, Nazli Aldemir and Marius Heimann for their kind helps, they made my life in the lab much easier and happier.

I would like to thank Prof. Dr. Xiaoyu Hu, Dr. Hao Jiang, Dr. Jingcheng, Dr. Mao Li and Dr. Shiping Wu for their help and support, especially at the difficult moment of my work and life. I also would like to thank them for their delicious Chinese foods which made me feel at home. Qirong, Yaya, Chengyang, Shurui, Shijie are thanked for their friendship and happy time we have had.

At last, I would love to express my special thanks to my parents, my sister and my brother for their understanding, support and deepest love during my whole life. Best thanks are also given to ChunChun who is always there for me. Thanks for her support, encouragement and love.

Table of contents

1. Introduction	1
1.1 Metal nanoparticles.....	1
1.1.1 Catalysis with metal nanoparticles	2
1.1.2 Surface plasmon resonance of metal nanoparticles	2
1.1.3 Surface enhanced Raman-scattering of metal nanoparticles	3
1.2 Gold nanoparticles.....	3
1.2.1 Synthesis of gold nanoparticles	3
1.2.2 Applications of gold nanoparticles	4
1.2.3 Self-assembly of gold nanoparticles	5
1.3 pH-responsive self-assembly of nanoparticles	5
1.3.1 pH-responsive self-assembly based on acidic ligands.....	6
1.3.2 pH-responsive self-assembly based on basic ligands	8
1.3.3 pH-responsive self-assembly based on zwitterionic ligands	9
1.3.4 pH-responsive self-assembly based on mixed-charged ligands.....	12
1.4 Template-assisted self-assembly of nanoparticles.....	13
2. Background Information	16
2.1 GCP binding motif	16
2.1.1 GCP-oxoanion binding interactions.....	16
2.1.2 Application of GCP binding motif.....	17
2.2 GCPZ binding motif	18
2.2.1 Self-association of GCPZ binding motif	18
2.2.2 Application of GCPZ binding motif	19
2.2.3 Solubility of GCPZ binding motif	20
3. Project and Objective	23
3.1 Dual pH-sensitive reversible self-assembly of gold nanoparticles.....	23
3.2 Multiple pH-sensitive reversible self-assembly of gold nanoparticles.....	24
3.3 One dimensional arrangement of gold nanoparticles	25

4. Dual pH-Sensitive Reversible Self-Assembly of Gold Nanoparticles	27
4.1 Introduction	27
4.2 Results and discussion	27
4.2.1 Synthesis of thiolated GCPZ derivative.....	27
4.2.2 Synthesis of thiolated TEG ligand.....	28
4.2.3 Synthesis of thiolated carboxylic acid ligand	29
4.2.4 Preparation of gold nanoparticles	29
4.2.5 Functionalization of gold nanoparticles.....	30
4.2.6 Self-assembly of AuNPs-1	32
4.2.7 Mechanism of dual pH-sensitive self-assembly	37
4.3 Conclusions	52
5. Multiple pH-Sensitive Reversible Self-Assembly of Gold Nanoparticles	53
5.1 Introduction	53
5.2 Results and discussion	53
5.2.1 Synthesis of thiolated GCP derivative	53
5.2.2 GCPZ and GCP co-functionalized AuNPs	54
5.2.3 Self-assembly of AuNPs-1-4	58
5.2.4 Application of multi-PSRSA in removing metal ions	73
5.3 Conclusions	80
6. One Dimensional Arrangement of Gold Nanoparticles	81
6.1 Introduction	81
6.2 Results and discussion	81
6.2.1 Synthesis of building blocks with GCPs.....	81
6.2.2 One dimensional arrangement of AuNPs on nanofiber template	82
6.3 Conclusions	90
7. Summary and Outlook.....	91
7.1 Dual pH-sensitive reversible self-assembly of gold nanoparticles.....	91
7.2 Multiple pH-sensitive reversible self-assembly of gold nanoparticles.....	93
7.3 One-Dimensional arrangement of gold nanoparticles	95

8. Experimental Section	96
8.1 General experimental and analytical methods	96
8.2 Synthesis of thiolated GCPZ ligand	99
8.3 Synthesis of TEG derivative.....	108
8.4 Synthesis of thiolated carboxyl ligand.....	110
8.5 Synthesis of thiolated GCP ligand.....	112
8.6 Preparation of Gold nanoparticles	115
8.7 Functionalization of Gold nanoparticles.....	116
9. Appendix	117
9.1 List of abbreviations	117
9.2 AFM measurement	119
9.3 UV/Vis measurement	120
9.4 ¹ H NMR and ¹³ C NMR.....	132
9.5 Curriculum vitae	148
9.6 List of Publications.....	149

1. Introduction

1.1 Metal nanoparticles

Nanomaterials are materials with at least one dimension between 1 and 100 nm. In 1857 Michael Faraday prepared stable gold sols and elucidated the mechanism of formation of colloidal metals.¹ Since those early days, further investigations have been carried out in the field of metal nanoparticles (NPs). Different metal NPs with various shapes (Figure 1.1) have been achieved by using chemical methods,² which are based on the (bio)chemical reduction of metal salts in aqueous or organic solvents in the presence of a variety of stabilizers.

Structures	Shapes	Schematic drawings	Metals
single-crystal	perfect/truncated cube ^[a]		Pd, Ag, Au, Pt, Cu, Rh, Bi, Fe
	perfect/truncated octahedron ^[a]		Pd, Ag, Au, Pt
	perfect/truncated tetrahedron ^[a]		Ag, Au, Pt, Rh
	rectangular bar		Pd, Ag, Pt
	octagonal rod		Pd, Au, Fe, Co, Ni
singly twinned	rectangular or octagonal wire		Pb, In, Sn, Sb, Fe, Co
	right bipyramid		Pd, Ag
multiply twinned	beam		Ag
	decahedron ^[a]		Pd, Ag, Au
	icosahedron ^[a]		Pd, Au
	five-fold twinned pentagonal rod		Pd, Ag, Au, Cu
	five-fold twinned pentagonal wire		Ag, Au, Cu
disc	triangular/hexagonal plate		Pd, Ag, Au, Cu, Pb, Bi, Co, Ni
	disc		Sn, Co

Figure 1.1: A summary of different shapes that been achieved for various metal NPs. Adapted and reproduced with permission from the Wiley-VCH, copyright 2009.²

¹ M. Faraday, *Philos. Trans. R. Soc. London*, **1857**, 147, 145.

² Y. Xia, Y. Xiong, B. Lim, S. E. Skrabalak, *Angew. Chem. Int. Ed.* **2009**, 48, 60-103.

1.1.1 Catalysis with metal nanoparticles

It is well known that palladium and platinum **NPs** can be used as catalysts in many chemical reactions.³ Due to the size and good dispersibility, heterogeneous catalysts in nanoscale can offer large surface-to-volume ratios and thus high activities. Geometrically speaking, nonspherical **NPs** can provide plenty of corners, vertices, defects, kinks, and steps. The catalytic activity and selectivity of metal **NPs** could be controlled by varying the number of such defects.⁴ Moreover, the exposed crystallographic facets are also important for activity and selectivity controls. Therefore, metal **NPs** with different sizes and shapes are desirable as catalysts in numerous fields such as waste reduction and chemical industry.

1.1.2 Surface plasmon resonance of metal nanoparticles

When light in a specific range (UV-Vis-NIR) interacts with the interface between metal **NPs** and the dielectric continuum, this excites the collective oscillation of conduction electrons, so-called surface plasmon polaritons. For metal **NPs**, the optical properties are mainly determined by localized surface plasmons that give rise to so called localized surface plasmon resonance (**SPR**) that can be observed in absorption and scattering spectra.⁵

Ag **NPs** and Au**NPs** are commonly used as plasmonic metals. Here it has to be taken into account, that the localized electromagnetic fields associated with the excitation of surface plasmons are unevenly distributed around nonspherical metal **NPs**, leading to shape-dependent **SPR** spectra. The **SPR** spectra of **NPs** also depend on the **NP**-size. For instance, spherical Au**NPs** with a diameter of 7.8 nm exhibit a **SPR** band around 523 nm (Figure 1.2a). In contrast, rod-shaped Au**NPs** exhibit two separate **SPR** bands: transverse **SPR** band at around 530 nm and longitudinal **SPR** peak around 900 nm (Figure 1.2b).

³ A. Roucoux, J. Schulz, H. Patin, *Chem. Rev.* **2002**, *102*, 3757-3778.

⁴ N. Herron, D. L. Thorn, *Adv. Mater.* **1998**, *10*, 1173-1184.

⁵ V. Myroshnychenko, J. Rodriguez-Fernandez, I. Pastoriza-Santos, A. M. Funston, C. Novo, P. Mulvaney, L. M. Liz-Marzan, F. J. Garcia de Abajo, *Chem. Soc. Rev.* **2008**, *37*, 1792-1805.

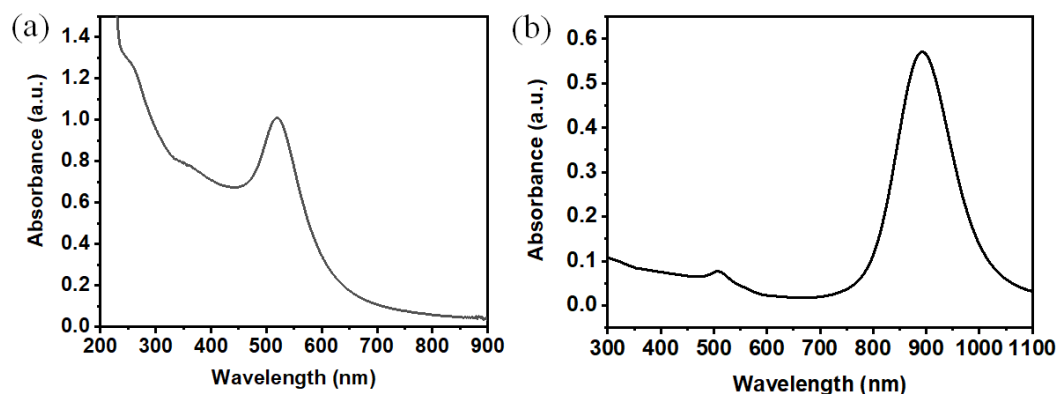


Figure 1.2 Typical UV-Vis-NIR spectrum of (a) spherical AuNPs and (b) rod-shaped AuNPs.

1.1.3 Surface enhanced Raman-scattering of metal nanoparticles

Raman scattering is the inelastic scattering of a photon, which the energy of scattered photons is lower than incident photons, detected via observation of the red-shift in wavelength. Raman spectroscopic technique is non-invasive, and provides rich structural information, which can be used for sensitive detection and identification of molecules. However, the intensity of scattered light is very low since Raman scattering cross-sections of molecules are extremely small. While, with the help of metal NPs, the Raman scattering intensity is greatly enhanced.⁶ This phenomenon is known as surface enhanced Raman-scattering (SERS).

1.2 Gold nanoparticles

Different from bulk gold, AuNPs can show vivid colours which depend on the sizes and shapes of NPs. Related to their beauty, AuNPs have attracted lots of attention from chemists, physicists and biomedical practitioners. As a typical metal NPs, AuNPs have the properties we mentioned above, such as strong SPR and SERS. Besides these properties, AuNPs also exhibit properties which are different from others, such as good biocompatibility and low cytotoxicity.

1.2.1 Synthesis of gold nanoparticles

Since the first scientific report describing the production of colloidal AuNPs, a variety of methods for the synthesis of AuNPs have been developed. Most of these synthetic methods follow the similar strategy, by using the reducing agent to reduce solvated gold salt and using surface capping ligands to stabilize the produced AuNPs. For instance, the well-known *Brust-Schiffrin* method is based on

⁶ W. E. Smith, *Chem. Soc. Rev.* **2008**, 37, 955-964.

the reduction of HAuCl_4 in the presence of a reducing agent like sodium borohydride and stabilizing ligands, such as alkylthiols (Figure 1.3). The size of the particles can be controlled by varying the reaction conditions, such as temperature or the ratio of gold to thiol ligand.⁷ Usually this reaction is carried out in unpolar solvent such as toluene, thus the prepared nanoparticles can be transferred to aqueous solution by using a phase-transfer reagent. Combining with a successive *Murray* place-exchange reaction⁸, gold nanoparticles can be functionalized with a wide range of functional thiols, e.g. for targeting biomolecules or enabling cellular uptake.

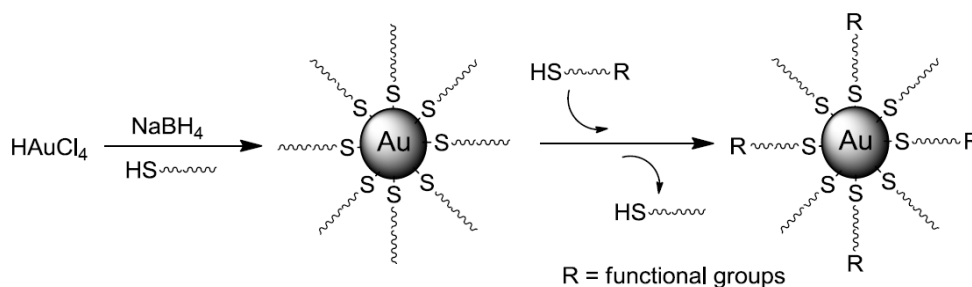


Figure 1.3 Schematic representation of the generation of functionalized gold nanoparticles by using *Brust-Schiffrin* method and *Murray* place-exchange reaction.

1.2.2 Applications of gold nanoparticles

Because of the unique properties, **AuNPs** can be applied in wide range of fields, e.g. in biological applications. Due to the efficient conversion of light into heat, **AuNPs** can be used in photothermal therapy.⁹ Because of their surface chemistry, **AuNPs** can act as artificial antibodies with appropriate ligands on their surface.¹⁰ The binding affinity of such antibodies can be controlled by changing the surface functionalization, such as the density of binding ligands. **AuNPs** with ultrasmall size (2 nm) can easily penetrate into cells and even enter the cell nucleus.¹¹ **AuNPs** can also be used in biological diagnosis since their intense photophysical properties. In addition, as a contrast agent for CT-scanning, **AuNPs** can increase imaging contrast due to their ability to absorb copious amounts

⁷ a) M. Brust, J. Fink, D. Bethell, D. J. Schiffrin, C. Kiely, *J. Chem. Soc., Chem. Commun.* **1995**, 1655-1656. b) M. Brust, M. Walker, D. Bethell, D. J. Schiffrin, R. Whyman, *J. Chem. Soc., Chem. Commun.* **1994**, 801-802.

⁸ M. J. Hostetler, A. C. Templeton, R.W. Murray, *Langmuir* **1999**, *15*, 3782-3789.

⁹ B. Li, Y. Wang, J. He, *ACS Appl. Mater. Interfaces* **2019**, *11*, 7800-7811.

¹⁰ G.-H. Yan, K. Wang, Z. Shao, L. Luo, Z.-M. Song, J. Chen, R. Jin, X. Deng, H. Wang, Z. Cao, *Proc. Natl. Acad. Sci. U. S. A., Early Ed.* **2018**, *115*, E34-E43.

¹¹ V. Sokolova, G. Nzou, S. B. van der Meer, T. Ruks, M. Heggen, K. Loza, N. Hagemann, F. Murke, B. Giebel, D. M. Hermann, A. J. Atala, M. Epple, *Acta Biomater.* **2020**, *111*, 349-362.

of X-ray radiation.¹² Because of their multivalency, **AuNPs** can be designed as a vector which allows to deliver unstable drugs or poorly soluble imaging contrast agents to inaccessible regions of the body.¹³ More importantly, all the benefits supported by **AuNPs** can be combined into a single construct, allowing simultaneous targeting, diagnostic, and therapeutic functionality.

1.2.3 Self-assembly of gold nanoparticles

The term self-assembly is used to describe the spontaneous formation of assemblies or patterns from building blocks by noncovalent interactions such as electrostatic interactions, van der Waals interactions, hydrogen bonds, hydrophobic/hydrophilic interactions. The self-assembly of **AuNPs** into functional and ordered structure is important for the fabrication of efficient photonic or sensor devices. In addition, the self-assembly of **NPs** is a powerful method to adjust properties of **NPs** by changing their effective sizes or morphologies. For instance, the **SPR** property of **AuNPs** is related to the size and shape of **NPs**, which can be well controlled by self-assembly (Figure 1.4).¹⁴

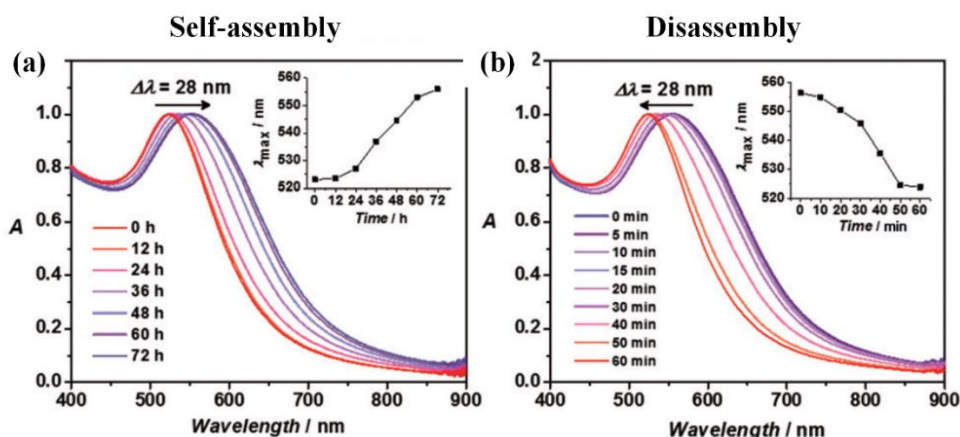


Figure 1.4 The change in SPR of **AuNPs** during (a) self-assembly and (b) disassembly. Adapted and reproduced with permission from the Wiley-VCH, copyright 2016.¹⁴

1.3 pH-responsive self-assembly of nanoparticles

The colloidal stability of **NPs** mainly depends on their surface charge, which basically comes from the terminal functional groups of the ligands. Due to the electrostatic repulsions, charged **NPs** are

¹² R. Popovtzer, A. Agrawal, N. A. Kotov, A. Popovtzer, J. Balter, T. E. Carey, R. Kopelman, *Nano Lett.* **2008**, *8*, 4593-4596.

¹³ E. C. Dreaden, A. M. Alkilany, X. Huang, C. J. Murphy, M. A. El-Sayed, *Chem. Soc. Rev.* **2012**, *41*, 2740-2779.

¹⁴ H. He, M. Feng, Q. Chen, X. Zhang, H. Zhan, *Angew. Chem. Int. Ed* **2016**, *55*, 936-940.

usually stable in polar solvent. Decreasing the value of surface charge leads to the decrease of electrostatic repulsions, which can induce the self-assembly of **NPs**.

The pH-sensitive reversible self-assembly (**PSRSA**) of **NPs** has attracted increasing interest in various biological applications such as cellular imaging¹⁵ and drug delivery¹⁶. Typically, **PSRSA**-based self-assemblies were constructed by introducing pH-sensitive ligands on **NPs**.¹⁷ For these functionalized **NPs**, the quantity of surface charge always depends on the pH value in the solution, which allows the **NPs** to self-assemble and disassemble in a pH-sensitive fashion.

1.3.1 pH-responsive self-assembly based on acidic ligands

As pH-responsive ligands, acidic functional ligands, such as carboxylic acids, phenols and organic phosphoric acids, are non-charged at acidic pH values, while they are deprotonated at basic pH, resulting in negatively charged species. Due to the pH-responsibility, a variety of acidic ligands have been used for creating the pH-sensitive self-assembly system.¹⁸

Acidic ligands functionalized **NPs** are dispersed at basic pH value owing to the electrostatic repulsions between negatively charged **NPs**, while the **NPs** assemble at basic pH due to the protonation of acidic ligands. For instance, Fan *et al.* designed a pH-responsive self-assembly system based on **AuNPs** functionalized with commercial organic molecules, namely 4-mercaptobenzonic acid (**4-MBA**) and oleylamine (**OL**) (Figure 1.5a).¹⁹ The functionalized **AuNPs** self-assemble to form nanovesicles at acidic pH value due to the protonation of **4-MBA**. The nanovesicles dissociate into individual **NPs** in alkaline conditions. In addition, the dissociated **NPs** can reassemble to regenerate nanovesicles when the **4-MBA** is protonated again. The assembly-disassembly-reassembly sequence of **4-MBA**-coated **AuNPs** was confirmed by TEM (Figure 1.5b-1.5d) and this reversible behaviour could be repeated over 5 cycles.

¹⁵ B. Dong, S. Du, C. Wang, H. Fu, Q. Li, N. Xiao, J. Yang, X. Xue, W. Cai, D. Liu, *ACS Nano* **2019**, *13*, 1421-1432.

¹⁶ J. Song, J. Zhou, H. Duan, *J. Am. Chem. Soc.* **2012**, *134*, 13458-13469.

¹⁷ M. Grzelczak, L. M. Liz-Marzan, R. Klajn, *Chem. Soc. Rev.* **2019**, *48*, 1342-1361.

¹⁸ a) D. W. Wang, B. Kowalczyk, I. Lagzi, B. A. Grzybowski, *J. Phys. Chem. Lett.* **2010**, *1*, 1459-1462. b) Y. Tan, L. Liu, Y. Wang, J. Liu, *Adv. Opt. Mater.* **2018**, *6*, 1701324. c) I. Lagzi, B. Kowalczyk, D. Wang, B. A. Grzybowski, *Angew. Chem. Int. Ed.* **2010**, *49*, 8616-8619.

¹⁹ C. Fan, T. Bian, L. Shang, R. Shi, L.-Z. Wu, C.-H. Tung, T. Zhang, *Nanoscale* **2016**, *8*, 3923-3925.

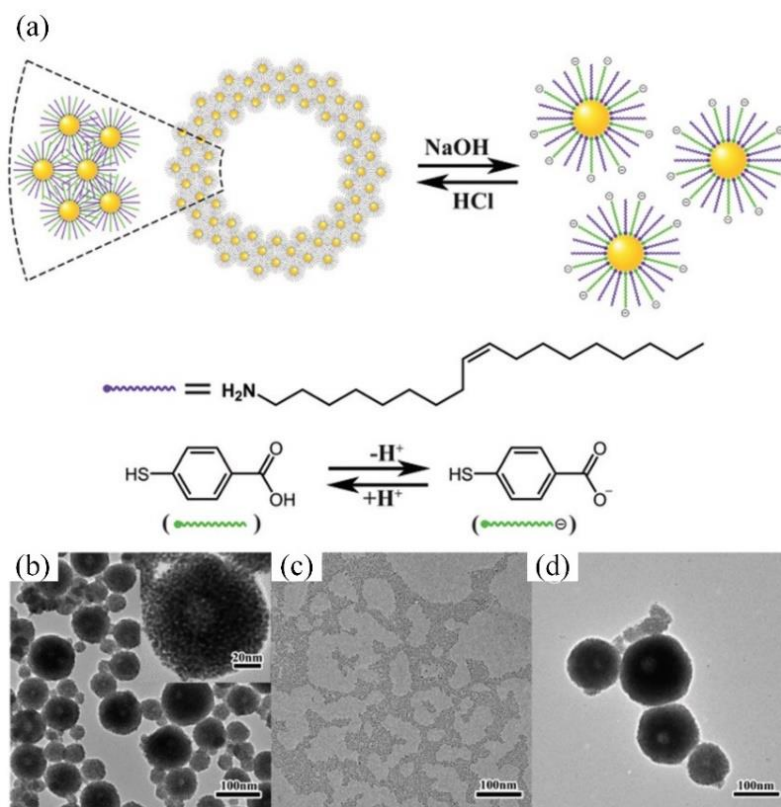


Figure 1.5: a) Schematic representation of pH-responsive self-assembly of 4-MBA-coated NPs, b-d) TEM images of (b) self-assembled AuNPs, (c) disassembled individual AuNPs and (d) reassembled AuNPs. Adapted and reproduced with permission from the Royal Society of Chemistry, copyright 2016.¹⁹

The by-product (water or salt) from the pH cycles usually limits the number of assembly/disassembly cycles. To overcome this limitation, photoacids or photobases can be used, which can transiently change solution pH upon exposure to light.²⁰ Samanta *et al.* designed a pH-sensitive self-assembly system based on AuNPs functionalized with 6-mercaptopropionic acid (MHA), in which a water-soluble photoacid MCH^+ (structure is shown in Figure 1.6) was used for pH switching (Figure 1.6).²¹ NPs functionalized with MHA acid are dispersed in an aqueous solution of MCH^+ due to the electrostatic repulsions which are caused by deprotonated COOH groups. Visible-light irradiation induces the ring-opening reaction of MCH^+ resulting in the release of H^+ ions, which causes protonation of terminal COOH moieties and triggers NP self-assembly. The resulting aggregates are able to disassemble when the irradiation is discontinued. This assembly/disassembly sequence can be repeated at least 30-40 cycles.

²⁰ P. K. Kundu, D. Samanta, R. Leizrowice, B. Margulis, H. Zhao, M. Börner, T. Udayabhaskararao, D. Manna, R. Klajn, *Nat. Chem.* **2015**, 7, 646-652.

²¹ D. Samanta, R. Klajn, *Adv. Opt. Mater.* **2016**, 4, 1373-1377.

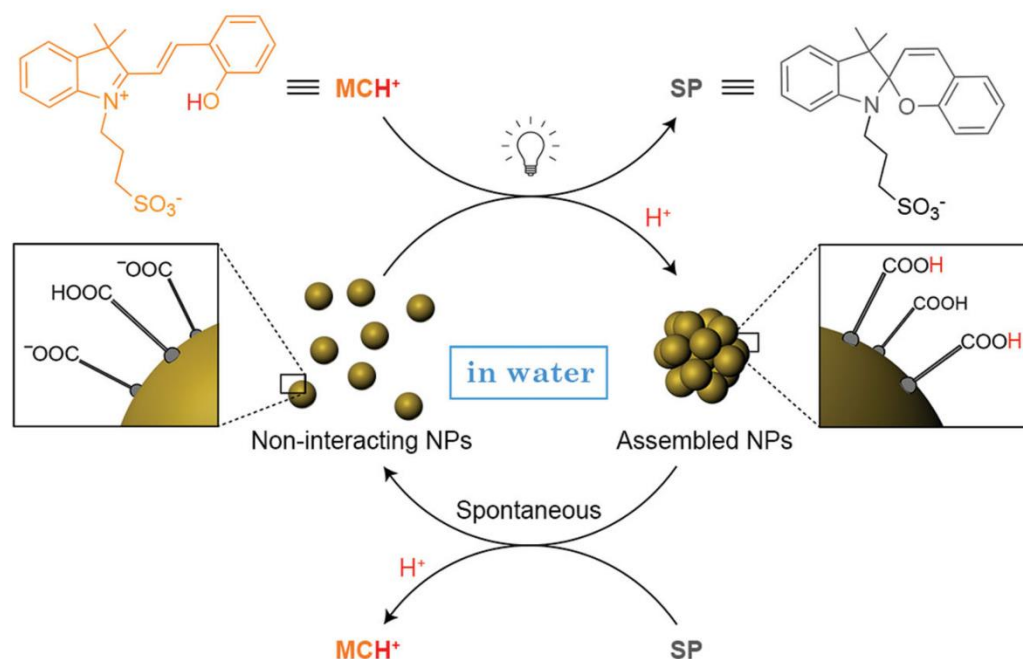


Figure 1.6: Schematic representation of pH-responsive self-assembly of **MHA**-coated **NPs** in water by using photoacid **MCH⁺** for pH switch. Adapted and reproduced with permission from the Wiley-VCH, copyright 2016.²¹

1.3.2 pH-responsive self-assembly based on basic ligands

Different from acidic **NPs**, **NPs** decorated with basic ligands show an opposite self-assembly behaviour, which disassemble in protonated state at acidic pH but assemble in deprotonated state at basic pH. In recent decades, various basic ligands had been applied in the pH-responsive self-assembly of **NPs**.¹⁷

For example, Ma *et al.* developed a pH-responsive self-assembly system by decorating **NPs** with three types of molecules, modified polyethylene glycol (**PEG**), dibutylamine (**Bu**) and pyrrolidinamine (**Py**).²² As shown in Figure 1.7, modified **AuNPs** are well dispersed in a solution of pH 6.8, while they self-assemble as the pH switches to 7.2. Hydrophobic interactions and steric repulsions were considered to be the main driving force for the self-assembly/disassembly of **NPs**. At pH 6.8 or lower, amines on **NPs** are protonated, the steric repulsions of **PEG** are stronger than the hydrophobic effect of amine groups resulting in the dispersed **NPs**. While at pH = 7.2, the deprotonation of amines increases the hydrophobic interactions so that it could overcome the steric repulsions and trigger the self-assembly of **AuNPs**.

²² J. Ma, Z. Hu, W. Wang, X. Wang, Q. Wu, Z. Yuan, *ACS App. Mater. Interfaces* **2017**, *9*, 16767-16777.

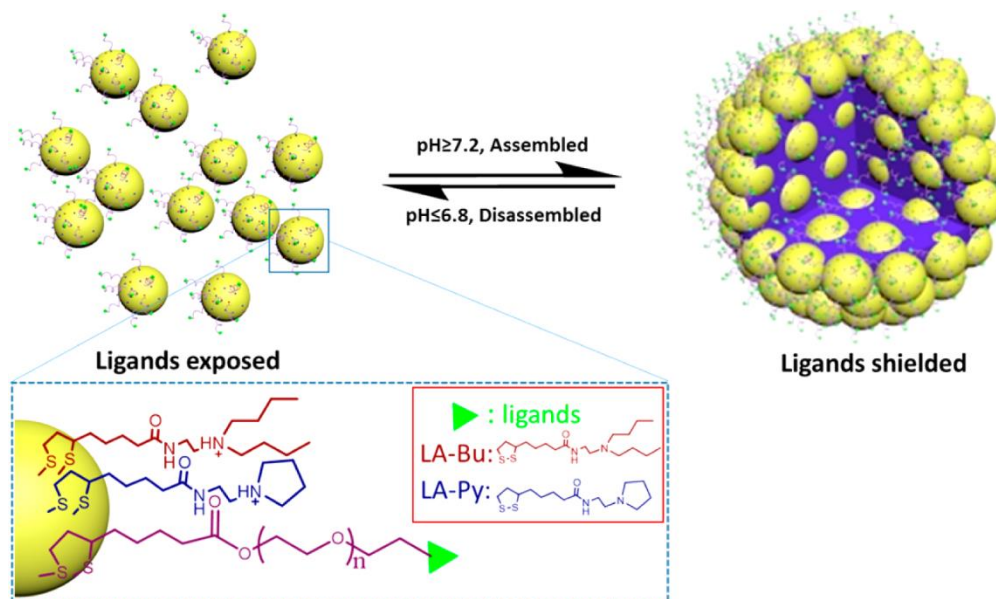


Figure 1.7: Schematic representation of pH-responsive self-assembly of amines-coated AuNPs. Adapted and reproduced with permission from the American Chemical Society, copyright 2017.²²

Besides the organic basic ligands such as dibutylamine and pyrrolidinamine, polymeric ligands which are containing basic units were also used in pH-sensitive self-assembly.²³ However, the mode of action for the assembly/disassembly remains unchanged.²⁴

1.3.3 pH-responsive self-assembly based on zwitterionic ligands

Compare to basic or acidic ligands, zwitterionic ligands such as cysteine and glutathione (**GSH**) are more “advanced” owing to their pH-responsibility to both acidic and basic surroundings. Zwitterionic ligands bearing both positive charged and negative charged groups, may also provide some useful properties for NPs, such as the improvement of biocompatibility and the enhancement of cellular uptake.²⁵ In contrast to the pH-sensitive self-assembly behaviours of NPs functionalized with single acidic or basic ligands, which we discussed above, the pH-responsive self-assembly behaviour of NPs functionalized with zwitterionic ligands can give rise to a multi-switching

²³ a) J. Song, J. Zhou, H. Duan, *J. Am. Chem. Soc.* **2012**, *134*, 13458-13469. b) J. Song, L. Cheng, A. Liu, J. Yin, M. Kuang, H. Duan, *J. Am. Chem. Soc.* **2011**, *133*, 10760-10763.

²⁴ a) Z. Tian, C. Yang, W. Wang, Z. Yuan, *ACS Appl. Mater. Interfaces* **2014**, *6*, 17865-17876. b) L. Cheng, A. Liu, S. Peng, H. Duan, *ACS Nano* **2010**, *4*, 6098-6104.

²⁵ a) T. Mizuhara, K. Saha, D. F. Moyano, C. S. Kim, B. Yan, Y. K. Kim, V. M. Rotello, *Angew. Chem. Int. Ed* **2015**, *54*, 6567-6570. b) H. Wei, N. Insin, J. Lee, H. S. Han, J. M. Cordero, W. Liu, M. G. Bawendi, *Nano Lett.* **2012**, *12*, 22-25. c) Y. Jiang, S. Huo, T. Mizuhara, R. Das, Y.-W. Lee, S. Hou, D. F. Moyano, B. Duncan, X.-J. Liang, V. M. Rotello, *ACS Nano* **2015**, *9*, 9986-9993.

behaviour: It should be expected that **NPs** self-assemble at medium pH (e.g. neutral pH) and disassemble at acidic pH and basic pH.

As a typical zwitterionic ligand, cysteine contains a thiol unit which can covalently link to the surface of gold nanoparticles. Taking advantage of the carboxylic acid and amine in the cysteine-structure, cysteine can be directly used for generating functionalized **AuNPs** without further modification.²⁶ As shown by Zhong *et al* (Figure 1.8),²⁷ the modified **NPs** self-assemble in a pH between 5-7, while **AuNPs** are dispersed at pH above 11 at elevated temperatures. The driving force of such self-assembly behaviour was attributed to the electrostatic interactions between the zwitterionic cysteines.

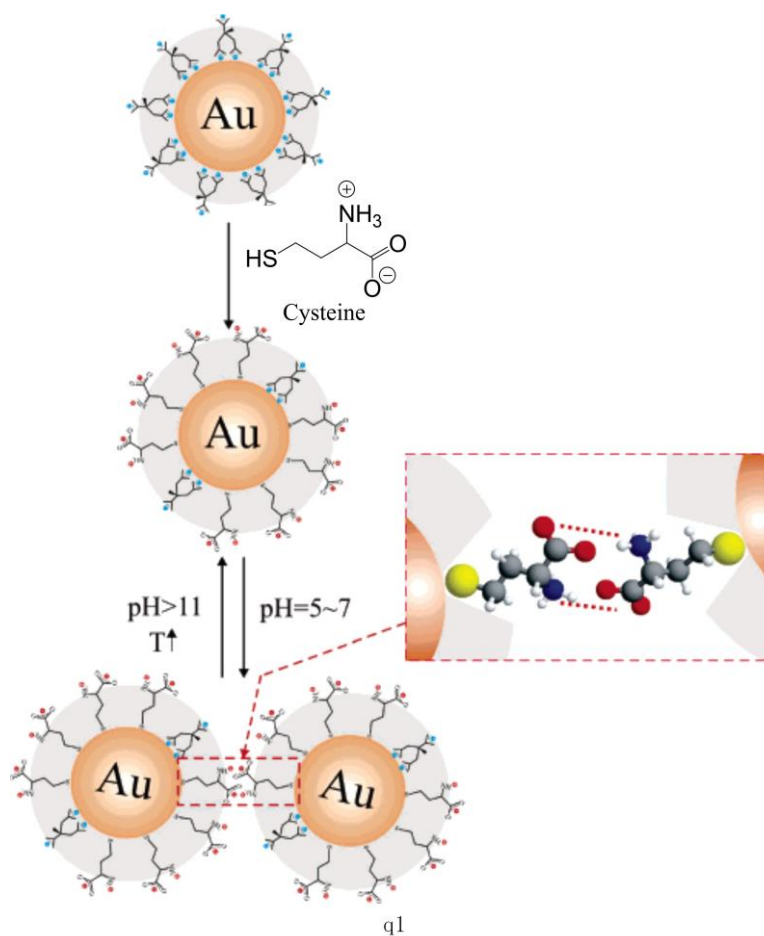


Figure 1.8: Schematic representation of pH-responsive self-assembly of cysteine-coated **AuNPs**. Adapted and reproduced with permission from the American Chemical Society, copyright 2007.²⁷

²⁶ a) A. Mocanu, I. Cernica, G. Tomoaia, L.-D. Bobos, O. Horovitz, M. Tomoaia-Cotisel, *Colloids Surf., A* **2009**, 338, 93-101. b) I. Petean, G. H. Tomoaia, O. Horovitz, A. Mocanu, M. Tomoaia-Cotisel, *J. Optoelectron. Adv. Mater.* **2008**, 10, 2289-2292.

²⁷ I.-I. S. Lim, W. Ip, E. Crew, P. N. Njoki, D. Mott, C.-J. Zhong, Y. Pan, S. Zhou, *Langmuir* **2007**, 23, 826-833.

GSH is a tripeptide (γ -Glu-Cys-Gly) containing a thiol, a positive ammonium-group and two negative carboxylates (Figure 1.9a). As a zwitterionic ligand, **GSH** was used for **NP** self-assembly by various groups.²⁸ For instance, Zhong *et al.* reported a pH-responsive self-assembly system based on **AuNPs** and **GSH**. In presence of **GSH**, **NPs** are found to assemble at $\text{pH} < 4.5$ and disassemble at $\text{pH} > 4.5$ (Figure 1.9b).²⁹ In this case, hydrogen bonds between $-\text{COOH}$ units were considered as the driving force of self-assembly. Additionally, except for hydrogen bonding, other interactions such as electrostatic interaction,³⁰ metal–ligand coordination³¹ and van der Waals force³² were also investigated as the driving force of **GSH**-involved **NPs** self-assembly.

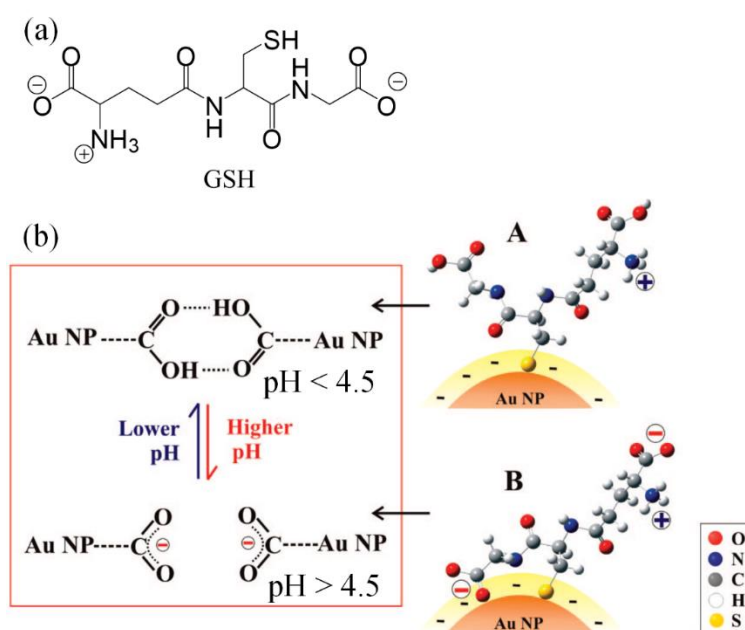


Figure 1.9: a) Molecular structure of **GSH**, b) schematic representation of pH-responsive self-assembly of **AuNPs** in presence of **GSH**. Adapted and reproduced with permission from the American Chemical Society, copyright 2008.²⁹

As discussed above, most zwitterionic ligands (such as cysteine and **GSH**) functionalized **NPs** show the similar self-assembly behaviour as acidic ligands functionalized **NPs**, which self-assemble at one pH range (lower pH) and disassemble in another specific pH range (higher pH). Unexpectedly,

²⁸ E. Moaseri, J. A. Bollinger, B. Changalvaie, L. Johnson, J. Schroer, K. P. Johnston, T. M. Truskett, *Langmuir* **2017**, *33*, 12244-12253.

²⁹ I. I. S. Lim, D. Mott, W. Ip, P. N. Njoki, Y. Pan, S. Zhou, C.-J. Zhong, *Langmuir* **2008**, *24*, 8857-8863.

³⁰ P. K. Sudeep, S. T. S. Joseph, K. G. Thomas, *J. Am. Chem. Soc.* **2005**, *127*, 6516-6517.

³¹ S. Basu, S. K. Ghosh, S. Kundu, S. Panigrahi, S. Praharaj, S. Pande, S. Jana, T. Pal, *J. Colloid Interface Sci.* **2007**, *313*, 724-734.

³² Z. Sun, W. Ni, Z. Yang, X. Kou, L. Li, J. Wang, *Small* **2008**, *4*, 1287-1292.

the disassembly of the **NPs** functionalized with zwitterionic ligands in the protonated state (at low pH) was not observed.

1.3.4 pH-responsive self-assembly based on mixed-charged ligands

Comparable to using zwitterionic ligands, functionalizing **NPs** with a binary mixture of positively and negatively charged ligands simultaneously also results in formation of mixed-charged **NPs**.³³ In this approach, the content of surface components and charges can be precisely controlled, which is one of the key techniques for further biological application of **NPs**.³⁴ Moreover, such **NPs** may show a multiple pH-sensitive self-assembly behaviour.

For example, Pillai *et al.* reported the functionalization of **NPs** with a binary mixture of 11-mercaptopundecanoic acid (**MUA**) and positively charged *N,N,N*-trimethyl-(11-mercaptopundecyl)-ammonium ion (**TMA**) (Figure 1.10a).³⁵ The ratio of **MUA** to **TMA** on **NPs** can be well controlled. As shown in Figure 1.10b, the well-designed mixed-charged **AuNPs** (**MUA/TMA** = 2.5) are stable at low pH (e.g. pH = 3). At such pH, **MUA** ligands are protonated so that **NPs** had net positive charges due to the inherently positive charged **TMA** group. The positively charged **NPs** are stable with electrostatic repulsions. Conversely, at high pH (e.g. pH = 11), **NPs** have negative charges due to the deprotonated **MUA** ligands, leading to the dispersion of **NPs**. At pH 6-7, due to the weak electrostatic repulsions, the **NPs** show self-assembly behaviour because of the Van der Waals forces between **NPs** and the hydrogen bonds between **MUA** ligands.

³³ a) X. Liu, H. Huang, Q. Jin, J. Ji, *Langmuir* **2011**, *27*, 5242-5251. b) X. Liu, Q. Jin, Y. Ji, J. Ji, *J. Mater. Chem.* **2012**, *22*, 1916-1927. c) P. J. Bonitatibus Jr, A. S. Torres, B. Kandapallil, B. D. Lee, G. D. Goddard, R. E. Colborn, M. E. Marino, *ACS Nano* **2012**, *6*, 6650-6658.

³⁴ a) P. P. Pillai, B. Kowalczyk, W. J. Pudlo, B. A. Grzybowski, *J. Phys. Chem. C* **2016**, *120*, 4139-4144. b) M. Borkowska, M. Siek, D. V. Kolygina, Y. I. Sobolev, S. Lach, S. Kumar, Y.-K. Cho, K. Kandere-Grzybowska, B. A. Grzybowski, *Nat. Nanotechnol.* **2020**, *15*, 331-341. c) X. Liu, Y. Chen, H. Li, N. Huang, Q. Jin, K. Ren, J. Ji, *ACS Nano* **2013**, *7*, 6244-6257. d) X. Liu, H. Li, Q. Jin, J. Ji, *Small* **2014**, *10*, 4230-4242.

³⁵ P. P. Pillai, S. Huda, B. Kowalczyk, B. A. Grzybowski, *J. Am. Chem. Soc.* **2013**, *135*, 6392-6395.

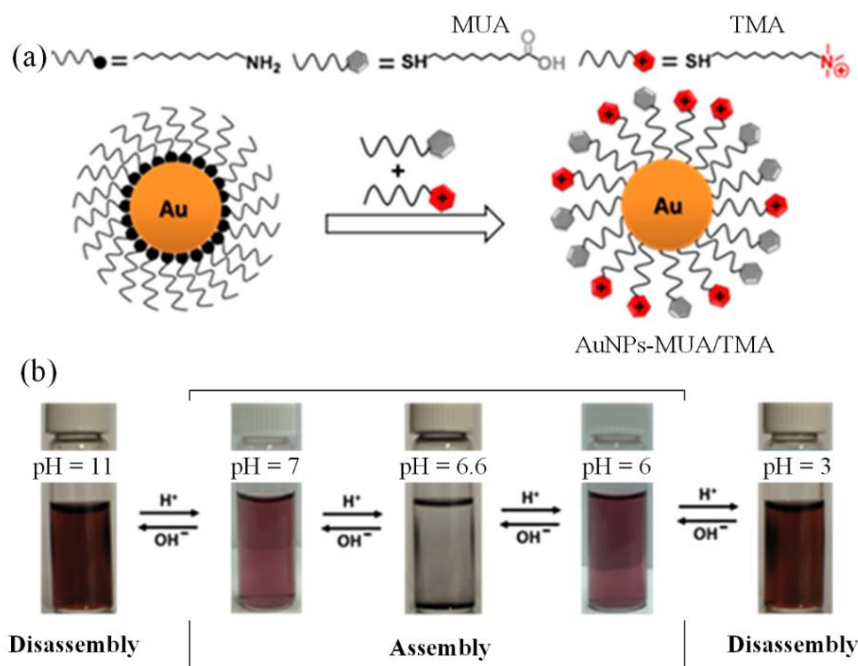


Figure 1.10: a) Scheme of functionalization of AuNPs with a mixture of MUA and TMA thiols. b) Images of mixed-charged AuNPs at different pH values (MUA/TFA = 2.5). Adapted and reproduced with permission from the American Chemical Society, copyright 2013.³⁵

As discussed above, various pH-induced reversible systems that rely on acidic or basic ligands have been designed and investigated. However, most of the reported research achieves only can be classified as mono-PSRSA, in which NPs assemble in one specific pH range but disassemble in another pH range. In contrast, a multi-pH responsive system which shows a multi-fold assembly/disassembly behaviour at different pH-borders is more attractive. A few multi-PSRSA systems based on protein or mixed-charged ligands (binary mixture of positively charged ligands and negatively charged ligands) have been reported.³⁶ However, for more “advance” zwitterionic ligands which can response to both acid and base, such as cysteine and glutathione, the design of a multi-pH responsive system is still challenging.

1.4 Template-assisted self-assembly of nanoparticles

The properties of AuNPs can be modulated by adjusting the shape, size, interparticle spacing and dielectric environment.³⁷ Self-assembly is an efficient “bottom-up” strategy for controlling the

³⁶ a) M. S. Strozyk, M. Chanana, I. Pastoriza-Santos, J. Pérez-Juste, L. M. Liz-Marzán, *Adv. Funct. Mater.* **2012**, 22, 1436-1444. b) P. P. Pillai, S. Huda, B. Kowalczyk, B. A. Grzybowski, *J. Am. Chem. Soc.* **2013**, 135, 6392-6395.

³⁷ Y. Ofir, B. Samanta, V. M. Rotello, *Chem. Soc. Rev.* **2008**, 37, 1814-1825.

properties of **NPs**. In recent years, numerous self-assembly approaches have been reported for organizing **NPs** in one, two and three dimensions, either through direct interactions or using templates indirectly.³⁸ Theoretically, templates are considered as surface-modified substrates because their intrinsic functionalized units can selectively induce nanoparticle delocalization and rearrangement. Various types of templates, such as single molecule, synthetic polymers, well-designed DNAs, and natural proteins have been used for **AuNPs** self-assembly.³⁸

Single molecular templates are easily designed and synthesized, but their application in **NP** self-assembly is challenging owing to the limited number of binding sites between the template and **NP**. However, many self-assembly systems based on stimuli-responsive molecules have been successfully developed, which demonstrates the applicability of single molecules as self-assembled templates in **NP** self-assembly.³⁹ For instance, **AuNPs** functionalized with a halogen bonding donor were found to aggregate in the presence of a single molecular self-assembled template with abundant halogen bonding acceptors on it (Figure 1.11).⁴⁰

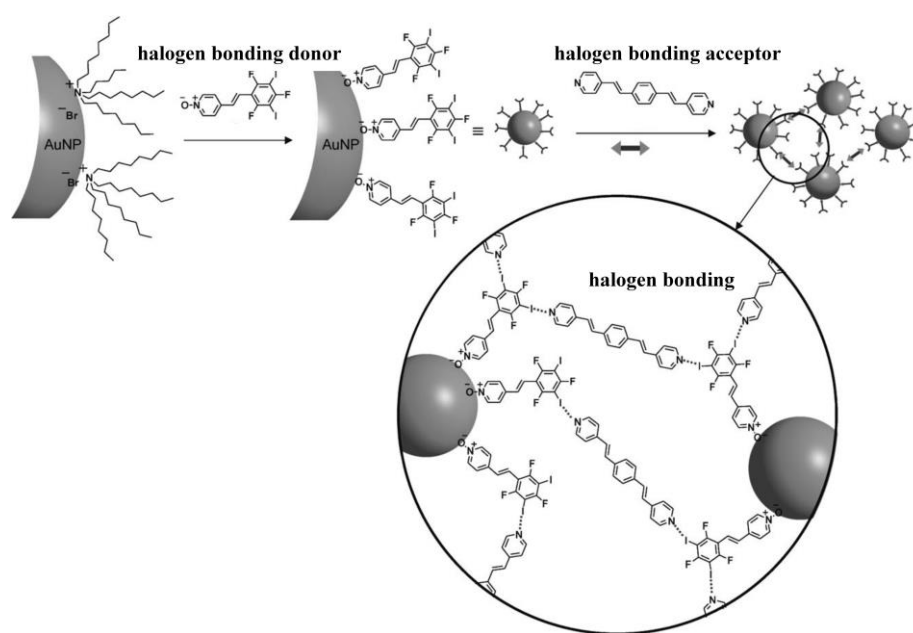


Figure 1.11: Schematic representation of self-assembly of **AuNPs** based on halogen-bonding. Adapted and reproduced with permission from the Wiley-VCH, copyright 2010.⁴⁰

DNA has become one of the most popular templates for controlling **NP** self-assembly since the concept was proposed in 1996.⁴¹ There are two categories of **NP** assembly based on DNA-templates:

³⁸ M. Grzelczak, J. Vermant, E. M. Furst, L. M. Liz-Marzán, *ACS Nano* **2010**, *4*, 3591-3605.

³⁹ K. Naka, H. Itoh, Y. Chujo, *Langmuir* **2003**, *19*, 5496-5501.

⁴⁰ T. Shirman, T. Arad, M. E. Van Der Boom, *Angew. Chem. Int. Ed.* **2010**, *49*, 926-929.

⁴¹ C. A. Mirkin, R. L. Letsinger, R. C. Mucic, J. J. Storhoff, *Nature* **1996**, *382*, 607-609.

nonspecific electrostatic and sequence-specific assemblies. The former is performed by attaching surface-modified NPs to a DNA template via electrostatic interactions.⁴² The latter takes advantage of the Watson-Crick base pairing and the materials can self-assemble into well-defined structures by DNA-based molecular recognition.⁴³ Additionally, due to helical structure of DNA, the self-assembly based on DNA templates can induce chirality in the arrangement of NPs (Figure 1.12).⁴⁴

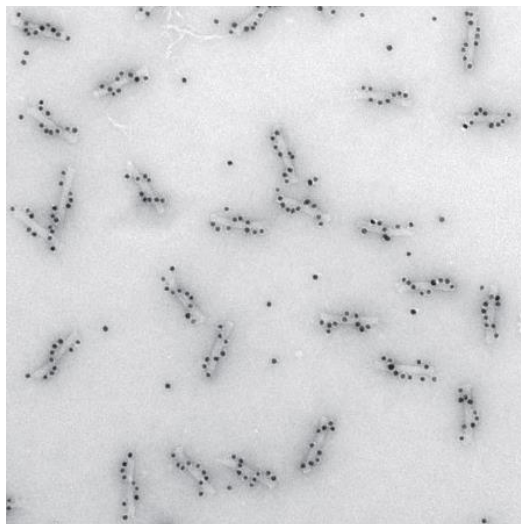


Figure 1.12: TEM image of assembled left-handed gold nanohelices by using DNA templates. Adapted and reproduced with permission from the Springer Nature BV, copyright 2012.⁴⁴

By using templates such as a single molecules or DNA, the self-assembly of NPs has been achieved on different length scales from nanometers to micrometers. In order to generate structures that feature self-assembled NPs on a macroscopic scale, polymers have been considered as hypothetical templates.⁴⁵ Despite plenty of templates have been already investigated, the discovery of novel templates with specific structure and deserved properties is still one of the excitements in NPs science.

⁴² a) H. Nakao, H. Shiigi, Y. Yamamoto, S. Tokonami, T. Nagaoka, S. Sugiyama, T. Ohtani, *Nano Lett.* **2003**, *3*, 1391-1394. b) M. G. Warner, J. E. Hutchison, *Nat. Mater.* **2003**, *2*, 272-277.

⁴³ a) N. C. Seeman, *Nature* **2003**, *421*, 427-431. b) T. A. Taton, C. A. Mirkin, R. L. Letsinger, *Science* **2000**, *289*, 1757-1760.

⁴⁴A. Kuzyk, R. Schreiber, Z. Fan, G. Pardatscher, E.-M. Roller, A. Högele, F. C. Simmel, A. O. Govorov, T. Liedl, *Nature* **2012**, *483*, 311-314.

⁴⁵ a) S. B. Darling, *Prog. in Polym. Sci.* **2007**, *32*, 1152-1204. b) A. Haryono, W. H. Binder, *Small* **2006**, *2*, 600-611. c) Y. Zhao, K. Thorkelsson, A. J. Mastroianni, T. Schilling, J. M. Luther, B. J. Rancatore, K. Matsunaga, H. Jinnai, Y. Wu, D. Poulsen, *Nat. Mater.* **2009**, *8*, 979-985.

2. Background Information

2.1 GCP binding motif

2.1.1 GCP-oxoanion binding interactions

The guanidiniocarbonyl-pyrrole (**GCP**) unit was invented and developed by Carsten Schmuck as a specific binding motif for oxoanions, especially for carboxylates on peptides.⁴⁶ As shown in Figure 2.1, **GCP** was designed based on the guanidine-unit providing two directional hydrogen bonds for binding carboxylates. The core pyrrole-unit and carboxyl amide provide additional hydrogen bond donors. The **GCP** motif shows a strong ability in binding carboxylates either in nonpolar or polar solvent, due to this specific hydrogen bond pattern, aided by additional electrostatic interactions. For instance, **GCP**-unit strongly binds to acetate with an association constant of K up to 2800 M^{-1} in a DMSO/Water (40%, v/v) mixture.⁴⁶ Moreover, the association constant between carboxylates and well-designed **GCP** motifs can reach 10^3 M^{-1} in water.⁴⁷

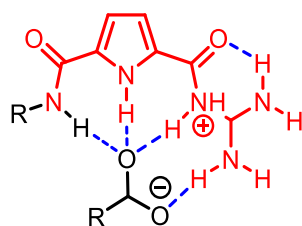


Figure 2.1: Schematic representation of the binding between **GCP** and carboxylate.

⁴⁶ C. Schmuck, *Chem. Commun.* **1999**, 843-844.

⁴⁷ C. Schmuck, L. Geiger, *J. Am. Chem. Soc.* **2005**, *127*, 10486-10487.

2.1.2 Application of GCP binding motif

Making use of its superior binding ability towards anions, **GCP** was widely applied for protein recognition⁴⁸, gene transfection⁴⁹ and other biological applications. The **GCP** motif was also used in constructing advanced materials, such as pH-switchable supramolecular gels⁵⁰ and self-assembled nanorods, nanofibers and nanoparticles.⁵¹ Samanta *et al.* designed a two-component self-assembly system based on the strong interaction between the **GCP** unit and carboxylic group (Figure 2.2).⁵¹ A flexible short dendrimer containing four **GCP** motifs **B1** was synthesized as the building block which can efficiently form a two-component self-assembly with Na₄EDTA to form supramolecular networks. The networks were observed by AFM and TEM in a pH range from 5 to 8, since the ion-pair formation between **GCP** unit and carboxylate can efficiently occur at this pH range. Either adding base or acid resulted in destroying the assembled behaviour so as to converting the nanostructure into its subunits. Thus, a self-assembled system with dual pH responsiveness was created. The above pH-sensitive self-assembly was performed in the mixture of water and DMSO, because the interactions between **GCP** and carboxylate are strong enough to trigger the self-assembly even in polar solvent.

⁴⁸ a) Q. Q. Jiang, L. Bartsch, W. Sicking, P. R. Wich, D. Heider, D. Hoffmann, C. Schmuck, *Org. Biomol. Chem.* **2013**, *11*, 1631-1639. b) Q.-Q. Jiang, W. Sicking, M. Ehlers, C. Schmuck, *Chem. Sci.* **2015**, *6*, 1792-1800. c) M. Ehlers, J.-N. Grad, S. Mittal, D. Bier, M. Mertel, L. Ohl, M. Bartel, J. Briels, M. Heimann, C. Ottmann, E. Sanchez-Garcia, D. Hoffmann, C. Schmuck, *ChemBioChem* **2018**, *19*, 591-595. d) A. Gigante, J. N. Grad, J. Briels, M. Bartel, D. Hoffmann, C. Ottmann, C. Schmuck, *Chem. Commun.* **2019**, *55*, 111-114. e) L. Bartsch, M. Bartel, A. Gigante, J. Iglesias-Fernandez, Y. B. Ruiz-Blanco, C. Beuck, J. Briels, N. Toetsch, P. Bayer, E. Sanchez-Garcia, C. Ottmann, C. Schmuck, *ChemBioChem* **2019**, *20*, 2921-2926. f) C. Vallet, D. Aschmann, C. Beuck, M. Killa, A. Meiners, M. Mertel, M. Ehlers, P. Bayer, C. Schmuck, M. Giese, S. K. Knauer, *Angew. Chem. Int. Ed.* **2020**, *59*, 5567-5571.

⁴⁹ a) H. Y. Kuchelmeister, A. Gutschmidt, S. Tillmann, S. Knauer, C. Schmuck, *Chem. Sci.* **2012**, *3*, 996-1002. b) S. Junghanel, S. Karczewski, S. Backer, S. K. Knauer, C. Schmuck, *ChemBioChem* **2017**, *18*, 2268-2279. c) K. Samanta, P. Jana, S. Backer, S. Knauer, C. Schmuck, *Chem. Commun.* **2016**, *52*, 12446-12449. d) M. Li, M. Ehlers, S. Schlesiger, E. Zellermann, S. K. Knauer, C. Schmuck, *Angew. Chem. Int. Ed.* **2016**, *55*, 598-601. e) P. Jana, K. Samanta, S. Backer, E. Zellermann, S. Knauer, C. Schmuck, *Angew. Chem. Int. Ed.* **2017**, *56*, 8083-8088.

⁵⁰ D. Aschmann, S. Riebe, T. Neumann, D. Killa, J.-E. Ostwaldt, C. Wölper, C. Schmuck, J. Voskuhl, *Soft Matter* **2019**, *15*, 7117-7121.

⁵¹ K. Samanta, C. Schmuck, *Chem. Commun.* **2015**, *51*, 16065-16067.

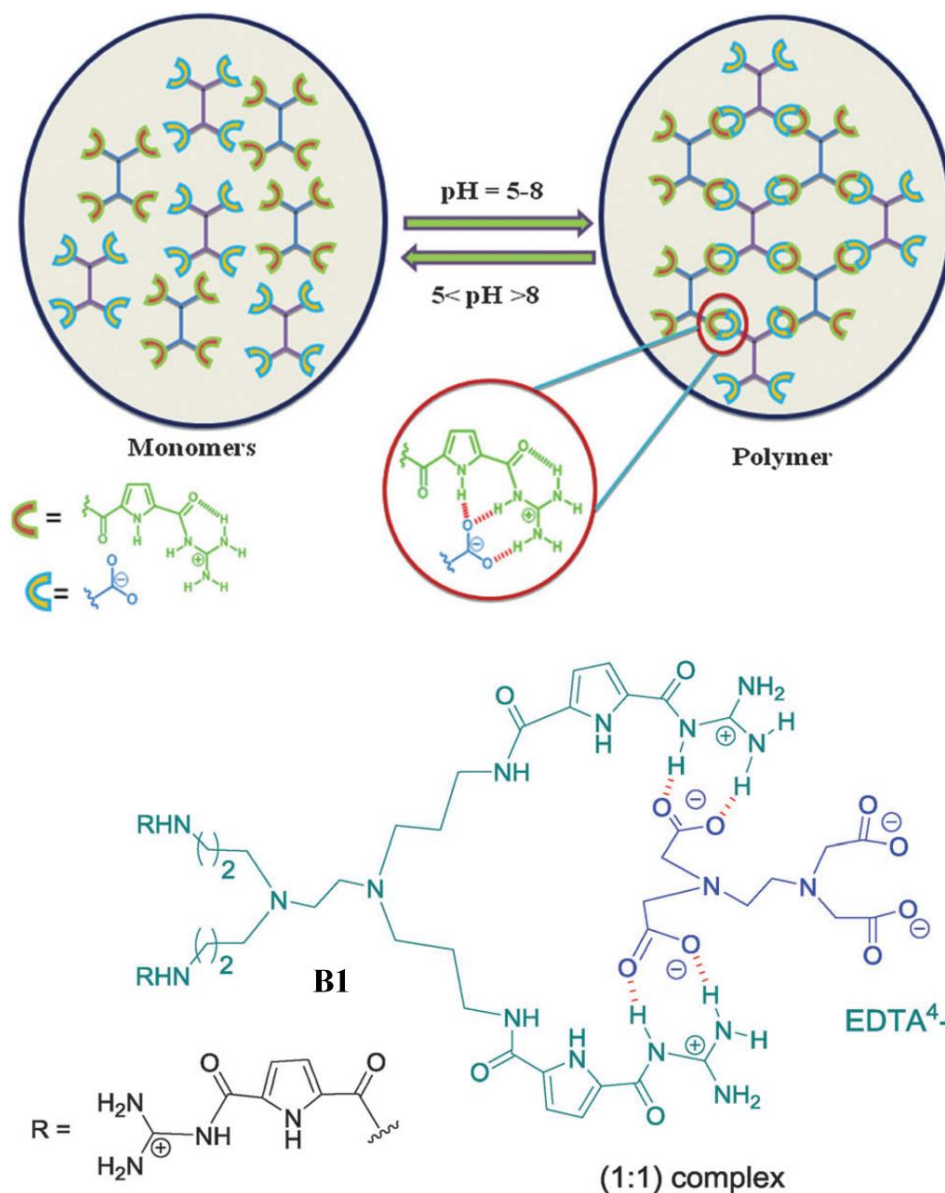


Figure 2.2: Two-component self-assembly of **B1** and Na₄EDTA leads to supramolecular networks which exhibit dual pH responsiveness. Adapted and reproduced with permission from the Royal Society of Chemistry, copyright 2015.⁵¹

2.2 GCPZ binding motif

2.2.1 Self-association of GCPZ binding motif

As a self-complementary motif, guanidiniocarbonyl pyrrole carboxylate zwitterion (**GCPZ**) was designed by Carsten Schmuck in 1999.⁵² Bearing the cationic guanidinium-unit and an anionic carboxylate, **GCPZ** is able to form a stable head-to-tail dimer with high association constant in

⁵² C. Schmuck, *Eur. J. Org. Chem.* **1999**, 2397-2403.

DMSO (10^{12} M^{-1})⁵² and even in water (170 M^{-1})⁵³. Remarkably, the self-association of **GCPZ** is pH-switchable (Figure 2.3). Owing to the highly complementary hydrogen bonds and electrostatic interactions, two the **GCPZ** units tend to dimerize in a pH range of 5-8. However, the dimerization is suppressed at pH values below 5 or above 8 due to the presence of unfavourable electrostatic repulsion.

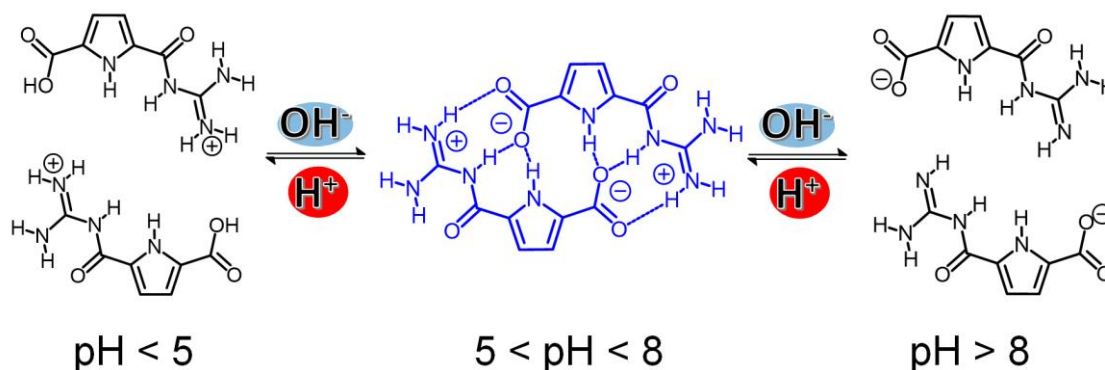


Figure 2.3: Schematic representation of pH switchable self-association of **GCPZ**.

2.2.2 Application of **GCPZ** binding motif

The pH-dependant self-complementarity enables the **GCPZ** motifs to be applied in the area of material science, such as stimuli-responsive nanomaterials, supramolecular gels and polymer modifications.⁵⁴

For instance, Hisamatsu *et al.* reported a supramolecular gel based on the self-assembly of low-molecular-weight organic molecules (Figure 2.4).⁵⁵ A building block containing a tetrahedral pentaerythritol core and four **GCPZ** arms was designed and synthesized. The investigation with respect to its aggregation and gelation was performed in DMSO. At low concentrations (0.1 mM), building block **B2** exists in the monomeric form, with two pairs of intramolecular ion pairs among the four zwitterionic arms. With increasing concentration (1-25 mM), intermolecular polymeric species of **B2** was formed due to the interactions between **GCPZ** motifs. Upon further increasing

⁵³ C. Schmuck, W. Wienand, *J. Am. Chem. Soc.* **2003**, *125*, 452-459.

⁵⁴ a) C. Schmuck, *Synlett* **2011**, 1798-1815; b) T. Fenske, H.-G. Korth, A. Mohr, C. Schmuck, *Chem. Eur. J.* **2012**, *18*, 738-755. c) P. Jana, C. Schmuck, *Chem. Eur. J.* **2017**, *23*, 320-326; d) M. Externbrink, S. Riebe, C. Schmuck, J. Voskuhl, *Soft Matter* **2018**, *14*, 6166-6170. e) G. Gröger, V. Stepanenko, F. Würthner, C. Schmuck, *Chem. Commun.* **2009**, 698-700; f) G. Gröger, W. Meyer-Zaika, C. Böttcher, F. Gröhn, C. Ruthard, C. Schmuck, *J. Am. Chem. Soc.* **2011**, *133*, 8961-8971; g) K. Grossert, W. Sicking, E. Zellermann, C. Schmuck, *Supramol. Chem.* **2018**, *30*, 395-403.

⁵⁵ Y. Hisamatsu, S. Banerjee, M. B. Avinash, T. Govindaraju, C. Schmuck, *Angew. Chem. Int. Ed.* **2013**, *52*, 12550-12554.

concentrations to 40 mM, the systems began to gelate. The strong pH dependent self-association property of the **GCPZ** unit resulted in a reversible switching ability from gel to sol by addition of base or acid. In addition, the supramolecular gel showed a temperature responsiveness, where heating (100°C) resulted in the corresponding sol and cooling reformed the gel state again.

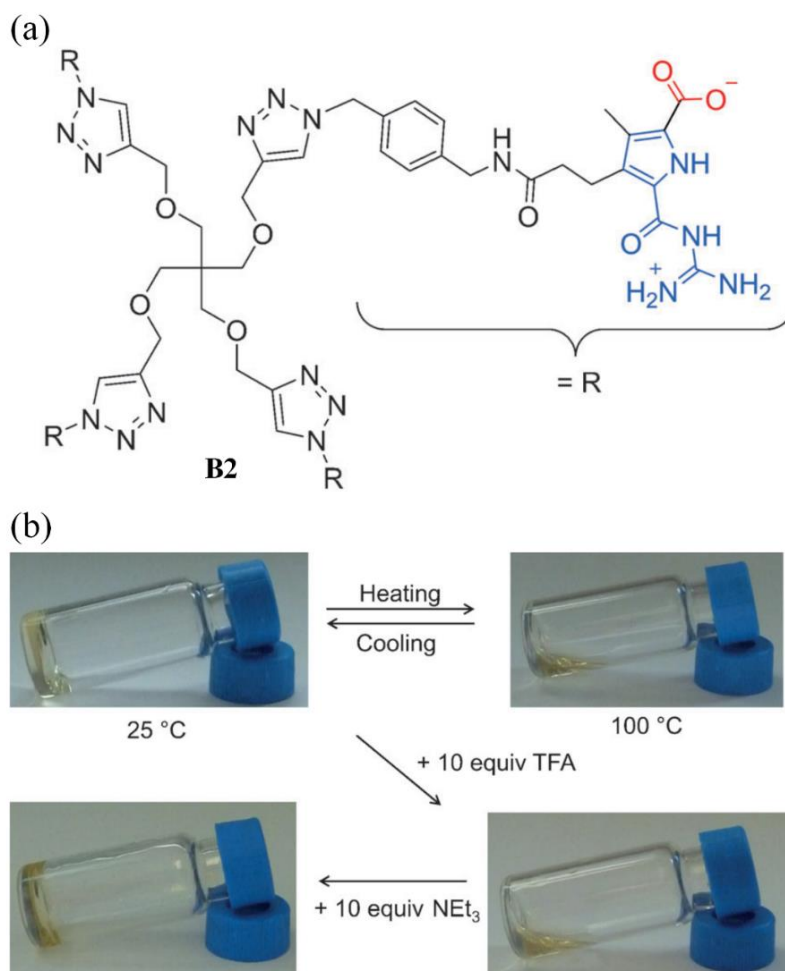


Figure 2.4: a) Gelator **B2** based on quadruple **GCPZ**, b) photo of reversible gel–sol transitions of a gel of **B1** in DMSO upon heating/cooling and addition of acid/base. Adapted and reproduced with permission from the Wiley-VCH, copyright 2013.⁵⁵

2.2.3 Solubility of GCPZ binding motif

GCPZ is a versatile binding motif, not only because of its pH-dependent self-association, but also because of its varying solubility in different protonation states. In 1999, the first synthesized **GCPZ** binding motif (without any additional substituents on the pyrrole core) showed a pH-dependent solubility.⁵⁶ Protonated **GCPZ** is soluble in methanol or DMSO and can be recrystallized from water. In contrast, zwitterionic **GCPZ** is virtually insoluble in all solvents other than DMSO, due

⁵⁶ C. Schmuck, *Eur. J. Org. Chem.* **1999**, 2397-2403.

to the formation of the overall neutral self-complementary pair. Finally, deprotonated **GCPZ** shows a good solubility in methanol and water.

The poor solubility in water limits the application of the **GCPZ** binding motif in biological science. In order to improve the water solubility of **GCPZ**-containing molecules, different water-soluble units were introduced. For the mono **GCPZ** unit, two triethylene glycol (**TEG**) chains were attached to the pyrrole ring to improve its solubility in aqueous solvents (Figure 2.5).⁵⁷ This **TEG** modified **GCPZ** molecule, **B3**, has a high solubility in water.

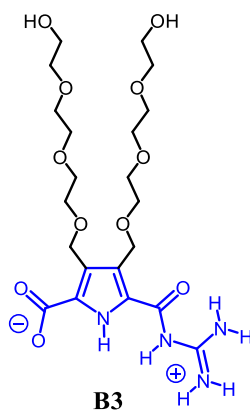


Figure 2.5: TEG modified **GCPZ** building block **B3**.

Since the hydroxyl-terminated ethylene-glycols enhance the solubility in water, a new strategy for design of water-soluble **GCPZ** was developed by using polyglycerol dendrons.⁵⁸ The **GCPZ** unit was attached by click reaction to biocompatible first-generation to third-generation [**G1-G3**] polyglycerol dendrons, resulting in the dendrons **B4**, **B5** and **B6** (Figure 2.6), which possess either 4, 8, or 16 hydroxy-groups on the terminus. As expected, second generation and third generation zwitterionic dendrons **B5** and **B6** are extremely easy to dissolve in water, while the first generation zwitterionic dendrons **B4** which has four hydroxyl groups was not soluble in water.

⁵⁷ C. Schmuck, W. Wienand, *J. Am. Chem. Soc.* **2003**, *125*, 452-459.

⁵⁸ M. Merschky, M. Wyszogrodzka, R. Haag, C. Schmuck, *Chem. Eur. J.* **2010**, *16*, 14242-14246.

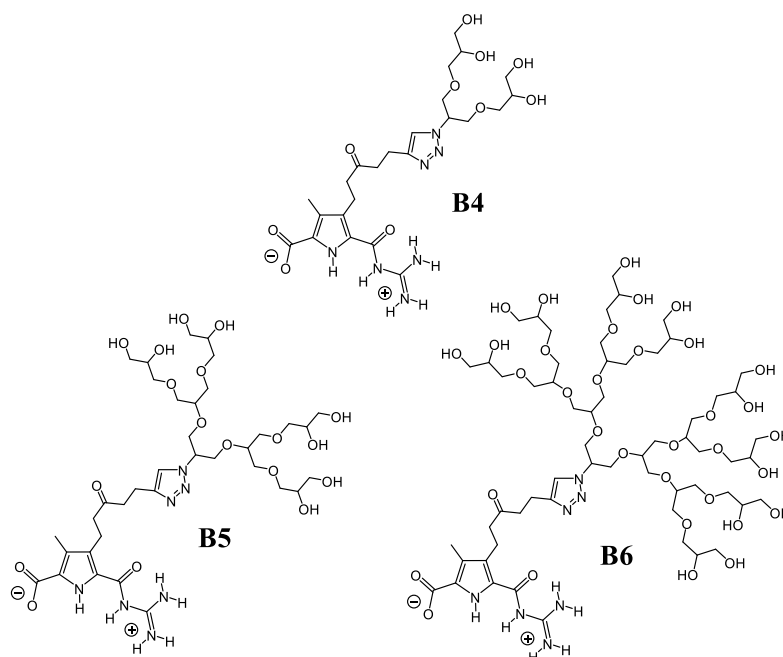


Figure 2.6: Molecular structure of polyglycerol dendrons modified **GCPZ** motif **B4**, **B5** and **B6**.

Besides hydroxy-groups, charged ammonium-units, were also used to improve the water solubility of the molecule featuring **GCPZ** units. Fleischer *et al.* synthesized a **GCPZ** modified polyethylenimine **B7** which is soluble in aqueous solution (Figure 2.7).⁵⁹ The loading of **GCPZ** binding motifs in **B7** was determined as 40%, and its water solubility can be attributed to the 60% of residual amino groups.

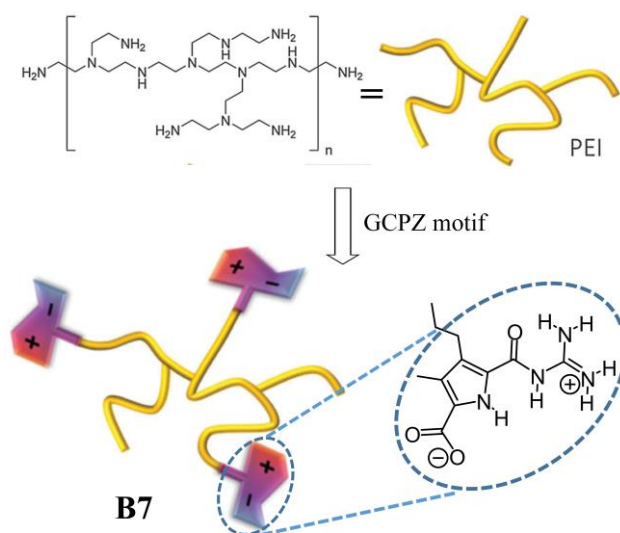


Figure 2.7: Schematic representation of **GCPZ** motifs modified PEI. Adapted and reproduced with permission from the Royal Society of Chemistry, copyright 2014.⁵⁹

⁵⁹ M. Fleischer, C. Schmuck, *Chem. Commun.* **2014**, 50, 10464-10467.

3. Project and Objective

The aim of this dissertation is to develop novel systems for the self-assembly of **NPs** based on noncovalent interactions, especially using **GCP** and **GCPZ** as binding motifs. Besides new multi-**PSRSA** systems, the directed self-assembly of **NPs** onto a template will be developed. Moreover, the mechanism of the self-assembly of metallic nanoparticles, the role of the attached binding motifs and the importance of different noncovalent interactions for the assembly will be investigated.

AuNPs are used as the nanoparticle core throughout these investigations due to their large surface, controllable size and their ability to be modified on the surface easily with different desirable functionalities. The self-assembly of modified **AuNPs** is characterized using UV/Vis, DLS, SEM and TEM to verify and determine the functionalities on the surface as well as to illustrate the particle's physical properties and the aggregation behaviour.

3.1 Dual pH-sensitive reversible self-assembly of gold nanoparticles

The aim of this project is to take advantage of the special properties of **GCPZ** as the functional motif. Due to its special dual pH responsiveness and extremely strong ionic hydrogen bonding between two **GCPZ** motifs, a dual pH-sensitive self-assembly system can be designed. To achieve this goal, the surface of gold nanoparticles should be modified with **GCPZ** motifs. The functionalized **GCPZ** ligands (Figure 3.1) are designed to be composed of three subunits: the thiol group for linking to the **AuNP** surface and stabilizing the **AuNP** core, the flexible linker for solubility and flexibility improvement and the **GCPZ** motif for providing the noncovalent interactions for self-assembly. Non-**GCPZ** functionalized molecule **N** with the terminal hydroxyl is chosen as a control and background ligand. The functionalized **AuNPs** are prepared by using thiol ligand-exchange reaction on the surface.

The pH-induced self-assembly behaviour of functionalized **AuNPs** is investigated in different neat solvents but also in solvent mixtures. The interactions between the **AuNPs** are adjusted by varying the concentration of **GCPZ** motifs on **AuNPs** and changing the contents of the mixed solvent. The mechanism of self-assembly is studied in detailed.

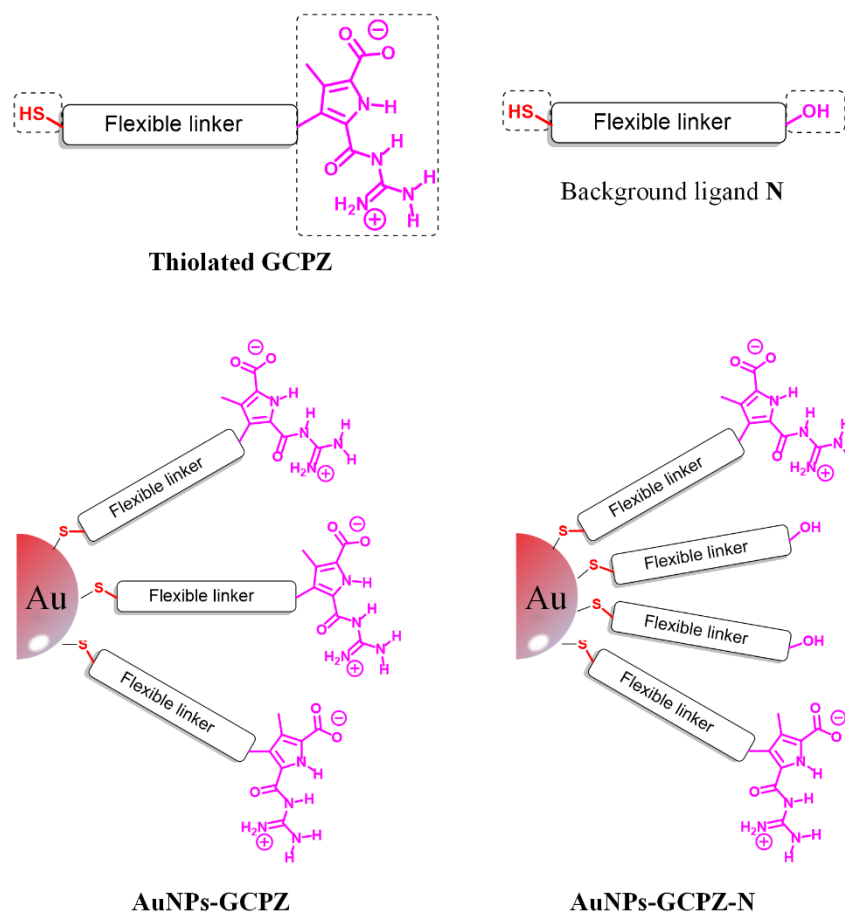


Figure 3.1: Schematic representation of the structure of the thiolated **GCPZ** ligand, background ligand **N**, **GCPZ** functionalized gold nanoparticles (**AuNPs-GCPZ**) and **GCPZ/N** co-functionalized gold nanoparticles (**AuNPs-GCPZ-N**).

3.2 Multiple pH-sensitive reversible self-assembly of gold nanoparticles

In this project, a **GCP** motif with cationic guanidinium but without carboxylate unit is added in addition to the **GCPZ**-ligands on **AuNPs** in order to develop a multi-**PSRSA** system in aqueous solvents. In order to achieve this goal, a **GCP** ligand containing a thiol group, a triethylene glycol chain and a **GCP** unit is designed. For functionalization, the **AuNPs** functionalized with both **GCPZ** and **GCP** ligands modified (**AuNPs-GCPZ-GCP**) are prepared and characterized (Figure 3.2). The multi-**PSRSA** of such functionalized **AuNPs** is investigated in water and monitored using UV/Vis, DLS and TEM measurement. Moreover, the temperature sensitive self-assembly behaviour of **GCP** and **GCPZ** functionalized **AuNPs** is investigated. The influence about the **GCPZ/GCP** ratio on the **AuNPs** surface impacting on the self-assembly behaviour are also studied. After developing the multi-**PSRSA** system, the application of such system will be explored, such as removing toxic metal ions form the solution.

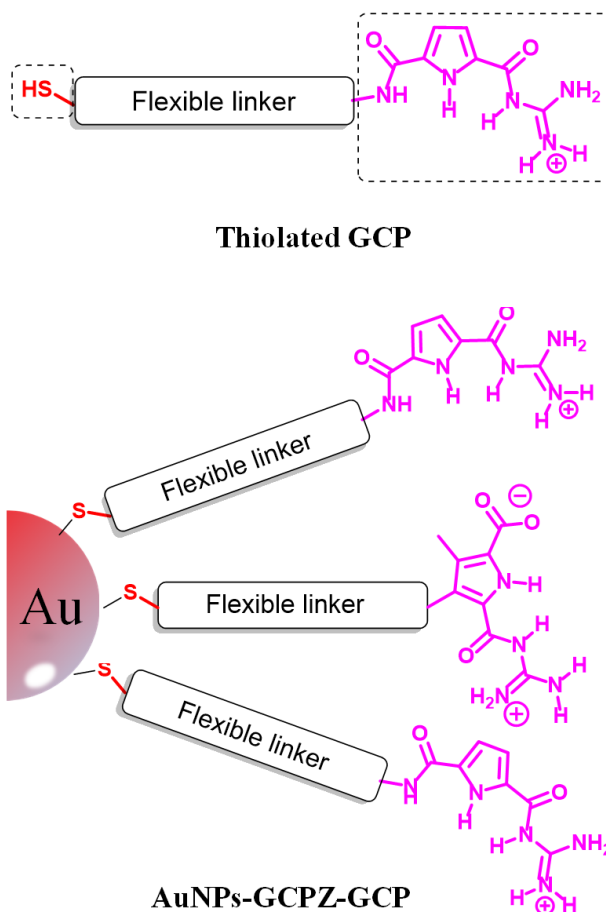


Figure 3.2: Schematic representation of the structure of the thiolated **GCP** ligand and **GCPZ/GCP** co-functionalized gold nanoparticles (**AuNPs-GCPZ-GCP**).

3.3 One dimensional arrangement of gold nanoparticles

This project focuses on developing a template that can be used for the self-assembly of **NPs** via supramolecular interactions. The aim of this project is to achieve a one-dimension (**1D**) arrangement of **AuNPs**. The template itself is made by supramolecular self-assembly of molecular building blocks, so that a self-assembly on two hierarchical levels (self-assembly of the template, then self-assembly of **NPs** on the template) leads to the desired final structure. Therefore, the design and synthesis of a molecule which can self-assemble to a linear architecture stands were investigated first. The design of this compound is based on two subunits, one aromatic core to assist the formation of nanofibers via π - π -stacking and **GCP** motifs to improve water solubility and provide hydrogen bonding donors of attachment of the **NPs** (Figure 3.3). The synthesis of the desired template molecule was performed in collaboration with Mr. Dennis Aschmann and Mr. Thorben Neumann. In order to make sure that **AuNPs** could attach to the self-assembled template, the surface of **AuNPs** should be decorated with carboxylate-groups, which allow an interaction with the **GCP**-functionalized template. After that, the important step is to control the hierarchical self-assembly of

the template itself and the **NPs** on the template, so that an optimal **1D** arrangement of **AuNPs** can be achieved. This was investigated by various measurements, such as AFM, TEM and SEM.

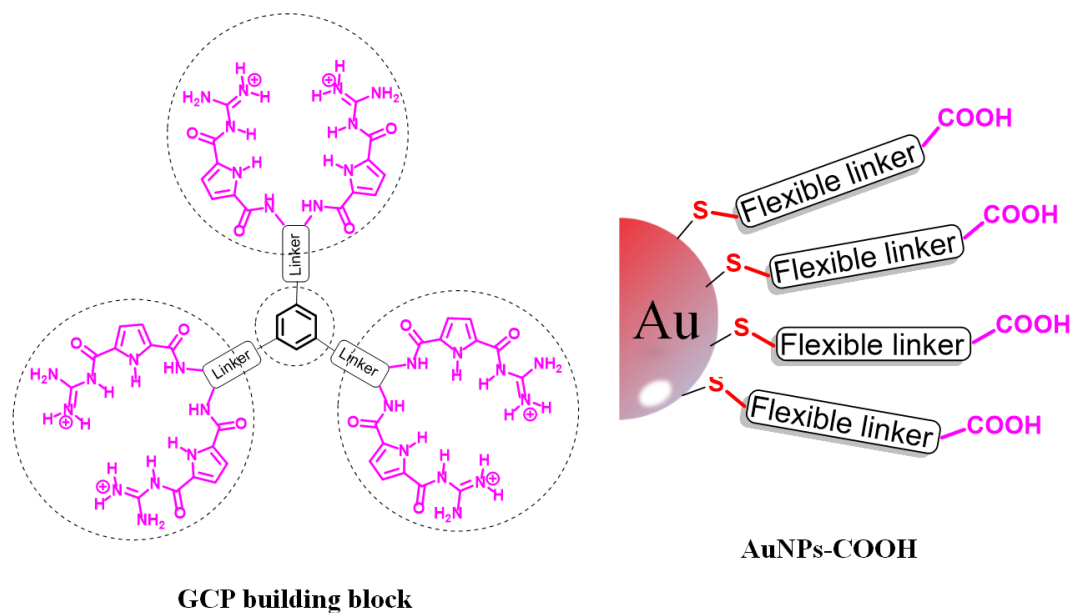


Figure 3.3: Schematic representation of a six-GCPs containing molecule and carboxylic acids functionalized gold nanoparticles (**AuNPs-COOH**).

4. Dual pH-Sensitive Reversible Self-Assembly of Gold Nanoparticles

4.1 Introduction

In this chapter, we report the dual-PSRSA of AuNPs based on their decoration with the self-complementary GCPZ ligands. The assembly of such functionalized AuNPs was found at neutral pH due to the supramolecular pairing of the GCPZ groups. The resulting self-assembled system can be switched back to the disassembled state by adjusting the pH values.

4.2 Results and discussion

4.2.1 Synthesis of thiolated GCPZ derivative

In order to functionalize AuNPs, the thiolated GCPZ derivative (**1**) was synthesized over 9 steps. A triethylene glycol (TEG) chain was introduced to improve the solubility and supply the flexibility. As shown in Figure 4.1, commercially available triethylene glycol was reacted with 3-bromoprop-1-ene in the presence of sodium hydroxide as the base to give the monoether (**8**) which was purified by column chromatography to remove the diether. This compound was again alkylated with ethyl bromoacetate in the presence of the strong base sodium hydride to give the ester (**9**). After that saponification of the ethyl ester group with aqueous lithium hydroxide was carried out in the mixture of THF to afford the carboxylic acid (**10**). The compound **10** then coupled with *tert*-butyl (2-aminoethyl) carbamate in a mixture of DMF and THF by using PyBOP as an amidation reagent and DIPEA as a base to give the Boc-protected amine (**11**). The subsequent addition reaction of thioacetic acid to the terminal olefin of **11** (thiol ene reaction) was performed in the presence of azobis(isobutyronitrile) (AIBN) in MeOH under reflux to afford thioacetate (**12**). This compound then followed a Boc-deprotection in TFA to give the TFA salt (**13**). The TFA salt (**13**) was coupled with the GCPZ motif⁶⁰ in a mixture of DMF and THF in presence of PyBOP and DIPEA to give the protected GCPZ ligand (**14**). The thiol ester group of this compound was cleaved off by hydrolyzation with LiOH to give free thiol GCPZ ligand (**15**). In the last step, TFA was used to remove the Boc group to obtain the desired thiolated GCPZ (**1**).

⁶⁰ Y. Hisamatsu, S. Banerjee, M. B. Avinash, T. Govindaraju, C. Schmuck, *Angew. Chem. Int. Ed.* **2013**, *52*, 12550-12554.

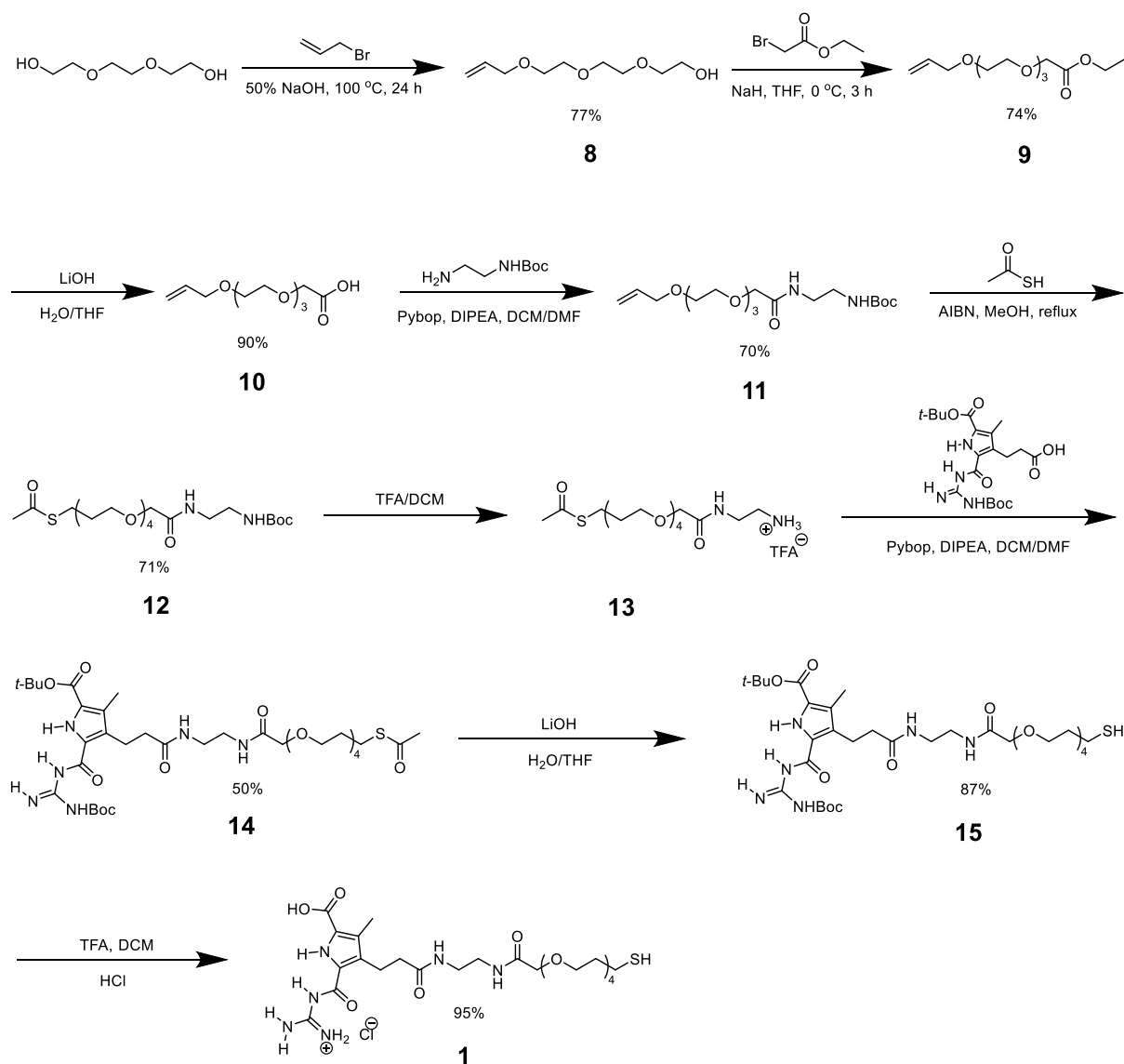


Figure 4.1: Synthetic scheme of the thiolated GCPZ derivative (**1**)

4.2.2 Synthesis of thiolated TEG ligand

The thiolated TEG (**2**) was synthesized as an uncharged background ligand. As shown in Figure 4.2, the synthesis started from the addition reaction of thioacetic acid to the terminal olefin of **8** in the presence of AIBN in MeOH under reflux to afford thioacetate (**16**). After that, this thioacetate compound was acidified to give the free thiol product in a yield of 80% (**2**).

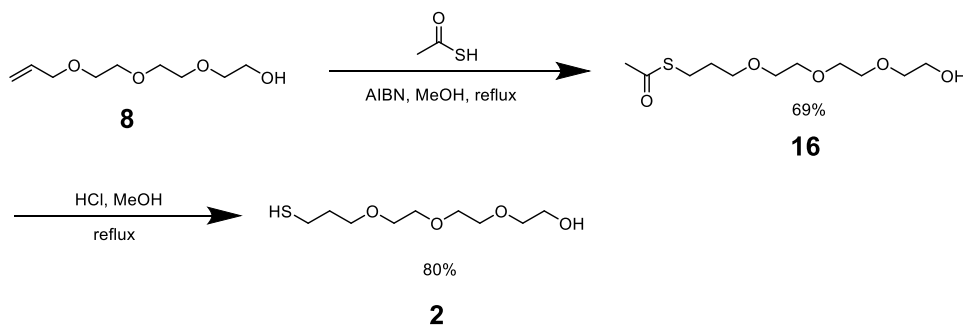


Figure 4.2: Synthetic scheme of the thiolated TEG ligand (2)

4.2.3 Synthesis of thiolated carboxylic acid ligand

The thiolated carboxylic acid (3) was synthesized to obtain an additional ligand which is easy to charge negatively under neutral and basic conditions. As shown in Figure 4.3, the addition of thioacetic acid to the terminal olefin of **9** was performed in the presence of AIBN in MeOH under reflux to receive the thioacetate (17). In the next step, the thiol ester group of this compound was cleaved off by hydrolysis with LiOH to give the desired thiolated carboxylic acid (3).

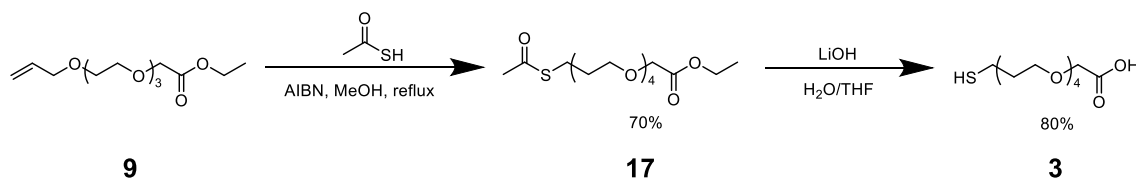


Figure 4.3: Synthetic scheme of the thiolated carboxylic acid (3)

4.2.4 Preparation of gold nanoparticles

Compared to thiol stabilized AuNPs, the place-exchange reaction is much easier on amine-protected AuNPs due to the weaker interaction between AuNPs and an amine ligand. In our project, gold nanoparticles were synthesised in toluene according to a modified literature procedure.⁶¹ For the preparation of AuNPs, tetrabutylammonium borohydride (TBAB) and hydrazine were used as reducing agents, dodecylamine (DDA) and didodecyldimethylammonium bromide (DDAB) were used as stabilizers. As shown in Figure 4.4, prepared AuNPs show a mean size of 7.2 nm and have a narrow size distribution. These could subsequently be used for functionalization with thiol-based ligands.

⁶¹ R. Klajn, K. J. M. Bishop, B. A. Grzybowski, *Proc. Natl. Acad. Sci. USA* **2007**, *104*, 10305-10309.

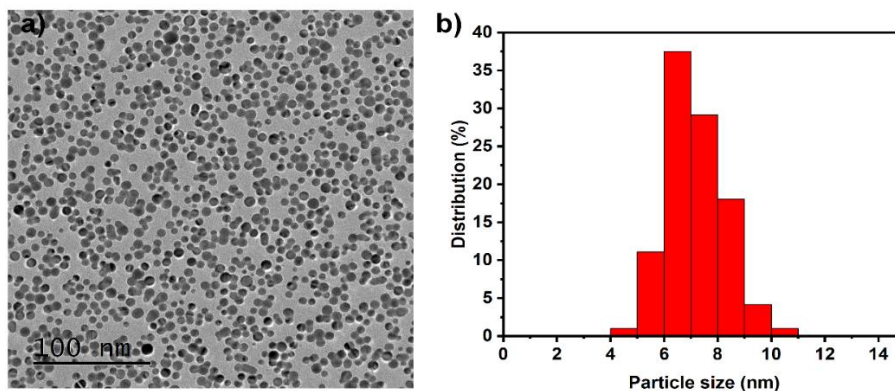


Figure 4.4: a) TEM image and b) Size-distribution histograms of **DDA**-coated **AuNPs** prepared in toluene solution. Adapted and reproduced with permission from the Wiley-VCH, copyright 2020.⁶²

4.2.5 Functionalization of gold nanoparticles

Four types of functionalized **AuNPs** were prepared, the **GCPZ** functionalized **AuNPs-1**, the **TEG** functionalized **AuNPs-2**, the carboxyl functionalized **AuNPs-3** and the **GCPZ/TEG** co-functionalized **AuNPs-1-2**. For the **AuNPs** modified with a single ligand (**AuNPs-1**, **AuNPs-2** and **AuNPs-3**), the functionalization was performed by using the place-exchange reaction with an excess of functional thiol ligands. For the **AuNPs** modified with two different ligands (**AuNPs-1-2**), a modification of a literature-procedure⁶³ was used for functionalization. As shown in Figure 4.5, in the first step, **DDA** coated **AuNPs** were functionalized with the β equivalent of **GCPZ** ($\beta < 1$; equivalent to the number of Au binding sites) under vortex for 30 minutes. Then, $1 - \beta$ equivalent of **TEG** was introduced, and the mixture was vortexed for another 30 minutes. The functionalized **AuNPs** were washed with methanol to remove the remaining unbound ligands. The concentration of **1** was altered by functionalizing the **AuNPs** in the presence of different ratios of ligand **1** and ligand **2** (see experiment section for details).

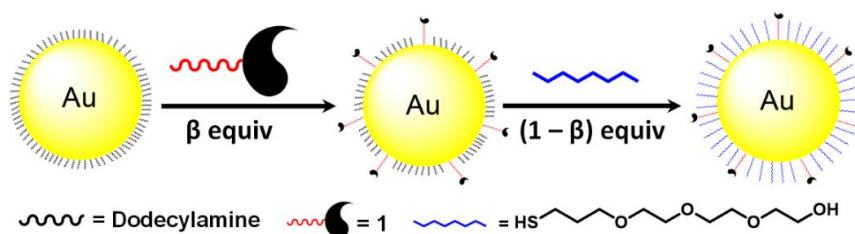


Figure 4.5: Schematic representation of two step functionalization of **AuNPs** with thiolated **GCPZ** (**1**) and **TEG** ligands (**2**).

⁶² H. He, J. E. Ostwaldt, C. Hirschhäuser, C. Schmuck, J. Niemeyer, *Small* **2020**, *16*, 2001044.

⁶³ Z. Chu, Y. Han, T. Bian, S. De, P. Král, R. Klajn, *J. Am. Chem. Soc.* **2019**, *141*, 1949-1960.

Thus, the amount of **GCPZ**-containing ligand on the surface of the **NPs** could be controlled. Since the surface coverage might differ from the number β used for the functionalization, it is important to determine the content of the **GCPZ**-containing ligand experimentally. Typically, $^1\text{H-NMR}$ was used to determine the amount of ligand on **NPs**, but a disadvantage of this measurement is the requirement of high concentrations of **AuNPs**. Therefore, UV/Vis measurement was also used due to the advantage of high accuracy and simple operation. However, such measurement is only suitable for the ligands with an UV/Vis absorption.

In this project, we used actual molar fraction θ of the **GCPZ**-containing ligand **1** to characterize the composition of the ligands on **AuNPs-1-2**. UV/Vis measurements were used to determine the value θ based on the absorption band of pyrrole at 308 nm. The values θ was calculated as $\theta = N_1 / N_s$, where the N_1 and N_s are representing the number of **1** on **NP** and the number of binding sites on **Au**. In order to determine the number of **1** on **NP** we determined the molar absorptivity (ϵ) of **1** by recording a series of UV/Vis absorption spectra of solutions of **1** in water (pH=11) at different concentrations (Figure 4.6; $\epsilon = 2.32 \cdot 10^4 \text{ M}^{-1}\text{cm}^{-1}$).

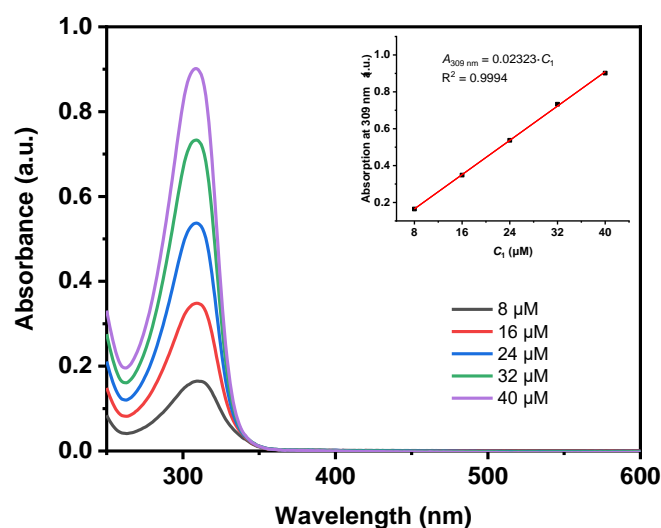


Figure 4.6: UV/Vis absorption spectra of aqueous solutions (pH = 11) of **1** at different concentrations. Optical path length = 10 mm. Adapted and reproduced with permission from the Wiley-VCH, copyright 2020.⁶²

The number of **1** on a **AuNP** was subsequently determined using equation 4-1.

$$N_1 = \frac{A_1 - A_2}{\epsilon \times C_{NP}} \quad (4-1)$$

A_1 and A_2 represent the absorbance of **AuNPs-1** (or **AuNPs-1-2**) and **AuNPs-2** at 309 nm, respectively, C_{NP} is the concentration of **AuNPs** in the solution, here, $C_{NP} = 68 \text{ nM}$.

The number of binding sites on Au was determined as equation 4-2 by fully covered **AuNPs-1**.

$$N_s = \frac{A_{1f} - A_2}{\epsilon \times C_{NP}} \quad (4-2)$$

Where A_{1f} represents the absorbance of fully covered **AuNPs-1** at 309 nm.

According to equation 4-1 and equation 4-2, the actual molar fraction of **1** (θ) can be calculated as equation 4-3.

$$\theta = \frac{N_1}{N_s} = \frac{A_1 - A_2}{A_{1f} - A_2} \quad (4-3)$$

The UV/Vis spectra of **AuNPs** with different θ in Figure 4.7a confirm that our functionalization procedure allows us to control the molar fraction of **GCPZ** on **AuNPs**. The markers in Figure 4.7b denote the dependence of θ on β for **NPs** functionalization. The θ was increasing with higher β , while there was a deviation between θ and β . This suggests that not all **GCPZ** ligands in solution could be attached on the surface of **AuNPs**. We also found that this deviation increased with even higher values of β which may be caused by different factors the steric demand of **GCPZ** ligands.

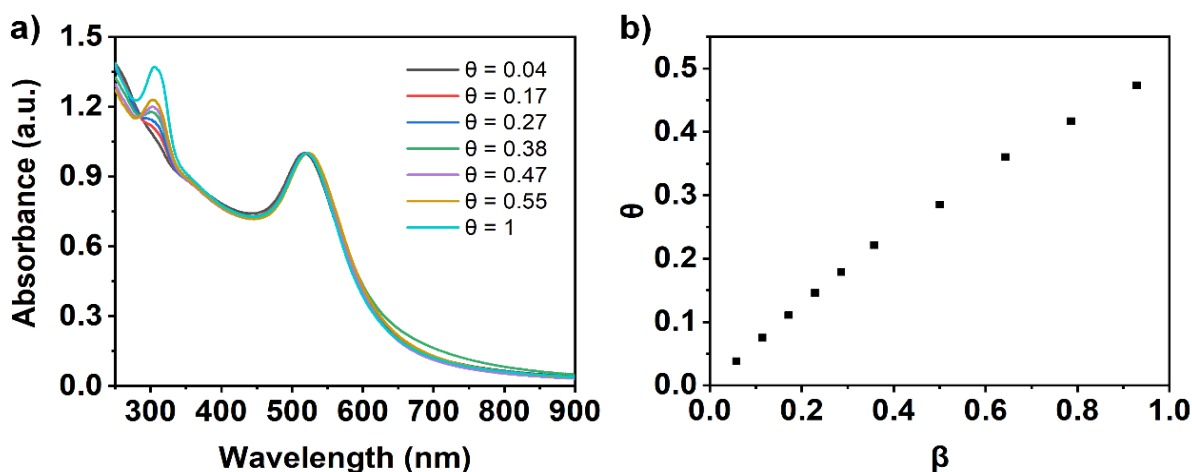


Figure 4.7: a) UV/Vis absorption spectra of **AuNPs-1-2** at different θ value. b) Dependence of θ on β for **NPs** functionalization. Adapted and reproduced with permission from the Wiley-VCH, copyright 2020.⁶²

4.2.6 Self-assembly of **AuNPs-1**

After the successful preparation of **GCPZ** functionalized **AuNPs**, we started to investigate the pH-sensitive self-assembly behaviour of **AuNPs-1**. At first, DMSO was chosen as one solvent due to the good solubility of **GCPZ** motifs in this solvent. In addition, water was also necessary due to the pH-switching which was performed by adding aqueous HCl or NaOH. Therefore, in this project, a mixture of DMSO and water was used for controlling and adjusting the reversible self-assembly. Induced by the **GCPZ** groups, a neutralization of the solution triggers the assembly of the

functionalized **AuNPs**, and the resulting self-assembled system can be switched back to the disassembled state by addition of acid or base (inducing protonation or deprotonation of the **GCPZ** ligands, Figure 4.8).

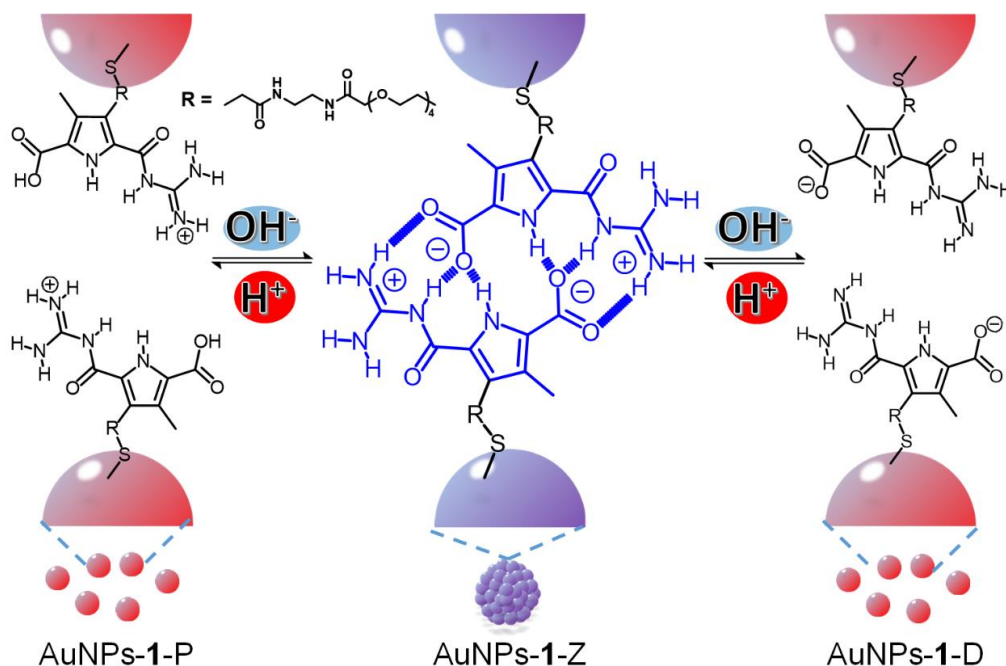


Figure 4.8: Schematic representation of the dual-PSRSA behaviour of **AuNPs-1**. Adapted and reproduced with permission from the Wiley-VCH, copyright 2020.⁶²

4.2.6.1 UV/Vis measurement

UV/Vis measurements were used to monitor the self-assembly process based on the strong **SPR** band of gold nanoparticles, which is sensitive to changes of the shape and the size. The aggregation of **AuNPs** leads to a red-shift of **SPR** band. Oppositely, the disassembly of aggregates induces the blue-shift of **SPR** band.

As shown by the first black line of Figure 4.9a, a strong **SPR** band of functionalized gold nanoparticles at basic pH (**AuNPs-1-D**, **D** for deprotonated) in a mixture of DMSO and water (10%, v/v) at 523 nm is found. The addition of 10 μ L of 0.1 M HCl neutralized ligand **1** on the surface of **NPs**, resulting in the corresponding zwitterionic state (**AuNPs-1-Z**, **Z** for zwitterionic). This leads to a red-shift of the **SPR** absorption from 523 nm to 540 nm within 60 min (Figure 4.9a), indicating the self-assembly of **AuNPs-1**. After subsequent further addition of 10 μ L 1 M aqueous HCl, ligand **1** was protonated to give **AuNPs-1-P** (**P** for protonated). The **SPR** band was blue-shifted from 540 nm to 523 nm in 2 min (Figure 4.9b), which shows the disassembly of **AuNPs-1-P**. In the reverse manner, addition of aqueous NaOH led to re-formation of the assembled zwitterionic nanoparticles

(Figure 4.9c). Further addition of NaOH regenerated the deprotonated and disassembled state (Figure 4.9d).

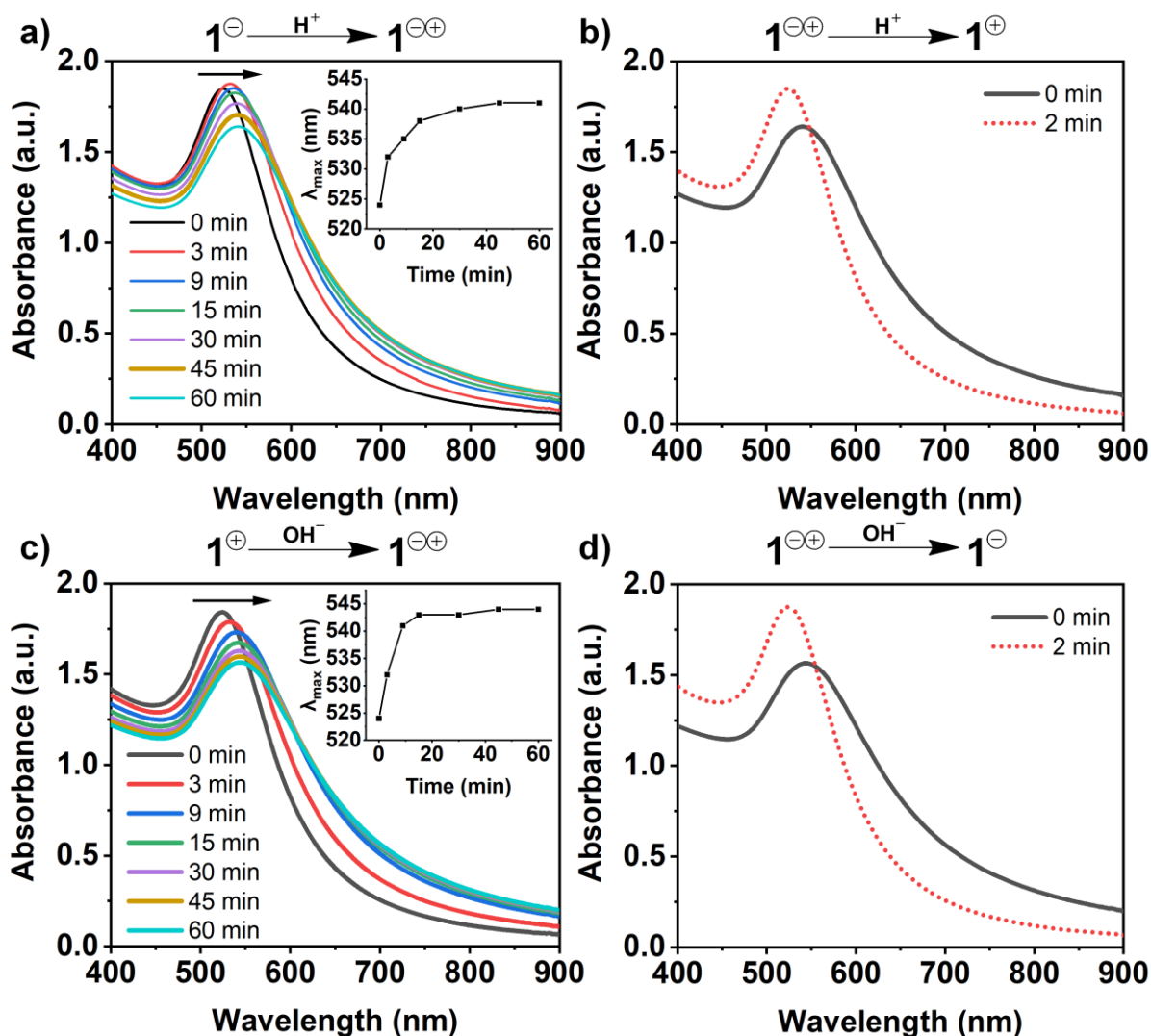


Figure 4.9: UV/Vis absorption spectra of **AuNPs-1** in a 10/1 DMSO/water mixture. a) Addition of 10 μL 0.1M HCl to **AuNPs-1-D**, inset: time-dependent red-shift of the absorption maximum, b) subsequent addition of 10 μL 1 M HCl, c) then, neutralization by addition of 10 μL 1 M NaOH, inset: time-dependent red-shift of the absorption maximum, d) deprotonation by addition of 10 μL 0.1 M NaOH. Adapted and reproduced with permission from the Wiley-VCH, copyright 2020.⁶²

After the results of the UV/Vis measurements of **AuNPs-1**, we investigated the self-assembly behaviour of **AuNPs** which is functionalized by background ligand **2**. Ligand **2** obtains no **GCPZ**-units, and therefore no change of the **SPR** band was observed with adding base or acid to adjust the pH (Figure 4.10). This indicates that the **GCPZ**-unit in **1** is responsible for the dual **PSRSA**.

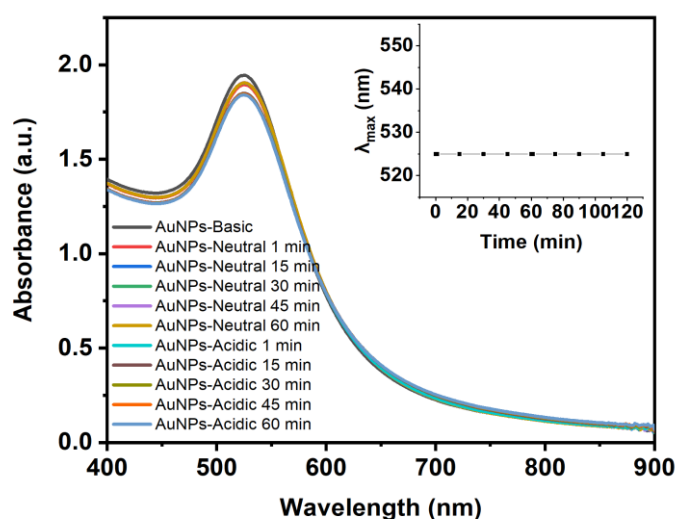


Figure 4.10: Continuous monitoring of the absorption spectra of **AuNPs-2** in DMSO/Water (10%) solution under basic, neutral and acidic condition, inset: Changes in the wavelength maximum of **AuNPs-2** for increasing times. Adapted and reproduced with permission from the Wiley-VCH, copyright 2020.⁶²

4.2.6.2 DLS measurement

In addition to the UV/Vis measurements, dynamic light scattering (DLS) of **AuNPs-1** solutions also confirmed the presence of the dual **PSRSA**. The hydrodynamic radii of the **AuNPs-1** species differ drastically at different pH values (Figure 4.11a): **AuNPs-1-P** and **AuNPs-1-D** show a mean size of 10 nm, while the size of the **AuNPs-1-Z** assemblies is well over 1000 nm. In addition to the change in size, the colour of the solution switched from deep red to purple by neutralizing **AuNPs-1** at neutral condition and then regained its initial deep red colour by protonating or deprotonating **AuNPs** (Figure 4.11b).

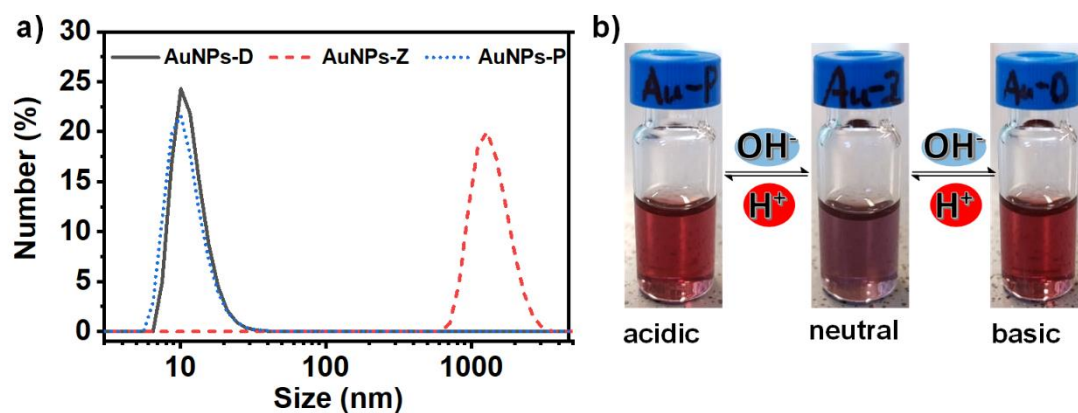


Figure 4.11: a) DLS measurements and b) Photos of **AuNPs-1** in a 10/1 DMSO/water mixture in different protonation states, protonated (blue line), deprotonated (black line) and zwitterionic (red line). Adapted and reproduced with permission from the Wiley-VCH, copyright 2020.⁶²

4.2.6.3 TEM and SEM measurements

Furthermore, the self-assembly process could be followed by transmission electron microscopy (TEM). Figures 4.12a-4.12c show the TEM images of **AuNPs-1** at different protonation states. The protonated **AuNPs-1** (Figure 4.12a) and deprotonated **AuNPs-1** (Figure 4.12c) show similar size distributions and no significant self-assembly was observed. The **AuNPs-1** in the zwitterionic state show a strong aggregation, which proves the occurrence of the dual **PSRSA** of **AuNPs-1**. The distance between two adjacent **AuNPs** were measured from 1.3 nm to 2.0 nm which is consistent with the size of dimeric **GCPZ** ligand **1** as determined by force-field calculations ($5.39 \text{ nm} \times 1.22 \text{ nm}$, Figure 4.12d), assuming that the TEG-chain will not be fully extended due to the multivalent interaction.

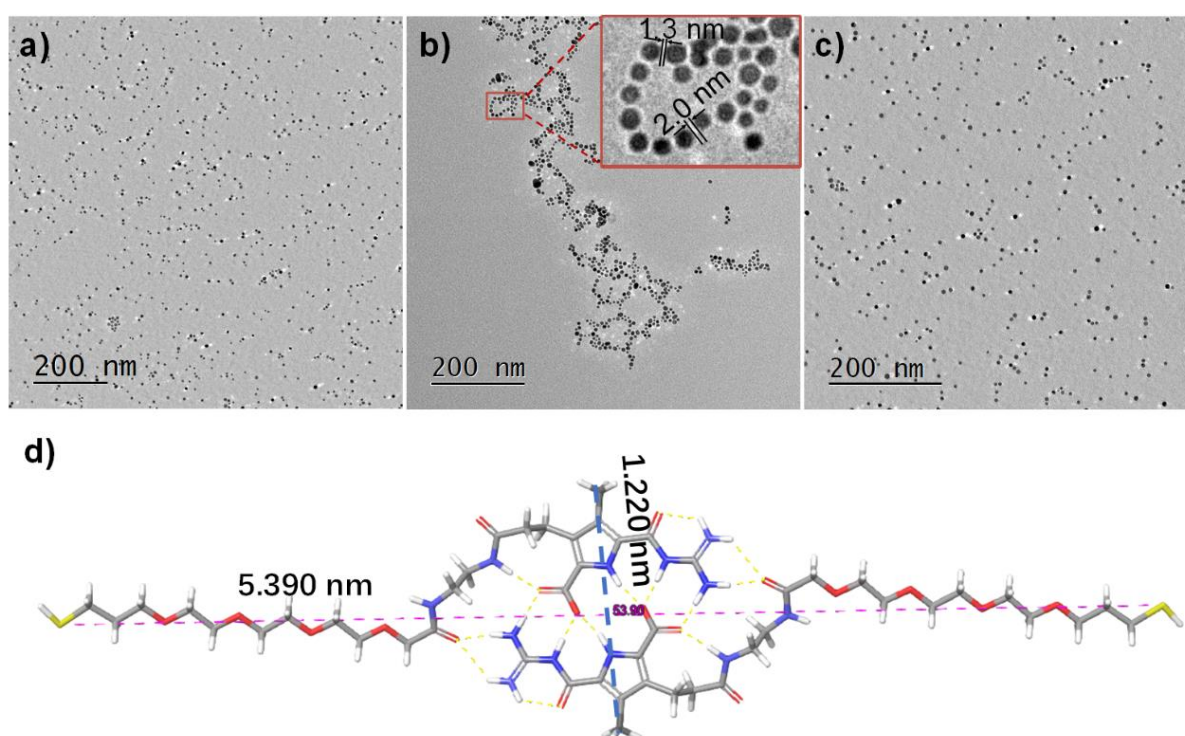


Figure 4.12: TEM images of **AuNPs-1** in a 10/1 DMSO/water mixture in different protonation states, protonated (a), zwitterionic (b) and deprotonated (c). d) Optimized structure of dimeric **GCPZ** ligand **1**. Adapted and reproduced with permission from the Wiley-VCH, copyright 2020.⁶²

Here, a control sample using **AuNPs-2** under neutral conditions was also measured by TEM. However, no comparable self-assembly aggregations were observed (Figure 4.13).

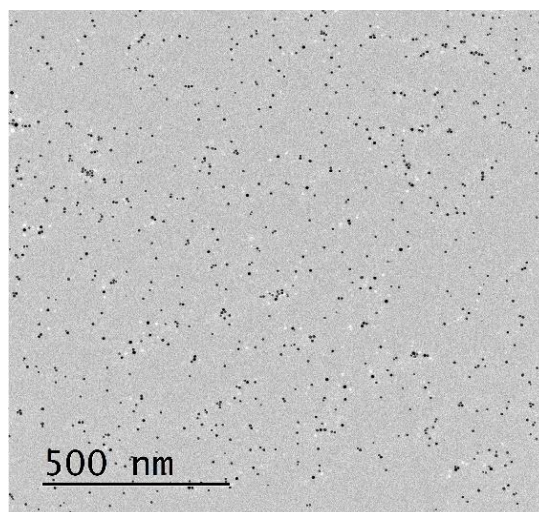


Figure 4.13: TEM image of AuNPs-2 in DMSO/Water (10%) solution under neutral condition. Adapted and reproduced with permission from the Wiley-VCH, copyright 2020.⁶²

Scanning electron microscope (SEM) was also used to monitor the self-assembly process. Protonated and deprotonated AuNPs-1 are not showing any self-assembly, while obvious aggregations were found in the zwitterionic state (Figure 4.14).

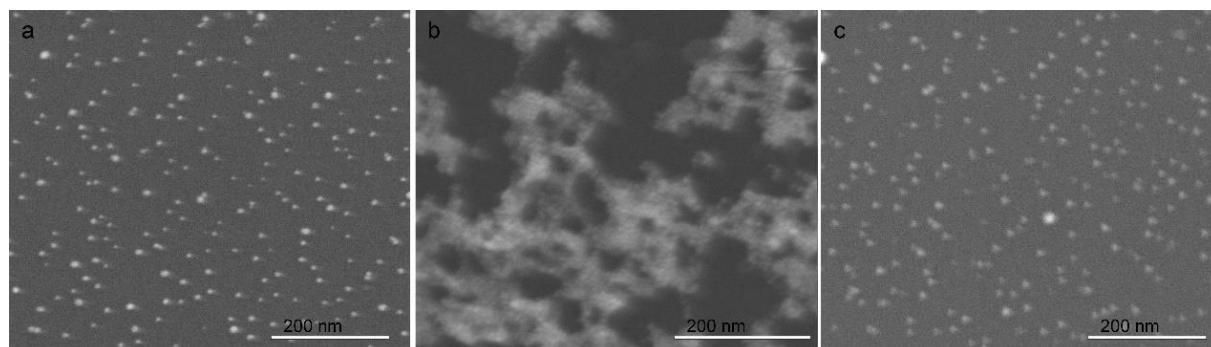


Figure 4.14: SEM images of AuNPs-1 in a 10/1 DMSO/water mixture in different protonation states, protonated (a), zwitterionic (b) and deprotonated (c). Adapted and reproduced with permission from the Wiley-VCH, copyright 2020.⁶²

4.2.7 Mechanism of dual pH-sensitive self-assembly

The self-assembly behaviour of NPs is the result of competition between attractive and repulsive interactions between the particles. In addition, the extent noncovalent interactions between the ligands on NPs depends on their concentration and the solvent composition. For instance, the hydrogen bonds are weaker in the more polar solvent because of the increasing competitive solvation of donor and acceptor sites by polar solvent molecules. In this part, we tried to adjust the noncovalent interactions by varying the concentration of **1** (θ -values) on the nanoparticle surface and water content of the water/ DMSO mixtures (C_w , v/v). We expected different self-assembly

behaviours by varying effective strength of the noncovalent interactions. More important, the observed self-assembly behaviours of **AuNPs** in different parameter will help us to understand the mechanism of self-assembly.

During these investigations, three types of **PSRSA** were found: no self-assembly, Mono-**PSRSA** and Dual-**PSRSA**. As illustrated in Figure 4.15, dual-**PSRSA** functionalized **NPs** assemble in the zwitterionic state and disassemble in the deprotonated and protonated state. In case of mono-**PSRSA**, functionalized **NPs** assemble in the protonated and zwitterionic state and disassemble only in the deprotonated state.

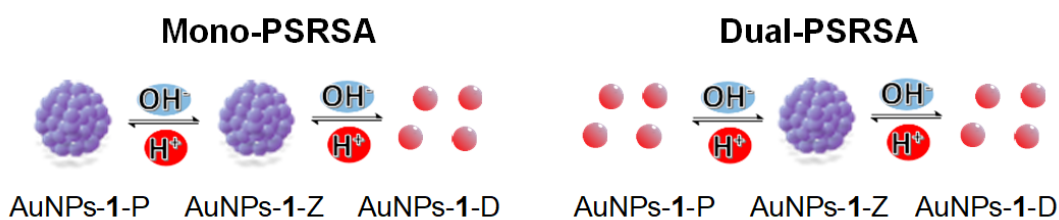


Figure 4.15: Illustration of mono-**PSRSA** and dual-**PSRSA** behaviour. Adapted and reproduced with permission from the Wiley-VCH, copyright 2020.⁶²

4.2.7.1 The effect of concentration of **1** on the reversible self-Assembly

In order to investigate the influence of the θ -values on the self-assembly behaviour, the C_w of the mixture was set to 0.1. The self-assembly of **AuNPs** with different θ values was monitored by UV/Vis measurements. We expected that higher θ -values would favour the self-assembly based on a higher possible number of noncovalent interactions, resulting in stronger association between the nanoparticles due to multivalent effects. As expected, we found that the concentration of ligand **1** on the **NPs** plays an important role in order to achieve a dual-**PSRSA** behaviour. As shown in Figure 4.16, for $\theta \leq 0.15$, no obvious shift of **SPR** band was observed when the protonation state of **AuNPs** changed, indicating the self-assembly of functionalized **NPs** was not possible. For $\theta \geq 0.18$, the red shift of **SPR** band indicates the self-assembly of functionalized **AuNPs** occurred in the zwitterionic form. The addition of base or acid leads to the disassembly of **NPs**, thus demonstrating a dual-**PSRSA** behaviour. These findings suggest the self-assembly can only happen at high θ values ($\theta \geq 0.18$) which are resulting in stronger supramolecular interactions.

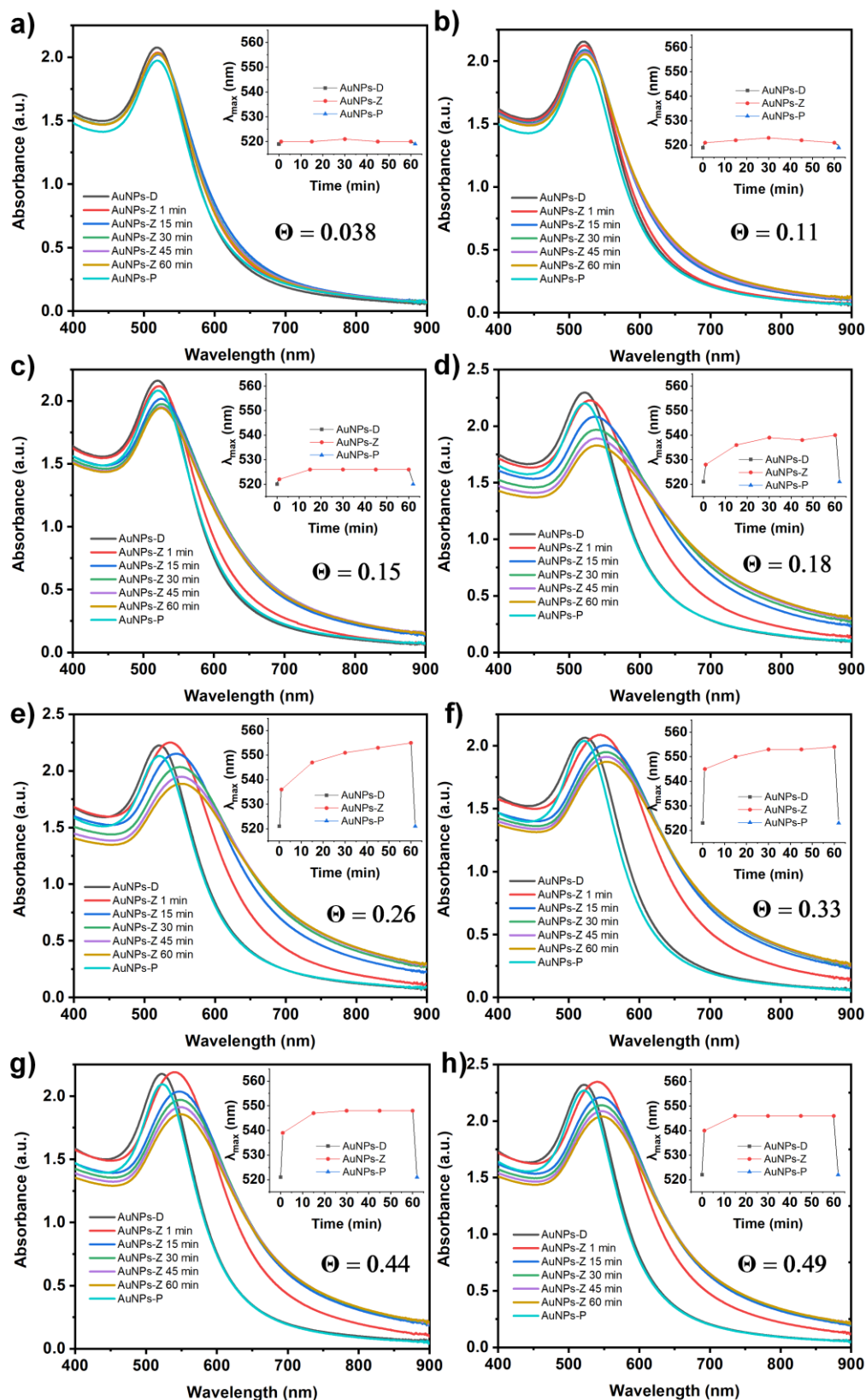


Figure 4.16: Continuous monitoring of the absorption spectra of AuNPs-1-2 in DMSO/Water (10%) under deprotonation, neutralization and protonation, where the θ value is: a) 0.038, b) 0.11, c) 0.15, d) 0.18, e) 0.26, f) 0.33, g) 0.44, h) 0.49, respectively. The insets are plots of the SPR absorbance change as a function of time. Adapted and reproduced with permission from the Wiley-VCH, copyright 2020.⁶²

4.2.7.2 The effect of water content on the reversible self-assembly

For the influence of C_W on the reversible self-assembly, we investigated the self-assembly behaviour of **AuNPs-1-2** ($\theta = 0.25$) in solvent mixtures with different C_W values. As shown in Figure 4.17, with a θ -value of 0.25, **AuNPs-1-2** show a dual-PSRSA behaviour at $C_W = 0.05$ and $C_W = 0.1$. Here, the SPR band of **AuNPs** was red-shifted at neutral pH and showed at the original wavelength (523 nm, the SPR band of dispersed **AuNPs**) at both basic and acidic pH values. With increasing value of C_W ($C_W \geq 0.20$), the blue-shift of SPR band to 523 nm at acidic pH was not observed, only mono-PSRSA was obtained, indicating that a disassembly occurs at basic pH, while the disassembly of protonated NPs did not take place. These findings suggest that the C_W has an essential influence on the dual-PSRSA too.

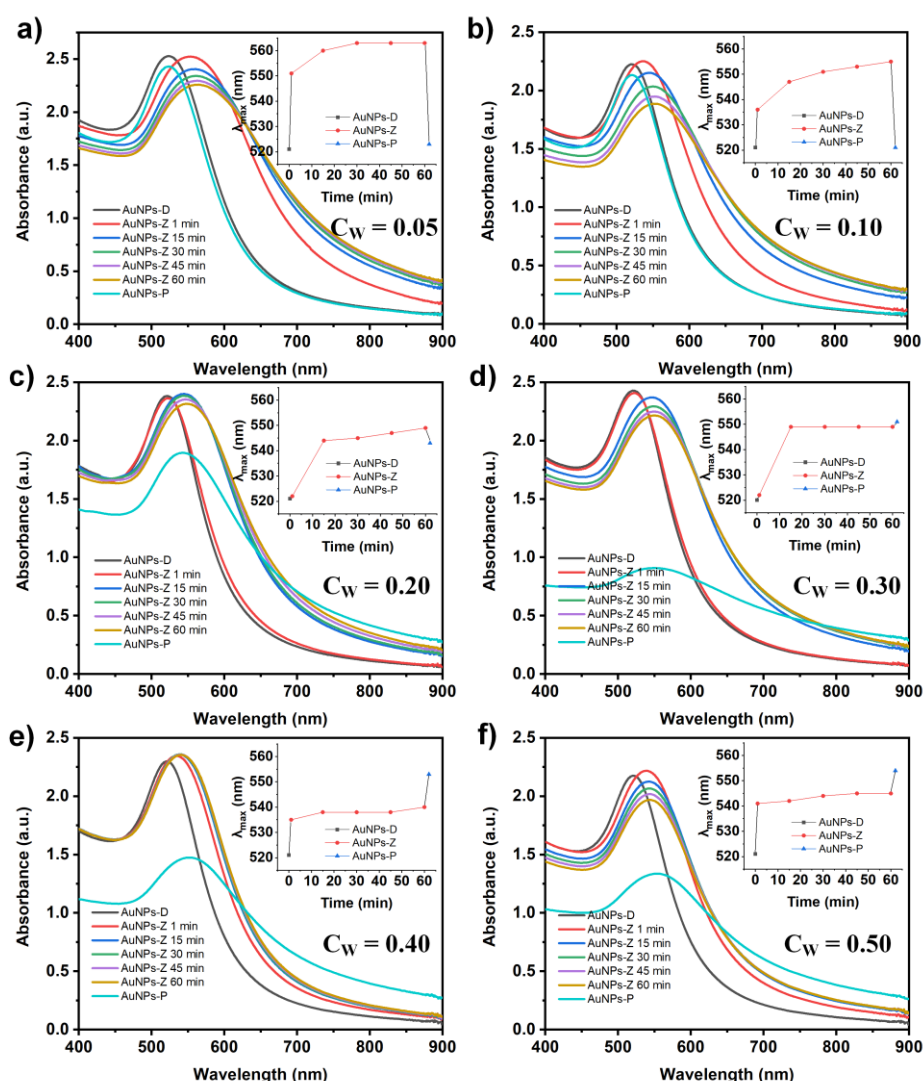


Figure 4.17: Continuous monitoring of the absorption spectra of **AuNPs-1-2** ($\theta = 0.25$) in a mixture of DMSO and water with different C_W , a) 0.05, b) 0.10, c) 0.20, d) 0.30, e) 0.40, f) 0.50. The insets are plots of the SPR absorbance change as a function of time. Adapted and reproduced with permission from the Wiley-VCH, copyright 2020.⁶²

4.2.7.3 The effect of solvent on the reversible self-assembly

In addition, we also investigated the self-assembly behaviour of **AuNPs-1-2** ($\theta = 0.25$) in different solvents with a C_w of 0.1. The solubility of **NPs** mainly depends on the concentration or the kind of ligand on the surface. Since the **GCPZ** ligand has good solubility in DMSO instead of in the other solvents, we expect different self-assembly consequences of **GCPZ** functionalized **AuNPs** in different solvents.

Here, UV/Vis measurements were not only used to monitor the self-assembly, but also used to check the dispersibility of **AuNPs** in different solvent. As shown in Figure 4.18a, **AuNPs-1-2** with different protonated states were not able to be dispersed in a THF/water mixture due to the poor solubility. In a methanol/water mixture (Figure 4.18b), only irreversible aggregates of **AuNPs** were observed at different pH values. In the other solvent mixtures (acetonitrile, ethanol, water, acetone, and DMF; Figure 4.18c - 4.18g), **AuNPs-1-2** were dispersed at basic pH and self-assembled at neutral pH, while the disassembly at acidic pH was suppressed, exhibiting a mono-**PSRSA** behaviour which was the same as in the DMSO mixture with high water content. Despite investigating different water/solvent mixtures, the dual-**PSRSA** could only be obtained in the water/DMSO mixture.

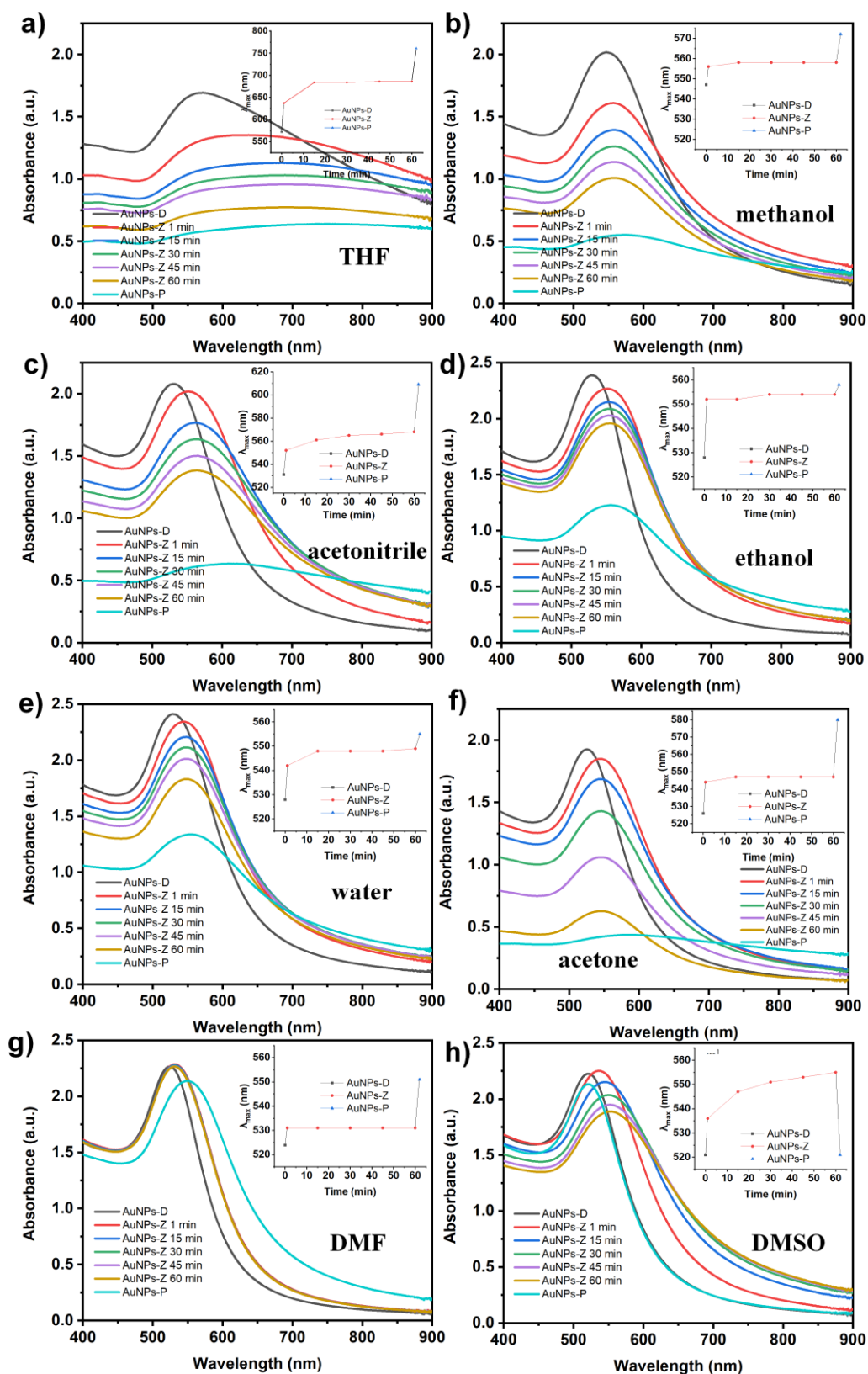


Figure 4.18: Continuous monitoring of the absorption spectra of AuNPs-1-2 ($\theta = 0.25$) under deprotonation, neutralization and protonation in the mixture of water (10%) with different solvents, a) THF, b) methanol, c) acetonitrile, d) ethanol e) water, f) acetone, g) DMF h) DMSO. The insets are plots of the SPR absorbance change as a function of time. Adapted and reproduced with permission from the Wiley-VCH, copyright 2020.⁶²

4.2.7.4 The mechanism of the reversible self-assembly

As discussed above, both the concentrations of **GCPZ** on **NPs** and the water content have a strong effect on the self-assembly behaviour. Therefore, different θ/C_w combinations were investigated. Figure 4.19 shows the different assembly behaviours depending on the θ value and the water content C_w . We find three different regimes: One with no self-assembly, one with mono-**PSRSA** behaviour (assembly in the protonated and zwitterionic state, disassembly only in the deprotonated state) and one with the desired dual-**PSRSA**-behaviour (assembly in the zwitterionic state, disassembly both in deprotonated and protonated state).

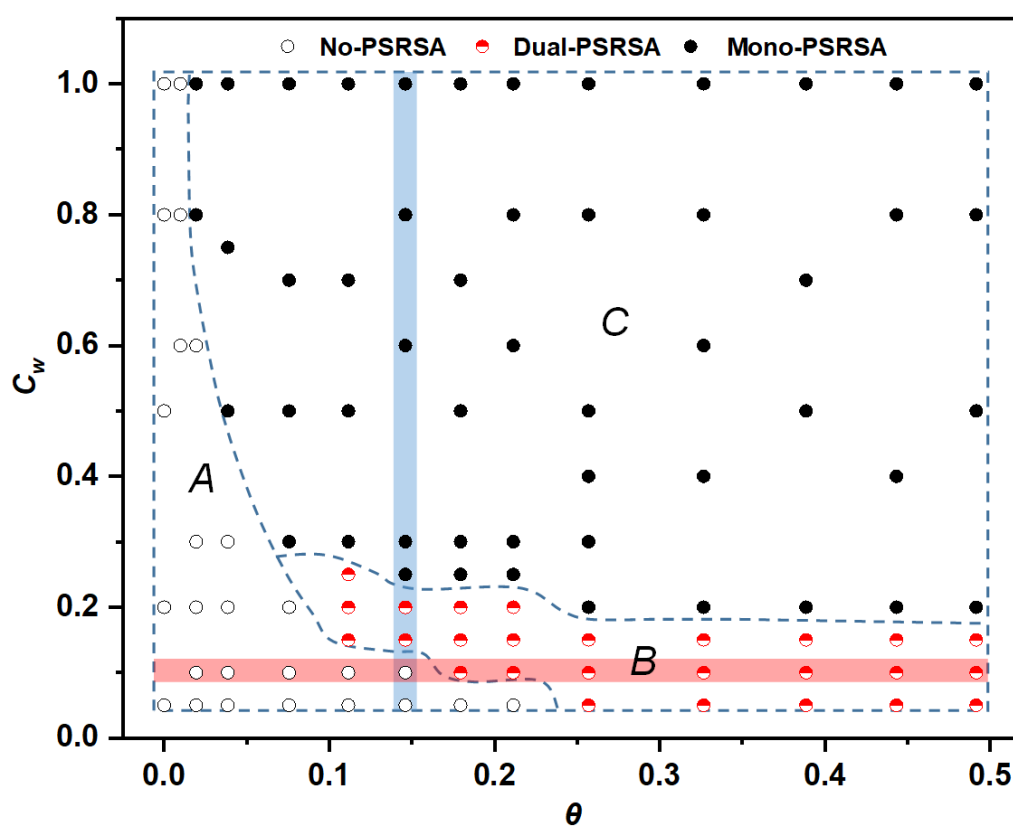


Figure 4.19: Different pH-induced reversible assembly behaviour of **AuNPs-1-2** for different θ - and C_w -values. Adapted and reproduced with permission from the Wiley-VCH, copyright 2020.⁶²

As discussed, for $C_w = 0.1$, we observed that the concentration of **1** on the **NPs** plays an important role on **PSRSA** behaviour. The same effect was also found in the other C_w values. For instance, when the C_w is 0.2, no self-assembly of functionalized **NPs** was observed for $\theta \leq 0.075$. For $\theta \geq 0.1$, the functionalized **AuNPs** showed a dual-**PSRSA** behaviour, while further increase of θ value ($\theta \geq 0.26$) led to mono-**PSRSA**. In addition, the C_w is also essential for **PSRSA** at different θ values. For example, at $\theta = 0.15$, with low C_w ($C_w \leq 0.1$), **AuNPs-1-2** are fully dispersed

independent on the pH value. With increasing value of C_w ($0.15 \leq C_w \leq 0.25$), **AuNPs-1-2** exhibit a dual-**PSRSA** behaviour. With $C_w \geq 0.30$, only mono-**PSRSA** was obtained.

In total, we investigated a total of 103 points in the θ / C_w parameter space, resulting in a pseudo-phase diagram with areas of fully dispersed **NP** (low θ , low C_w), dual-**PSRSA** behaviour ($0.11 < \theta < 0.49$ and $0.05 < C_w < 0.25$) and mono-**PSRSA** behaviour (high θ , high C_w). This allows for the exact choice of suitably functionalized **NPs** when a certain self-assembly behaviour is desired in a specific water/DMSO mixture.

The hydrophobic effect in reversible self-assembly

While the general trends in self-assembly behaviour at different θ - and C_w -values are according to our expectations, we were surprised that no disassembly could be achieved at acidic pH for **NPs** with high concentrations of the **GCPZ**-based ligand **1** (high θ -values) at water contents exceeding 30% (or even lower in some cases). In order to explain this assembly behaviour, hydrogen bonding between protonated carboxyl groups and the electrostatic interaction between **GCPZ** ligands have been considered. However, as shown in Figure 4.19, with increasing of C_w , self-assembly behaviour changed from dual-**PSRSA** to mono-**PSRSA** ($\theta = 0.26$) or changed in the sequence of no-**PSRSA**--dual-**PSRSA** to mono-**PSRSA** ($\theta = 0.15$). It is inconsistent with the fact that the hydrogen bonding and electrostatic interaction between **GCPZ** ligands decrease with increasing C_w .⁶⁴ This indicates that the self-assembly behaviour in area C (Figure 4.19) couldn't be attributed to electrostatic interaction between **GCPZ** units or hydrogen bonding alone, but other noncovalent interactions must also be present in this regime.

As we mentioned, **AuNPs-1-2** also showed a mono-**PSRSA** behaviour in mixtures of water (10%) and other solvents, such as DMF and acetone (Figure 4.18). Based on this behaviour, we consider hydrophobic interactions as an additional driving force of self-assembly. Unlike polar interactions such as electrostatic interactions and hydrogen bonding, hydrophobic interactions rely on a microphase-separation between nonpolar molecules (or parts thereof) and water molecules. This effect has also been used for the self-assembly of nanoparticles.⁶⁵ Taking into account on the pH-

⁶⁴ C. Schmuck, W. Wienand, *J. Am. Chem. Soc.* **2003**, *125*, 452-459

⁶⁵ a) A. Sánchez-Iglesias, N. Claes, D. M. Solís, J. M. Taboada, S. Bals, L. M. Liz-Marzán, M. Grzelczak, *Angew. Chem. Int. Ed.* **2018**, *57*, 3183-3186. b) J. P. Coelho, G. Gonzalez-Rubio, A. Delices, J. O. Barcina, C. Salgado, D. Avila, O. Pena-Rodriguez, G. Tardajos, A. Guerrero-Martinez, *Angew. Chem. Int. Ed.* **2014**, *53*, 12751-12755. c) S. Merkens, M. Vakili, A. Sánchez-Iglesias, L. Litti, Y. Gao, P. V. Gwozdz, L. Sharpnack, R. H. Blick, L. M. Liz-Marzán, M. Grzelczak, *ACS Nano* **2019**, *13*, 6596-6604.

dependent solubility of the GPCZ-unit (also see chapter 2.2.3),⁶⁶ it is reasonable to consider the hydrophobic effect in pH-induced assembly of nanoparticles.

In order to estimate the compatibility of the **GCPZ**-unit with aqueous solvent, we investigated the solubility of ligand **1** at different pH-values (Figure 4.20). Based on the UV-absorption of saturated solutions, we found that the water solubility of ligand **1** at basic pH (pH = 11) is about 10^3 times higher than at acidic pH (pH = 2), and 10^4 times higher than at neutral pH (pH = 7). While the lower solubility of the zwitterionic ligand is expected (based on self-pairing, leading to an overall uncharged molecule), the vastly different solubilities of the negatively charged, deprotonated ligand and the positively charged, protonated ligand are unexpected.

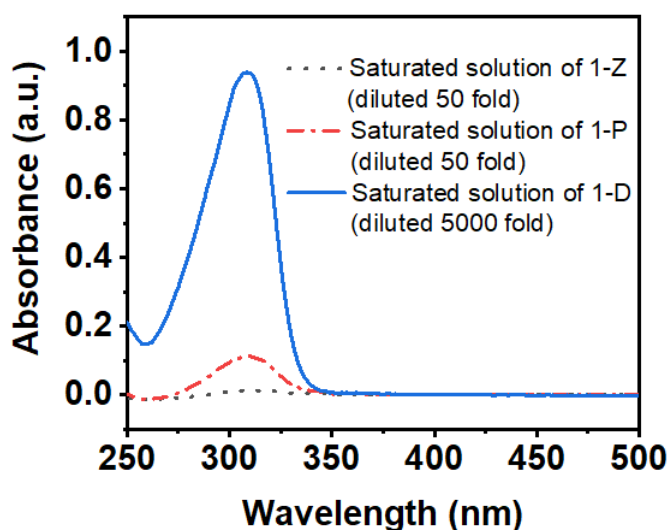


Figure 4.20: UV/Vis absorption spectra of saturated solutions of **1** in water at different pH values. Adapted and reproduced with permission from the Wiley-VCH, copyright 2020.⁶²

This indicates that the hydrophobic effects of the neutralized form of **1** are stronger than the protonated form, and the hydrophobic effects of the deprotonated form could be negligible. With increasing of C_w , the hydrophobic effects increase and are strong enough to overcome the electrostatic repulsion. This leads to the self-assembly at neutral pH exhibiting the dual-**PSRSA**. Further increasing of the C_w , the increased hydrophobic effects of protonated **1** lead to the suppression of disassembly at acidic pH, which results in mono-**PSRSA**. For this reason, we found a tendency for mono-**PSRSA** at high water-concentrations, only at DMSO-concentrations exceeding 75%, the solubility of both **AuNPs-1-2-P** and **AuNPs-1-2-D** is high enough to allow for dual-**PSRSA** behaviour. Since the aggregation of **AuNPs-1-2-P** at high water amount was caused

⁶⁶ D. Fuchs, J. Fischer, F. Tumakaka, G. Sadowski, *Ind. Eng. Chem. Res.* **2006**, *45*, 6578-6584.

by the hydrophobic effects, a decrease in C_W caused the disassembly of aggregated **AuNPs-1-2-P** (Figure 4.21).

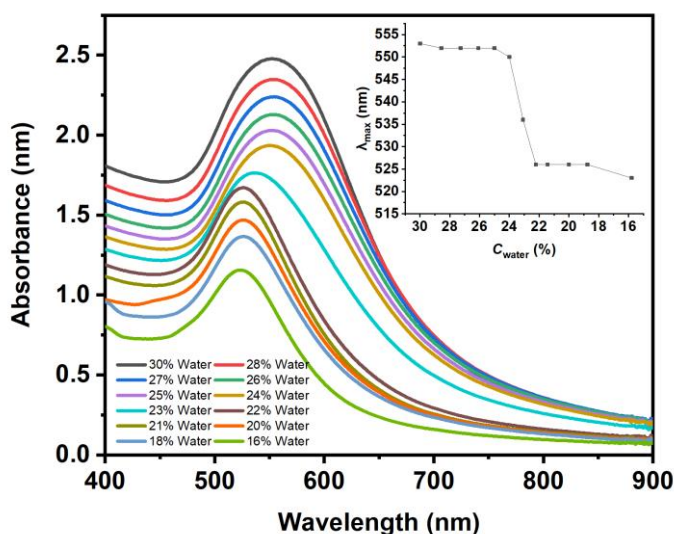


Figure 4.21: Changes of UV/Vis spectra of assembled **AuNPs-1-2-P** ($\theta = 0.11$, $C_W = 0.3$) under decreasing C_W by adding DMSO. Adapted and reproduced with permission from the Wiley-VCH, copyright 2020.⁶²

Reversibility of pH-induced self-assembly

We also checked the reversibility of the dual-PSRSA behaviour of functionalized **AuNPs**. UV/Vis was used to monitor the change in SPR band of **AuNPs-1-2** ($\theta = 0.25$) with different pH values, starting at a water content of $C_W = 0.1$. As shown in Figure 4.22a, the reversible self-assembly between **AuNPs-1-2-D** and **AuNPs-1-2-Z** can be repeated more than 20 cycles with no significant difference between the first and last cycle. In contrast, when the cationic state is involved in the switching cycle, reversibility is decreased. For instance, the reversibility between **AuNPs-1-2-P** and **AuNPs-1-2-Z** can be only repeated 8 cycles (Figure 4.22b). For switching between **AuNPs-1-2-D**, **AuNPs-1-2-Z** and **AuNPs-1-2-P**, we could only complete 3 cycles (Figure 4.22c). As we discussed above, the water content influences the self-assembly behaviour. Here, we attribute the decrease of reversibility to the fact that the water content is increased with each acid/base addition (Figure 4.22d), and the cationic state is more sensitive to the water content, leading to incomplete disassembly after a certain number of switching cycles.

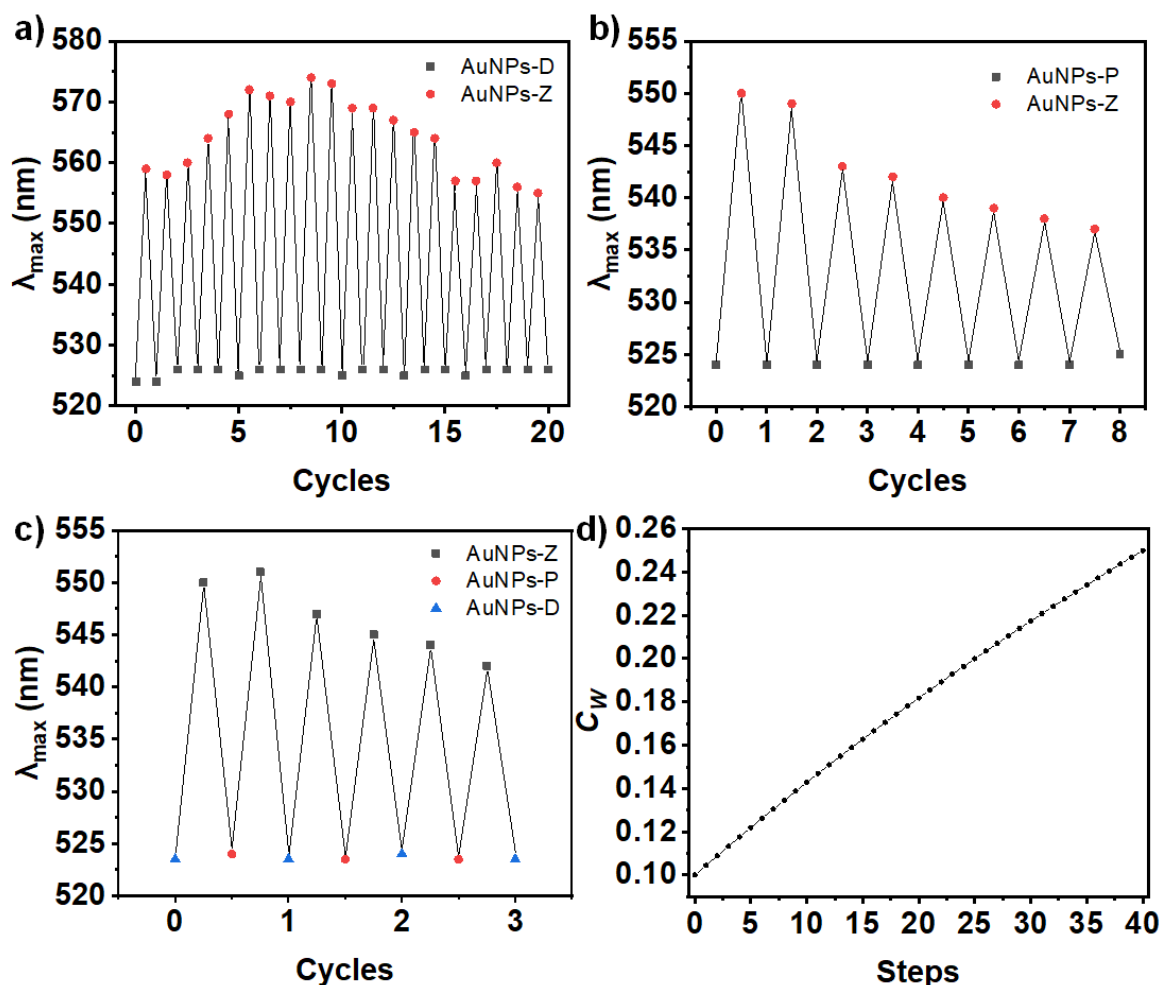


Figure 4.22: a-c) Cycles of AuNPs-1-2 ($\theta = 0.25$) between different state, a) between AuNPs-1-2-D and AuNPs-1-2-Z, b) between AuNPs-1-2-P and AuNPs-1-2-Z, c) between AuNPs-1-2-D, AuNPs-1-2-Z and AuNPs-1-2-P. d) Changes of C_w for increasing steps of adding base or acid. Adapted and reproduced with permission from the Wiley-VCH, copyright 2020.⁶²

The electrostatic interaction between GCPZ ligands in reversible self-assembly

The GCPZ dimer forms a stable ion pair even in water ($K = 160 \text{ M}^{-1}$). Therefore, it is significant to investigate the role of electrostatic interaction between **1** in PSRSA. We expected that the strong electrostatic interaction between GCPZ-units could be the main driving force of PSRSA. While the self-assembly behaviour at high water content should be attributed to hydrophobic effects. For further investigation of the importance of the different supramolecular interactions on self-assembly, we used the AuNPs-1-2 in pure DMSO ($C_w = 0$), where the hydrophobic effect is negligible. Figure 4.23 shows the UV/Vis absorption spectra of AuNPs-1-2-Z with different θ values in pure DMSO at neutral condition. AuNPs-1-2-Z are fully dispersed at low θ value (below 0.11). With the increasing θ -values, the SPR absorption of NPs is red shifted, indicating the self-assembly. The aggregates even precipitate from the solution when the θ value is above 0.26. As indicated by the

changes in the absorption spectra, the colour of **AuNPs-1-2-Z** changes from deep red to purple with increasing θ , then switches to a colourless solution due to the precipitation of aggregates. Both, the absorption and colour changing of **AuNPs-1-Z** proves that the electrostatic interactions between ligands **1** could be responsible for the assembly in pure DMSO without the hydrophobic effects. It indicates that the electrostatic interaction between **GCPZ** plays an important role in **PSRSA** at low C_w -values.

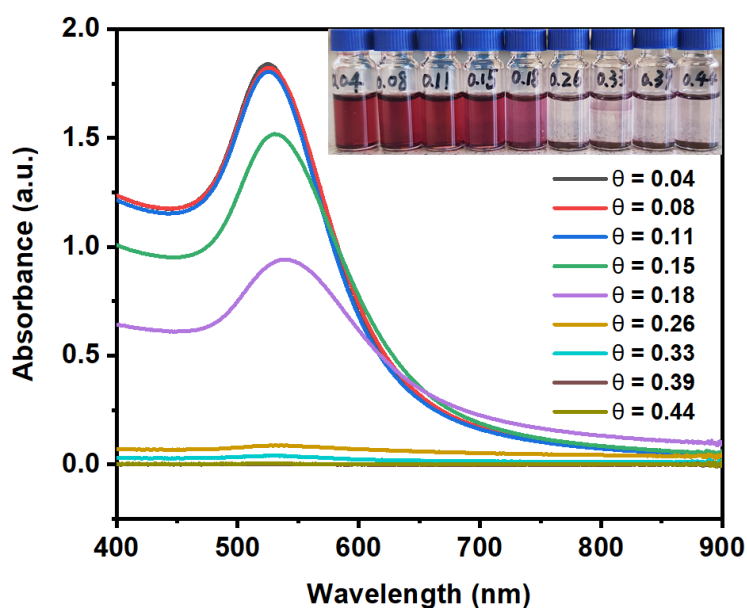


Figure 4.23: UV/Vis absorption spectra and photos of **AuNPs-1-2-Z** in DMSO with different θ values under neutral condition. Adapted and reproduced with permission from the Wiley-VCH, copyright 2020.⁶²

The mechanism of pH-induced self-assembly

The pH-sensitive hydrophilic/hydrophobic nature of **GCPZ** ligand is the key to understand the self-assembly behaviours of **AuNPs-1-2** at molecular level: As shown in Figure 4.24, self-pairing of the zwitterionic **GCPZ** leads to the forming of an overall uncharged, hydrophobic dimer. In comparison, the deprotonated **GCPZ** is very hydrophilic due to the negatively charged carboxylate group. In contrast, even the formation of the positively charged guanidinium could increase the overall hydrophilicity, the protonated **GCPZ** is still hydrophobic which is caused by the protonation of the carboxylic acid group. The hydrophobic effect is known to get increased as the raising of C_w -value. Inversely, the H-bond-assisted electrostatic interaction between **GCPZs** is tuning weaker as the increasing C_w . It means that these two opposite properties could be utilized to control the composition of the driving force by changing the value of C_w . Furthermore, both interactions are influenced by the density of the zwitterionic ligand (θ).

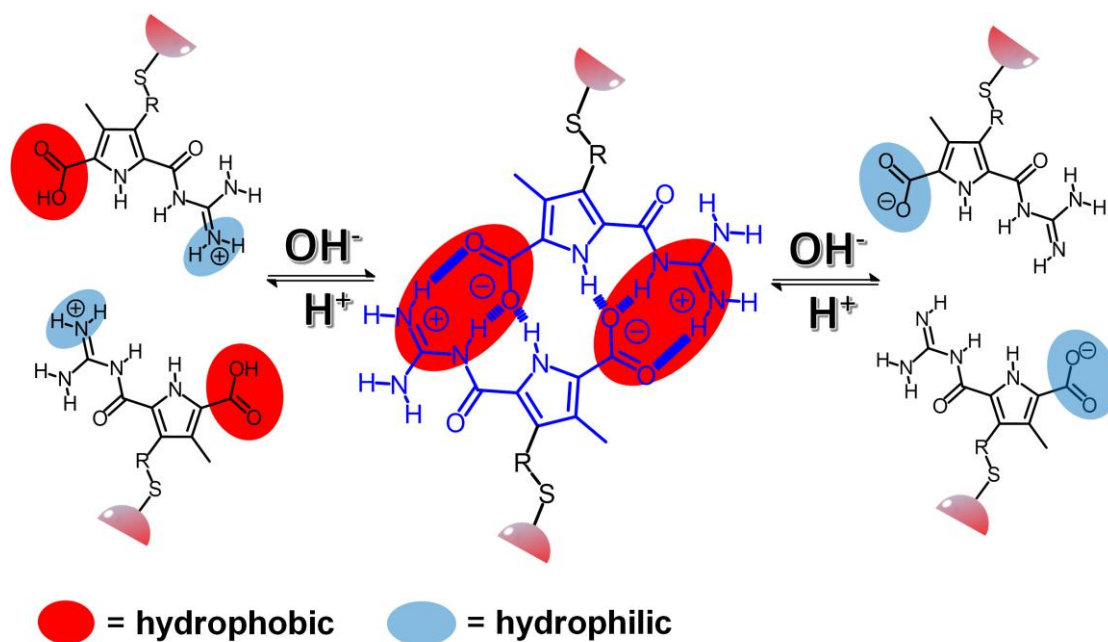


Figure 4.24: Scheme of pH-sensitive electrostatic interaction and solubility of **AuNPs-1** at different states. Adapted and reproduced with permission from the Wiley-VCH, copyright 2020.⁶²

In order to confirm the hydrophobic effect of the protonated carboxyl group, we investigated the self-assembly behaviour of **AuNPs-2** in comparison **AuNPs** functionalized with carboxylic acid ligands (**AuNPs-3**) in water as well as in DMSO/water mixture. In pure water ($C_w = 1$), the absorption spectra show that **AuNPs-3** were dispersed at pH = 12, slightly clustered at pH = 7 and seriously aggregated at pH = 2 due to the protonation of the carboxyl groups (Figure 4.25d). In contrast, no significant aggregation of **AuNPs-2** was observed in pure water at different pH values (Figure 4.25c), indicating the self-assembly of **AuNPs-3** was caused by carboxyl groups. We also measured the zeta-potential of **AuNPs-2** (Figure 4.25a) and **AuNPs-3** (Figure 4.25b) in the aqueous solution with different pH values. Due to the negative charge of COOH, **AuNPs-3** exhibit a lower zeta-potential than **AuNPs-2** at all pH values (pH 2 to pH 11), indicating that the electrostatic repulsions between **AuNPs-3** are stronger. In a DMSO/water (10%) mixture ($C_w = 0.1$), no self-assembly of **AuNPs-3** was found even at different pH values (Figure 4.26), suggesting the self-assembly of **AuNPs-3** was induced by the hydrophobic effect of the protonated carboxyl group.

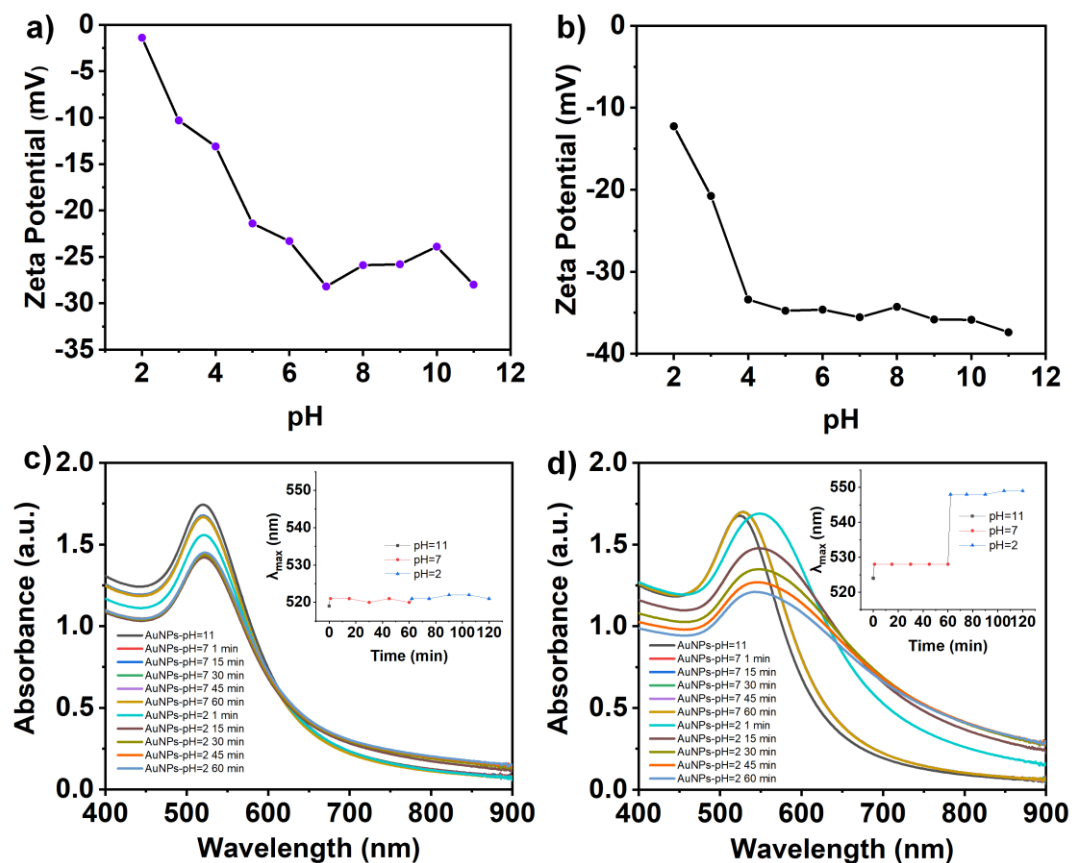


Figure 4.25: a-b) Zeta-potential of aqueous AuNPs-2 solutions (a) and AuNPs-3 aqueous solution (b) at different pH values, c-d) continuous monitoring of the absorption spectra of AuNPs-2 (c) and AuNPs-3 (d) in aqueous solution at different pH value. Adapted and reproduced with permission from the Wiley-VCH, copyright 2020.⁶²

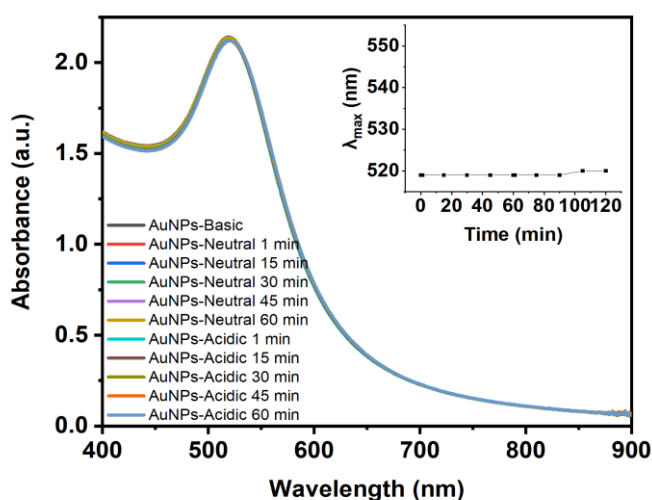


Figure 4.26: Continuous monitoring of the absorption spectra of AuNPs-3 in DMSO/Water (10%) solution under basic, neutral and acidic condition. Adapted and reproduced with permission from the Wiley-VCH, copyright 2020.⁶²

Based on the electrostatic interactions and hydrophobic effects, the mechanism of **PSRSA** of **AuNPs-1-2** with different C_w - and θ -values is shown in Figure 4.27. Due to the strong electrostatic repulsions and weak hydrophobic effects of the deprotonated **AuNPs-1-2** (**AuNPs-1-2-D**), NPs are mono-dispersed at basic pH value, which is independent of C_w - and θ -values. With the addition of HCl, the **GCPZ** ligands are neutralized to form a zwitterionic state. In area B, the self-assembly of **AuNPs-1-2-Z** is induced by hydrophobic effects and electrostatic interactions between **GCPZ** ligands. Indeed, the contribution of the electrostatic interactions and the hydrophobic effect highly depends on the θ -value and C_w . In area A with low θ values, the **AuNPs-1-2** are fully dispersed independent of pH and C_w value, due to insufficient electrostatic and/or hydrophobic effects induced by ligand **1**. While in area C with medium to high θ values and high C_w values, the self-assembly of **AuNPs-1-2-Z** is mainly driven by the hydrophobic effects, since the electrostatic interactions between **GCPZ** are too weak at high C_w . When the **AuNPs-1-2** are protonated, the electrostatic interactions between **GCPZs** are vanished and the state of **AuNPs-1-2-P** depends on the competition of hydrophobic effects and electrostatic repulsions between NPs. At low C_w (area B), the disassembly of **AuNPs-1-2-D** is due to the electrostatic repulsions which are stronger than the hydrophobic effects. However, in area C (high C_w), an overcompensation of charge repulsion by hydrophobic effects leads to the self-assembly of **AuNPs-1-2-P**. Therefore, different **PSRSA** behaviours are presented in area A, B and C with different C_w - and θ -values.

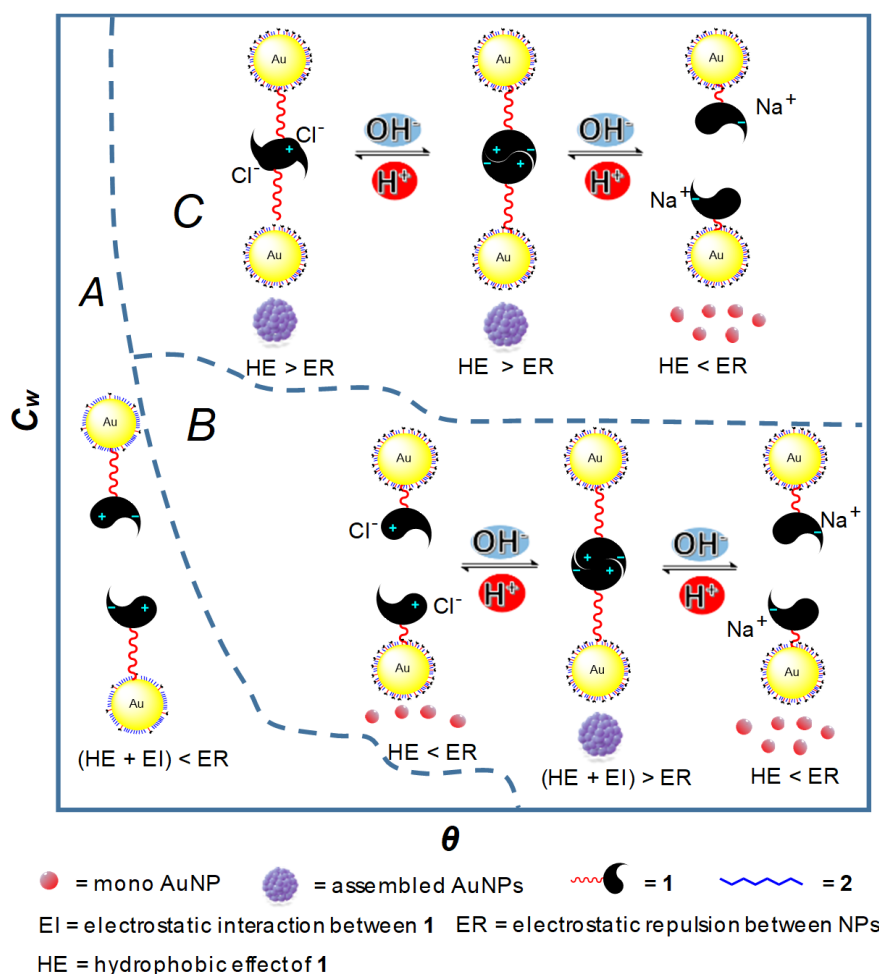


Figure 4.27: Suggested mechanism of self-assembly of AuNPs-1-2 at different θ / C_w values. Adapted and reproduced with permission from the Wiley-VCH, copyright 2020.⁶²

4.3 Conclusions

In summary, we developed a dual **PSRSA** system by integrating a **GCPZ** pH-switchable property with **AuNPs**. This dual **PSRSA** system can be precisely controlled and is switchable among no-**PSRSA**, mono-**PSRSA** and dual-**PSRSA** by adjusting the degree of functionalization (θ -value) and solvent-mixture (C_w). More important, we found that even for small zwitterionic molecules, the hydrophobic effect is playing a crucial role in **PSRSA** of NPs. However, the electrostatic interactions between zwitterions which were used to be considered as the main driving force in zwitterionic ligands triggered self-assembly, only can induce the self-assembly at low C_w -values. These findings are important for people to understand the molecular interactions on NPs and develop new multi-**PSRSA** systems.

5. Multiple pH-Sensitive Reversible Self-Assembly of Gold Nanoparticles

5.1 Introduction

In the previous chapter, we have developed a dual-**PSRSA** capable **NPs** based on the **GCPZ** binding motif. The functionalized **NPs** could assemble in neutral pH and disassemble in basic or acidic pH in DMSO/water mixtures. Compared to the situation in an organic solvent or solvent mixtures, the self-assembly in water is more attractive, because water is the main component in human cells and it will supply an opportunity to make of the **NPs** in biological applications. Unfortunately, neither **GCPZ** (see chapter 4), cysteine nor glutathione functionalized **NPs** (see chapter 1.3.3), didn't show any dual-**PSRSA** and only showed the mono-**PSRSA** in pure water. Although dual-**PSRSA** systems based on serum and mixed positively/negatively charged ligands have been developed, functionalized **NPs** with simple zwitterionic molecules for dual-**PSRSA** in water have not yet been reported. More importantly, there are only few reports about multi-**PSRSA** which can response to more than three-pH-ranges.

This chapter describes the development of **AuNPs** that are capable of a multi **PSRSA** in pure water. The **PSRSA** is based on a functionalized **AuNPs** which are co-decorated with different ratios of the **GCP** and self-complementary **GCPZ** ligands. The self-assembly behaviour of such functionalized **AuNPs** (**AuNPs-GCPZ-GCP**) was observed at pH = 1, pH = 7 and pH = 13. In turn, disassembly of the **NPs** could be achieved at pH = 3 and pH = 11. The functionalized **AuNPs** also showed a thermo-sensitive reversible self-assembly at pH = 1 and pH = 13. We found that the ratio of **GCP** and **GCPZ** on **AuNPs** is the key factor for the multi-**PSRSA** of **AuNPs**. Furthermore, we are operating this multi-**PSRSA** system in the application of removing the mercury ions from polluted water phases.

5.2 Results and discussion

5.2.1 Synthesis of thiolated GCP derivative

The **GCP motif** is a positively charged ligand at neutral and basic pH. Here, we desired attaching the **GCP** motif to **AuNPs** as one functional group. Thus, the thiolated **GCP** derivative (**4**) was

synthesized by 3 steps (Figure 5.1). The synthesis started with **GCP** motif⁶⁷ which was coupled with a short **TEG** chain **13** (*vide supra*) in DMF by using PyBOP as the coupling reagent and DIPEA as a base to give thiolated **GCP** (**18**). After that, **18** underwent a BOC deprotection in TFA to give thiol ester protected **GCP** ligand (**19**). In the last step, the thiol ester group was cleaved by hydrolyzation with LiOH to give thiolated **GCP** (**4**).

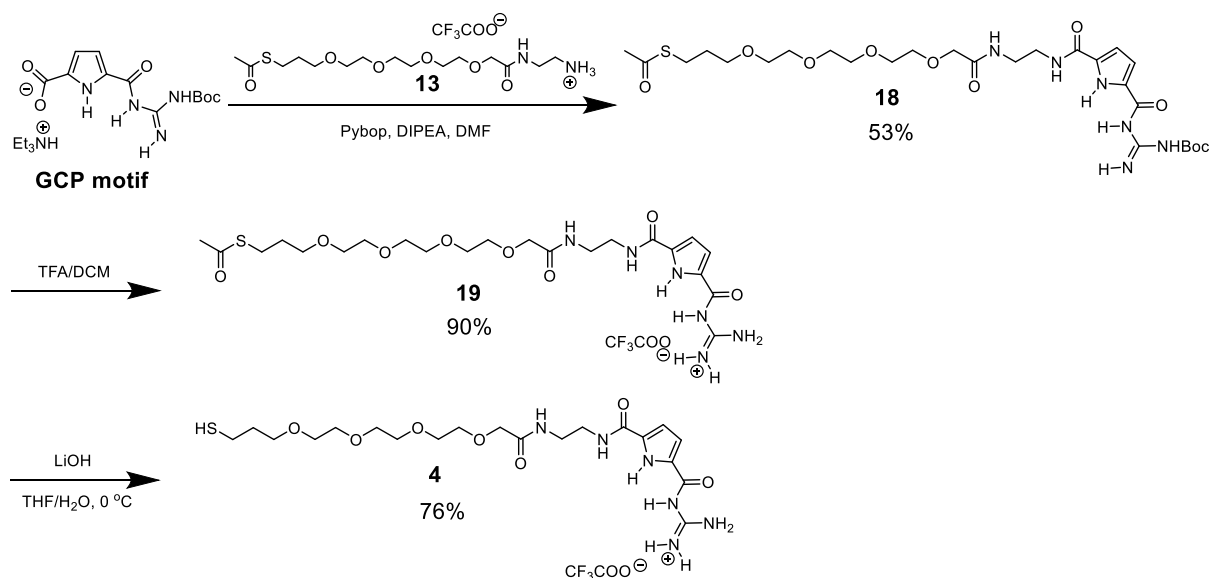


Figure 5.1: Synthetic scheme of thiolated **GCP** derivative (**4**)

5.2.2 GCPZ and GCP co-functionalized AuNPs

GCPZ can form extremely stable self-complementary dimers by H-bond enforced ion pairs at a pH range between 5 and 8 in aqueous solution. However, the dimer can easily be dissociated when the pH value is above 8 or below 5. In chapter 4, we used **GCPZ** to construct a dual-**PSRSA** system in DMSO/water mixtures. The **GCPZ** functionalized **NPs** only showed a mono-**PSRSA** in aqueous solution because of the hydrophobic effect in acidic pH range, hence we additionally introduced the positively charged **GCP** ligands onto **AuNPs** to either enhance the electrostatic repulsion or to counteract the hydrophobic effect at acidic solution.

The co-functionalized **AuNPs-GCPZ-GCP** (**AuNPs-1-4**) were prepared via a two-step procedure (Figure 5.2). First, dodecylamine-coated **AuNPs** were modified with β equivalents ($\beta < 1$; equivalent with respect to the number of binding sites on Au) of **GCPZ** ligand **1** under vortex for 30 min. After that, $1-\beta$ equivalents of **GCP** ligand **4** were added directly to the solution. The mixture

⁶⁷ M. Li, M. Ehlers, S. Schlesiger, E. Zellermann, S. K. Knauer, C. Schmuck, *Angew. Chem. Int. Ed.* **2016**, *55*, 598-601.

was vortexed for another 30 min. The **AuNPs-1-4** were washed with methanol to remove unreacted ligands (see experimental section for details).

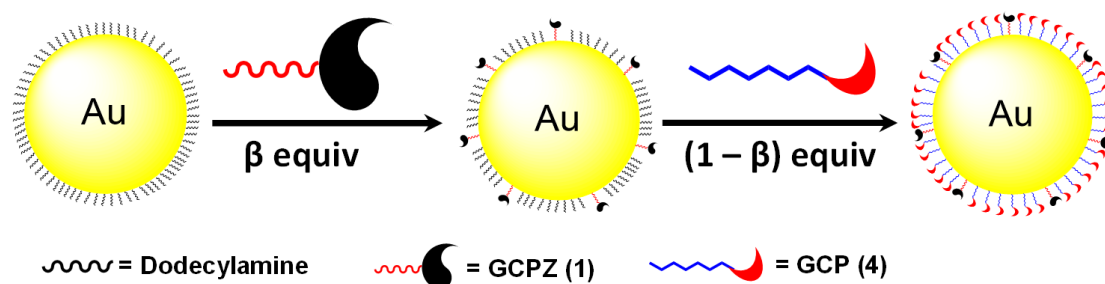


Figure 5.2: Two step functionalization of AuNPs with GCPZ and GCP ligands.

In chapter 4, we used UV/Vis measurement to determine the concentration of **GCPZ** on **AuNPs** based on the absorption band of pyrrole at 308 nm. Unfortunately, the **GCP** ligand shows a similar UV/Vis spectrum as its **GCPZ** counterpart. This increases the difficulty to identify the relative molecular concentrations of **GCPZ** and **GCP** on **AuNPs-1-4**.

In this project we designed a method based on UV/Vis measurements to determine the concentration of **GCPZ** and **GCP** on **AuNPs-1-4** (GCPZ_{Au} and GCP_{Au} , respectively). In order to identify the $\text{GCPZ}_{\text{Au}}/\text{GCP}_{\text{Au}}$ ratio on NPs by using UV/Vis measurement, we assumed that the functionalization of **AuNPs** with **GCPZ** only occurred in the first step and **GCP** reacted to **AuNPs** in second step individually. Therefore, the concentration of GCPZ_{Au} could be measured by using **GCPZ** and thiolated alcohol (2) co-functionalized **AuNPs** (**AuNPs-1-2**) with the same coating concentration. We already measured the concentration of **GCPZ** on **AuNPs-1-2** with the different coating concentration in chapter 4. With the known concentration of **GCPZ**, the concentration of GCP_{Au} could also be determined by UV/Vis measurement.

First, we determined the molar absorptivity (ϵ) of **GCPZ** and **GCP** both at pH 2 and pH 12 by recording a series of UV/Vis absorption spectra of **GCPZ** and **GCP** at different concentrations. The reason for the requirement to determine two molar absorptivity at different pH values (2 and 12) is that **AuNPs** with special $\text{GCPZ}_{\text{Au}}/\text{GCP}_{\text{Au}}$ ratio can only disperse under acidic or basic condition. As shown in Figure 5.3, **GCPZ** has a molar absorptivity (ϵ_1) of $1.62 \cdot 10^4 \text{ M}^{-1}\text{cm}^{-1}$ at 309 nm at pH 2 and $2.34 \cdot 10^4 \text{ M}^{-1}\text{cm}^{-1}$ at 309 nm at pH 12, while **GCP** has a molar absorptivity (ϵ_4) of $2.03 \cdot 10^4 \text{ M}^{-1}\text{cm}^{-1}$ at 309 nm at pH 2 and $2.59 \cdot 10^4 \text{ M}^{-1}\text{cm}^{-1}$ at 309 nm at pH 12.

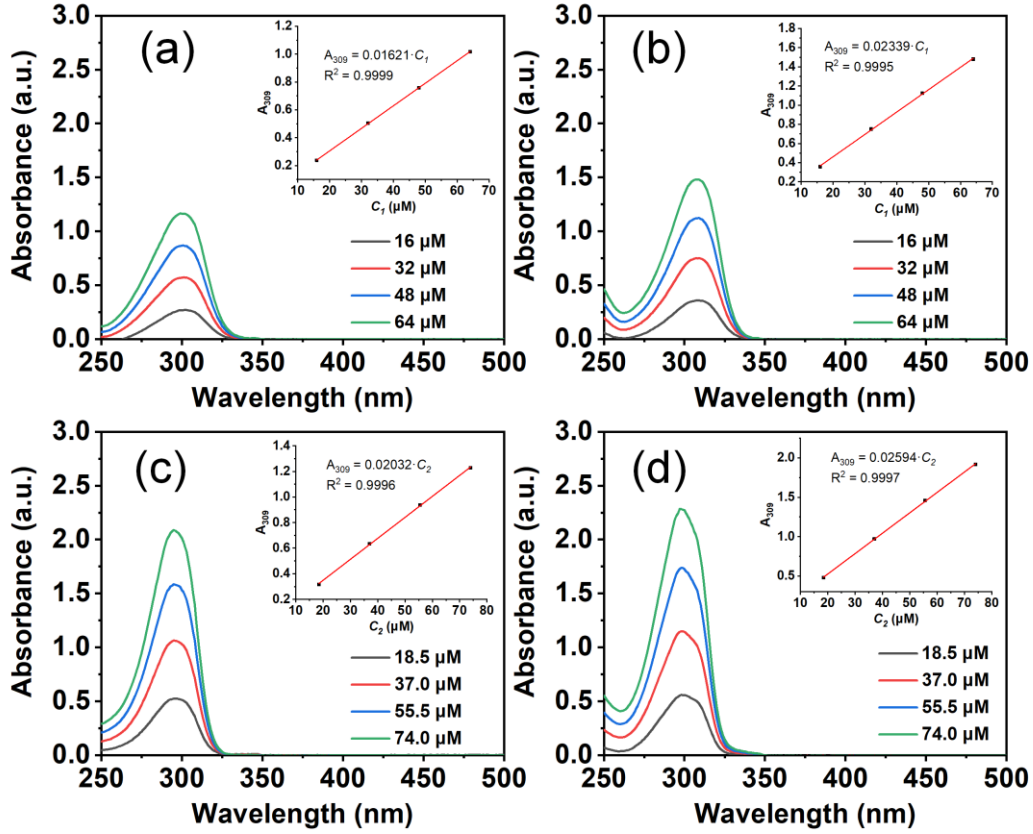


Figure 5.3: UV/Vis absorption spectra of **GCPZ (1)** and **GCP (4)** aqueous solution at different pH values and concentrations, (a) **GCPZ**, pH = 2, (b) **GCPZ**, pH = 12, (c) **GCP**, pH = 2, (d) **GCP**, pH = 12. Light pass length = 10 mm.

The concentration of **GCP**-ligand (**4**) on **NPs** (C_{4NP}) can be determined as equation 5-1:

$$C_{4NP} = \frac{A_{1-4} - A_{1-2}}{\varepsilon_4} \quad (5-1)$$

A_{1-4} and A_{1-2} represent the absorbance of **AuNPs-1-4** and **AuNPs-1-2** at 309 nm with the same β and pH values, respectively.

The concentration of **GCPZ (1)** on **NPs** (C_{1NP}) can be determined as equation 5-2:

$$C_{1NP} = \frac{A_{1-2} - A_2}{\varepsilon_1} \quad (5-2)$$

Here A_2 is the absorbance of **AuNPs-2** at 309 nm.

Hence, the ratio C_{1NP}/C_{4NP} can be calculated as followed equation 5-3:

$$\frac{C_{1NP}}{C_{4NP}} = \frac{A_{1-2} - A_2}{A_{1-4} - A_{1-2}} \times \frac{\varepsilon_4}{\varepsilon_1} \quad (5-3)$$

In equation 5-3, all values were measured at pH = 12 because of the assembly and disassembly behaviours of **AuNPs-1-2**. In some cases, **AuNPs-1-4** with special β values can't be dispersed at

basic pH, indicating that the measurement of A_{1-4} (pH 12) is not possible. For these cases, the ratio C_{INP}/C_{ANP} was determined at acidic condition and the value of A_{1-4} , ε_4 and ε_1 were measured at pH 2. In this case, A_{1-2} (pH 2) which cannot be measured at acidic pH values was calculated by the equation 5-4:

$$A_{1-2}^{pH\ 2} = (A_{1-2}^{pH\ 12} - A_2) \times \frac{\varepsilon_1^{pH\ 2}}{\varepsilon_1^{pH\ 12}} + A_2 \quad (5-4)$$

The molar ratio of components of “mixed” self-assembled monolayers affects the way the NPs are self-assembling.⁶⁸ Unfortunately, predicting the composition of a binary mixture is not trivial, and the assumption that the molar ratio of ligands in the solution will be preserved on NPs is often wrong.⁶⁹ Here, we investigated the relationship between the molar ratios of **GCPZ/GCP** on **AuNPs-1-4** and in solution. As shown in Figure 5.4, the molar ratio of **GCPZ** and **GCP** on **AuNPs** depends on the molar ratio of these two ligands in the solution. The slope of the linear fitting line is 0.99. It indicates that the molar ratio of **GCPZ** and **GCP** on **NPs** is almost as the same as that in solution. Comparing to the reported **AuNPs** functionalized with mixed ligands, the molar ratio of a binary mixture on **GCPZ** and **GCP** co-functionalized **AuNPs** show a direct dependency on the ratio in this solution. This may be caused by the similar linker-unit and steric demand of thiolated **GCPZ** and **GCP** ligands. We also believe that using purified **AuNPs** which are cleaned before functionalization by removing excess DDA after **AuNPs** generation in solution also plays an important role.

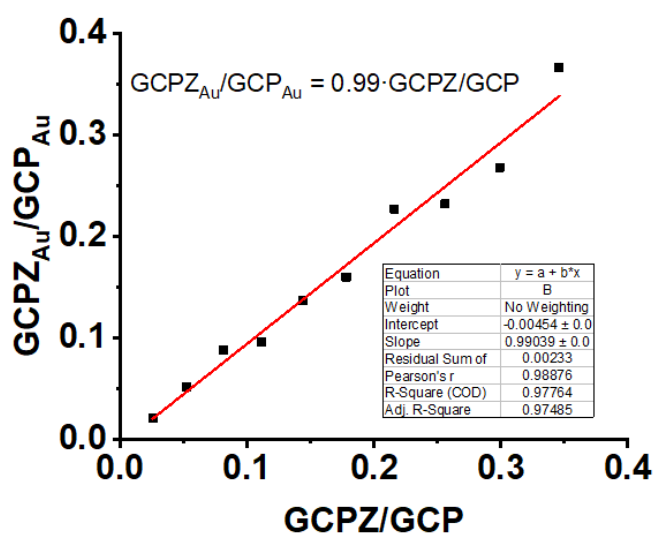


Figure 5.4: Molar ratio of **GCPZ** to **GCP** on **AuNPs** as a function of the molar ratio in solution.

⁶⁸ H. Kim, R. P. Carney, J. Reguera, Q. K. Ong, X. Liu, F. Stellacci, *Adv. Mater.* **2012**, *24*, 3857-3863.

⁶⁹ Z. Chu, Y. Han, P. Král, R. Klajn, *Angew. Chem. Int. Ed.* **2018**, *130*, 7141-7145.

5.2.3 Self-assembly of AuNPs-1-4

Induced by the **GCPZ** and **GCP** groups, **AuNPs-1-4** assemble in a neutral solution (pH = 7). The resulting self-assembled system can be switched back to the disassembled state by addition of acid (pH = 3) or base (pH = 11). Further addition of acid (pH = 1) or base (pH = 13) makes the disassembled **AuNPs** self-assemble again. In addition, the self-assembly at pH 1 and pH 13 are both temperature sensitive. Heating up the system leads to the disassembly of assembled **NPs**, while cooling down the system re-triggers the self-assembly of **AuNPs-1-4** (Figure 5.5).

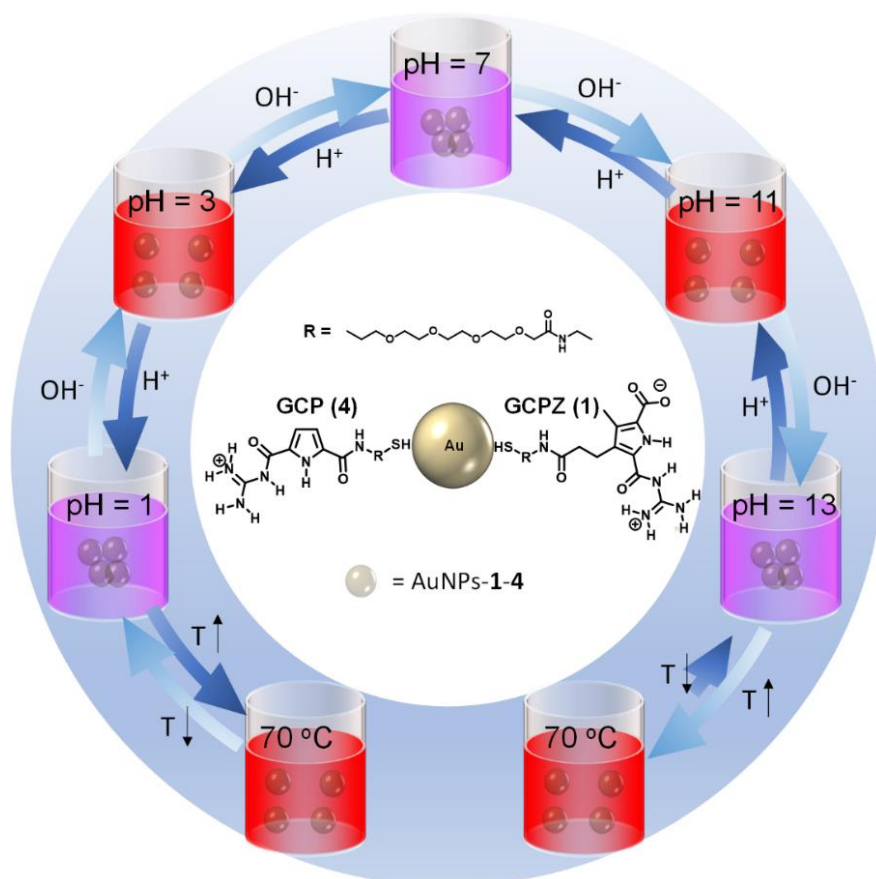


Figure 5.5: Schematic representation of the multi-PSRSA and thermo-sensitive behaviours of **AuNPs-1-4**.

In summary, and to our surprise, **AuNPs-1-4** show a multi-PSRSA which can respond to five different pH ranges. However, the concept of dual-PSRSA described in chapter 4 can only respond to three different pH borders. For better understanding and discussing of the observed multi-PSRSA behaviours, here we classify them into a two-pH-range, three-pH-range, four-pH-range and five-pH-range PSRSA on the basis of the number pH-ranges that show a difference between assembled and disassembled state (Figure 5.6).

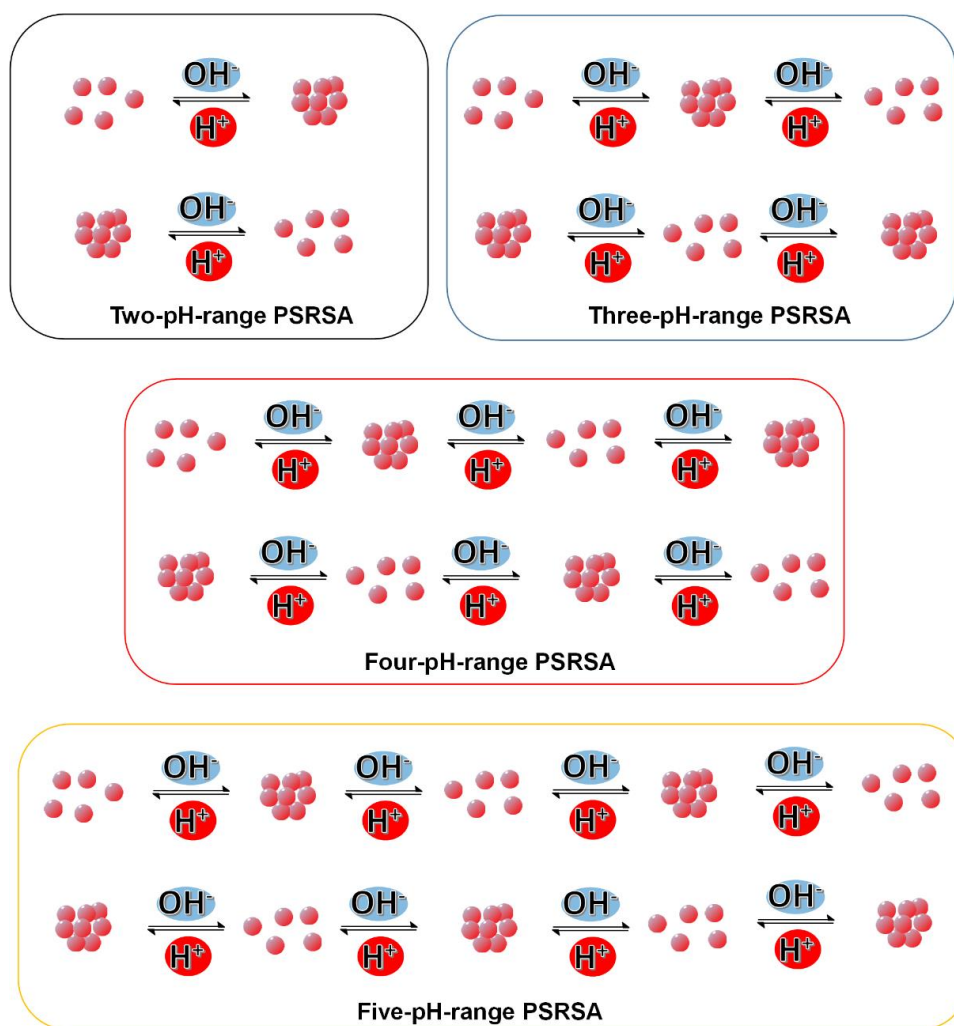


Figure 5.6: Illustration of different types of PSRSA behaviour.

5.2.3.1 Multi-PSRSA of AuNPs-1-4

UV/Vis measurement

As shown in Figure 5.7, the aqueous solution of AuNPs-1-4 (GCPZ/GCP ratio = 1/7) at pH = 7 exhibits a strong surface plasmon resonance (SPR) band at 557 nm. Switching the pH to 3 or 11 by adding of HCl or NaOH leads to a blue-shift of the SPR absorption from 557 to 524 nm, indicating the disassembly of AuNPs-1-4. After further addition of HCl or NaOH, the pH was changed to 1 or 13. This resulted in a red-shift of the SPR band from 524 nm to 555 nm (pH = 1) or from 524 to 560 nm (pH = 13), indicating the self-assembly of AuNPs. In brief, AuNPs-1-4 were dispersed at pH 3 and pH 11, while assembled at pH 1, pH 7 and pH 13. All self-assembly and disassembly behaviours mentioned above are reversible while switching the pH values.

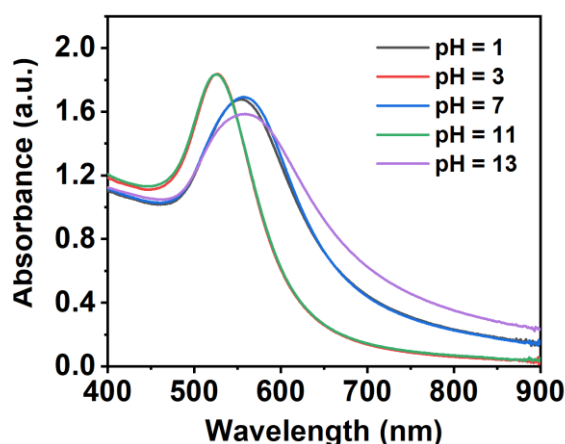


Figure 5.7: UV/Vis absorption spectra of AuNPs-1-4 (GCPZ/GCP = 1/7) at different pH values.

DLS measurement

Dynamic light scattering (DLS) measurements of AuNPs-1-4 dispersions also confirmed the multi-PSRSA behaviour. The results show the changes in the hydrodynamic radii of the AuNPs-1-4 species (Figure 5.8a). It shows a mean size of 10 nm at pH = 3 and pH = 11 which is consistent with the size of surface-coated AuNPs, indicating that AuNPs-1-4 are separated without any aggregation. In contrast, the size of particles is well over 700 nm at pH = 1, pH = 7 and pH = 13, indicating a self-assembled state of AuNPs-1-4. In accordance with the DLS results, the solutions of unassembled AuNPs-1-4 are in a deep red colour at pH = 3 and pH = 11, while the solutions of assembled AuNPs-1-4 are in a purple colour at pH = 1, pH = 7 and pH = 13 (Figure 5.8b).

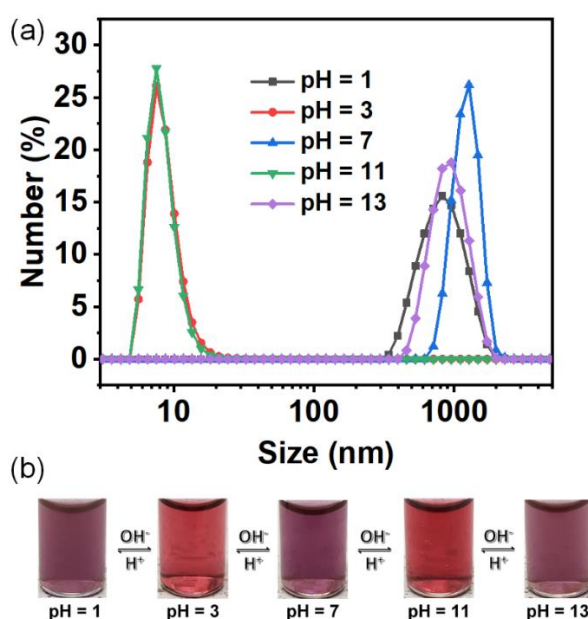


Figure 5.8: DLS measurement (a) and photos (b) of AuNPs-1-4 (GCPZ/GCP = 1/7) at different pH values.

TEM measurement

Furthermore, the morphologies of **AuNPs-1-4** were measured by TEM. Figure 5.9 shows the TEM images of **AuNPs-1-4** at different pH values. The **AuNPs-1-4** at pH = 3 (Figure 5.9b) and pH = 11 (Figure 5.9d) show a similar size distribution and no significant self-assembly was observed. However, aggregation of **AuNPs-1-4** in larger cluster were found at pH 1 (Figure 5.9a), pH 7 (Figure 5.9c) and pH 11 (Figure 5.9e). Thus, the TEM results also prove the occurrence of the multi-PSRSA of **AuNPs-1-4**.

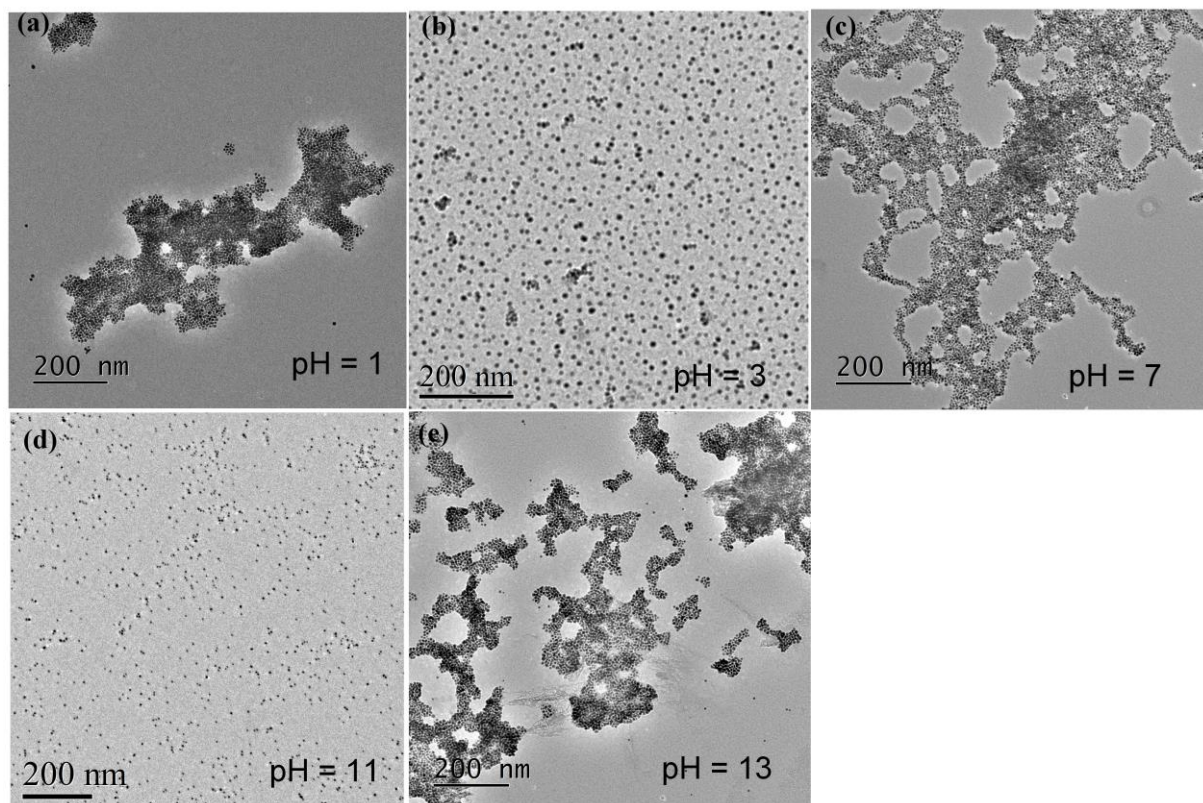


Figure 5.9: TEM images of **AuNPs-1-4** (GCPZ/GCP = 1/7) with different pH values, a) pH = 1, b) pH = 3, c) pH = 7, d) pH = 11 and e) pH = 13.

SEM measurement

For pH = 1, pH = 7 and pH = 13, SEM measurements are also performed to confirm the self-assembly of **AuNPs-1-4**. As shown in Figure 5.10, aggregates of **AuNPs-1-4** were formed in these three pH values. For pH = 1, the formed aggregates show a wide size distribution, and different sizes of clusters were observed (Figure 5.10a). For pH = 13, the aggregates of **AuNPs-1-4** show a more uniform size distribution (Figure 5.10c). In comparison to pH = 1 and pH = 13, the size of aggregates at pH = 7 was larger (Figure 5.10b), which is consistent with the DLS results (Figure 5.8).

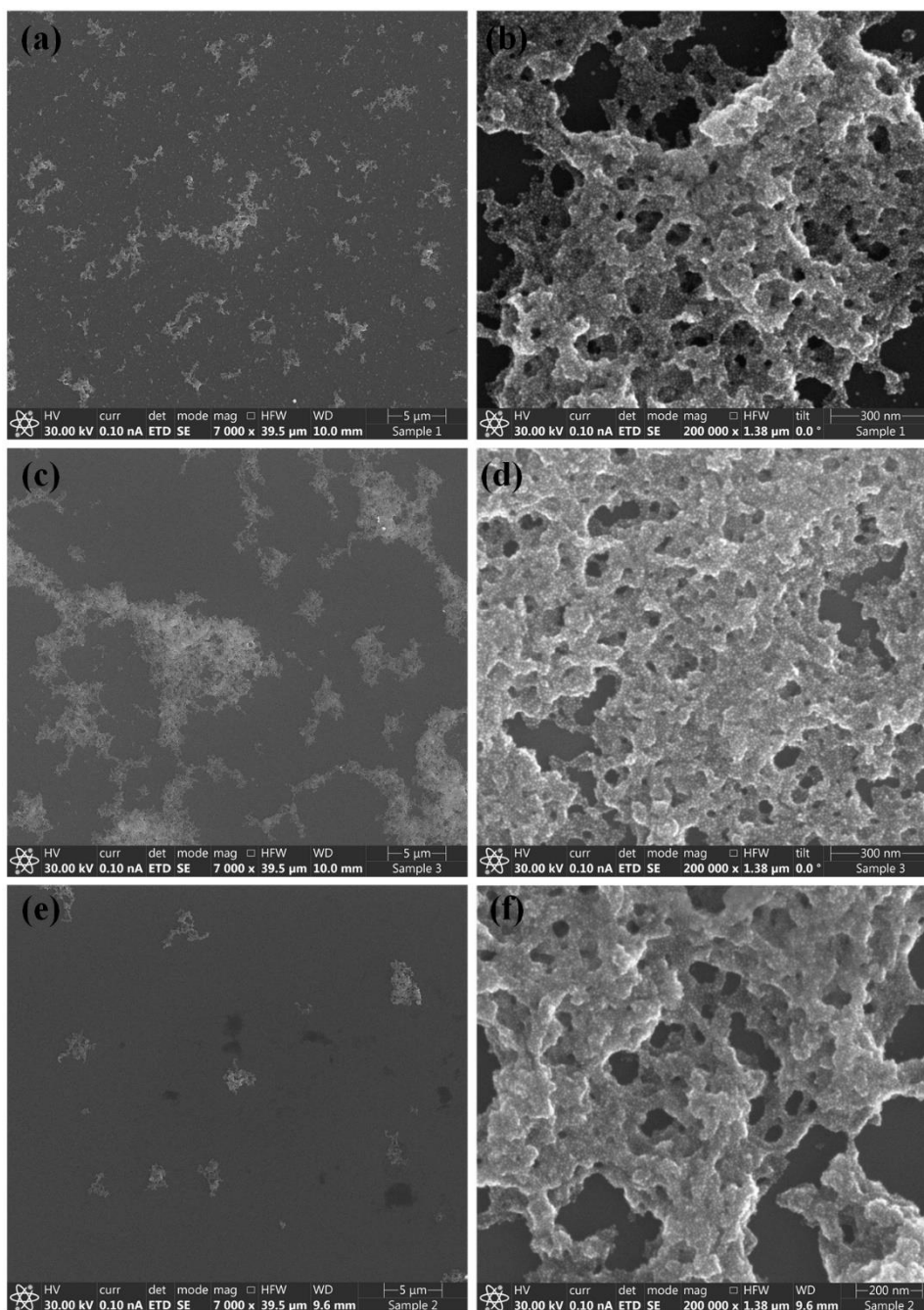


Figure 5.10: SEM images of aggregated AuNPs-1-4 at different pH values, a-b) pH = 1, c-d) pH = 7, e-f) pH = 13.

Reversibility of multi-PSRSA

As discussed above, the **PSRSA** behaviour which can respond to 5 different pH regions was confirmed by UV/Vis, DLS and TEM measurements. The reversibility of such multi-**PSRSA** was subsequently investigated since this is important to develop potential applications. Since the pH switching either between pH 1 to pH 3 or between pH 11 and pH 13 could bring about high concentrations of sodium chloride (from neutralization of HCl with NaOH) which may influence

the reversibility of self-assembly, we divided the whole cycle into three cycles. UV/Vis measurements were used to investigate the cycling between different pH values.

The change of the maximum absorbance wavelength (λ_{\max} , **SPR** band) at different pH values is shown in Figure 5.11. The results show a λ_{\max} at around 524 nm at pH 3 and pH 11, while the λ_{\max} is above 550 nm at pH 7, thus suggesting the reversible self-assembly of **AuNPs-1-4**. The cycle between these three pH values (pH 3, pH 7 and pH 11) can be repeated more than 10 times while the **AuNPs** are still showing a good reversibility (Figure 5.11a). For investigating the reversibility of self-assembly a high acidic and basic pH, intermittent centrifugation was used to avoid the influence of the high concentration NaCl. The reversible self-assembly between pH 1 and pH 3 can be repeated more than 15 cycles (Figure 5.11b) without any significant difference between the first and last cycle. For switching between pH 11 and pH 13, the cycle is also achieved more than 15 cycles (Figure 5.11c). Hence, the **AuNPs-1-4** show a good reversibility in switching between different pH values, so we believe that such **AuNPs-1-4** multi-PSRSA may have potential applications in controlled absorption-and-release cycles of pollutants by adjusting the pH.

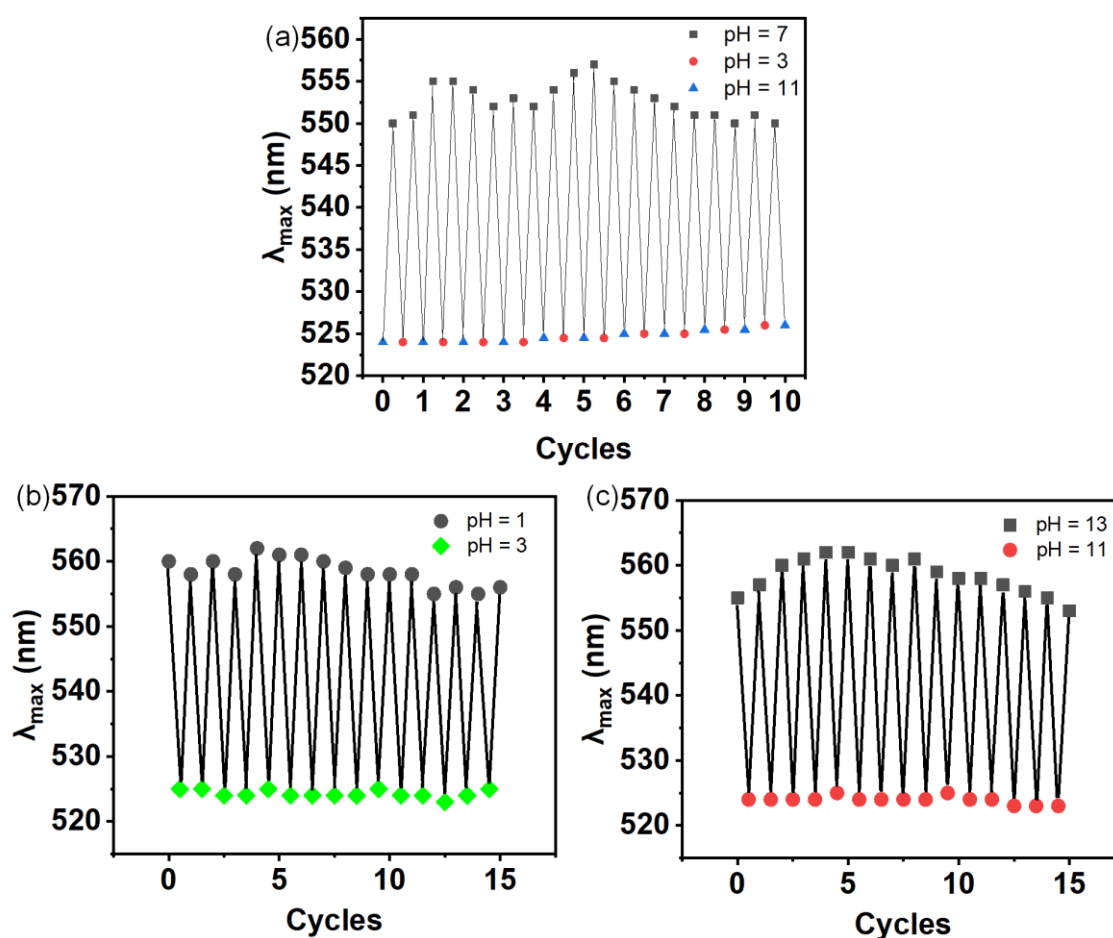


Figure 5.11: Cycles of reversible self-assembly of **AuNPs-1-4** ($\text{GCPZ}/\text{GCP} = 1/7$) between different pH values, (a) pH = 3, pH = 7 and pH = 11, (b) pH = 1 and pH = 3, (c) pH = 11 and pH = 13.

Influence of GCPZ/GCP ratio on multi-PSRSA

In order to investigate the mechanism behind the multi-PSRSA, we systematically varied the ratio of GCPZ (1) and GCP (4) on the AuNPs-1-4. As shown above (Figure 5.4), the ratio of GCP/GCPZ bound on the surface of AuNPs-1-4 is be the same as the ratio of GCP/GCPZ which is used in the synthesis. In this chapter, we will use the value of GCPZ/GCP ratio used in the synthesis to represent the GCPZ/GCP ratio on AuNPs.

The PSRSA of the functionalized AuNPs with different GCPZ/GCP ratios was then investigated in water. Figures 5.12-5.15 show the different assembly behaviours depending on the ratio of GCPZ/GCP. We found that AuNPs functionalized only with GCP (AuNPs-4) show a three-pH-range PSRSA which disassemble in a pH range from 1.2 to 5.0, while self-assembly in a pH range above 5 or below 1.2 is found (Figure 5.12a). GCPZ-only functionalized AuNPs (AuNPs-1) assemble at pH below 11 and disassembled at pH above 11, thus showing a two-pH-range PSRSA (Figure 12b). Notably, the assembly of AuNPs-1 at pH 13 was not observed, which is totally different from the self-assembly behaviour of AuNPs-1-4 (GCPZ/GCP = 1/7) at same pH value.

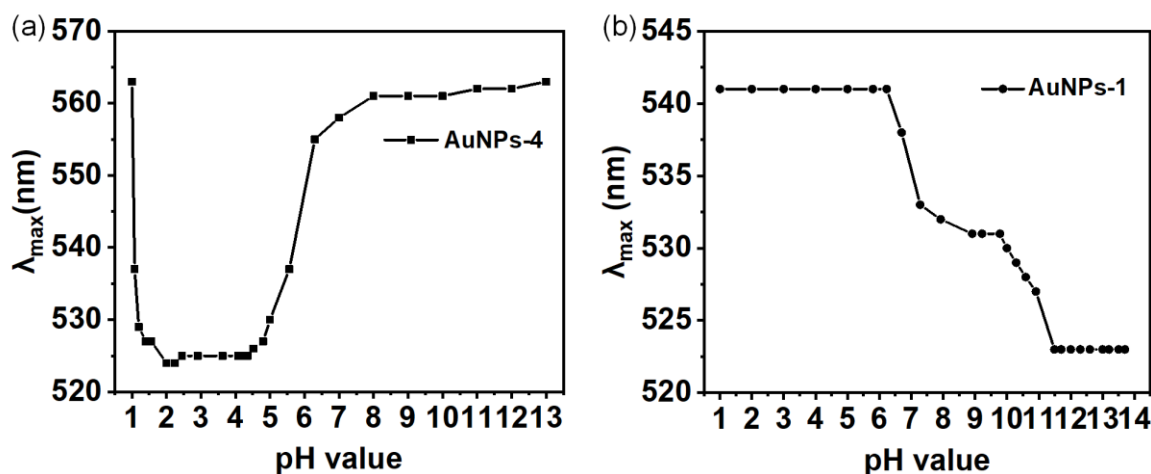


Figure 5.12: Wavelength of absorption maximum of AuNPs-4 (a) and AuNPs-1 (b) with different pH values.

Subsequently, the self-assembly behaviour of AuNPs with changing GCPZ/GCP ratios was investigated. For GCPZ/GCP = 1/19, the self-assembly behaviours of AuNPs-1-4 (Figure 5.13a) was like AuNPs-4 (Figure 5.12a). AuNPs-1-4 are dispersed in a pH range from 1.5 to 4.0 but are assembled when pH below 1.2 or above 4.5. For GCPZ/GCP = 1/12, an incomplete blue-shift of the SPR band was found in a pH range above 10 (Figure 5.13b), indicating that a partial disassembly occurs (compare to pH 9) at such pH values.

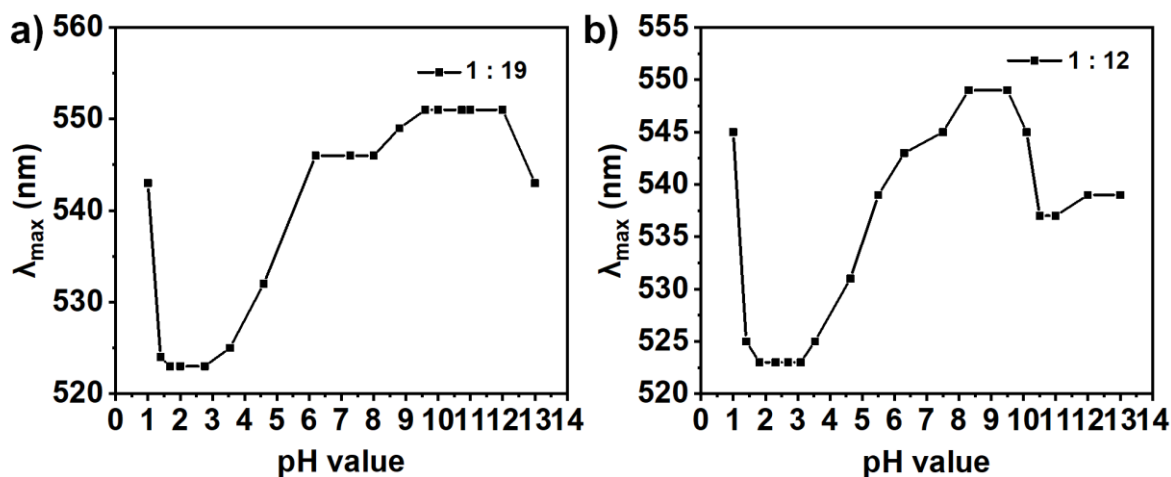
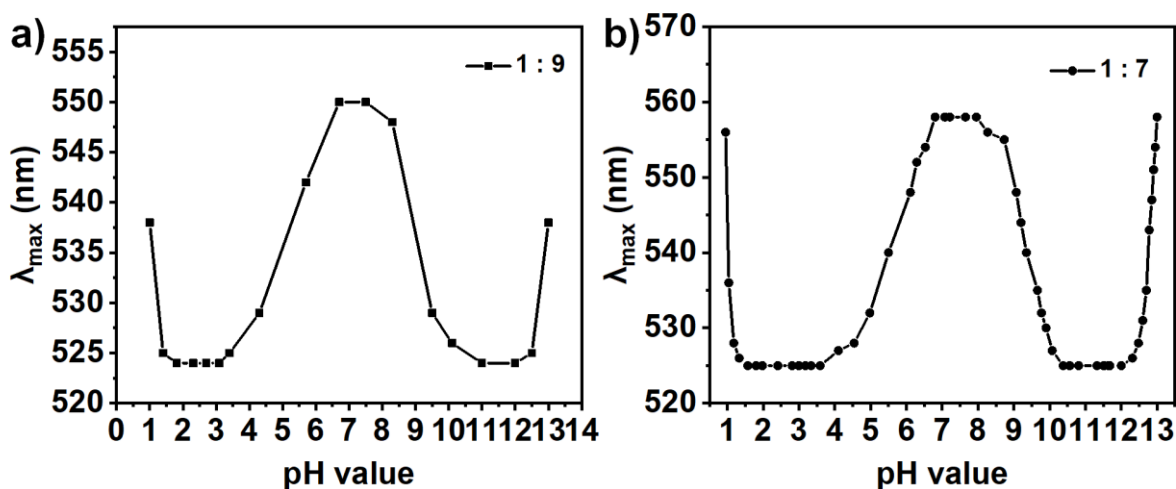


Figure 5.13: pH-dependent wavelength of absorption maximum of AuNPs-1-4 with different GCPZ/GCP ratio, (a)1/19, (b)1/12.

Further increasing the ratio of GCPZ/GCP (between 1/9 and 1/7) results in the complete disassembly of AuNPs-1-4 at $10 \leq \text{pH} \leq 12.5$ (Figure 5.14). Thus, a five-pH-range PSRSA is possible as discussed above (Figure 5.7-5.11).



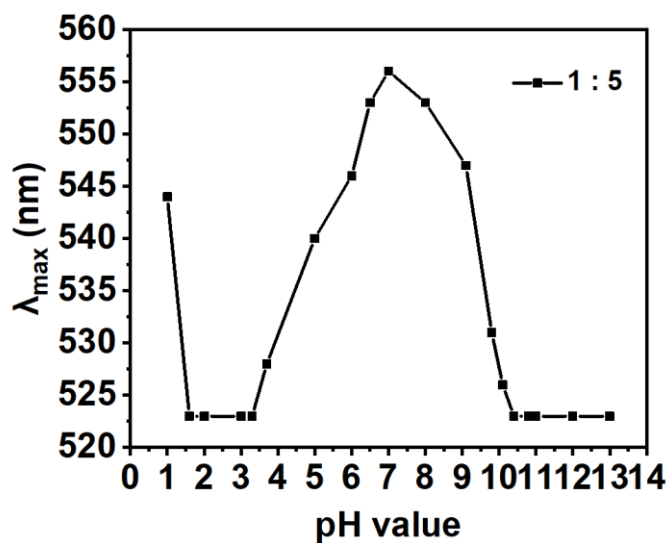


Figure 5.15: pH-dependent wavelength of absorption maximum of AuNPs-1-4 with a GCPZ/GCP ratio of 1/5.

Further increasing of GCPZ/GCP ratio leads to the suppression of disassembly at pH 3 (Figure 5.16), resulting in a two-pH-range PSRSA. This was as the same as a GCPZ-only functionalized AuNPs (AuNPs-1) (Figure 5.12b).

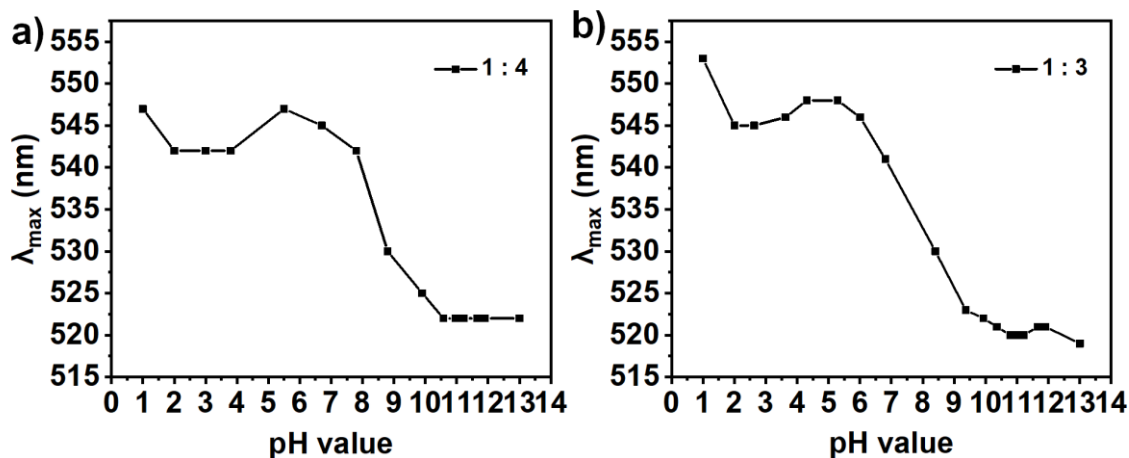


Figure 5.16: pH-dependent wavelength of absorption maximum of AuNPs-1-4 with different GCPZ/GCP ratio, (a)1/4, (b)1/3.

In conclusion, by varying the GCPZ/GCP ratio, four different type self-assembly behaviours were observed, from two-pH-range PSRSA to five-pH-range PSRSA.

Mechanism of multi-PSRSA

The self-assembly of AuNPs-1-4 could be well controlled by varying the GCPZ/GCP ratio, as a result four different types of self-assembly behaviour are achieved, from two-pH-range to five-pH-

range **PSRSA**. To the best of our knowledge, this is the first multi-**PSRSA** system based on metal nanoparticles which can respond to more than 4 different pH ranges. Therefore, it is valuable to understand the mechanism of this remarkable self-assembly behaviour.

In the last chapter, we proposed a mechanism for three-pH-range **PSRSA** of **AuNPs-1** based on hydrophobic effects and electrostatic interactions. We believe that hydrophobic effects are the main driving force for self-assembly of **AuNPs-1** at high water content, and the self-assembly/disassembly behaviours depends on the competition of hydrophobic effects and electrostatic repulsions. Herein, a possible mechanism of multi-**PSRSA** might be explained based on these two interactions. The self-assembly at pH = 7 was induced by the electrostatic interaction of the zwitterionic **GCPZ** and the hydrophobic effect of the deprotonated **GCP**. With the addition of base, the disassembly at pH = 11 was caused by the increasing electrostatic repulsion due to the deprotonation of carboxyl unit (**C-unit**) in **GCPZ**. In contrast, the electrostatic repulsion involved in the disassembly at pH = 3 was caused by protonation of guanidine-unit (**G-unit**) in **GCP** and **GCPZ**.

The disassembly at pH = 11 happened in ratios of **C/G** above 1/10, indicating that low concentration of negative charged **C-unit** can trigger the disassembly. The disassembly at pH = 3 occurred only when **G/C** ratio above 6, which means that the concentration of positive charged **G-unit** should be much higher than protonated **C-unit**. The reason could be the hydrophobic effect of protonated **C-unit** is much higher than deprotonated **G-unit**, which thus needs a larger relative content of positively charged **G-units** to be overcome.

Further addition of acid or base leads to the self-assembly of **AuNPs** at pH = 1 and pH = 13. These self-assembled states were not expected since no further protonation or deprotonation is expected. We measured the zeta-potential of **AuNPs-4** and **AuNPs-1-4** (**GCPZ/GCP** = 1/7) at different pH values. As shown in Figure 5.17b, with the decreasing of pH value from 6.5 to 2, the zeta potential of **AuNPs-1-4** increased from 0 mV to 49 mV. While further decreasing of pH value leads to the decreasing of zeta potential from 49 mV (pH 2) to 21 mV (pH 1). For basic pH range from 6.5 to pH 13, the zeta potential of **AuNPs** increasing gradually and then decreased from -41 mV to -28 mV while switching the pH value from 12 to 13. The same tendency of zeta potential changing was also observed for **GCP** functionalized **AuNPs** (Figure 5.17a). The change of zeta potential at pH 1 and pH 13 may be caused by high ionic strength, thus leading to a decreased electrostatic repulsion which could trigger the self-assembly of **NPs**.

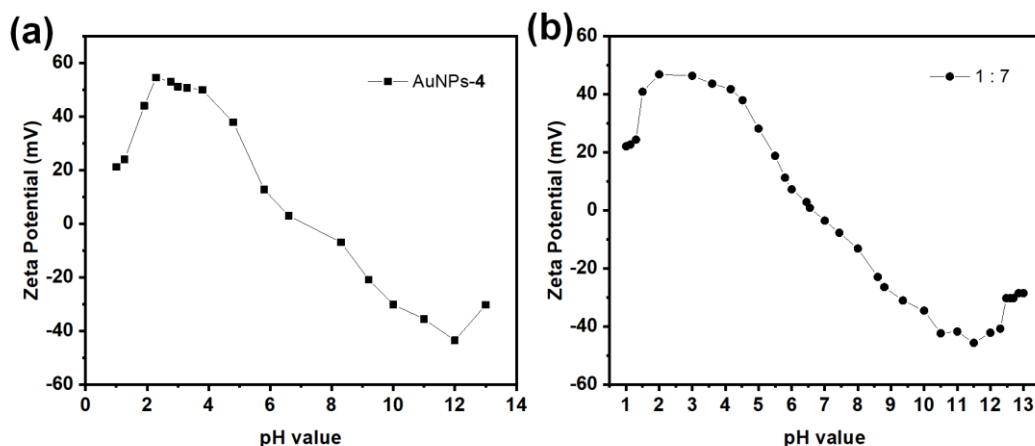


Figure 5.17: Zeta-potential of (a) AuNPs-4 and (b) AuNPs-1-4 (GCPZ/GCP = 1/7) at different pH values.

In order to confirm that the high ionic strength can trigger the self-assembly of AuNPs-1-4, a high concentration of NaCl was used instead of HCl and NaOH. As shown in Figure 5.18, AuNPs-1-4 were mono-dispersed at pH 3 and pH 11. The addition of NaCl resulted in the self-assembly of AuNPs. The minimum concentration of NaCl which can induce the self-assembly was 0.18 M and 0.06 M at pH 3 and pH 11 respectively. These concentrations are in the same order of magnitude as the concentration of HCl and NaOH that can trigger the self-assembly. This suggests that the assembly at pH 1 and pH 13 is caused by high ionic strength of the solution, which can alleviate the electrostatic repulsion between the AuNPs.

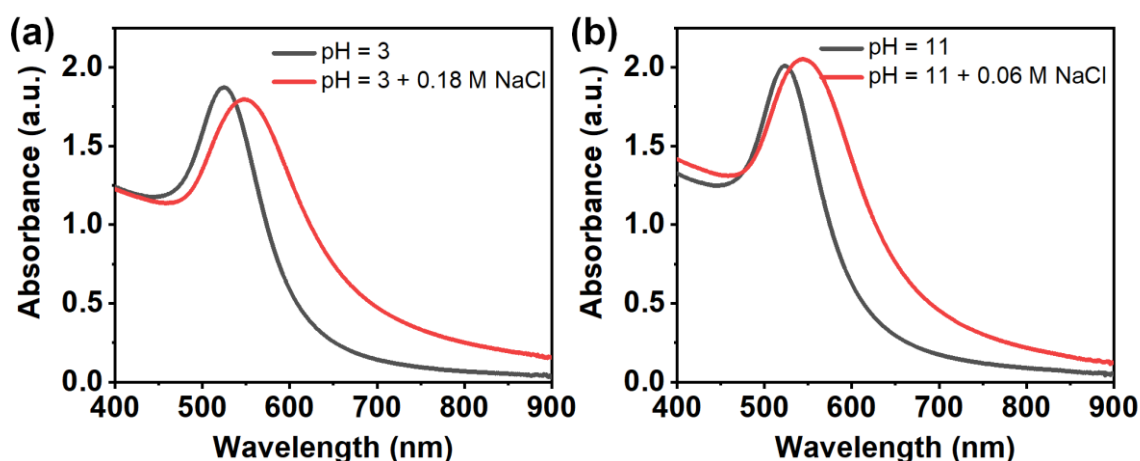


Figure 5.18: UV/Vis spectra of AuNPs-1-4 (GCPZ/GCP = 1/7) at pH 3 (a) and pH 11 (b) before and after addition of NaCl.

Such self-assembly at high ionic strength also depended on the ratio of GCPZ/GCP on AuNPs, so that self-assembly at pH 13 was not observed when the GCPZ/GCP ratio is above 1/5. Also, the exact nature of ligands on the surface also affects the self-assembly at high ionic strength. For

AuNPs functionalized with ligand **2** or ligand **3**, respectively, the UV/Vis spectra at pH 13 are the same as at pH 11 (Figure 5.19), indicating that no self-assembly occurs.

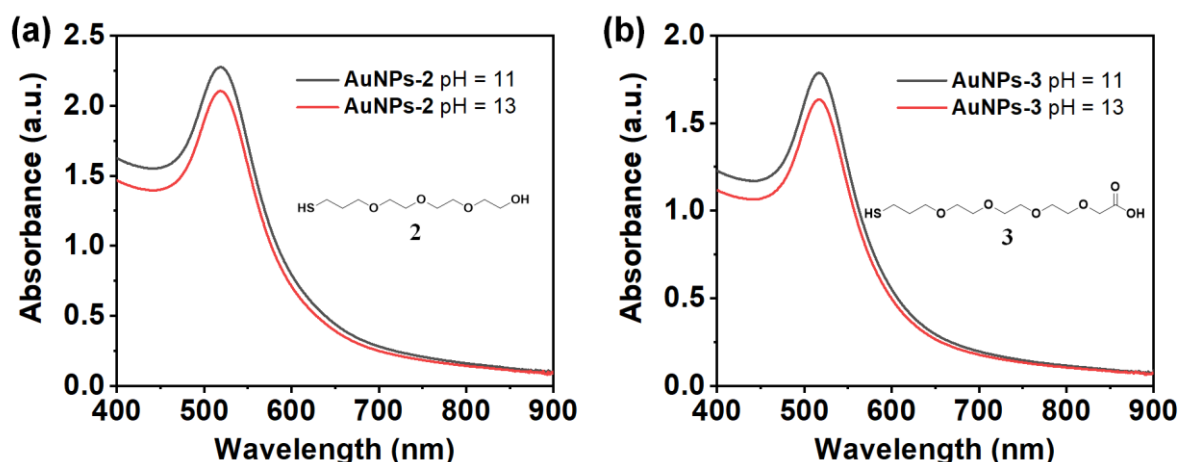


Figure 5.19: UV/Vis spectra of (a) AuNPs-2 and (b) AuNPs-3 at pH 11 and pH 13.

5.2.3.2 Thermo sensitive self-assembly of AuNPs-1-4

UV/Vis measurement

Another interesting effect that we observed upon investigation of the self-assembly behaviour is a temperature sensitivity. Here, the AuNPs are showing a change in assembly at pH = 1 and pH = 13 at different temperatures. Increasing the temperature from 20 °C to 70 °C leads to a blue-shift of SPR band of assembled NPs at pH = 1 from 555 nm to 525 nm in 2 min (Figure 5.20a). The SPR band red-shifts back upon cooling (Figure 5.20b), suggesting a reversible thermo-sensitive self-assembly of AuNPs-1-4 at pH 1. For the assembled AuNPs at pH 13, the SPR band also undergoes blue-shift from 560 nm to 525 nm in 2 min upon increasing the temperature from 20 °C to 70 °C (Figure 5.20c). In this case, cooling (from 70 °C to 20 °C) resulted in a less pronounced red-shift (Figure 5.20d). This suggests that at pH 13 heating induces the disassembly of assembled AuNPs at pH 13, while cooling only results in partial reassembly.

We also investigated the thermo sensitive self-assembly behaviour of AuNPs-2 and AuNPs-3 at pH 1 and pH 13. As shown in Figure 5.21a-5.21b, AuNPs-2 and AuNPs-3 are mono-dispersed at pH 13, which is independent of temperature. For pH 1, increasing the temperature to 70 °C leads to some red-shifts of SPR band of AuNPs-2 (Figure 5.21c) and AuNPs-3 (Figure 5.21d), while no reversible thermo-sensitive self-assembly is observed during the heating/cooling sequence. These findings suggest that the thermo sensitive self-assembly behaviour also depends on the ligand on the surface of AuNPs.

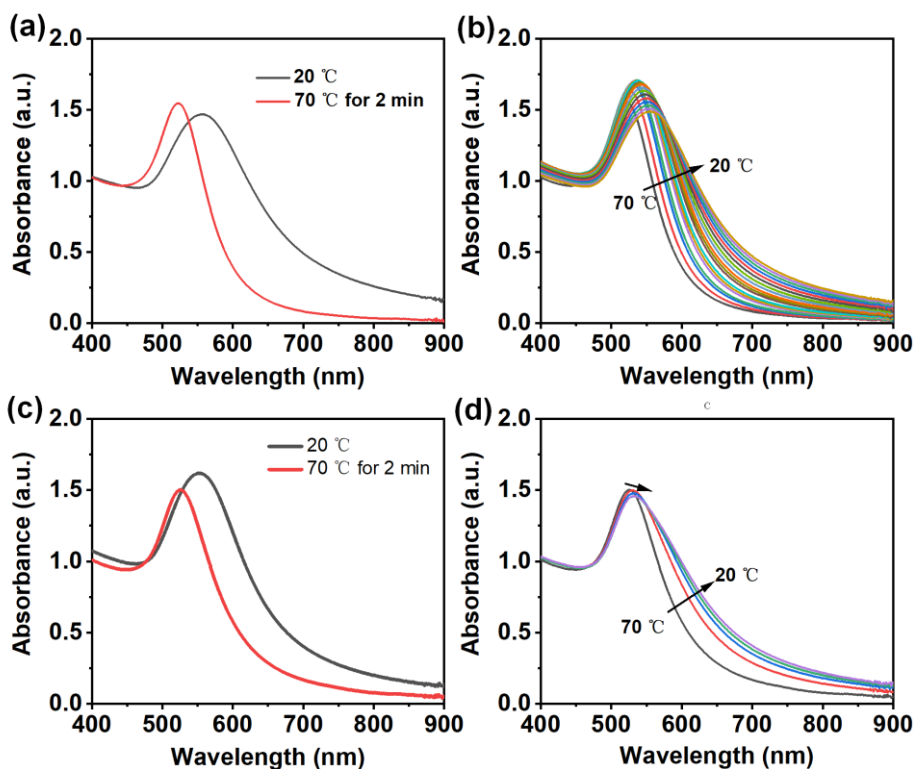


Figure 5.20: UV/Vis absorption spectra of AuNPs-1-4 (GCPZ/GCP=1/7) with different temperatures, (a) pH=1, from 20 °C to 70 °C, (b) pH=1, from 70 °C to 20 °C, (c) pH=13, from 20 °C to 70 °C, (d) pH=13, from 70 °C to 20 °C.

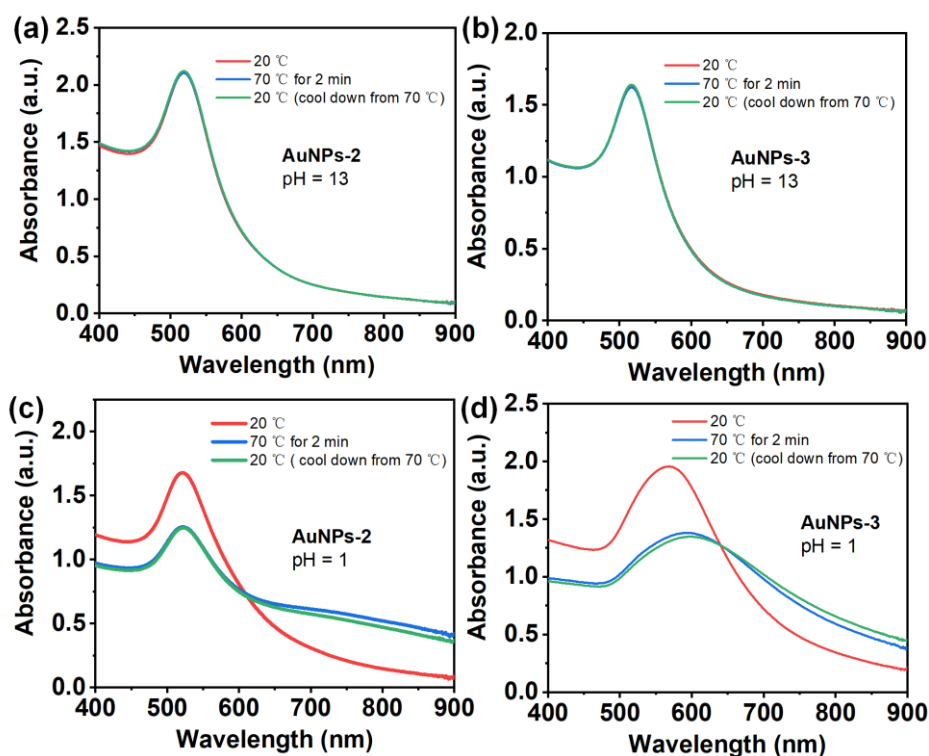


Figure 5.21: UV/Vis absorption spectra of (a) AuNPs-2 (pH=13), (b) AuNPs-3 (pH=13), (c) AuNPs-2 (pH=1) and (d) AuNPs-3 (pH=1) with different temperatures.

Reversibility of thermo-sensitive self-assembly

As discussed above, the aggregation of **AuNPs** at pH 1 and pH 13 can be reversed by increasing the temperature to 70 °C. The redispersed **AuNPs** will self-assemble again by cooling the solution down. Reversibility of this cycle has been experimentally demonstrated by UV/Vis spectroscopy during several heating-cooling cycles, showing the thermo-sensitive assembly/disassembly can be repeated more than 20 cycles (Figure 5.22).

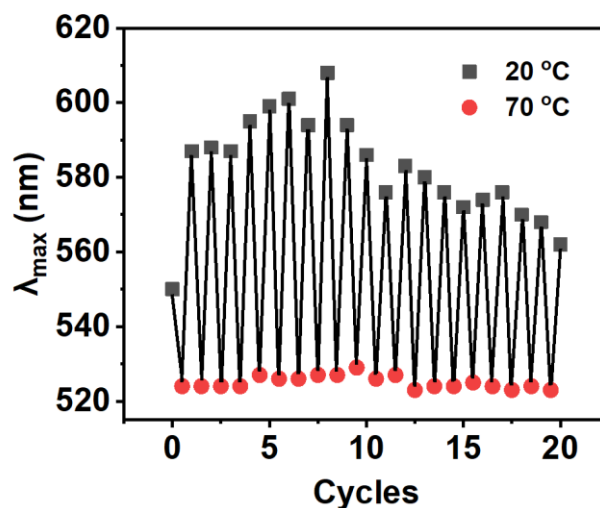


Figure 5.22: Cycles of reversible self-assembly of **AuNPs-1-4** ($\text{GCPZ}/\text{GCP} = 1/7$) at pH 1 between 20 °C and 70 °C.

As already discussed, the reversibility disassembly/reassembly of **AuNPs-1-4** at pH 13 was incomplete. Cooling the solution down leads to a partial self-assembly of **AuNPs**, and it was found that the duration of the heating time influences the degree of reassembly (Figure 5.23). After 40 min at 70 °C, the disassembly of **AuNPs** at pH 13 was irreversible, resulting in dispersion of **AuNPs** at both 70 °C and 20 °C. This may be due to the hydrolysis of amine bond at high basic and high temperature, which made the linker-**GCP** molecule no longer intact and changed the self-assembly behaviour.

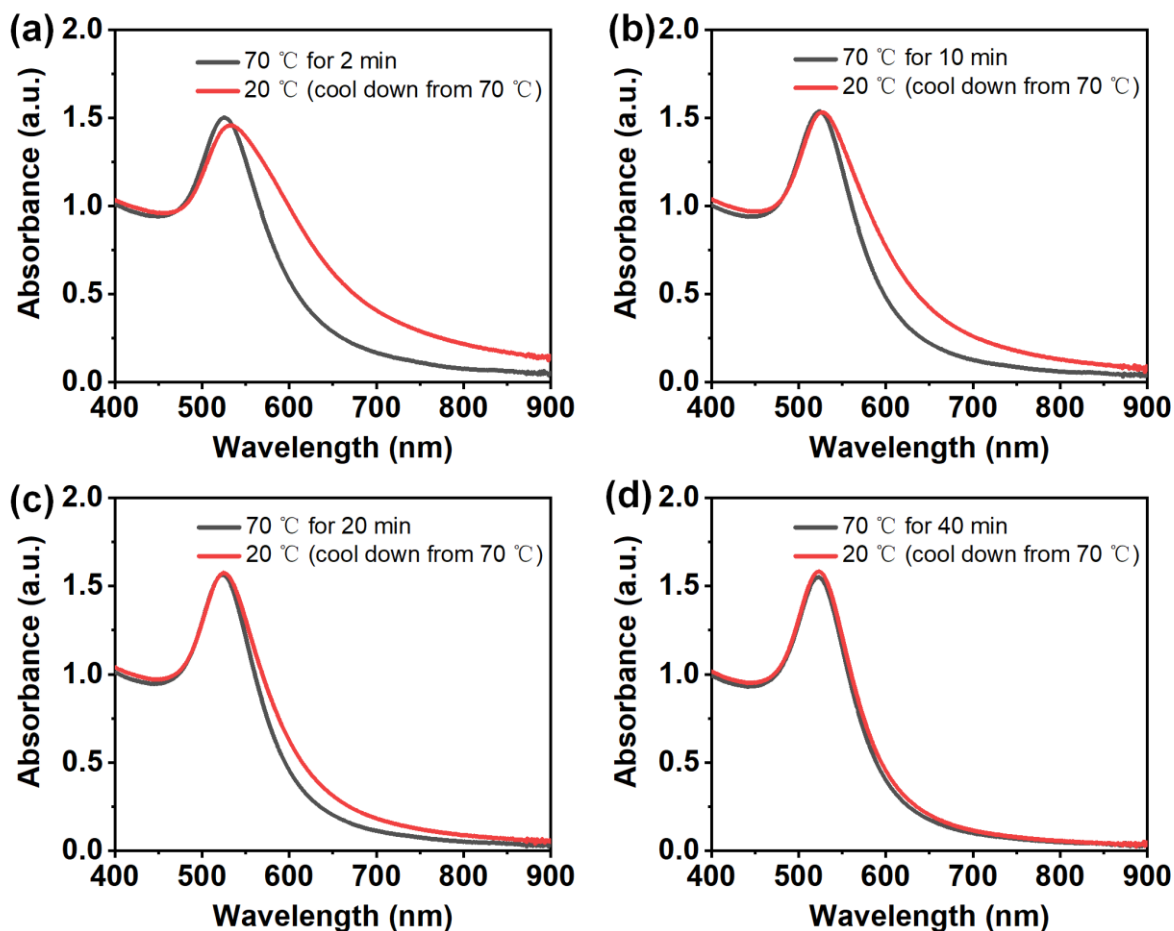


Figure 5.23: UV/Vis absorption spectra of AuNPs-1-4 (GCPZ/GCP =1/7) at pH = 13 with different heating durations, (a) 2 min, (b) 10 min, (c) 20 min, (d) 40 min.

Mechanism of the thermo-sensitive self-assembly

Temperature is easily accessible stimulus which can be delivered and removed quickly and non-invasively. Thermally responsive nanomaterials are usually designed by functionalizing NPs with molecules that exhibit temperature-dependent properties, such as conformation and intermolecular interactions. In our system, the thermo sensitive self-assembly at pH 1 and pH 13 may be attributed to the large changes in electrostatic repulsion potential (V_{elec}) upon varying the temperature. The electrostatic repulsion potential (V_{elec}) between the AuNPs can be estimated by linear superposition approximation⁷⁰:

$$V_{elec} = \varepsilon \Psi_i^2 \frac{a_i^2}{h_m + 2a_i} e^{-h_m/L_e} \quad (5-5)$$

⁷⁰ Y. Wang, G. Chen, M. Yang, G. Silber, S. Xing, L. H. Tan, F. Wang, Y. Feng, X. Liu, S. Li, H. Chen, *Nat. Commun.* **2010**, *1*, 87.

$$L_e = \kappa^{-1} = \left(\frac{\varepsilon k T}{2 e^2 I} \right)^{1/2} \quad (5-6)$$

Where ε is the dielectric constant of the medium, Ψ_i is the surface potential of the particle, a_i is the radius of the particle, h_m is the separation distance of the neighbouring particle centers. $L_e = \kappa^{-1}$ is the Debye screening length, calculated from the dielectric constant ε of the medium, the Boltzmann constant k , the temperature T , the elementary charge e and the ionic strength I of the electrolyte.

According to equation 5-5 and 5-6, as V_{elec} is proportional to $\exp(-\sqrt{I})$ and $\exp(-1/\sqrt{T})$, high ionic strength and low temperature leads to weak repulsion potential, resulting in the self-assembly of **AuNPs**. Furthermore, the V_{elec} increases with the increasing of the temperature and the high temperature leads to the disassembly of aggregated **AuNPs**. Therefore, the reversible thermo sensitive self-assembly can be induced by varying the temperature.

5.2.4 Application of multi-PSRSA in removing metal ions

The metal-ion-triggered self-assembly of nanoparticles has been widely investigated since it has been applied for the use of **NPs** as metal ion sensors. But the investigation in the removal of toxic metal ions, such as Hg^{2+} and Cu^{2+} , based on the self-assembly of metal **NPs** has rarely been reported. Herein, we intend to use our multi-**PSRSA** system to remove toxic metal ions from water. In our concept, the dispersed **AuNPs** collect the toxic ions partially on the surface of the nanoparticles at first. Secondly, these nanoparticles undergo aggregation by changing the pH or temperature, leading to precipitation of the **NPs** together with the toxic ions. Thirdly, the precipitate is collected by centrifugation so that the toxic metal ions are removed from solution. Finally, the metal ions can be liberated from the loaded nanoparticles and the clean nanoparticles can once again be precipitated. This leads to a solution of the toxic ions and regenerated **NPs**.

For instance, the schematic procedure of removal of Hg^{2+} and Cu^{2+} is shown in Figure 5.24. After addition of mixed metal ions into the solution of **AuNPs-1-4**, Hg^{2+} and Cu^{2+} were caught by **AuNPs-1-4** at $7 \leq \text{pH} \leq 11$. By adjusting the pH value of solution to 7, the **AuNPs** which are loaded with the toxic metal ions were self-assembled and precipitated from the solution in a few hours. The supernatant-1 which includes all other ions was removed by centrifugation and the precipitated **NPs** were re-dispersed in an aqueous solution ($\text{pH} = 3$). The Hg^{2+} and Cu^{2+} were released from the nanoparticles at $\text{pH} = 3$. The clean **AuNPs** assembled and precipitated by switching the pH to 1. Finally, the supernatant-2 contains Hg^{2+} and Cu^{2+} , which were thus removed. The precipitated **NPs** can be recycled in a basic solution ($\text{pH} = 11$).

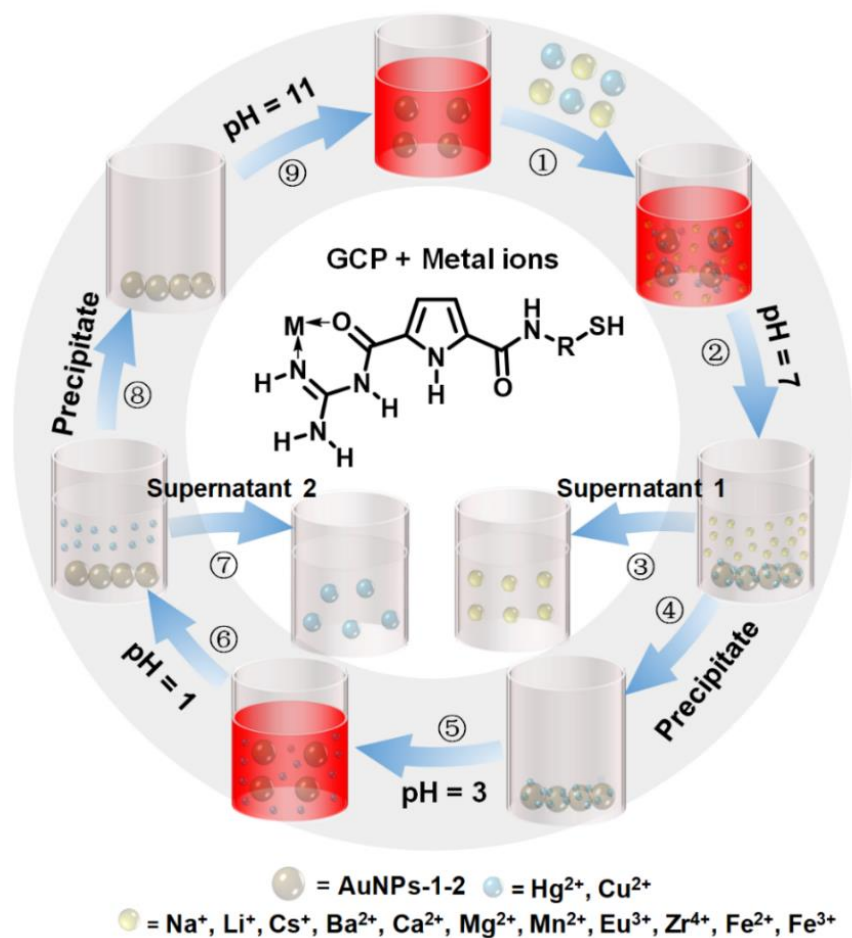


Figure 5.24: Scheme of removing metal ions by using multi-PSRSA of AuNPs-1-4.

5.2.4.1 Coordination of metal ion with GCP ligands

The key point in the concept of removing metal ion by using multi-PSRSA of AuNPs is the pH-dependent absorption of metal ions. Fortunately, we found our GCP ligand can coordinate with metal ions such as Hg²⁺ and Cu²⁺, and this interaction depends on the pH value. Thus, in this concept, the GCP-unit not only acts as a supramolecular binding motif for the assembly/disassembly of the NPs, but also as a metal-binding unit. In order to investigate the metal ion coordination of GCP ligands, we measured the UV/Vis absorption spectrum of GCP ligand with different metal ions (Hg²⁺, Cu²⁺, Zn²⁺, Na⁺, Li⁺, Cs⁺, Ba²⁺, Ca²⁺, Mg²⁺, Mn²⁺, Eu³⁺, Zr⁴⁺, Fe²⁺ and Fe³⁺).

As shown in Figure 5.25, the UV/Vis absorption spectrum of solution of GCP ligand 4 (pH = 3) shows a peak of the pyrrole unit at 296 nm and no change was observed within the addition of different kinds of metal ions.

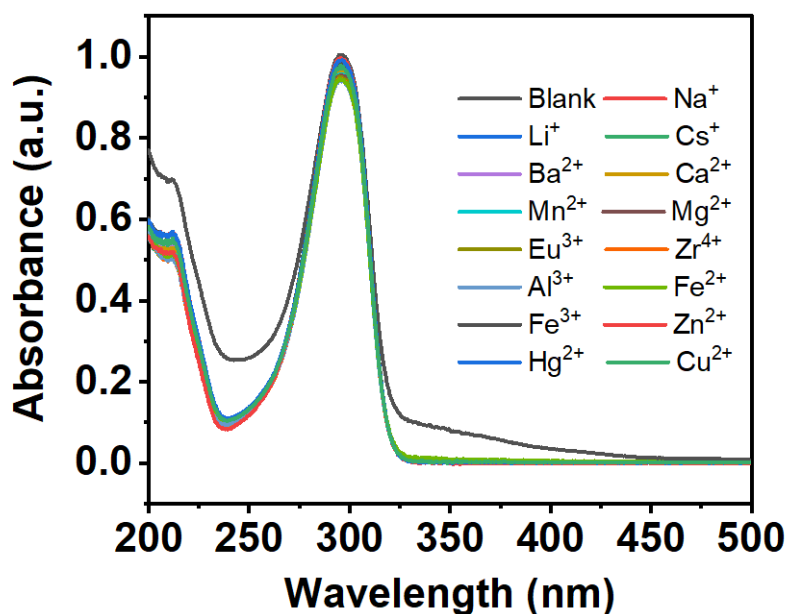


Figure 5.25: UV/Vis absorption of **GCP** ligand with different metal ions at pH = 3.

For the neutral solutions (pH = 7, Figure 5.26a), the addition of Zn^{2+} , Hg^{2+} or Cu^{2+} leads to a red-shift of absorption peak from 298 nm to 316 nm, indicating the coordination of **GCP** with Zn^{2+} , Hg^{2+} or Cu^{2+} . In addition, coordination of these metal ions leads to the decreasing in absorption of **GCP** solution. Compare to Zn^{2+} and Hg^{2+} , the decrease in absorption caused by Cu^{2+} was more significant (from 1.04 to 0.43). This could provide the opportunity for the detection of copper ions with the **GCP** unit. In contrast, no obvious red-shift of the pyrrole peak was observed when the other metal ions were added. The same results were also obtained in a pH 11 solution (Figure 5.26b). The absorption peak had a red-shift when the Zn^{2+} , Hg^{2+} or Cu^{2+} was added, while no change occurred with the addition of the other metal ions.

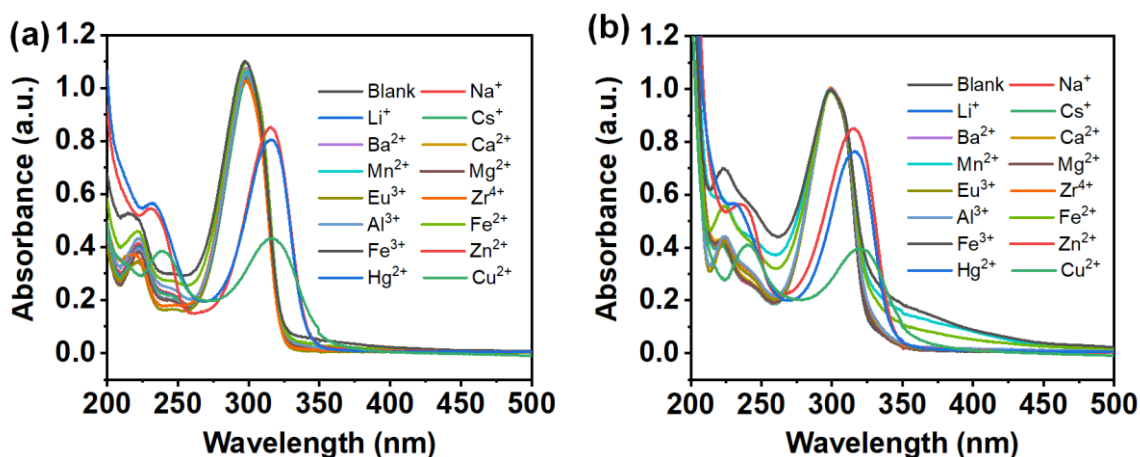


Figure 5.26: UV/Vis absorption of **GCP** ligand with different metal ions at (a) pH = 7 and (b) pH = 11.

The UV/Vis data at different pH values shows that the coordination of **GCP** with Zn^{2+} , Hg^{2+} or Cu^{2+} occurred at neutral (pH 7) and basic (pH 11) solution. In order to investigate the exact pH range for coordination, we measured the UV/Vis spectrum of **GCP** ligand (**4** in Figure 5.1) with and without metal ions (Zn^{2+} , Hg^{2+} or Cu^{2+}) at different pH values (between pH 2 and 12). For **GCP** ligand only, a slight red-shift of pyrrole unit (from 296 nm to 298 nm) was observed due to the deprotonation of **GCP**-unit (Figure 5.27a). For the **GCP**/ Zn^{2+} mixture (Figure 5.27b), the absorption peak of **GCP** remained unchanged at a pH value below 5. Increasing of pH values (pH 5 to pH 7) led to a red-shift of the absorption peak from 295 nm to 316 nm. No further change was found when further increasing the pH (pH 7 to pH11). This suggests that pH 5 is the critical value for the coordination of **GCP** with Zn^{2+} , indicating that coordination happens obviously in a pH range above 5. The same critical value was observed in the **GCP**/ Hg^{2+} (Figure 5.27c) and **GCP**/ Cu^{2+} (Figure 5.27d) mixtures, which means the coordination of **GCP**-unit with Hg^{2+} and Cu^{2+} occurred in a pH range above 5. No coordination was observed when the pH value was below 5.

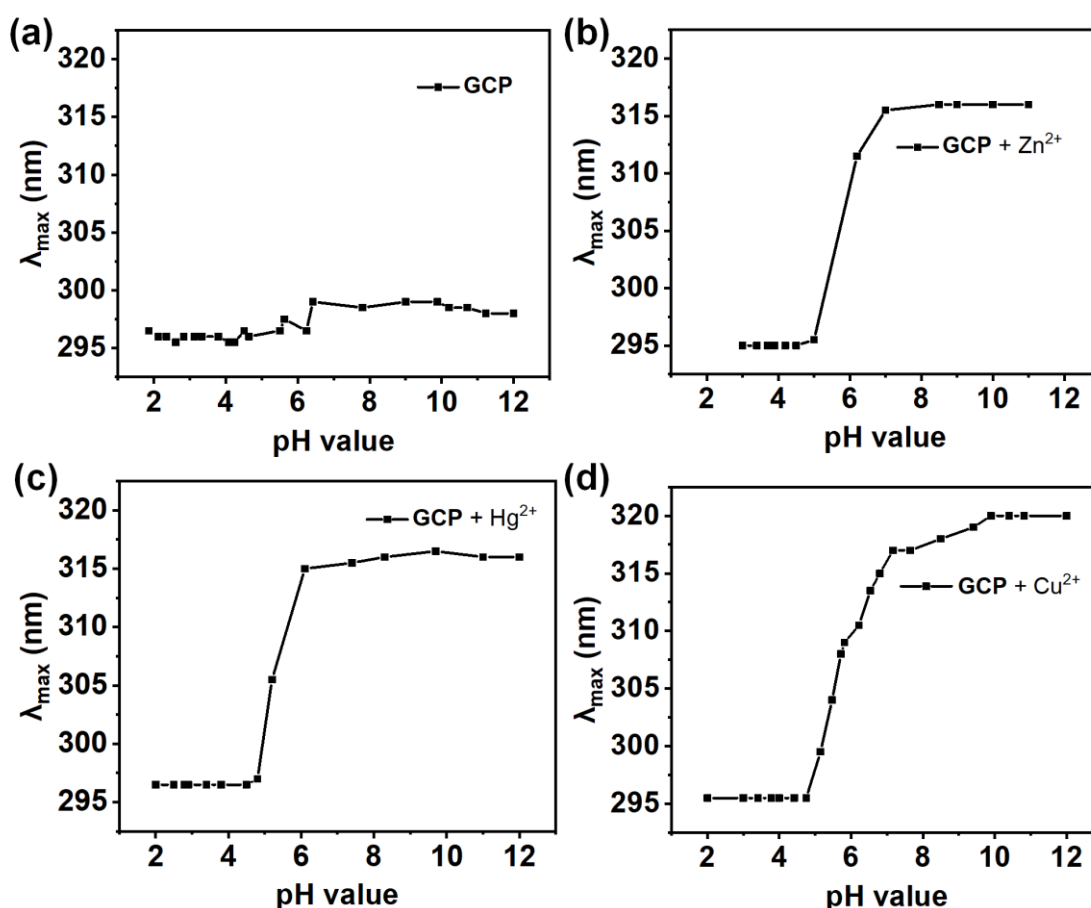


Figure 5.27: pH-dependent absorption peak of **GCP** ligand with different metal ions, (a) blank, (b) Zn^{2+} , (c) Hg^{2+} and (d) Cu^{2+} .

5.2.4.2 Water solubility of metal ions at basic pH value

The water solubility of metal ions plays an important role in the design of removal metal ions from aqueous solution. It is known that many metal ions show poor solubilities in basic condition due to the precipitation of metal hydroxide/oxide. In order to check if this might interfere with our suggested cycle for metal removal, a preliminary measurement was performed to identify the solubility of Zn^{2+} , Hg^{2+} and Cu^{2+} in the presence of **GCPZ** (**1** in Figure 4.1) as the detector (Figure 5.28). In brief, a $10\ \mu\text{M}$ solution of metal ions in aqueous medium was prepared by diluting the stock solution ($10\ \text{mM}$) with milli-Q water. Subsequently, the pH value of the solution was adjusted to 11 by addition of aqueous NaOH ($0.1\ \text{N}$), and the insoluble product was removed by centrifugation. Both of **GCP** and **GCPZ** ligands can be used as the detector for metal ions (Zn^{2+} , Hg^{2+} and Cu^{2+}) due to the containing of **GCP**-unit. Here, the concentration of metal ions in supernatant was determined by UV/Vis by using **GCPZ** as the detector because of its good solubility at basic pH values.

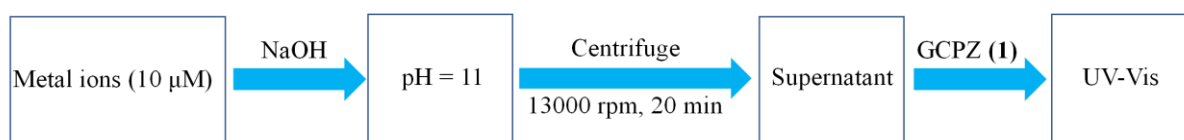


Figure 5.28: Determination of the solubility of metal ions (Hg^{2+} , Cu^{2+} and Zn^{2+}) at pH 11.

As discussed, coordinating with Hg^{2+} , Cu^{2+} and Zn^{2+} leads to the red-shift of the UV absorption of **GCP**-containing ligand. This phenomenon means that the **GCPZ** could be used as a sensor for the detection of Hg^{2+} , Zn^{2+} and Cu^{2+} . Hence, we measured the UV/Vis of supernatant of different metal ions with increasing concentration of **GCPZ** ligands (Figure 5.29). In the supernatant of Cu^{2+} and Zn^{2+} , no red-shift of UV absorption was observed, indicating the concentration of soluble metal ions at pH 11 was too low to be detected ($< 0.1\ \mu\text{M}$). However, for the supernatant of Hg^{2+} , the wavelength of absorption maximum of **GCPZ** kept in the value of 319 nm at low concentration (below $7\ \mu\text{M}$), which was caused by the coordination of **GCPZ** with Hg^{2+} . Further increasing the concentration of **GCPZ** (above $7\ \mu\text{M}$) led to the blue-shift of UV absorption due to the presence of free **GCPZ** ligands. These findings suggest that the Hg^{2+} shows a minor solubility in a pH = 11 aqueous solution.

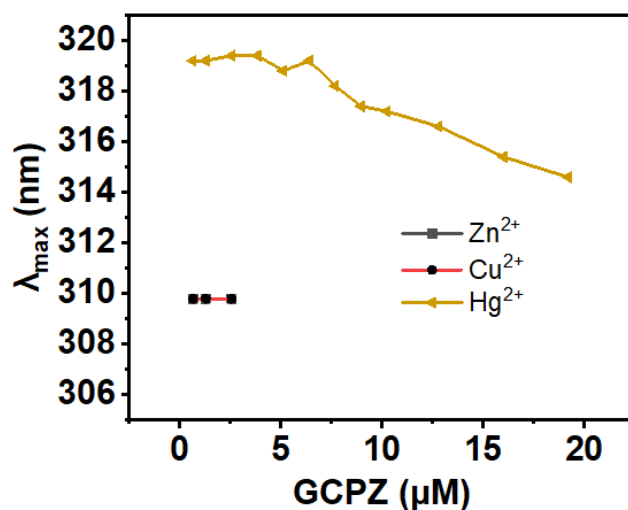


Figure 5.29: The change in wavelength of absorption maximum with increasing concentration of **GCPZ** in the supernatant containing different metal ions.

In order to confirm the unexpected solubility of Hg^{2+} at basic aqueous pH values, inductively coupled plasma - optical emission spectrometry (ICP-OES) was used to determine the concentration of Hg^{2+} in the supernatant (Figure 5.30). The ICP data shows that the concentration of Hg^{2+} in supernatant is 1584 $\mu\text{g/L}$ (7.9 μM) which is close to the initial concentration of Hg^{2+} (10 μM). This suggests that the Hg^{2+} still has a minor solubility at high basic pH values.

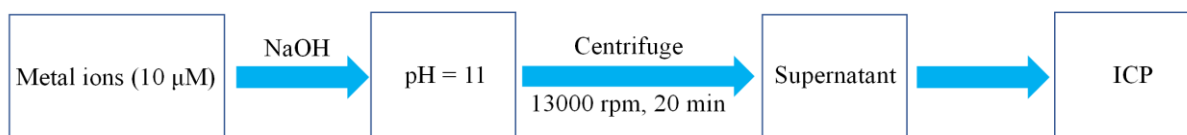


Figure 5.30: Determination of the solubility of Hg^{2+} at pH 11 by ICP.

With the help of UV/Vis and ICP measurements, we demonstrated that the Cu^{2+} and Zn^{2+} are highly insoluble at pH 11, while Hg^{2+} shows a much better solubility at such pH value. Interestingly, the poor solubility did not affect the coordination between **GCP** and metal ions (Hg^{2+} , Cu^{2+} and Zn^{2+}) at basic pH values (Figure 5.26b). This may indicate that the metals are stabilized by **GCP**-coordination, so that the precipitation is thermodynamically or kinetically hindered. However, for a real application, a solubility even in the absence of **GCP** is necessary.

5.2.4.3 Preliminary investigation of removing Hg^{2+} from solution

Among the heavy metal ions, mercury (II) is considered to be one of the most harmful pollutants due to severe damage to kidney function, immune system and central nervous system.⁷¹ The development of comprehensive strategies for removal of mercury ions is very important in materials chemistry and environmental science.

Following the steps in Figure 5.24, we investigated the collection and releasing of Hg^{2+} by using **AuNPs-1-4** as a pH-sensitive adsorbent. The photos illustrating the different steps are shown in Figure 5.31.

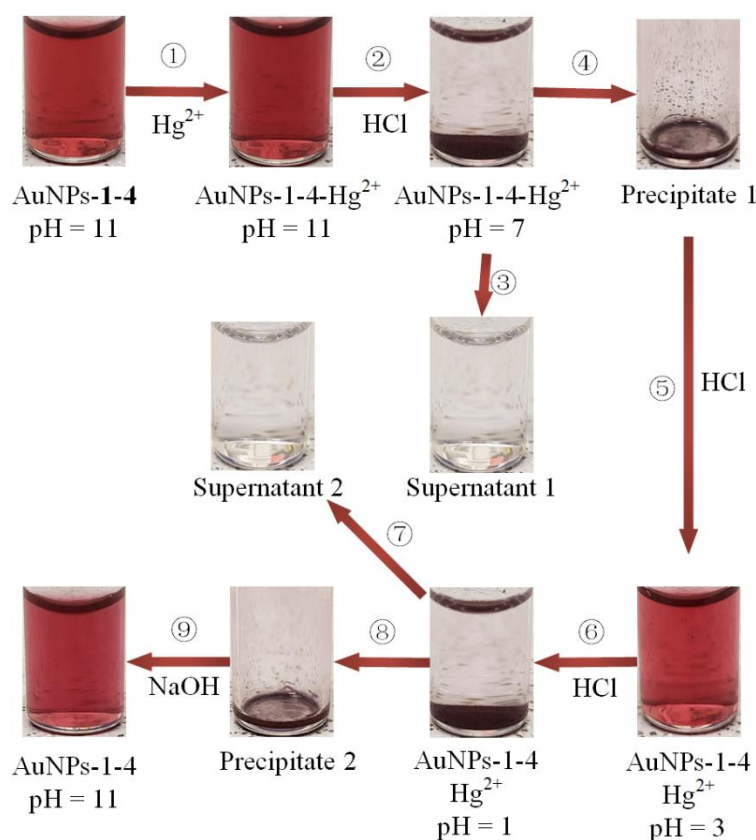


Figure 5.31: Photos in different steps of adsorption and release of Hg^{2+} by using **AuNPs-1-4** as the adsorbent.

ICP was used to determine the concentration of Hg^{2+} in supernatant-1, precipitate-1 and precipitate-2 (Table 5.1). The ICP data shows that the concentration of Hg^{2+} in supernatant-1 is $8.5 \mu\text{g/L}$ ($0.04 \mu\text{M}$), and the concentration of Hg^{2+} in precipitate-1 (adding water to keep the same value as supernatant-1) is $2010 \mu\text{g/L}$ ($10 \mu\text{M}$). This means that 99.6% of Hg^{2+} was absorbed by **AuNPs-1-4**. After the releasing procedures at acidic pH, the concentration of Hg^{2+} in precipitate 2 was

⁷¹ D. Dai, Z. Li, J. Yang, C. Wang, J.-R. Wu, Y. Wang, D. Zhang, Y.-W. Yang, *J. Am. Chem. Soc.* **2019**, *141*, 4756-4763.

determined as 145 $\mu\text{g/L}$ (0.7 μM), indicating the 92.8% of absorbed Hg^{2+} was released and recovered.

Table 5.1: Concentration of Hg^{2+} in supernatant 1, precipitate 1 and precipitate 2.

Samples	Supernatant 1	Precipitate 1	Precipitate 2
Concentration of Hg^{2+} ($\mu\text{g/L}$)	8.5	2010	145

Inspiring by the preliminary data and the positive result, more investigations in this project are on-going.

5.3 Conclusions

In summary, we developed pH-switchable **AuNPs** based on co-functionalization with **GCPZ** and **GCP** ligands. The reversible self-assembly of functionalized **AuNPs** can be precisely controlled, and allows for 4 types of pH-switchable self-assembly/disassembly states which can respond to 2, 3, 4 or 5 pH ranges. The exact self-assembly behaviour depends strongly on the ratio of **GCPZ**/**GCP** on the nanoparticles. In addition, functionalized **AuNPs** show a thermo-sensitive self-assembly/disassembly at $\text{pH} = 1$ and $\text{pH} = 13$. The multi-**PSRSA** capable **NPs** could be used in the removal of Hg^{2+} from aqueous solution. The **AuNPs** could be recycled again after removal of the toxic metal. Thus, this research not only shows a multi-**PSRSA** system and gives out the main principles for the design of multi pH-switchable **NPs**, but also indicates the application of multi pH-sensitive **NPs**.

6. One Dimensional Arrangement of Gold Nanoparticles

6.1 Introduction

Supramolecular interactions have excellent ability in spatially organizing components for the construction of dynamic and reversible hybrid materials. By supramolecular interactions, well-designed functional units and building blocks can form a variety of self-assembled structures, such as nanoparticles, nanofibers and nanotubes. On the basis of the fascinating directional noncovalent interactions, the formation of advanced supramolecular architectures with specific stimuli-responsive properties could be employed as stimuli-sensitive templates in **NPs** self-assembly research. However, while the arrangement of **NPs** on polymers, DNAs and other macromolecules has been reported, the hierarchical self-assembly of well-ordered arrays of **AuNPs** on supramolecularly assembled templates has rarely been explored.

In this chapter, we report a supramolecularly self-assembled architecture, a **GCP** containing nanofiber, as a template for the arrangement of **AuNPs**. In this fashion, **AuNPs** can be one dimensionally organized onto the nanofiber by supramolecular interaction which offers a way to control the **AuNPs** surface plasmon absorption wavelengths.

6.2 Results and discussion

6.2.1 Synthesis of building blocks with GCPs

An overview of our strategy is to generate a supramolecular template in the form of a nanofiber, which then acts as a template for the subsequent self-assembly of **AuNPs**. As shown in Figure 6.1, The **GCP** building block **5** was obtained by a 6-steps synthesis. The synthesis and characterization were carried out by Mr. Dennis Aschmann and Mr. Thorben Neumann, so it will not be described in detail here.

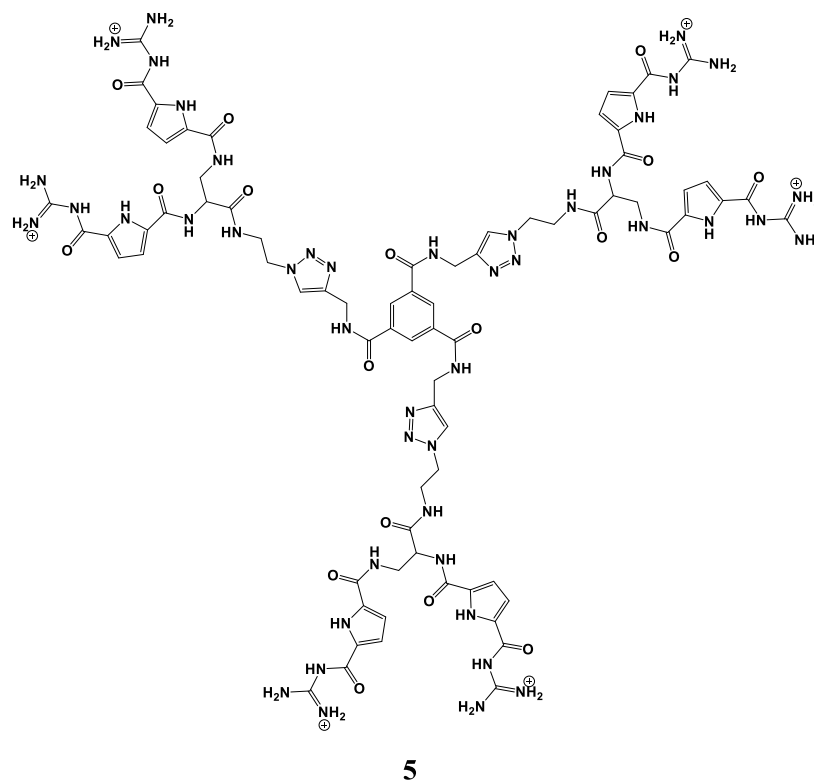


Figure 6.1: Molecular structure of building block 5.

6.2.2 One dimensional arrangement of AuNPs on nanofiber template

As shown in Figure 6.2, the **1D** arrangement of **AuNPs** was carried out by 2 steps. In the first step, the three-armed **GCP**-containing monomer carries out a self-assembly process to generate nanofiber which were then used as a template for the arrangement of **AuNPs**. In this fashion, carboxylic acid decorated **AuNPs** could well-organized onto the nanofiber skeleton by multiple hydrogen bonds and electrostatic interaction between the guanidinium-units on the surface of nanofiber and the carboxylates on the **AuNPs**.

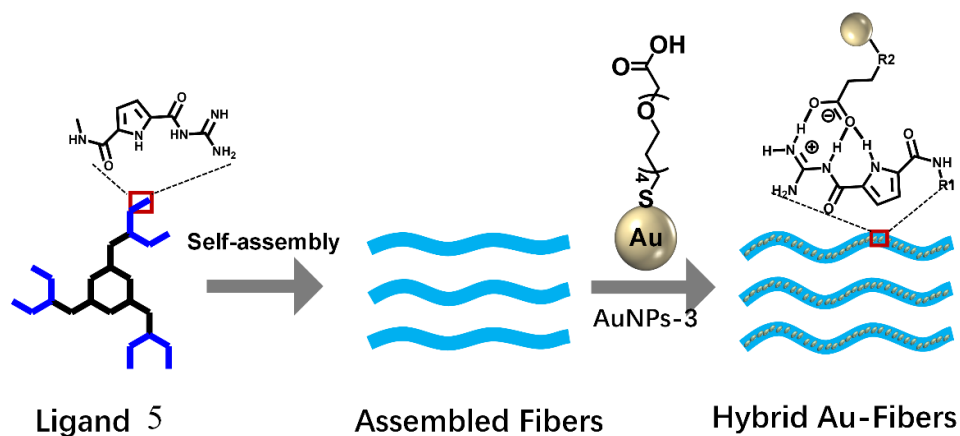


Figure 6.2: Scheme of **1D** arrangement of **AuNPs**.

6.2.2.1 Self-assembly of building block with GCPs (A)

The self-assembled nanofiber was obtained by dissolving three-armed molecule **5** in water (100 μM). The AFM image (Figure 6.3) reveals the formation of nanofibers with diameter of 10-20 nm which is similar to the size of **AuNPs** (7-8 nm). In addition, the length of nanofibers is greater than 10 μm , combining with the positively charged **GCP** bind motifs makes the nanofibers an ideal platform for one dimensional arrangement of **AuNPs**.

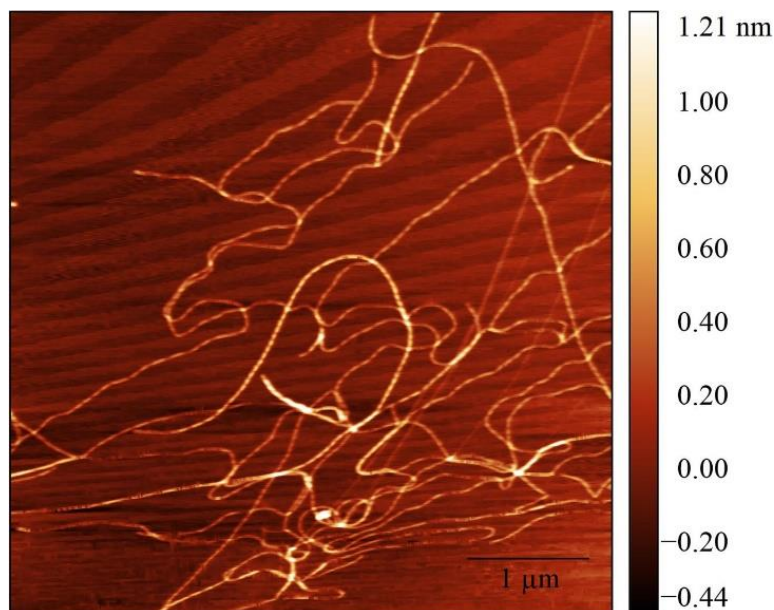


Figure 6.3: AFM image of self-assembled nanofibers by molecule **5** (100 μM).

6.2.2.2 Change of surface plasmon resonance

With this template in hand we started to investigate the self-assemble behaviour of **AuNPs-3** on nanofibers. The nanofiber-**AuNPs** self-assembly process was performed and controlled by continuously adding a solution containing the nanofibers to an aqueous solution of **AuNPs-3**. UV/Vis absorption was used to monitor and detect the surface plasmon resonance (**SPR**) band which reveals the self-assembly process between the nanofiber and **AuNPs**. As shown in Figure 6.4, originally dispersed **AuNPs-3** (32 nM) exhibits a strong surface **SPR** band at 518 nm, while stepwise addition of nanofiber template (0.4 μM for each step) led to a red-shift of **SPR** band from 518 nm to 537 nm (at 3.2 μM , i.e. after 8 steps). Further addition of nanofiber template induced the significant precipitation from the solution, indicating that concentration 3.2 μM is the critical condition for inducing precipitation. In this condition, the ratio of **5/AuNPs** is 100.

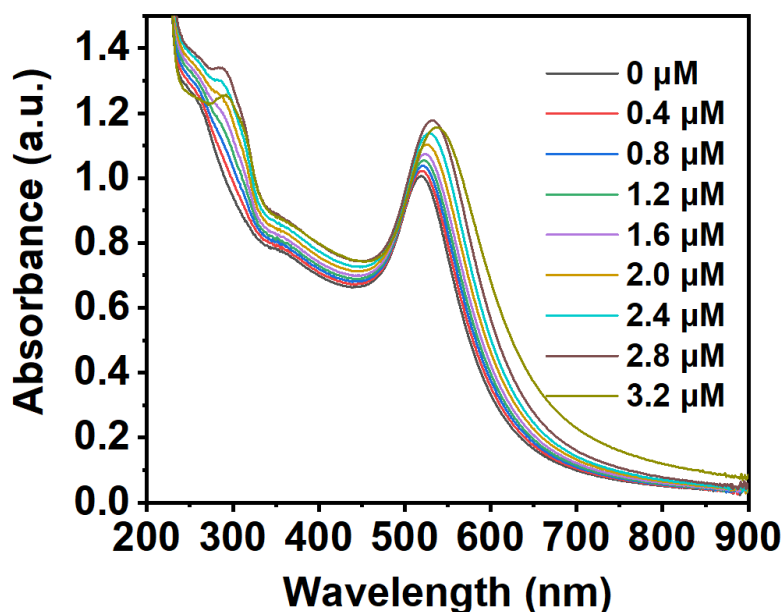


Figure 6.4: UV/Vis absorption of AuNPs-3 with different concentration of ligand 5.

Consistently with **SPR** changes, the colour of AuNPs-3 changed from the red to light purple. In this concentration regime ($<3.2 \mu\text{M}$ of 5), no precipitation was obtained (Figure 6.5).

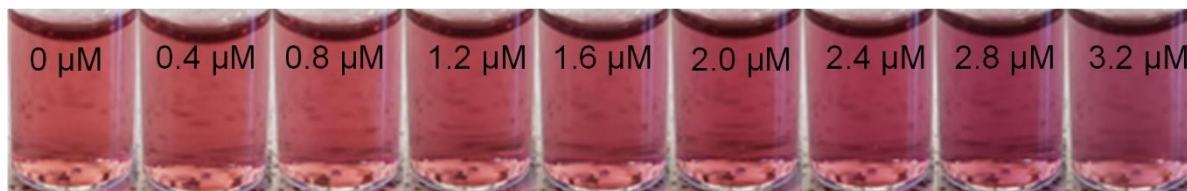


Figure 6.5: Photos of AuNPs-3 with different concentration of ligand 5

The influence of different addition methods has also been investigated. We varied the amounts added in the stepwise process (0.2 μM, 0.4 μM and 0.8 μM) while the total amount of nanofibers was kept as 3.2 μM. As shown in Figure 6.6, adding nanofibers in different step-sizes all lead to the **SPR** band red-shift. The **SPR** band of AuNPs-3 mainly depends on the total amount of nanofibers in the solution, the influence of how to add the nanofiber solution on **SPR** band changes is negligible.

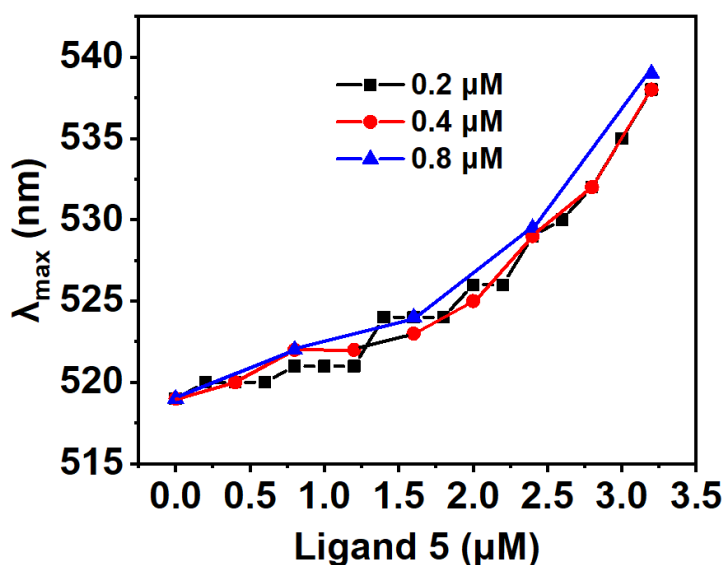


Figure 6.6: Absorption maximum of AuNPs on nanofiber templates with different intervallic adding amounts.

6.2.2.3 Influence of ratio between A and AuNPs

The arrangement of **AuNPs-3** on the nanofibers was investigated by TEM measurements. The samples for TEM measurement were prepared by gradually adding nanofiber solution (0.2 μM concentration increase for each step) until reaching the desired **5/AuNPs-3** ratio. The TEM images of **AuNPs** with different **5/AuNPs-3** ratios are shown in Figure 6.7-6.9. The best **1D** arrangement of **AuNPs** on the nanofibers was found when the ratio of **5/AuNPs-3** is 25:1 (Figure 6.7). A certain number of dispersed **AuNPs** which have no attachment onto nanofibers were also observed, indicating that under the employed concentration ratios, either the nanofibers were not abundant enough to complex all **AuNPs** or that the association constant of the **AuNPs** to the nanofibers is not high enough to ensure full complexation.

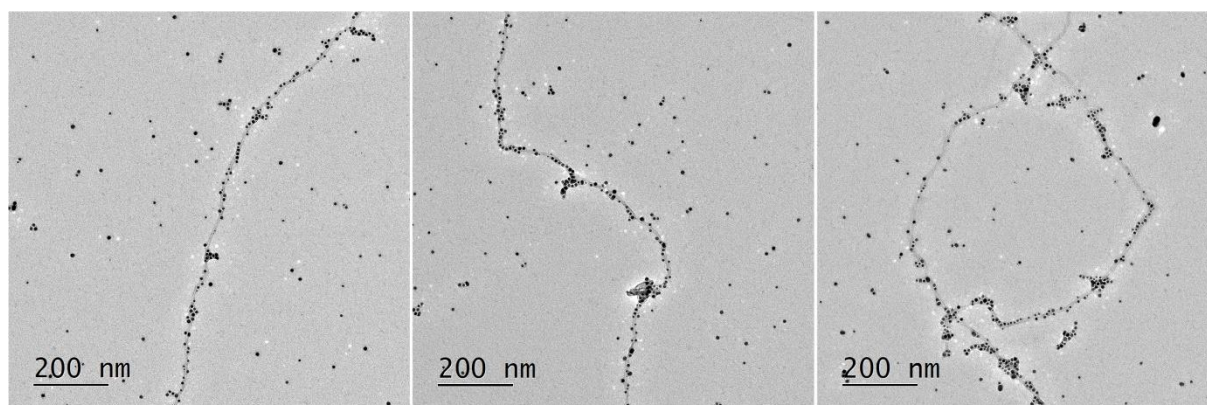


Figure 6.7: TEM images of AuNPs (**5/AuNPs-3** = 25/1) after step-by-step adding nanofiber templates.

When increasing the **5/AuNPs-3** ratio ($5/\text{AuNPs-3} = 75/1$), the **AuNPs**-nanofiber assemblies started to crosslink to each other resulting the creation of a knotted network. Meanwhile, the number of freely dispersed **AuNPs** dropped down significantly (Figure 6.8).

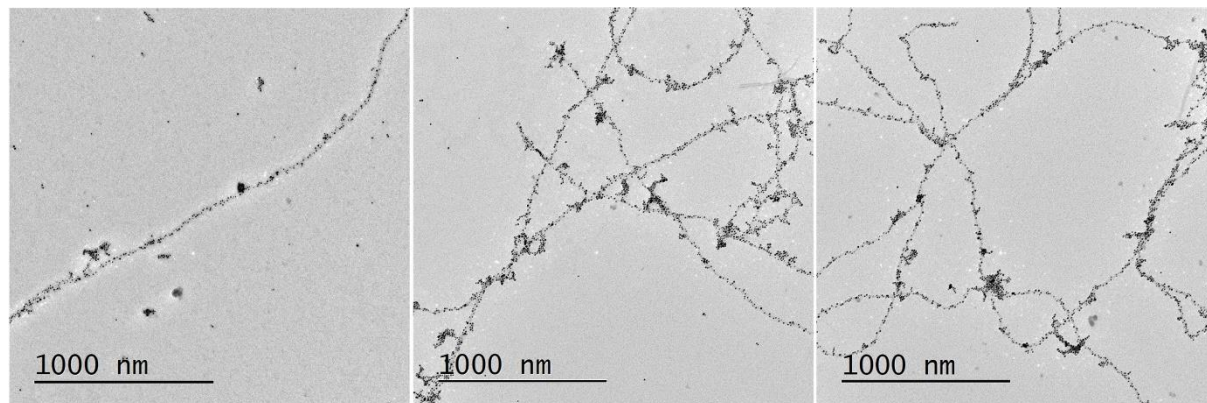


Figure 6.8: TEM images of **AuNPs** ($5/\text{AuNPs-3} = 75/1$) after step-by-step adding nanofiber templates.

When $5/\text{AuNPs}$ ratio increased to $100/1$, this led to the significant aggregation of **AuNPs**, with not structured **AuNPs**-nanofiber complex being observable in TEM images (Figure 6.9).

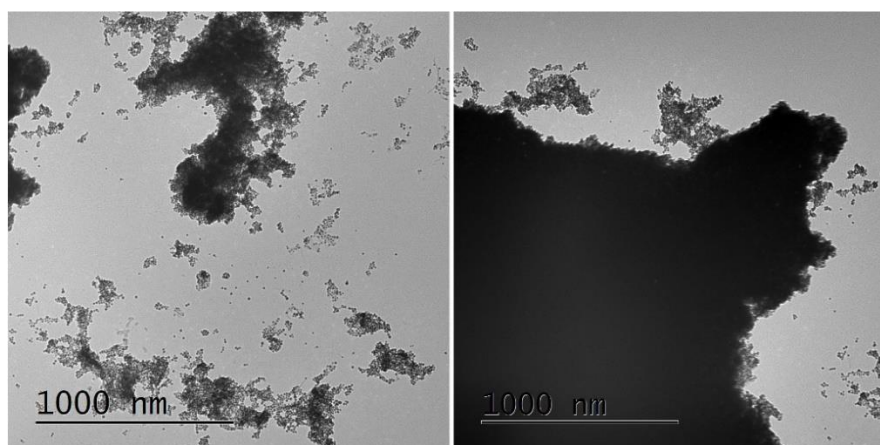


Figure 6.9: TEM images of **AuNPs** ($5/\text{AuNPs} = 100/1$) after step-by-step adding nanofiber template.

SEM was also used to detect the assembly result of **AuNPs**-nanofiber with a high ratio of $5/\text{AuNPs}$ ($100/1$), since it was not able to check the detailed assembly behaviour between **AuNPs** and nanofibers in TEM measurement. Both aggregated nanoparticles and **AuNPs**-nanofiber assembly architectures were found in SEM images (Figure 6.10). **AuNPs** are supposed to attach onto nanofiber template firstly. Afterward, the **AuNPs**-nanofiber architectures were going to aggregate together at higher $5/\text{AuNPs}$ ratio to cause the formation of aggregated clusters.

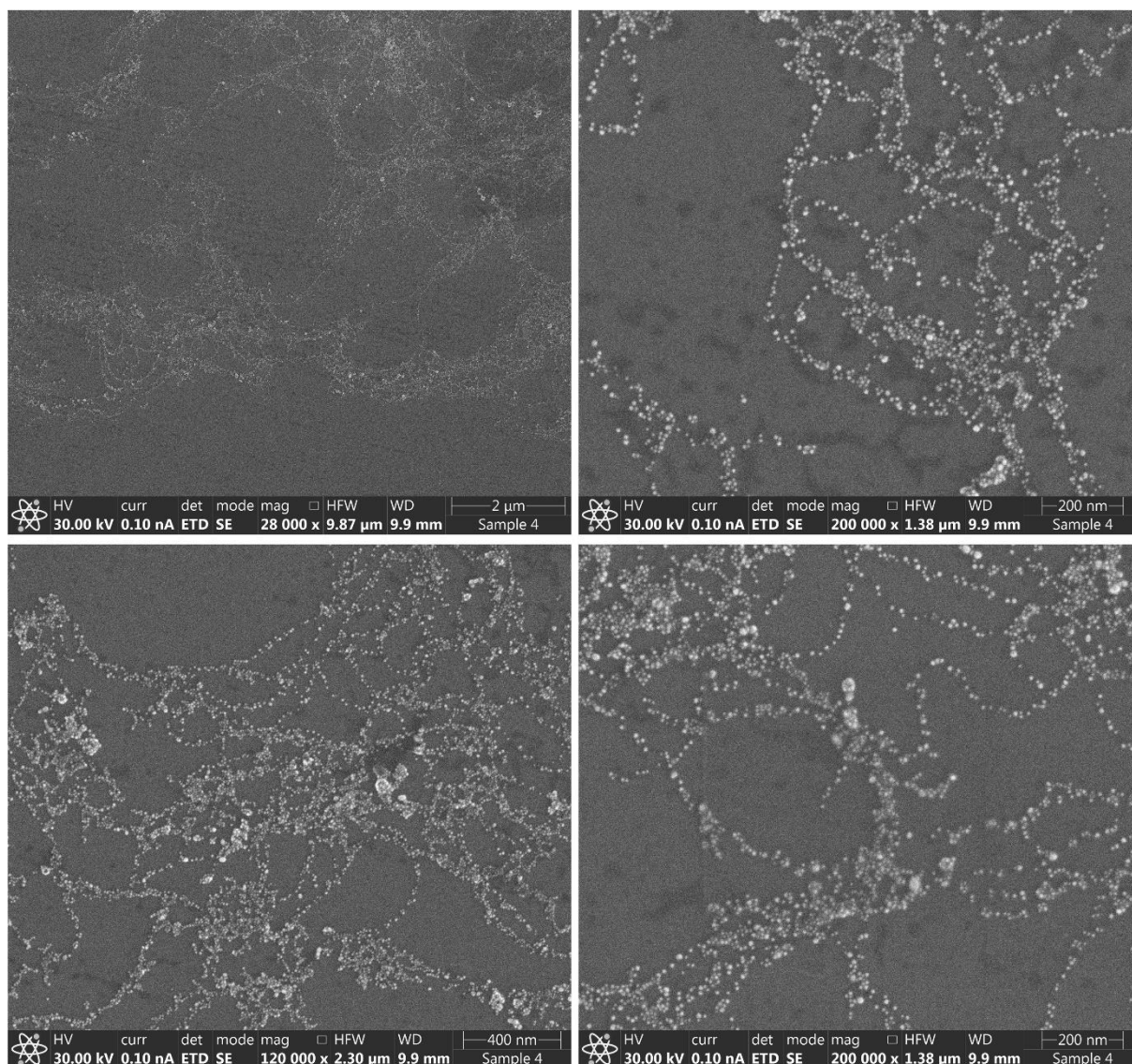


Figure 6.10: SEM images of AuNPs ($5/\text{AuNPs} = 100/1$) after step-by-step adding nanofiber templates.

Because significant precipitation was observed when $5/\text{AuNPs}$ ratio was increased to 100:1, it is necessary to study the further assembly behaviour if $5/\text{AuNPs}$ at such higher ratios. For such purpose, we prepared samples with $5/\text{AuNPs}$ ratios even higher than 2500:1 by adding highly concentrated solutions of the nanofibers to AuNPs. TEM images show that only the small aggregates were observed instead of precipitation. Unfortunately, one-dimensional arrangement of AuNPs on the nanofiber was not found at such high $5/\text{AuNPs}$ ratios, suggesting that well-organized arrangement and attachment from AuNPs onto nanofibers only take place at a suitable ratio range of $5/\text{AuNPs}$ (from 25:1 to 75:1).

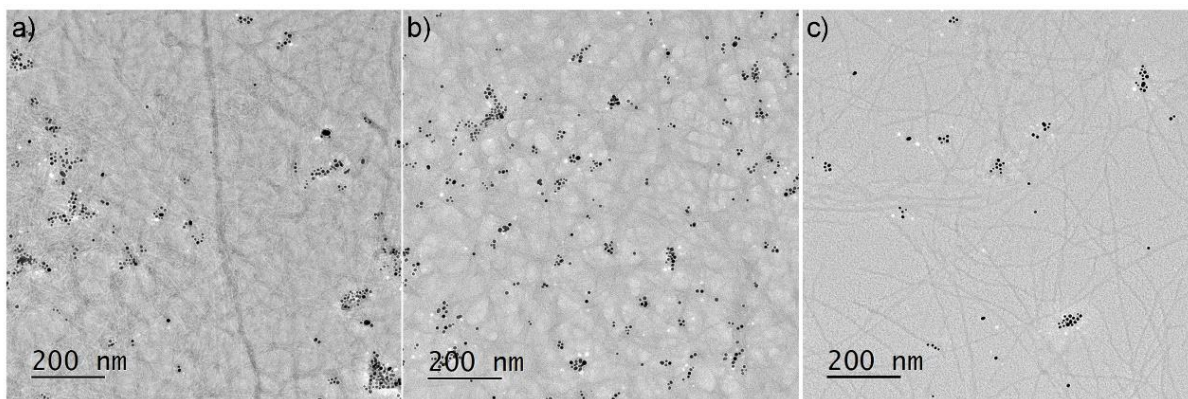


Figure 6.11: TEM images of AuNPs with different $5/\text{AuNPs}$ ratios by adding nanofibers into AuNPs solution, a) 2500 : 1, b) 5000 : 1, c) 7500 : 1.

In order to investigate the influence of the addition procedure in AuNPs arrangement, we prepared a sample with $5/\text{AuNPs}$ ratio 75:1 by adding nanofiber templates into AuNPs solution at one time. As shown in Figure 6.12, most AuNPs were deposited on the nanofiber templates to form AuNPs-nanofibers, while the rest of AuNPs aggregated together. This kind of aggregation was rarely observed in a step-by-step adding approach (vide supra). Hence, not only the $5/\text{AuNPs}$ ratio but also the approach how to add the nanofiber templates and AuNPs play an important role in controlling the one-dimensional arrangement of AuNPs on nanofibers.

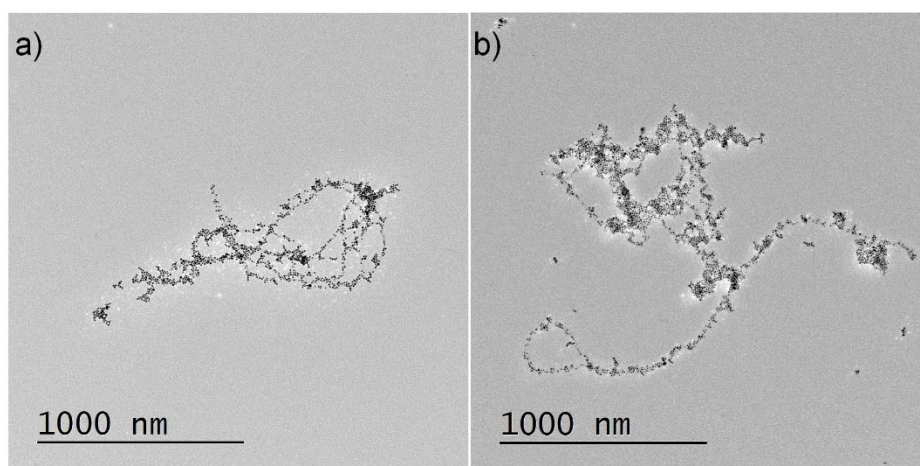


Figure 6.12: TEM images of AuNPs ($5/\text{AuNPs} = 75:1$) by adding AuNPs into template solution at one time.

DLS of AuNPs-3 dispersions was also performed to investigate the size change. The AuNPs-3 without templates show a hydrodynamic radius at 10 nm (Figure 6.13). Upon increasing the concentration of **5** from 0 μM to 2.6 μM , the average size of the AuNPs and AuNPs-nanofiber-aggregates changed from 10 nm to 170 nm gradually due to the increasing proportion of large nanofiber templates (around 400 nm). Further increasing concentration of **5** led to a rapid size-increase to 2000 nm, indicating the formation of bigger aggregations which were also found by

TEM measurement. A comparison experiment was performed by measuring the size of **GCP** nanofibers with different concentrations, but no significant size-change was observed.

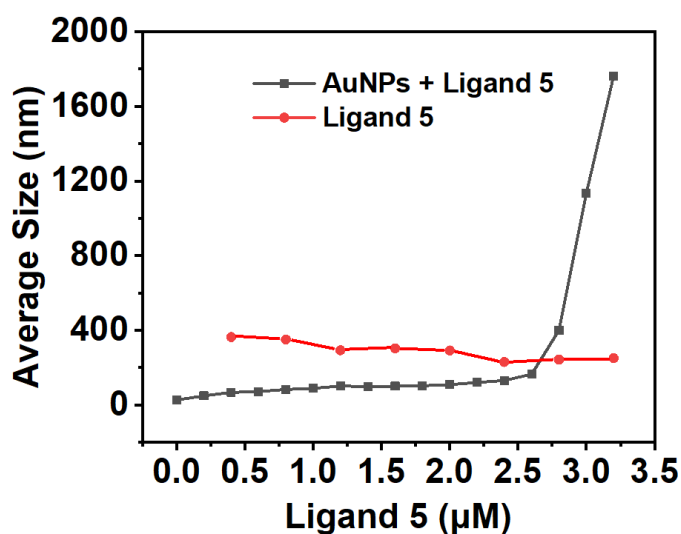


Figure 6.13: The sizes of **AuNPs**/Template and template solution with different concentration of ligand 5.

As zeta potential results shown, we believe that this aggregation was triggered by the decreasing of electrostatic repulsion between assembled **AuNPs**-nanofibers, which was caused by neutralization of the negative charged **AuNPs-3** as adding positive charged nanofiber templates (Figure 6.14).

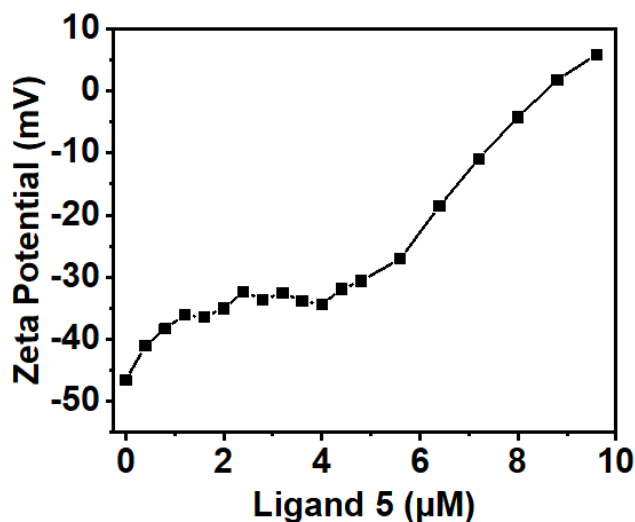


Figure 6.14: Zeta potential of **AuNPs**/Template solution with different concentration of 5.

6.2.2.4 pH switchable self-assembly

The **AuNPs**-nanofiber complexes are pH-switchable due to the pH-sensitive interactions between carboxylate ion and multiple hydrogen bonding donors on **GCP** motif. At pH = 7, **AuNPs**-

nanofibers which were prepared by using a ratio of $5/\text{AuNPs} = 75/1$ show a **SPR** band at 532 nm (Figure 6.15a). Adding NaOH aqueous solution leads to a blue-shift of **SPR** band from 532 nm to 518 nm at pH = 10, indicating the disassembly of **AuNPs**. In addition to change in **SPR** band, the colour of **AuNPs** also switched from slight purple to red. This self-assembly/disassembly behaviour is reversible, which can be repeated at least 15 times (Figure 6.15b). Unfortunately, this reversibility is only observed by the change in **SPR** band, while the change in morphology is not clear. Therefore, we don't know if this disassembly was caused by the disassembly of nanofiber templates or the **NPs** were removed from the nanofibers due to vanished interactions between **NPs** and templates.

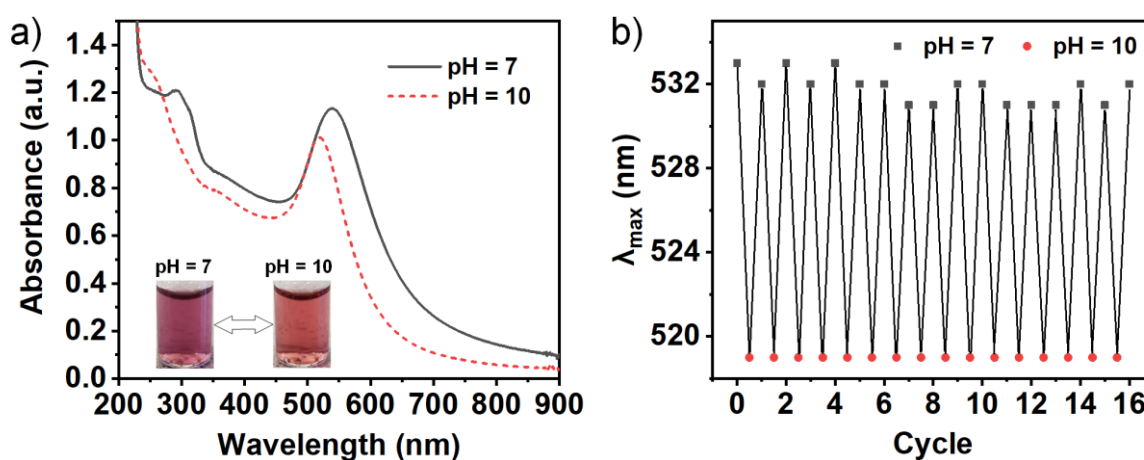


Figure 6.15: a) UV/Vis spectra and photos (inset) of **AuNPs** ($5/\text{AuNPs} = 75 : 1$) at different pH values. b) Cycles of reversible switching between pH = 7 and pH = 10.

6.3 Conclusions

In this chapter, we designed and synthesized a three-armed molecule which contains 6 positive charged **GCP** units. This molecule can be controlled to form nanofibers by supramolecular self-assembly. Carboxylic acids decorated **AuNPs** can be arranged onto the nanofiber template by interaction between **GCP** motifs and carboxylates. At the same time, this kind of arrangement is highly pH-switchable and repeatable. We find that the $5/\text{AuNPs}$ ratio plays a key role in the complexation of **AuNPs** on the nanofiber templates, one dimensional arrangement can only be achieved in a special range of $5/\text{AuNPs}$ ratios. In addition, the procedure of template adding also shows an obvious influence in **AuNPs** arrangement on nanofibers. Adding templates to **AuNPs** solution step-by-step can avoid the formation of particle cluster during the arrangement.

7. Summary and Outlook

This thesis focuses on developing novel self-assembled systems at the interface of supramolecular chemistry and nanomaterial science. Herein we introduced two supramolecular binding motifs **GCPZ** and **GCP** to the field of metal nanoparticles. Taking advantage of the supramolecular binding abilities of the **GCPZ** and **GCP** units, we developed various types of pH-sensitive and switchable self-assembly systems by decorating **AuNPs** with **GCPZ**, **GCP** and other supramolecular motifs.

7.1 Dual pH-sensitive reversible self-assembly of gold nanoparticles

The first part of this thesis dealt with the development of a dual pH-sensitive reversible self-assembly system by using **GCPZ** motifs as functional ligands due to their special dual pH responsiveness. A series of ligands featuring thiolalkylated PEG chains, with different terminal motifs (-OH, -COOH, -**GCPZ**) were synthesized for the functionalization of gold nanoparticles. The attachment of ligands onto gold nanoparticle surface were prepared by typical place-exchange reactions (Figure 7.1).

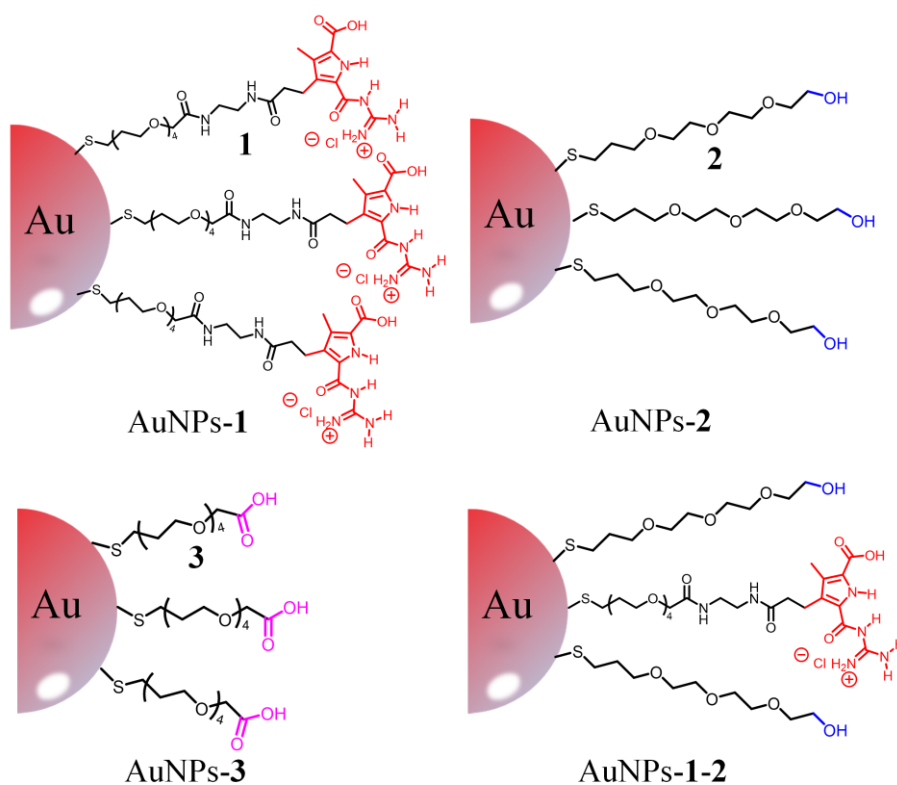


Figure 7.1: AuNPs functionalized with different ligands (AuNPs-1, AuNPs-2, AuNPs-3 and AuNPs-1-2).

The **GCPZ** functionalized gold nanoparticles (**AuNPs-1**) show a good dispersibility in the DMSO/water mixtures which was chosen as the solvent for self-assembly investigations. With the utilization of UV/Vis, DLS, TEM and SEM measurements, the dual pH-sensitive reversible self-assembly behaviour of **AuNPs-1** was observed. In neutral conditions, the zwitterionic **GCPZ** unit triggers the self-assembly of **AuNPs-1**. The resulting self-assembled nanoparticles can be switched back to the disassembled and separated state by adding acid or base (Figure 7.2). This assembly/disassembly process is reversible and repeatable for several times due to the switchable hydrogen bonding donors on **GCPZs** at different pH values.

In order to understand the mechanism behind the dual-**PSRSA**, the self-assembly behaviour of **AuNPs-1** with different θ -values was investigated in DMSO mixtures with different water-content (C_w). With varying θ - and C_w -values, the self-assembly behaviour of **AuNPs-1** can be divided to three types, namely no-**PSRSA**, mono-**PSRSA** and dual-**PSRSA**. We found that the exact self-assembly behaviour strongly depends both on the concentration of the **GCPZ**-ligands on the **AuNPs** (θ), and on the water content of the solvent mixtures (C_w). For instance, the dual-**PSRSA** only occurs at low C_w . At high C_w it only leads to mono-**PSRSA** which the disassembly under acidic conditions is suppressed. Hydrophobic effects were found to play a key role in self-assembling of functionalized nanoparticles (Figure 7.2). In addition, a combination of electrostatic and hydrophobic effects is the most likely responsible for the observed trends in self-assembly behaviour.

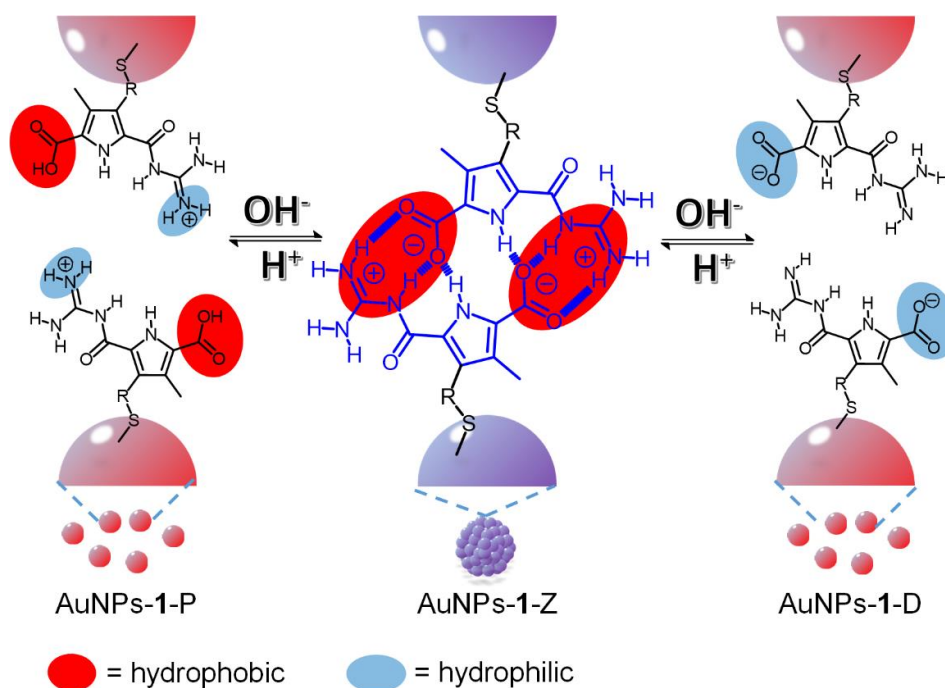


Figure 7.2: Schematic representation of the dual-**PSRSA** behaviour of **AuNPs-1**.

7.2 Multiple pH-sensitive reversible self-assembly of gold nanoparticles

The second topic in this thesis focuses on the development of nanoparticles that undergo multi pH-sensitive reversible self-assembly in aqueous solution. Based on the investigations and understandings of hydrophobic effects in the previous self-assembly system, we introduced positive charges on **AuNPs** to improve the water solubility and develop a multi-**PSRSA** by attaching **GCP** motifs to nanoparticle surface. As described in Figure, 7.3, a well-designed ligand (**4**) containing thiol, triethylene glycol chain and **GCP** motif was designed and synthesized. Afterward, **AuNPs** were further additionally functionalized with other **GCPZ** and **GCP** ligands (**AuNPs-1-4**). In order to obtain the desired multi-**PSRSA** system in water, **AuNPs-1-4** with different **GCPZ**/**GCP** ratios were also prepared.

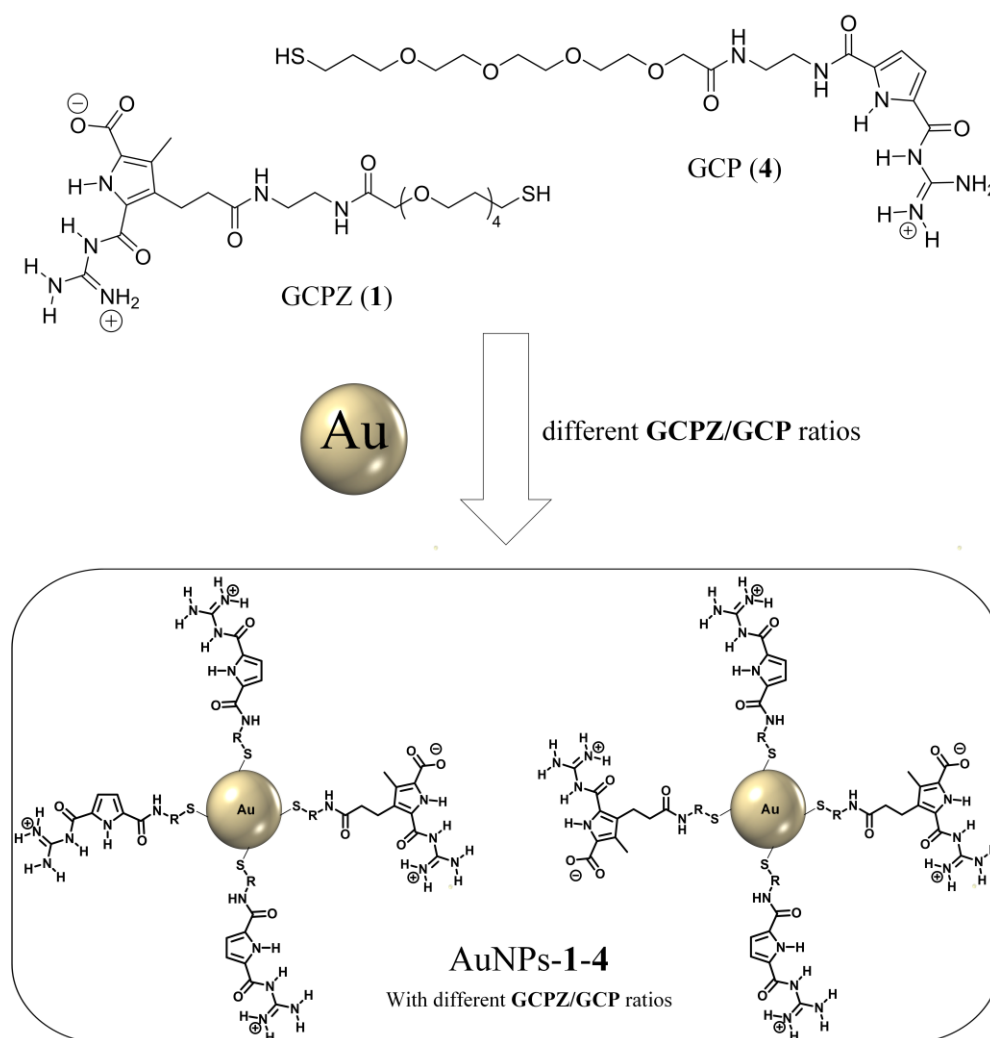


Figure 7.3: Preparation of **AuNPs-1-4** with different **GCPZ**/**GCP** motifs.

Surprisingly, **AuNPs-1-4** ($\text{GCPZ}/\text{GCP} = 1/7$) exhibited a multi-**PSRSA** which can response to 5 different pH values. Induced by the **GCPZ** and **GCP** motifs, **AuNPs-1-4** could self-assemble at pH 1, pH 7 and pH 13. In contrast, switching the pH to 3 or pH 11 led to the disassembly of **AuNPs**. In addition, the self-assemblies at pH 1 and pH 13 are temperature sensitive, so that cooling triggers the self-assembly of **AuNPs-1-4** and heating causes the disassembly of assembled **NPs**. This pH- and temperature-sensitive behaviour was confirmed by UV/Vis, DLS, SEM and TEM measurements. With various **GCPZ}/\text{GCP}** ratio on the **AuNPs**, the sensitive **PSRSA** self-assembly behaviour of **AuNPs-1-4** can be reversibly switched in different numbers of steps, ranging from assembly/disassembly between two different pH values all the way to a switchability between five different pH values (Figure 7.4).

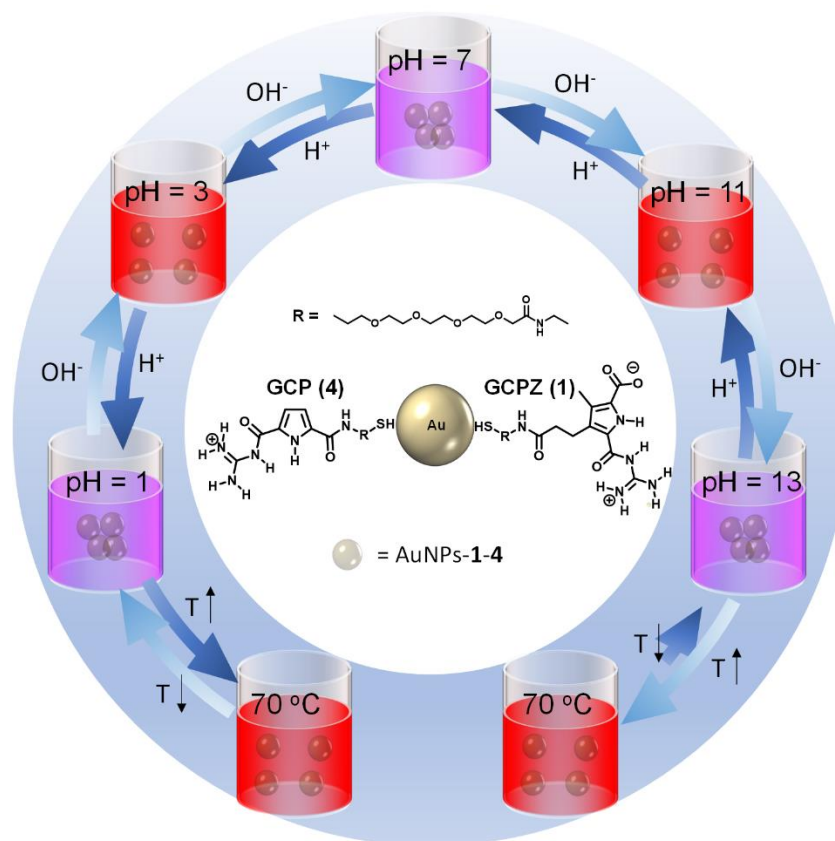


Figure 7.4: Schematic representation of the multi pH-sensitive and temperature-sensitive of **AuNPs-1-4**.

We also investigated the application of the multi-**PSRSA NPs**. Based on the multi-pH sensitive self-assembly behaviour and the versatile supramolecular motifs (**GCPZ** and **GCP**) on **NPs**, the investigation of removing harmful industrial metal ions (Hg^{2+}) was performed. The preliminary results have shown the affinity of **AuNPs-1-4** to Hg^{2+} so that **AuNPs-1-4** have a great potential to remove such ions from polluted water.

7.3 One-Dimensional arrangement of gold nanoparticles

In the last topic, we focused on developing a template-induced self-assembly of **AuNPs** on nanofibers, which were themselves based on noncovalent interactions. As shown in Figure 7.5, a three-armed molecule (**5**) which contains six **GCP** binding motifs were synthesized by our cooperation partner Dennis Aschmann and Thorben Neumann. In addition, carboxylic acids decorated **AuNPs** (**AuNPs-3**) which are able to bind to **GCP** motif through multiple hydrogen bonds were also prepared.

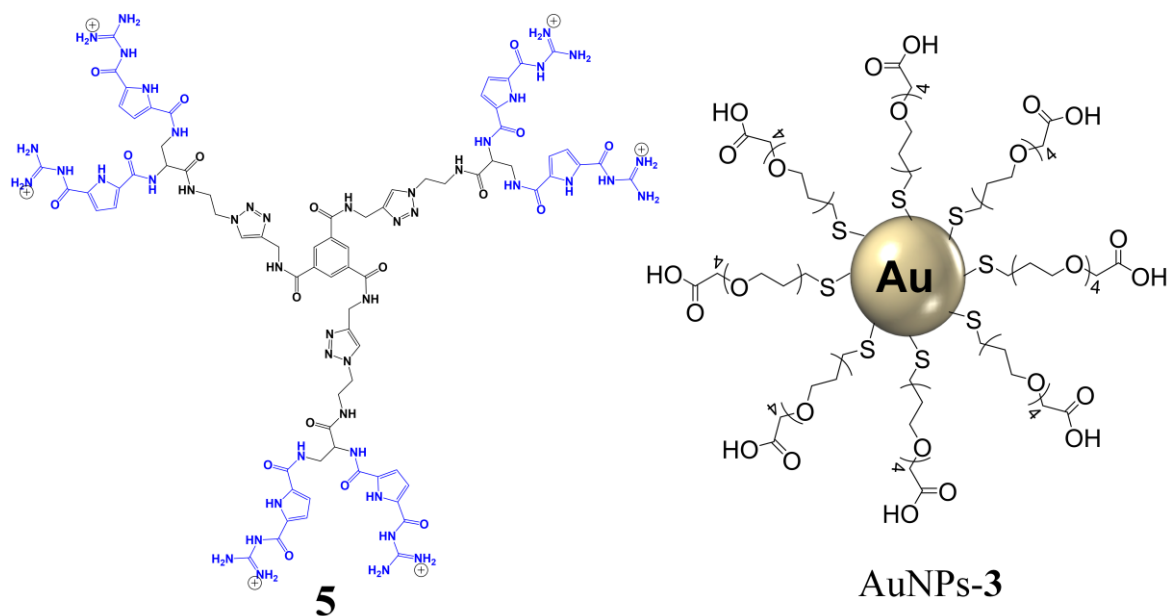


Figure 7.5: Three-armed molecule **5** with six **GCP**s and carboxylic acids decorated gold nanoparticles (**AuNPs-3**).

At first, we investigated the self-assembly of the **GCP** containing molecule **5** in aqueous solution. As shown by AFM, compound **5** self-assembles into nanofibers which could be used as a template for one dimensional arrangement of **AuNPs**. The arrangement of the **AuNPs** on the nanofiber-templates was investigated by UV/Vis, TEM and SEM. We found that **AuNPs-3** can be regularly deposited on the nanofiber template. Here, the **5/AuNPs** ratio plays a key role in the arrangement of **AuNPs**. One dimensional arrangement can only be achieved in a specific range of **5/AuNPs** (75/1 to 25/1). In addition, the addition procedure also has a significant influence on the **AuNPs** arrangement. Adding the nanofiber-template to the **AuNPs** solution in a step-by-step fashion avoid the formation of undesired nanoparticle clusters, thus leading to the desired **1D**-arrangement of **AuNPs** on the template.

8. Experimental Section

8.1 General experimental and analytical methods

Chemicals and Solvents

All commercial reagents were used as purchased without further purification unless otherwise stated. All solvents were dried and distilled before use in the reactions if necessary. Methanol was distilled before use. THF were distilled from sodium with benzophenone as indicator. DCM was distilled from calcium hydride. DMF was distilled from calcium hydride under reduced pressure. The milli-Q water was obtained from a Micropure apparatus from TKA. All solvents were stored under argon before use.

Vortex mixer

Functionalization of gold nanoparticle was carried out with the help of a Scientific Industries G-560E vortex mixer.

Centrifuge

Gold nanoparticles were centrifuged with a Kendro Biofuge-pico centrifuge.

Flash Chromatography

Flash chromatography was performed on columns packed with Silica gel 60M (40-63 μm) purchased from *Macherey-Nagel*. Organic solvents were used for flash chromatography without further purification.

Thin layer Chromatography (TLC)

Analytical TLC was carried out to monitor reactions and flash chromatography by using Polygram SIL G/UV254 TLC plates from *Macherey-Nagel*. The spots were visualized by fluorescence upon irradiation with 254 nm UV light or with the help of alkaline potassium permanganate developer.

Analytical HPLC

The analytical “High Performance Liquid Chromatography” (HPLC) was done with *Dionex* HPLC apparatus: P680 pump, ASI-100 automated sample injector, UVD-340U UV detector, UltiMate 3000 Column Compartment. The *YMC* ODS-A RP18 column with a pore size of 12 nm and a spherical size of 5 μm was utilized. Commercially available HPLC grade solvents and ultrapure water were used as eluents and solvent mixtures were reported in volume percent.

Preparative HPLC

The preparative HPLC was performed on a *MerckSep Tech* preparative HPLC apparatus equipped with a Knauer Dynamic Mixing Chamber and a Shimadzu SPD-10A UV detector. The YMC ODS-A RP18 column (15 cm × 3.0 cm, 5 μm) was utilized and the conditions were optimized via analytical HPLC on the corresponding YMC column.

NMR

¹H and ¹³C NMR spectra were recorded with *Bruker DMX 300*, *Bruker DRX 500* spectrometer. CDCl₃, MeOD and DMSO-d₆ were used as solvents and the spectra were calibrated by residual signals of the deuterated solvents as internal standard: CDCl₃, δ = 7.26 ppm (¹H-NMR), δ = 77.16 ppm (¹³C-NMR); DMSO-d₆, δ = 2.49 ppm (¹H-NMR), δ = 39.52 ppm (¹³C-NMR); MeOD, δ = 49.15 ppm (¹³C-NMR). The chemical shifts are reported in ppm (δ value). The coupling constants are reported in Hertz. The following abbreviations for the description of the signal multiplicity are used: s = singlet, d = doublet, t = triplet, q = quartet, m = multiplet, br = broad signal.

Fourier Transform Infrared Spectroscopy (FT-IR)

The IR spectra were measured on a *Jasco FT/IR-430* spectrometer with ATR attachment. The bands are reported in cm⁻¹.

Mass Spectrometry (MS)

High resolution ESI mass spectra were recorded with a *Bruker BioTOF III* spectrometer.

Melting Point

Melting points were measured with *Büchi* Melting Point B-540.

UV/Vis Spectroscopy

UV/Vis spectra were recorded with a *Varian Cary-300* spectrophotometer, standard quartz microcuvettes with 1 cm width were used. All spectra were recorded with baseline correction.

pH Meter

The pH was measured with a pH-Meter 766 Calimatic from Knickarray. The pH-meter was calibrated with commercially available buffer standards (pH = 4.00 and 11.00).

Dynamic Light Scattering

DLS measurements were performed at 25 °C with a Zetasizer-Nano ZS from Malvern.

Transmission Electron Microscopy (TEM)

TEM images were obtained on a Phillips CM 200 FEG field emission transmission electron microscope with an accelerating voltage of 200 kV. The samples were prepared by dropping the solution to cooper grid and then removed the solvent with filter paper.

Scanning Electron Microscopy (SEM)

SEM images were obtained on an ESEM Quanta 400 FEG microscope. The samples were prepared by dropping the solution to silicon plate and then removed the solvent with filter paper.

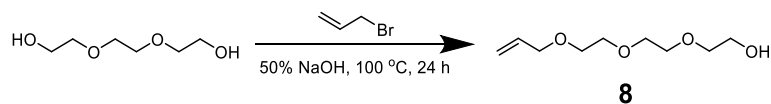
Atomic Force Microscopy (AFM)

AFM images were obtained in tapping mode using an Innova Scanning Probe Microscope from Veeco with a NanoDrive Controller and N-type silicon cantilever AC 160TS OLYMPUS. 6 μ L of prepared sample solution were dropped on freshly cleaved mica and then spin-coated at a speed of 400 rad/min for 10 min. The software Gwiddion-2.55 was used to analyze the AFM data.

8.2 Synthesis of thiolated GCPZ ligand

Synthesis of 2-(2-(2-(allyloxy)ethoxy)ethoxy)ethan-1-ol (**8**)

Described experiment: page 39, name of NMR-file: HB-001



A mixture of NaOH (2.00 g, 50.0 mmol, 1 eq) and triethylene glycol (56.0 g, 370 mmol, 7.4 eq) in water (2 mL) was stirred for 30 min at 100°C under an argon atmosphere, and then 3-bromoprop-1-ene (6.05 g, 50.0 mmol, 1 eq) was added. The reaction mixture was stirred at 100°C for 15 min and then allowed to cool down to room temperature. The reaction mixture was diluted with 50 mL brine and extracted with ethyl acetate. The combined organic layers were dried over MgSO₄ and concentrated in vacuo. The crude product was purified by column chromatography (cyclohexane/ethyl acetate = 1/4) to obtain **8** as a colorless oil.

C₉H₁₈O₄ 190.24 g/mol

Yield 7.30 g, 38.4 mmol, 77%

R_f = 0.26 (cyclohexane/ethyl acetate = 1/4).

¹H NMR (CDCl₃, 300 MHz): δ [ppm] = 2.41 (s, 1H), 3.53-3.76 (m, 12H), 4.02 (dt, *J* = 5.7, 1.4 Hz, 2H), 5.11-5.35 (m, 2H), 5.85-5.98 (m, 1H).

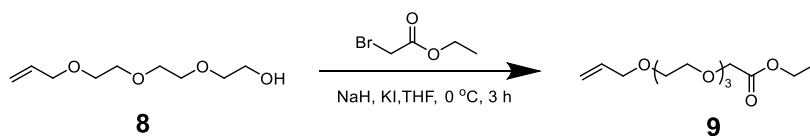
¹³C NMR (75 MHz, CDCl₃): 61.3, 69.1, 70.1, 70.3, 70.4, 71.9, 72.4, 116.8, 134.5.

¹H NMR and ¹³C NMR were consistent with those previously reported.⁷²

⁷² C. L. Yeung, P. Iqbal, M. Allan, M. Lashkor, J. A. Preece, P. M. Mendes, *Adv. Funct. Mater.* **2010**, *20*, 2657-2663.

Synthesis of ethyl 3,6,9,12-tetraoxapentadec-14-enoate (**9**)

Described experiment: page 41, repeated: page 73, name of NMR-file: HB-002



A mixture of **8** (7.22 g, 38.0 mmol, 1 eq), potassium iodide (1.25 g, 7.6 mmol, 0.2 eq) and NaH (1.82 g, 38.0 mmol, 1eq) in anhydrous THF (50 mL) was stirred at room temperature under argon atmosphere for 30 min and then cooled down to 0 °C. Then ethyl bromoacetate (8.6 mL, 76.0 mmol, 2 eq) was added and the reaction mixture was stirred for 3 h at 0 °C. The pH of the reaction solution was then adjusted to 7.0 with 5% aqueous citric acid and extracted with ethyl acetate. The combined organic layers were dried over MgSO₄ and concentrated in vacuo. The brown oil was purified by flash chromatography on silica gel (cyclohexane/ethyl acetate = 2/1) to give **9** as a clear oil.

C₁₃H₂₄O₆ 276.33 g/mol

Yield 7.76 g, 28.1 mmol, 74%

R_f = 0.21 (cyclohexane/ethyl acetate = 2/1).

¹H NMR (CDCl₃, 300 MHz): δ [ppm] = 1.28 (t, *J* = 7.1 Hz, 3H), 3.55-3.76 (m, 12H), 4.02 (dt, *J* = 5.7, 1.4 Hz, 2H), 4.14 (s, 2H), 4.21 (q, *J* = 7.5 Hz, 2H), 5.11-5.35 (m, 2H), 5.85-5.98 (m, 1H).

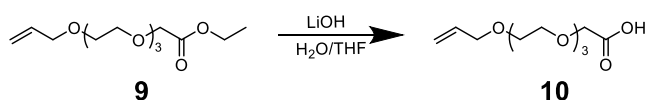
¹³C NMR (75 MHz, CDCl₃): δ [ppm] = 13.9, 60.4, 68.4, 69.2, 70.3, 70.6, 71.9, 116.6, 134.6, 170.1.

FT-IR (ATR): $\tilde{\nu}$ [cm⁻¹] = 3081, 2981, 2937, 2902, 2869, 1749, 1646, 1454, 1376, 1349, 1280, 1249, 1203, 1101, 1029, 998, 927, 848, 705.

HRMS (ESI): *m/z* = 299.1500 ([M+Na]⁺), calculated: 299.1465 (for [C₁₃H₂₄O₆Na]⁺).

Synthesis of 3,6,9,12-tetraoxapentadec-14-enoic acid (10)

Described experiment: page 42, repeated: page 145, name of NMR-file: HB-003



To a solution of **9** (2.32 g, 6.48 mmol, 1 eq) in 20 mL THF were added 20 mL of aqueous solution of lithium hydroxide (1.08 g, 25.6 mmol, 4 eq), and the resulting solution was stirred for 24 h at room temperature. The solution was acidified to pH 1 with 5% aqueous citric acid and extracted thrice with 50 mL of ethyl acetate. The combined organic phases were dried over Na₂SO₄ and concentrated under reduced pressure to afford **10** as slightly yellow oil.

C₁₁H₂₀O₆ 248.27 g/mol

Yield 2.08 g, 8.39 mmol, 90%

R_f = 0.52 (DCM/MeOH = 10/1)

¹H NMR (CDCl₃, 300 MHz): δ [ppm] = 3.55-3.78 (m, 12H), 4.03 (dt, *J* = 5.7, 1.4 Hz, 2H), 4.15 (s, 2H), 5.13-5.32 (m, 2H), 5.85-5.98 (m, 1H).

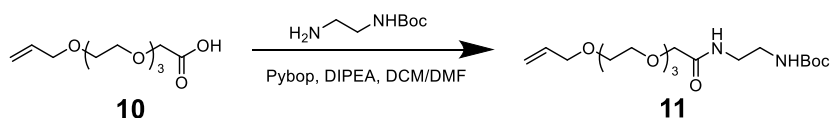
¹³C NMR (75 MHz, CDCl₃): δ [ppm] = 68.4, 69.2, 70.3, 70.4, 70.9, 72.0, 117.1, 134.4, 173.1.

FT-IR (ATR): $\tilde{\nu}$ [cm⁻¹] = 3448, 3077, 2911, 2869, 1737, 1644, 1452, 1425, 1349, 1245, 1209, 1097, 997, 927, 877, 850, 673, 620.

HRMS (ESI): *m/z* = 271.1199 ([M+Na]⁺), calculated: 271.1152 (for [C₁₁H₂₀O₆Na]⁺).

Synthesis of Boc protected amine (**11**)

Described experiment: page 45, repeat experiment: page 51, name of NMR-file: HB-004



A mixture of **10** (1.00 g, 4.03 mmol, 1 eq), PyBop (2.49 g, 4.78 mmol, 1.2 eq) and DIPEA (2.1 mL, 1.56 g, 12.1 mmol, 3 eq) was dissolved in 30 mL of dichloromethane and 6 mL of DMF. The solution was then stirred for 30 min and tert-butyl (2-aminoethyl) carbamate (1.10 g, 6.87 mmol, 1.7 eq) were added and stirring was continued overnight. The reaction solution was concentrated in vacuo and the residue was diluted with water, extracted with DCM. The combined organic phases were dried over Na₂SO₄ and concentrated under reduced pressure after filtration. The crude product was purified by column chromatography on silica gel (DCM/MeOH = 50/1) to afford **11** as a slightly brown oil.

C₁₈H₃₄N₂O₇ 390.48 g/mol

Yield 1.10 g, 2.82 mmol, 70%

R_f = 0.21 (DCM/MeOH = 50/1)

¹H NMR (CDCl₃, 300 MHz): δ [ppm] = 1.41 (s, 9H), 3.24-3.25 (m, 2H), 3.35-3.40 (m, 2H), 3.56-3.59 (m, 2H), 3.63-3.67 (m, 10H), 3.98 (s, 2H), 4.00-4.02 (m, 2H), 5.15-5.28 (m, 3H), 5.82-5.95 (m, 1H), 7.35 (s, 1H).

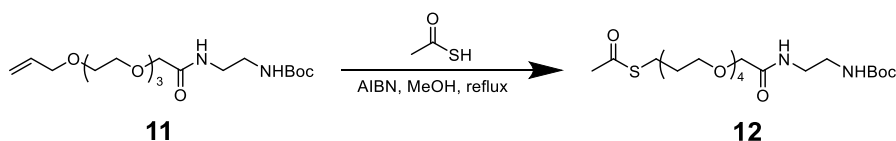
¹³C NMR (75 MHz, CDCl₃): δ [ppm] = 28.5, 39.4, 40.7, 69.2, 70.1, 70.3, 70.4, 70.6, 70.9, 72.3, 79.4, 117.5, 134.6, 156.5, 171.0.

FT-IR (ATR): $\tilde{\nu}$ [cm⁻¹] = 3417, 3320, 3083, 2975, 2929, 2877, 1677, 1521, 1455, 1392, 1367, 1348, 1274, 1249, 1164, 1101, 998, 941, 835, 781, 744, 617.

HRMS (ESI): m/z = 413.2258 ([M+Na]⁺), calculated. 413.2258 (for [C₁₈H₃₄N₂O₇Na]⁺).

Synthesis of Thioacetate (12)

Described experiment: page 47, repeated: page 55, name of NMR-file: HB-005



A solution of **11** (1.00 g, 2.56 mmol, 1 eq) and AIBN (205 mg, 1.25 mmol, 0.5 eq) in Methanol (20 mL) was purged with argon for 10 min and heated to reflux, before thioacetic acid (0.53 mL, 7.5 mmol, 2.9 eq) was added and the mixture was stirred under reflux overnight. The reaction mixture was then concentrated in vacuo and purified by column chromatography (DCM/MeOH = 50/1) to afford **12** as a slightly yellow oil.

C₂₀H₃₈N₂O₈S 466.59 g/mol

Yield 0.85 g, 1.82 mmol, 71%

R_f = 0.22 (DCM/MeOH = 50/1)

¹H NMR (CDCl₃, 300 MHz): δ [ppm] = 1.43 (s, 9H), 1.75-1.90 (m, 2H), 2.32 (s, 3H), 2.93 (t, J = 7.2 Hz, 2H), 3.25-3.28 (m, 2H), 3.37-3.42 (m, 2H), 3.50 (t, J = 6.2 Hz, 2H), 3.56-3.59 (m, 2H), 3.66-3.68 (m, 10H), 3.98 (s, 2H), 5.56 (s, 1H), 7.48 (s, 1H).

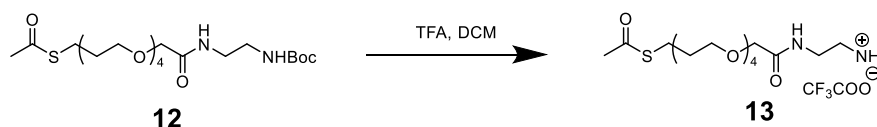
¹³C NMR (75 MHz, CDCl₃): δ [ppm] = 25.6, 28.1, 29.2, 30.3, 38.9, 40.3, 69.2, 69.8, 70.0, 70.2, 70.6, 78.6, 156.0, 170.4, 195.3.

FT-IR (ATR): $\tilde{\nu}$ [cm⁻¹] = 3342, 2971, 2925, 2869, 1687, 1525, 1452, 1390, 1363, 1270, 1249, 1168, 1105, 956, 860, 781, 755, 669, 624.

HRMS (ESI): m/z = 489.2290 ([M+Na]⁺), calculated: 489.2241 (for [C₂₀H₃₈N₂O₈SNa]⁺).

Synthesis of Thioacetate amine (TFA salt) (13)

Described experiment: page 47, name of NMR-file: HB-006



To a solution of the **12** (680 mg, 1.46 mmol, 1 eq) in dichloromethane (2 mL), trifluoroacetic acid (2 mL) was added and the reaction mixture was stirred at room temperature overnight. After removal of dichloromethane and trifluoroacetic acid under reduced pressure, the **13** was obtained as a yellowish oil which could be used for next synthesis step without further purification.

C₁₇H₃₁F₃N₂O₈S 480.50 g/mol

¹H NMR (CDCl₃, 300 MHz): δ [ppm] = 1.69-1.78 (m, 2H), 2.22 (s, 3H), 2.80 (t, $J = 7.2$ Hz, 2H), 3.15 (m, 2H), 3.44 (t, $J = 6.2$ Hz, 2H), 3.42-3.59 (m, 14H), 3.98 (s, 2H), 7.55 (s, 3H), 7.96 (s, 1H).

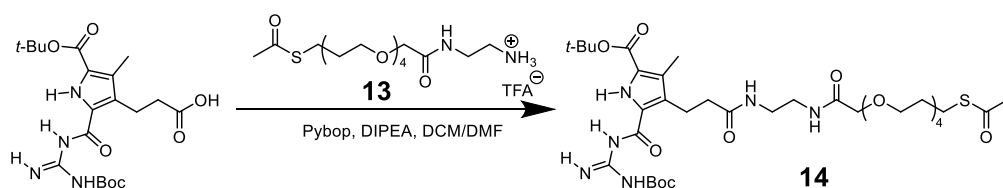
¹³C NMR (75 MHz, CDCl₃): δ [ppm] = 25.6, 29.2, 30.3, 37.0, 40.0, 69.6, 69.6, 69.8, 69.9, 69.9, 70.5, 173.2, 196.80.

FT-IR (ATR): $\tilde{\nu}$ [cm⁻¹] = 3324, 3093, 2910, 2875, 1671, 1540, 1457, 1432, 1353, 1295, 1249, 1199, 1172, 1126, 952, 833, 798, 721, 705, 628.

HRMS (ESI): $m/z = 367.1905$ ([M-CF₃COO]⁺), calculated: 367.1897 (for [C₁₅H₃₁N₂O₆S]⁺).

Synthesis of Boc protected GCPZ Thioacetate (**14**)

Described experiment: page 49, repeated: page 53, name of NMR-file: HB-007



Pyrrole carboxylic acid (380 mg, 0.87 mmol, 1 eq) which was synthesized according to previous report⁷³, PyBop (588 mg, 1.13 mmol, 1.3 eq), DIPEA (562 mg, 4.35 mmol, 5 eq) were dissolved in 10 ml dichloromethane (DCM) and 2 ml DMF. The solution was stirred for 30 min, then **13** (627 mg, 1.3 mmol, 1.5 eq) in 1 mL of DCM were added and stirring was continued overnight. The reaction solution was concentrated under reduced pressure and the residue was diluted with water, extracted with DCM. The combined organic phases were dried over Na₂SO₄ and concentrated in vacuo. The crude product was purified by column chromatography on silica gel (DCM/MeOH = 20/1) to obtain **14** as a gel-like solid. The sample thus obtained contained several minor impurities, which were removed in the next step.

C₃₅H₅₈N₆O₁₂S 786.94 g/mol

Yield 340 mg (0.43 mmol, 50%).

R_f = 0.16 (DCM/MeOH = 20/1)

¹H NMR (CDCl₃, 300 MHz): δ [ppm] = 1.50 (s, 9H), 1.54 (s, 9H), 1.77-1.90 (m, 2H), 2.22 (s, 3H), 2.29 (s, 3H), 2.48 (t, *J* = 5.9 Hz, 2H), 2.87 (t, *J* = 7.2 Hz, 2H), 3.09 (t, *J* = 7.2 Hz, 2H), 3.36 (m, 4H), 3.48-3.72 (m, 14H), 3.98 (s, 2H), 7.07 (s, 1H), 7.11 (s, 1H), 8.57 (s, 1H), 9.17 (s, 2H), 9.64 (s, 1H).

¹³C NMR (75 MHz, CDCl₃): δ [ppm] = 10.2, 21.5, 25.8, 28.0, 28.4, 29.4, 30.6, 37.5, 38.9, 39.7, 69.7, 69.9, 70.0, 70.1, 70.2, 70.3, 70.6, 81.2, 83.1, 121.9, 126.2, 128.3, 128.5, 153.7, 158.6, 160.7, 171.3, 171.4, 174.5, 196.0.

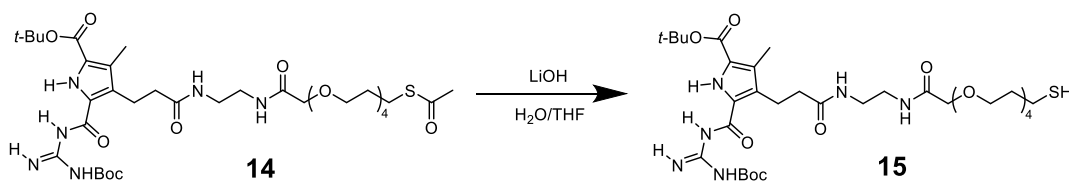
FT-IR (ATR): $\tilde{\nu}$ [cm⁻¹] 3382, 3278, 3085, 2975, 2929, 2873, 1724, 1683, 1629, 1529, 1454, 1392, 1367, 1297, 1238, 1143, 1101, 954, 838, 777, 752, 624.

HRMS (ESI): *m/z* = 789.3839 ([M+H]⁺), calculated: 787.3906 (for [C₃₅H₅₉N₆O₁₂S]⁺).

⁷³ J. Voskuhl, T. Fenske, M. C. A. Stuart, B. Wibbeling, C. Schmuck, B. J. Ravoo, *Chem. -Eur. J.* **2010**, *16*, 8300-8306.

Synthesis of Boc protected GCPZ Thiol (**15**)

Described experiment: page 51, repeated: page 139, name of NMR-file: HB-008



To a solution of **14** (180 mg, 0.23 mmol, 1 eq) in 5 mL THF was added 5 mL of an aqueous solution of lithium hydroxide (42 mg, 1 mmol, 4.3 eq), and the resulting solution was stirred for 4 h at 0 °C under argon atmosphere. The solution was neutralized with an aqueous citric acid solution (5%) and extracted 3 times with 50 mL of ethyl acetate. The combined organic phases were dried over Na₂SO₄ and concentrated under reduced pressure. The crude product was purified by column chromatography (ethyl acetate/MeOH = 20/1) to afford **15** as a gel-like solid.

C₃₃H₅₆N₆O₁₁S 744.90 g/mol

Yield 150 mg, 0.21 mmol, 87%

R_f = 0.27 (ethyl acetate /MeOH = 20/1)

¹H NMR (CDCl₃, 300 MHz): δ [ppm] = 1.48 (s, 9H), 1.53 (s, 9H), 1.85-1.97 (m, 2H), 2.22 (s, 3H), 2.41 (t, *J* = 5.9 Hz, 2H), 2.69 (t, *J* = 7.1 Hz, 2H), 3.09 (t, *J* = 7.2 Hz, 2H), 3.38 (m, 4H), 3.45-3.68 (m, 14H), 3.96 (s, 2H), 6.97 (t, *J* = 4.5 Hz, 1H), 7.49 (t, *J* = 5.2 Hz, 1H), 8.42 (s, 1H), 9.08 (s, 2H), 9.55 (s, 1H).

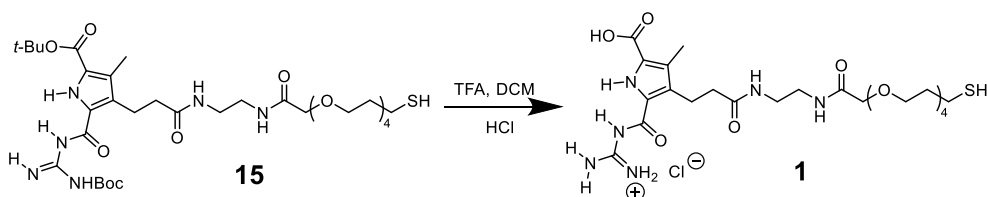
¹³C NMR (75 MHz, CDCl₃): δ [ppm] = 10.1, 21.3, 21.6, 28.0, 28.4, 33.6, 37.6, 38.7, 40.0, 67.9, 69.1, 70.1, 70.2, 70.3, 70.5, 70.9, 81.2, 83.1, 121.8, 126.1, 128.4, 128.5, 153.5, 158.5, 160.6, 171.3, 174.2.

FT-IR (ATR): $\tilde{\nu}$ [cm⁻¹] 3380, 3274, 2960, 2921, 2854, 1724, 1683, 1629, 1529, 1454, 1392, 1367, 1295, 1238, 1145, 1101, 975, 952, 842, 777, 752.

HRMS (ESI): *m/z* = 745.3814 ([M+H]⁺), calculated: 745.3801 (for [C₃₃H₅₇N₆O₁₁S]⁺).

Synthesis of Thiolated GCPZ (1)

Described experiment: page 53, name of NMR-file: HB-009



To a solution of **15** (100 mg, 0.13 mmol, 1 eq) in DCM (2 mL) was added trifluoroacetic acid (2 mL) and the reaction mixture was stirred at room temperature overnight. After removal of dichloromethane and TFA under reduced pressure, 10 mL of 1 M hydrochloric acid were added. The solution was lyophilised to get **1** as a yellowish solid.

C₂₄H₄₁ClN₆O₉S 625.13 g/mol

Yield 75 mg, 0.12 mmol, 95%

Melting point 134 °C.

¹H NMR (DMSO-d₆, 300 MHz): δ [ppm] = 1.75-1.88 (m, 2H), 2.22 (s, 3H), 2.24 (t, J = 5.9 Hz, 2H), 2.70 (t, J = 7.2 Hz, 2H), 2.91 (t, J = 7.6 Hz, 2H), 3.11 (d, J = 8.4 Hz, 4H), 3.20-3.60 (m, 14H), 3.84 (s, 2H), 7.76 (s, 1H), 7.86 (s, 1H), 8.43 (s, 4H), 11.90 (s, 1H), 12.18 (s, 1H), 13.07 (s, 1H).

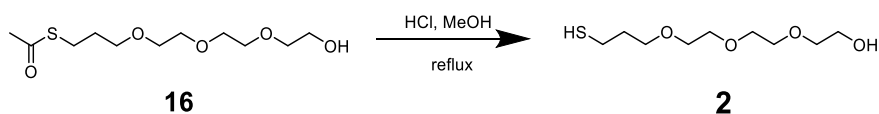
¹³C NMR (75 MHz, DMSO-d₆): δ [ppm] = 9.1, 20.6, 21.0, 33.3, 35.7, 38.1, 38.3, 60.2, 68.3, 69.4, 69.4, 69.5, 69.6, 69.7, 69.9, 70.2, 118.6, 122.8, 129.2, 134.1, 156.5, 161.0, 166.5, 169.4, 171.9.

FT-IR (ATR): $\tilde{\nu}$ [cm⁻¹] 3370, 3282, 3210, 2919, 2871, 2550, 1716, 1662, 1550, 1440, 1342, 1268, 1182, 1095, 946, 867, 781.

HRMS (ESI): m/z = 589.2618 ([M-Cl]⁺), calculated: 589.2650 (for [C₂₄H₄₁N₆O₉S]⁺).

Synthesis of 2-(2-(2-(3-mercapropoxy)ethoxy)ethoxy)ethanol (2)

Described experiment: page 62, name of NMR-file: HB-014



16 (500 mg, 1.88 mmol, 1 eq) was dissolved in 20 mL of 1 M HCl solution in methanol. The mixture was stirred under argon atmosphere at 70 °C for 5 h. Then, the reaction mixture was concentrated in vacuo and the crude product was purified by column chromatography with ethyl acetate to obtain **2** as a colourless oil.

C₉H₂₀O₄S 224.32 g/mol

Yield 337 mg, 1.50 mmol, 80%

R_f = 0.23 (ethyl acetate).

¹H NMR (CDCl₃, 300 MHz): δ [ppm] = 1.40 (t, *J* = 8.0 Hz, 1H), 1.81-1.94 (m, 2H), 2.63 (t, *J* = 7.2 Hz, 2H), 3.52-3.77 (m, 14H).

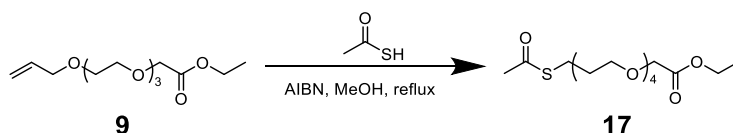
¹³C NMR (75 MHz, CDCl₃): δ [ppm] = 21.5, 33.8, 61.9, 69.2, 70.3, 70.5, 70.6, 70.8, 72.7.

¹H NMR and ¹³C NMR were consistent with those previously reported.⁷⁴

8.4 Synthesis of thiolated carboxyl ligand

Synthesis of Thioacetate (17)

Described experiment: page 57, name of NMR-file: HB-010



A solution of **9** (1.00 g, 3.6 mmol, 1 eq) and AIBN (296 mg, 1.8 mmol, 0.5 eq) in methanol (20 mL) was purged with argon for 10 min and heated to reflux, then thioacetic acid (0.65 mL, 6.2 mmol, 1.7 eq) was added and the mixture was stirred under reflux overnight. The reaction mixture was then concentrated in vacuo and the residue was purified by column chromatography (cyclohexane/ethyl acetate=2/1) to afford **17** as a colourless oil.

C₁₅H₂₈O₇S 352.44 g/mol

Yield 0.89 g, 2.5 mmol, 70%

R_f = 0.10 (cyclohexane/ethyl acetate=2/1)

¹H NMR (CDCl₃, 300 MHz): δ [ppm] = 1.28 (t, *J* = 7.1 Hz, 3H), 1.75-1.90 (m, 2H), 2.32 (s, 3H), 2.94 (t, *J* = 7.2 Hz, 2H), 3.47-3.94 (m, 14H), 4.14 (s, 2H), 4.21 (q, *J* = 7.5 Hz, 2H).

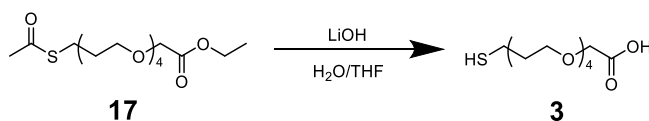
¹³C NMR (75 MHz, CDCl₃): δ [ppm] = 14.1, 25.8, 29.5, 30.4, 60.6, 68.6, 69.4, 70.1, 70.4, 70.46, 70.49, 70.7, 170.3, 195.5.

FT-IR (ATR): $\tilde{\nu}$ [cm⁻¹] 2985, 2938, 2867, 1751, 1689, 1538, 1509, 1430, 1353, 1278, 1203, 1105, 1027, 954, 850, 719, 671, 624.

HRMS (ESD): *m/z* = 375.1457 ([M+Na]⁺), calculated. 375.1448 (for [C₁₅H₂₈O₇SNa]⁺).

Synthesis of 15-mercapto-3,6,9,12-tetraoxapentadecan-1-oic acid (3)

Described experiment: page 59, name of NMR-file: HB-011



To a solution of **17** (200 mg, 0.57 mmol, 1 eq) in 5 mL THF were added 5 mL of an aqueous solution of lithium hydroxide (143 mg, 3.4 mmol, 6 eq), and the resulting solution was stirred for 24 h at room temperature under argon atmosphere. The solution was acidified to pH 1 with an aqueous solution of citric acid (5%) and extracted thrice with 50 mL of ethyl acetate. The combined organic phases were dried over Na₂SO₄ and concentrated under reduced pressure to get **3** as a colourless oil.

C₁₁H₂₂O₆S 282.35 g/mol

Yield 128 mg, 0.45 mmol, 80%

¹H NMR (CDCl₃, 300 MHz): δ [ppm] = 1.34 (t, *J* = 8.0 Hz, 1H), 1.91-2.02 (m, 2H), 2.76 (t, *J* = 7.1 Hz, 2H), 3.50-3.82 (m, 14H), 4.17 (s, 2H), 9.42 (s, 1H).

¹³C NMR (75 MHz, CDCl₃): δ [ppm] = 21.3, 33.6, 68.7, 69.1, 70.2, 70.39, 70.42, 70.6, 71.2, 173.1.

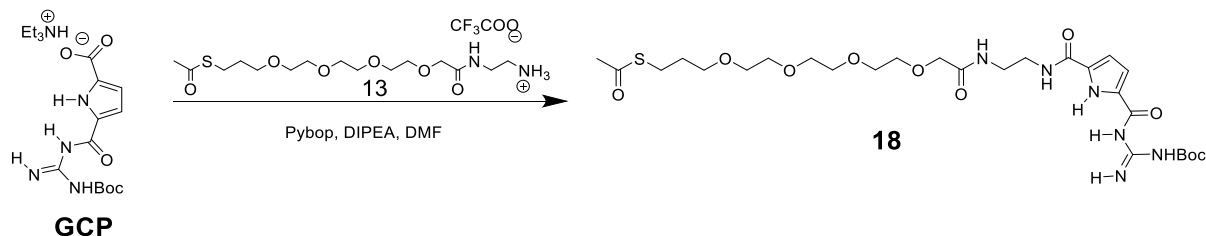
FT-IR (ATR): $\tilde{\nu}$ [cm⁻¹] = 3504, 2919, 2871, 2557, 1735, 1650, 1540, 1509, 1455, 1434, 1351, 1292, 1243, 944, 877, 673.

HRMS (ESI): *m/z* = 305.1048 ([M+Na]⁺), calculated. 305.1029 (for [C₁₁H₂₂O₆SNa]⁺).

8.5 Synthesis of thiolated GCP ligand

Synthesis of Boc protected GCP thioacetate (**18**)

Described experiment: page 75, name of NMR-file: GCP-S-001



Guanidiniocarbonyl pyrrole (**GCP**) was synthesized according to our previous works.⁷⁵ A solution of **GCP** (100 mg, 0.252 mmol, 1 eq), PyBOP (197 mg, 0.378 mmol, 1.5 eq) and DIPEA (129 mg, 1.00 mmol, 4 eq) in DMF (8 mL) was stirred for 30 min. Then **13** (145 mg, 0.302 mmol, 1.2 eq) in 1 mL of DMF were added and stirring was continued overnight. The reaction solution was concentrated under reduced pressure and the residue was diluted with water, extracted with DCM. The combined organic phases were dried over Na₂SO₄ and concentrated in vacuo. The crude product was purified by preparative HPLC to obtain **18** as a gel-like solid.

C₂₇H₄₄N₆O₁₀S 644.74 g/mol

Yield 86.1 mg, 0.134 mmol, 53%

¹H NMR (CDCl₃, 300 MHz): δ [ppm] 1.44 (s, 9H), 1.74-1.83 (m, 2H), 2.28 (s, 3H), 2.88 (t, *J* = 7.2 Hz, 2H), 3.45 (t, *J* = 6.3 Hz, 2H), 3.49-3.65 (m, 16H), 3.97 (s, 2H), 6.64 (d, *J* = 3.9 Hz, 1H), 6.80 (d, *J* = 3.9 Hz, 1H), 7.47 (t, *J* = 4.4 Hz, 1H), 7.71 (t, *J* = 5.5 Hz, 1H), 8.53 (br, 1H), 8.92 (br, 1H), 10.31 (s, 1H).

¹³C NMR (75 MHz, CDCl₃): δ [ppm] = 26.0, 28.1, 29.5, 30.7, 38.8, 40.5, 69.8, 70.2, 70.3, 70.4, 70.5, 70.6, 70.9, 83.3, 111.3, 114.3, 129.1, 158.6, 161.0, 171.8, 196.0.

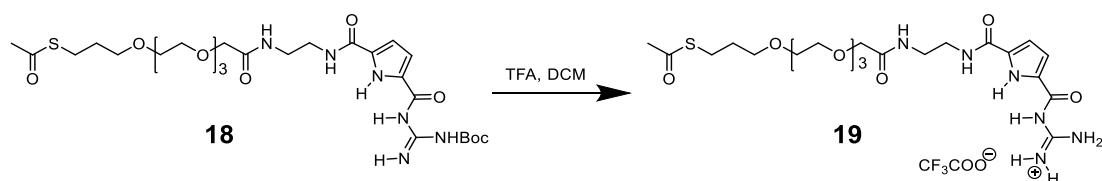
FT-IR (ATR): $\tilde{\nu}$ [cm⁻¹] 3375, 3273, 2920, 2870, 1722, 1685, 1627, 1540, 1466, 1435, 1394, 1369, 1340, 1290, 1263, 1236, 1143, 1103, 1047, 956, 840, 784, 754, 621.

HRMS (ESI): *m/z* = 645.2927 ([M+H]⁺), calculated. 645.2912 (for [C₂₇H₄₅N₆O₁₀S]⁺).

⁷⁵ H. Y. Kuchelmeister, A. Gutschmidt, S. Tillmann, S. Knauer, C. Schmuck, *Chem. Sci.* **2012**, *3*, 996-1002.

Synthesis of GCP thioacetate (19)

Described experiment: page 107, name of NMR-file: GCP-S-002



To a solution of **18** (70 mg, 0.11 mmol, 1 eq) in DCM (2 mL) was added trifluoroacetic acid (2 mL) and the reaction mixture was stirred at room temperature overnight. After removal of dichloromethane and TFA under reduced pressure, the residue was purified by preparative HPLC to get **19** as a gel-like solid.

C₂₄H₃₇F₃N₆O₁₀S 658.65 g/mol

Yield 65 mg, 0.099 mmol, 90%

¹H NMR (CDCl₃, 300 MHz): δ [ppm] = 1.75-1.84 (m, 2H), 2.28 (s, 3H), 2.88 (t, J = 7.2 Hz, 2H), 3.45-3.65 (m, 18H), 4.00 (s, 2H), 6.68 (s, 1H), 7.15 (s, 2H), 7.90 (s, 1H), 7.97 (s, 1H), 8.27 (s, 2H), 8.68 (s, 2H), 11.16 (s, 2H).

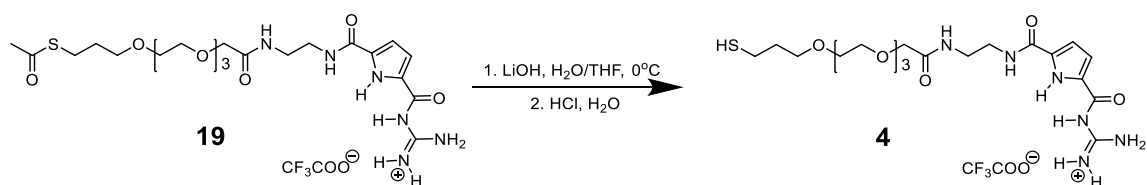
¹³C NMR (101 MHz, MeOD): δ [ppm] = 26.9, 30.6, 30.9, 39.9, 40.3, 70.7, 71.2, 71.3, 71.5, 71.6, 71.7, 72.0, 113.2, 116.3, 127.1, 134.1, 157.4, 161.7, 162.40, 173.6, 197.6.

FT-IR (ATR): $\tilde{\nu}$ [cm⁻¹] 3319, 3282, 3199, 3107, 2920, 2870, 1691, 1637, 1562, 1481, 1431, 1355, 1321, 1282, 1199, 1178, 1113, 1003, 955, 883, 856, 829, 809, 798, 750, 717, 698, 623.

HRMS (ESI): m/z = 545.2405 ([M-CF₃COO]⁺), calculated. 545.2388 (for [C₂₇H₄₅N₆O₁₀S]⁺).

Synthesis of GCP thioacetate (4)

Described experiment: page 107, name of NMR-file: GCP-S-003



4 mL of an aqueous solution of lithium hydroxide (13 mg, 0.31 mmol, 4 eq) was added to a solution of **19** (50 mg, 0.076 mmol, 1 eq) in 4 mL THF, and the resulting solution was stirred for 4 h at 0 °C under argon atmosphere. The solution was neutralized with an aqueous HCl (1 M) and concentrated in *vacuum*. The crude product was purified by HPLC to afford **4** as a TFA salt.

C₂₂H₃₅F₃N₆O₉S 616.61 g/mol

Yield 35.8 mg, 0.058 mmol, 76%

Melting point 115 °C.

¹H NMR (DMSO, 400 MHz): δ [ppm] = 1.70-1.77 (m, 2H), 2.28 (t, J = 7.8 Hz, 1H), , 3.27-3.30 (m, 4H), 3.43-3.58 (m, 14H), 3.88 (s, 2H), 6.86 (s, 2H), 7.05 (s, 1H), 7.86 (t, J = 5.6 Hz, 1H), 8.27 (s, 4H), 8.52 (t, J = 5.6 Hz, 1H), 11.08 (s, 1H), 12.35 (s, 1H).

¹³C NMR (101 MHz, MeOD): δ [ppm] = 21.9, 22.0, 35.0, 39.9, 40.3, 70.2, 71.3, 71.4, 71.5, 71.6, 71.7, 72.0, 113.2, 116.2, 127.0, 134.1, 157.4, 161.6, 162.4, 173.6.

FT-IR (ATR): $\tilde{\nu}$ [cm⁻¹] = 3327, 3192, 3103, 2927, 2870, 1707, 1689, 1657, 1603, 1556, 1477, 1433, 1400, 1382, 1340, 1282, 1253, 1197, 1116, 1089, 1068, 1000, 949, 852, 823, 775, 752, 698, 624.

HRMS (ESI): m/z = 525.2127 ([M-CF₃COOH+Na]⁺), calculated. 525.2102 (for [C₂₀H₃₄N₆O₇SNa]⁺).

8.6 Preparation of Gold nanoparticles

AuNPs were prepared using a known procedure.⁷⁶ 1.85 g of Didodecyldimethylammonium bromide (**DDAB**) were dissolved in 20 mL of toluene to make a stock solution. To 12.5 mL of the stock solution, 450 mg of Dodecylamine (**DDA**) and 50 mg of $\text{HAuCl}_4 \cdot 3\text{H}_2\text{O}$ were added and dissolved by sonication. To this mixture, 125 mg of Tetrabutylammonium bromide (**TBAB**) in 5 mL of the DDAB stock solution was added slowly under vigorous stirring. The resulting solution was aged for 24 h. 200 mg of $\text{HAuCl}_4 \cdot 3\text{H}_2\text{O}$, 1 g of Tetraoctylammonium bromide (**TOAB**), and 1.85 g of **DDA** were dissolved in 50 mL of toluene, 7 mL of aged solution was then added, followed by the dropwise addition of 131 μL of hydrazine dissolved in 20 mL of the stock solution under vigorous stirring.

⁷⁶ R. Klajn, K. J. M. Bishop, B. A. Grzybowski, *Proc. Natl. Acad. Sci. USA* **2007**, *104*, 10305-10309.

8.7 Functionalization of Gold nanoparticles

AuNPs functionalized with a single ligand

In a typical procedure, 0.1 mL of the prepared **AuNPs** solution was added to 2 mL of methanol. After centrifugation for 10 min, the supernatant solution was carefully removed and the precipitate was washed with methanol, dried at room temperature, and then re-dispersed in 0.6 mL of THF. To such solutions, 100 μ L of DMSO solution of ligand (**1** or **2**, 1.6 mM) was added, and the mixture was subjected to vortex for 30 min. Then, the functionalized **AuNPs** were precipitated from the solution, the supernatant was discarded and the **NPs** were washed with methanol and water, before being dried at room temperature. Finally, the dried functionalized **AuNPs** were re-dispersed in a mixture of 100 μ L aqueous solution of 0.01 M NaOH and 900 μ L of DMSO.

AuNPs functionalized with different ligands

AuNPs were functionalized according to a modified reported procedure,⁷⁷ 0.1 mL of the prepared **AuNPs** solution was added to 2 mL of methanol and centrifuged for 10 min, the supernatant solution was carefully removed and the precipitate was washed with methanol, dried at room temperature, and then redispersed in 0.6 mL of THF. To such solutions, β equivalents ($\beta < 1$; equiv with respect to the number of binding sites on Au, measured by full covered **AuNPs-1**) of **1** in DMSO solution were added. After vibration on a vortex for 30 min, $1 - \beta$ equivalents of **2** in DMSO were introduced, and the mixture was kept on vortex for another 30 min. After vortex, surface functionalization of **NPs** resulted in precipitation from the solution, and the supernatant was then discarded and the **NPs** were washed with methanol and water before being dried at room temperature. Finally, the dried functionalized **AuNPs** were re-dispersed in a mixture of DMSO and water under basic condition.

⁷⁷ Z. Chu, Y. Han, T. Bian, S. De, P. Král, R. Klajn, *J. Am. Chem. Soc.* **2018**, *141*, 1949-1960.

9. Appendix

9.1 List of abbreviations

°C	Celsius	DDAB	didodecyldimethylammonium bromide
δ	chemical shift	DIPEA	<i>N,N'</i> -diisopropylethyl amine
λ	Wavelength	DLS	dynamic light scattering
μ	micro	DMF	<i>N,N'</i> -dimethyl formamide
Ψ_i	surface potential	DMSO	dimethyl sulfoxide
ε	extinction coefficient /	DMSO- <i>d</i> 6	deuterated dimethyl sulfoxide
θ	actual molar fraction	e.g.	for example
ζ	zeta potential	eq	equivalent
abs	absolute	ESI	electrospray ionization
AFM	atomic force microscopy	FT-IR	fourier-transform infrared
AIBN	Azobisisobutyronitrile	g	gram
Ar	argon	G	guanidine
Au	gold	GCP	guanidiniocarbonyl pyrrole
AuNPs	gold nanoparticles	GCPZ	guanidiniocarbonyl pyrrole carboxylate
Boc	<i>tert</i> -butyloxycarbonyl		zwitterion
<i>t</i> Bu	<i>tert</i> -butyl	GSH	glutathione
Bu	dibutylamine	h	hour (s)
br	broad	HPLC	high performance liquid chromatography
c	concentration	HRMS	high resolution mass spectrometry
C	carboxyl	Hz	hertz
C _w	water content	I	Ionic strength
ca.	circa	IR	infrared
CDCl ₃	deuterated chloroform	K _{dim}	association constant
cm	centimeter	K _{sp}	solubility product constant
d	doublet / diameter	L	liter
D	deprotonated	L _e	Debye screening length
1D	one dimension	m	milli
DCM	dichloromethane	M	Mol/L
DMF	<i>N,N'</i> -dimethyl formamide	4-MBA	4-mercaptobenzonic acid
DMSO	dimethyl sulfoxide	6-MHA	6-mercaptocarboxylic acid
DMSO- <i>d</i> 6	deuterated dimethyl sulfoxide	m/z	Mass per charge
e.g.	for example	THF	tetrahydrofuran
DDA	Dodecylamine		
Me	methyl		

Appendix

MeOH	methanol		TMA	N,N,N-trimethyl(11-
MHz	megahertz			mercaptoundecyl)ammonium
min	minute (s)		TOAB	Tetraoctylammonium bromide
μ M	micromolar		UV	ultraviolet
mM	millimolar		UV/Vis	ultraviolet/ visible
Mp.	melting point		V	volume
MPLC	medium performance liquid chromatography		V_{elec}	electrostatic repulsion potential
MS	mass spectrometry		Z	zwitterionic
MUA	11-mercaptoundecanoic acid		V	volume
n	nano		V_{elec}	electrostatic repulsion potential
nm	nanometer		Z	zwitterionic
nM	nanomolar			
NMR	nuclear magnetic resonance			
NP	nanoparticle			
NPs	nanoparticles			
OL	oleylamine			
P	protonated			
PEG	polyethyleneglycol			
pH	pondus hydrogenii			
PIRSA	pH-induced reversible self-assembly			
pKa	logarithmic acid dissociation constant			
PSRSA	pH-sensitive reversible self-assembly			
ppm	parts per million			
Py	pyrrolidinamine			
PyBOP	benzotriazol-1-yl-N-oxy-tris(pyrrolidino)phosphonium hexafluorophosphate			
q	quadruplet			
r	radius			
RP	reversed phase			
rt	room temperature			
s	singulett / second (s)			
SEM	Scanning electron microscope			
SPR	surface plasmon resonance			
TFA	trifluoroacetic acid			

9.2 AFM measurement

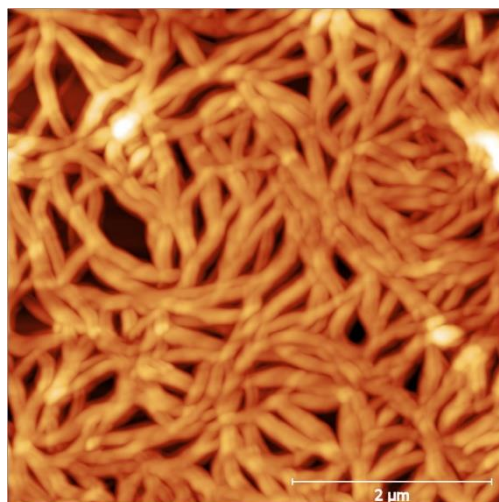


Figure 9.1: AFM image of **1-P** (1.6 mM) in DMSO.

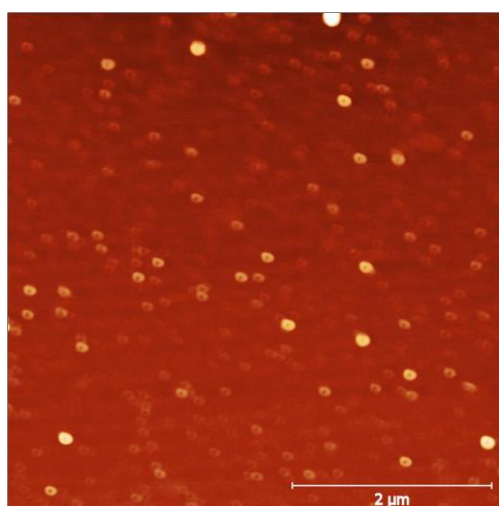


Figure 9.2: AFM image of **1-Z** (1.6 mM) in DMSO.

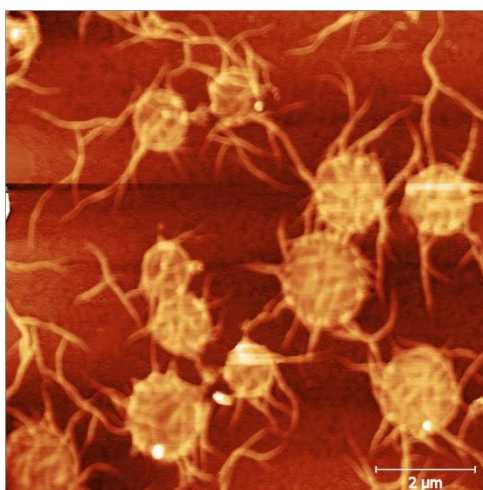


Figure 9.3: AFM image of **1-D** (1.6 mM) in DMSO.

9.3 UV/Vis measurement

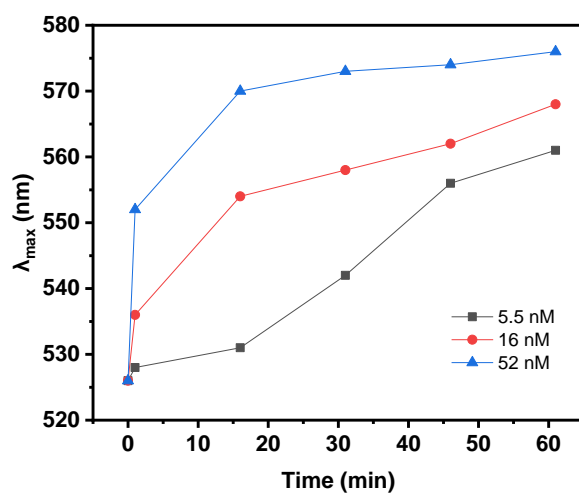


Figure 9.4: Time-dependent redshift of the absorption maximum (SPR) of AuNPs-1-Z with different concentration of AuNPs.

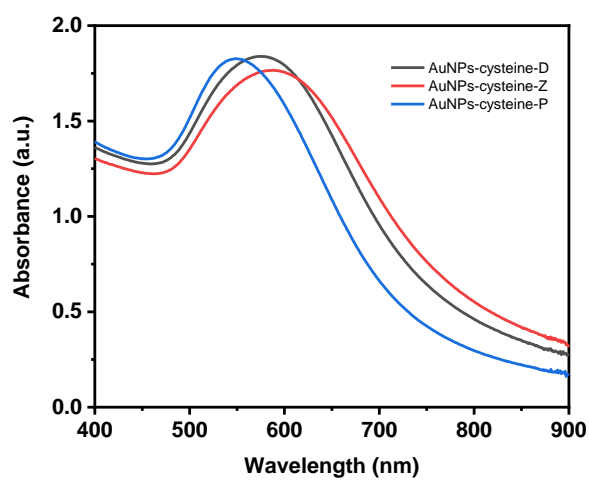


Figure 9.5: UV/Vis spectra of cysteine functionalized AuNPs in the DMSO/water (10%) mixture at different protonated states.

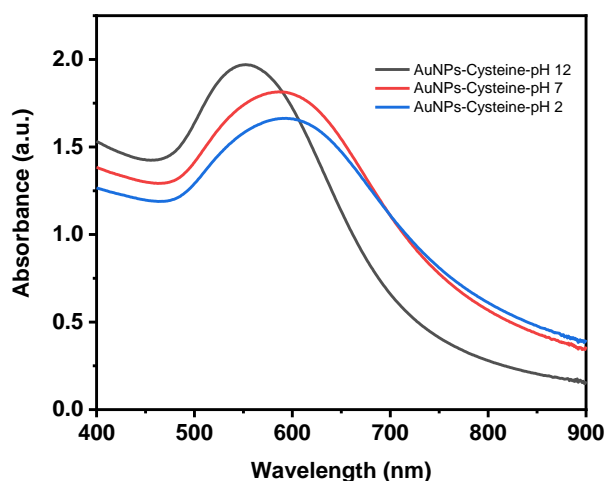


Figure 9.6: UV/Vis spectra of cysteine functionalized AuNPs in water at different pH values.

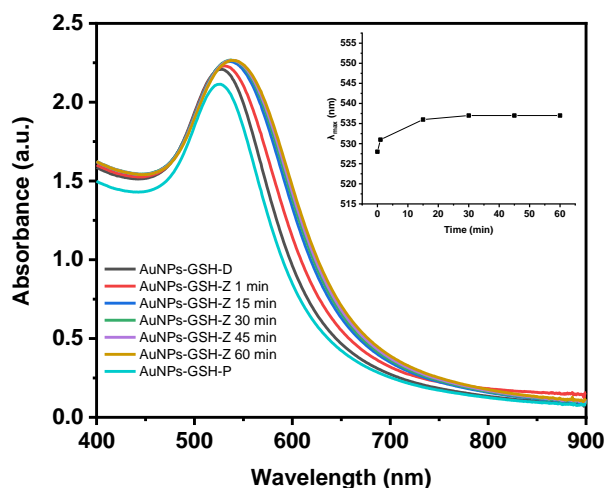


Figure 9.7: UV/Vis spectra of GSH functionalized AuNPs in the DMSO/water (10%) mixture at different protonated states.

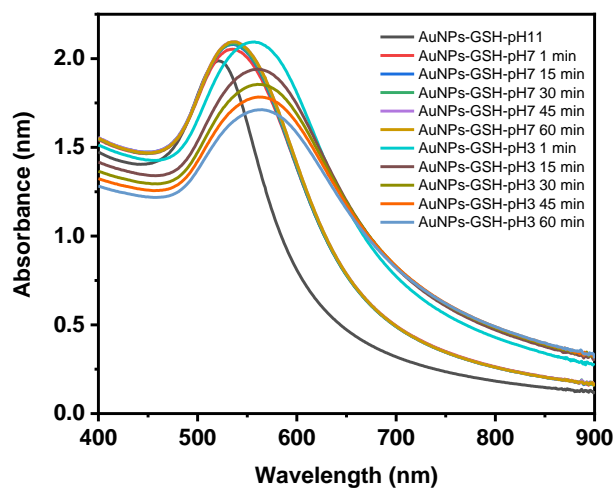


Figure 9.8: UV/Vis spectra of GSH functionalized AuNPs in water at different pH values.

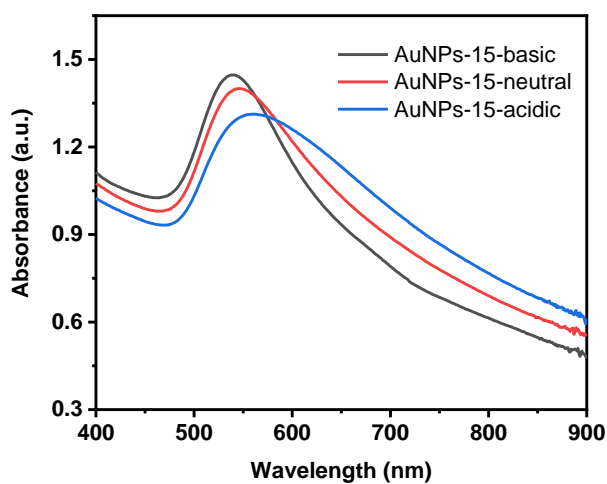


Figure 9.9: UV/Vis spectra of Boc-protected GCPZ (15) functionalized AuNPs (AuNPs-15) in the DMSO/water (10%) mixture at different pH values.

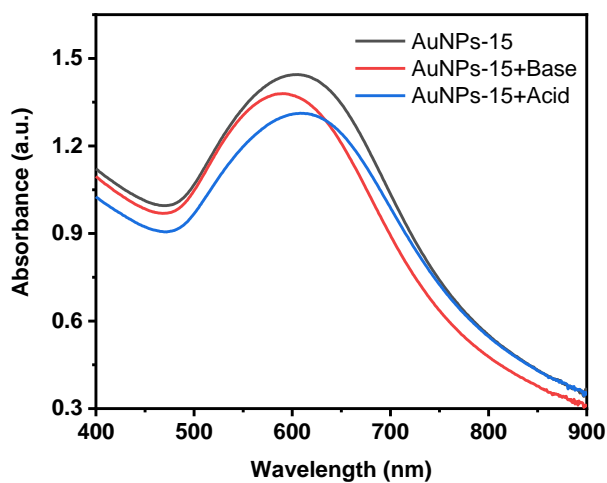


Figure 9.10: UV/Vis spectra of AuNPs-15 in the DMSO at different pH values.

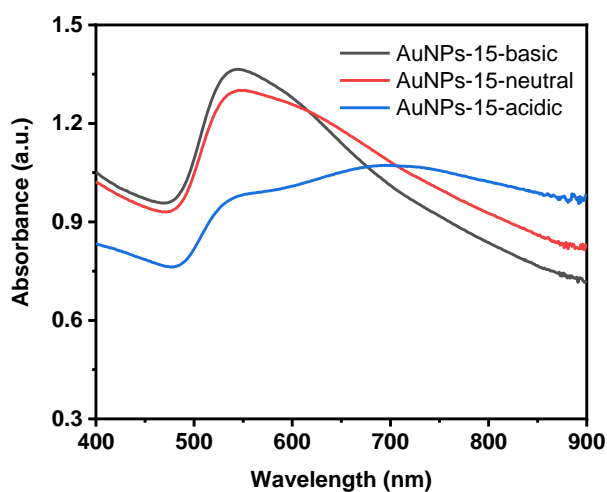


Figure 9.11: UV/Vis spectra of AuNPs-15 in the DMF at different pH values.

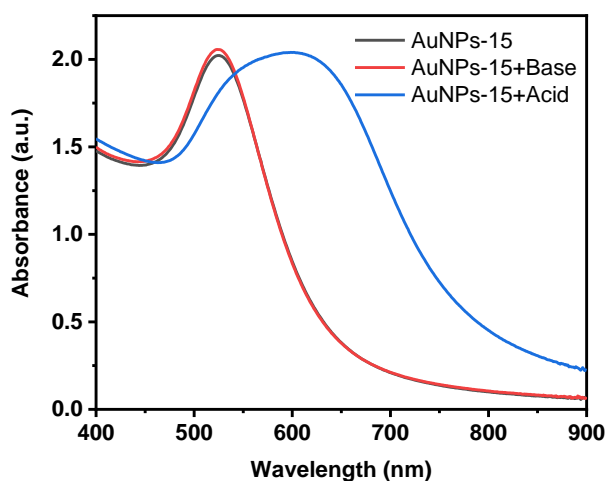


Figure 9.12: UV/Vis spectra of AuNPs-15 in the THF at different pH values.

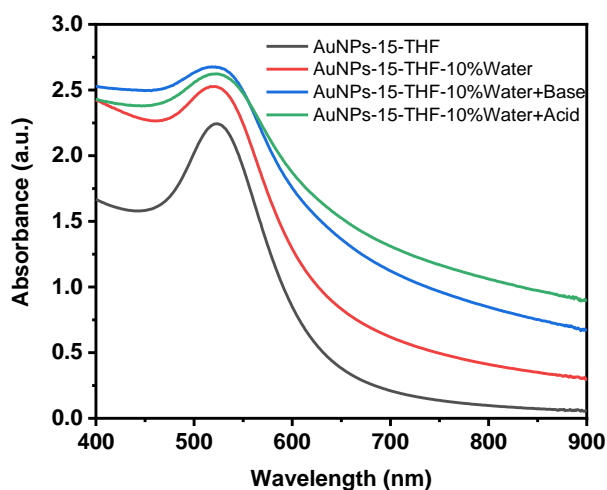


Figure 9.13: UV/Vis spectra of AuNPs-15 in different solvent and different pH values.

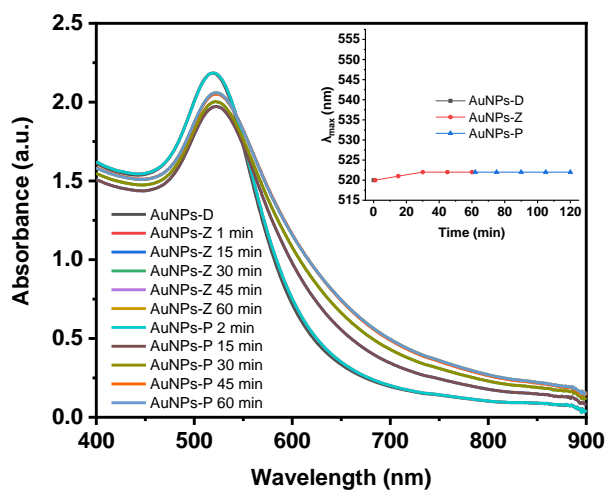


Figure 9.14: UV/Vis spectra of AuNPs-1-2 ($\theta = 0.01$) in the DMSO/water mixture ($C_w = 1$) at different protonated states, inset: changes in the wavelength maximum for increasing time.

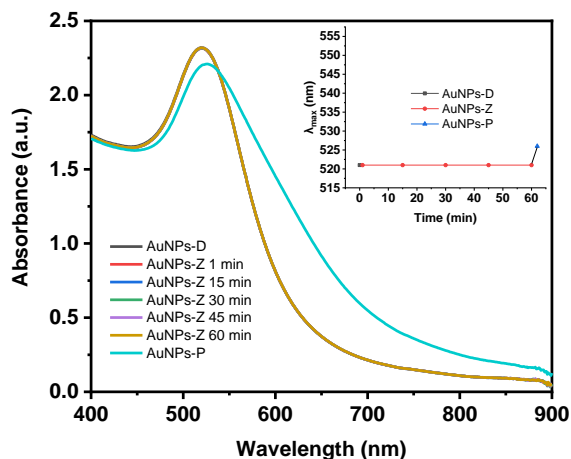


Figure 9.15: UV/Vis spectra of AuNPs-1-2 ($\theta = 0.01$) in the DMSO/water mixture ($C_w = 0.8$) at different protonated states, inset: changes in the wavelength maximum for increasing time.

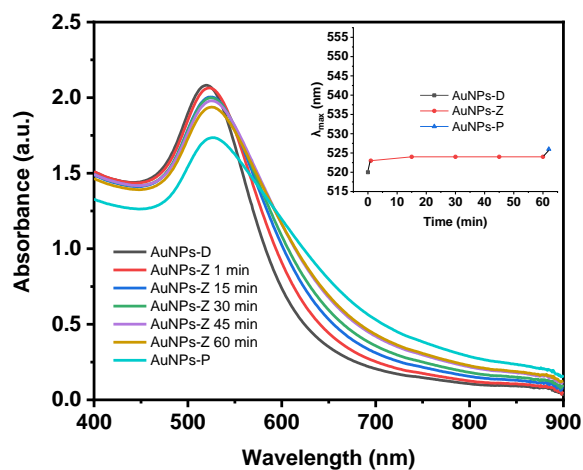


Figure 9.16: UV/Vis spectra of AuNPs-1-2 ($\theta = 0.02$) in the DMSO/water mixture ($C_w = 1$) at different protonated states, inset: changes in the wavelength maximum for increasing time.

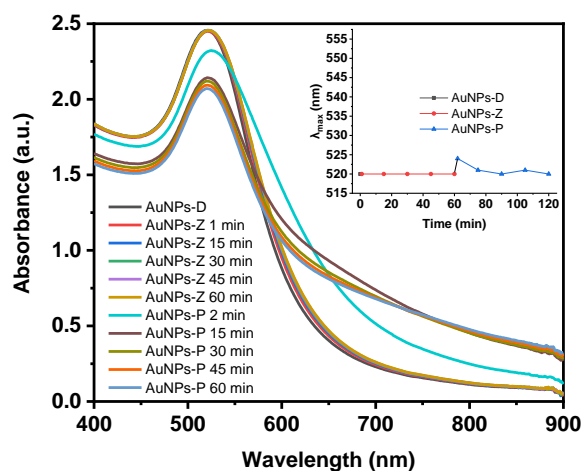


Figure 9.17: UV/Vis spectra of AuNPs-1-2 ($\theta = 0.02$) in the DMSO/water mixture ($C_w = 0.6$) at different protonated states, inset: changes in the wavelength maximum for increasing time.

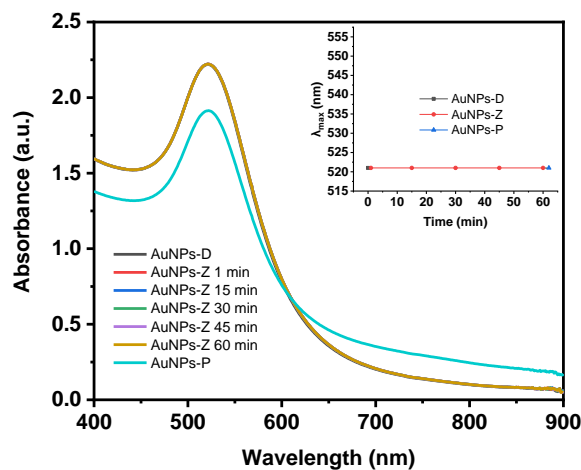


Figure 9.18: UV/Vis spectra of AuNPs-1-2 ($\theta = 0.02$) in the DMSO/water mixture ($C_w = 0.4$) at different protonated states, inset: changes in the wavelength maximum for increasing time.

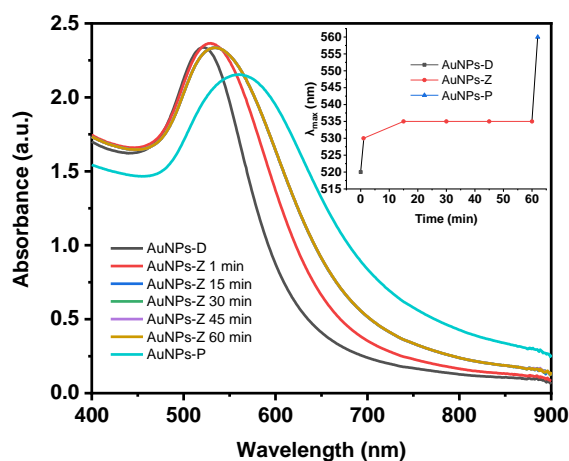


Figure 9.19: UV/Vis spectra of AuNPs-1-2 ($\theta = 0.04$) in the DMSO/water mixture ($C_w = 0.5$) at different protonated states, inset: changes in the wavelength maximum for increasing time.

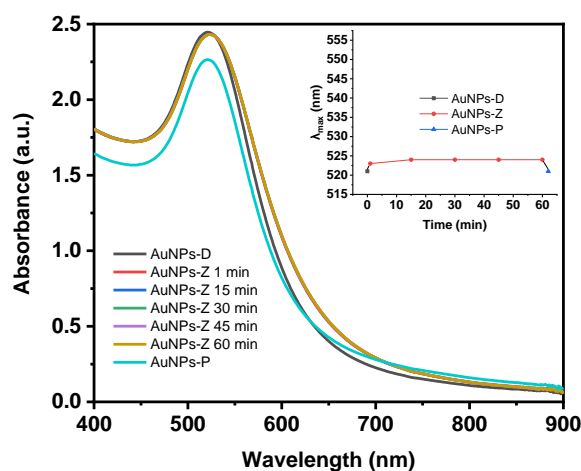


Figure 9.20: UV/Vis spectra of AuNPs-1-2 ($\theta = 0.04$) in the DMSO/water mixture ($C_w = 0.3$) at different protonated states, inset: changes in the wavelength maximum for increasing time.

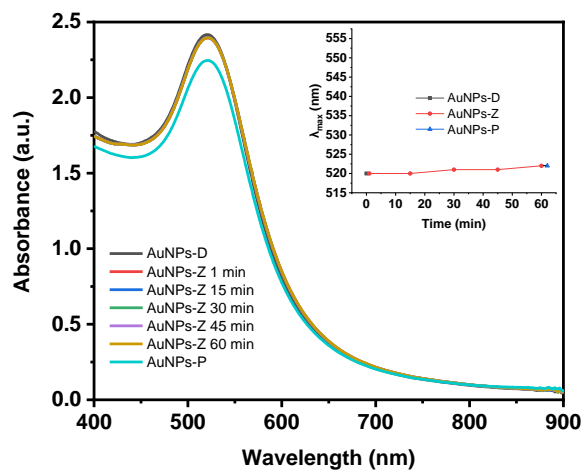


Figure 9.21: UV/Vis spectra of AuNPs-1 ($\theta = 0.08$) in the DMSO/water mixture ($C_w = 0.2$) at different protonated states, inset: changes in the wavelength maximum for increasing time.

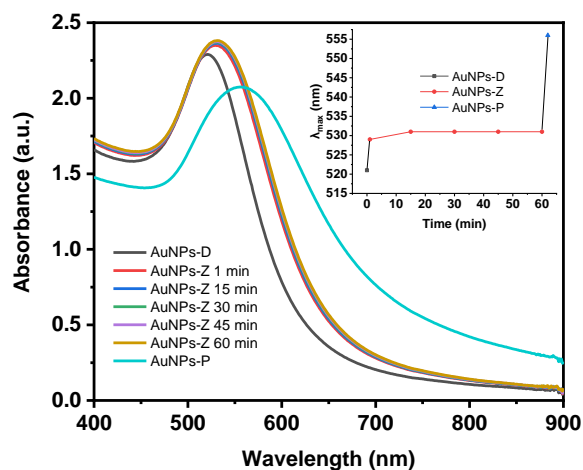


Figure 9.22: UV/Vis spectra of AuNPs-1-2 ($\theta = 0.11$) in the DMSO/water mixture ($C_w = 0.5$) at different protonated states, inset: changes in the wavelength maximum for increasing time.

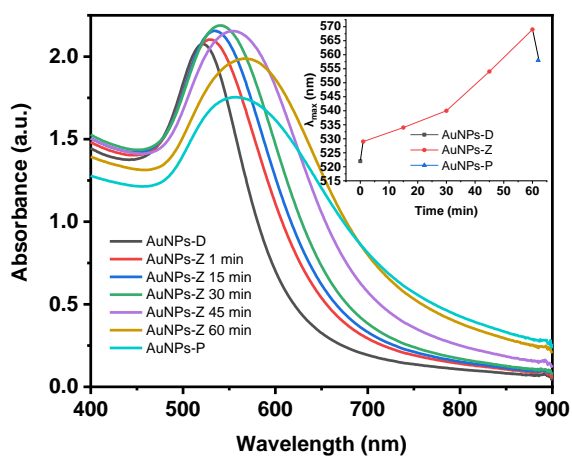


Figure 9.23: UV/Vis spectra of AuNPs-1 ($\theta = 0.11$) in the DMSO/water mixture ($C_w = 0.3$) at different protonated states, inset: changes in the wavelength maximum for increasing time.

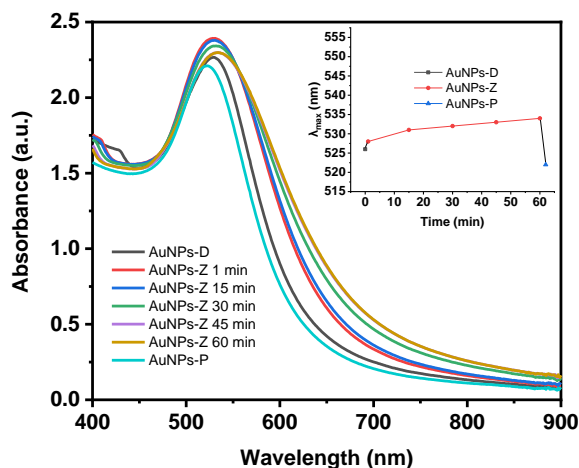


Figure 9.24: UV/Vis spectra of AuNPs-1-2 ($\theta = 0.11$) in the DMSO/water mixture ($C_w = 0.2$) at different protonated states, inset: changes in the wavelength maximum for increasing time.

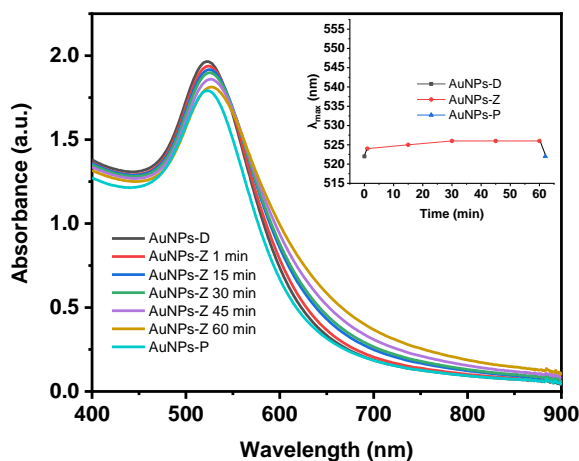


Figure 9.25: UV/Vis spectra of AuNPs-1-2 ($\theta = 0.11$) in the DMSO/water mixture ($C_w = 0.15$) at different protonated states, inset: changes in the wavelength maximum for increasing time.

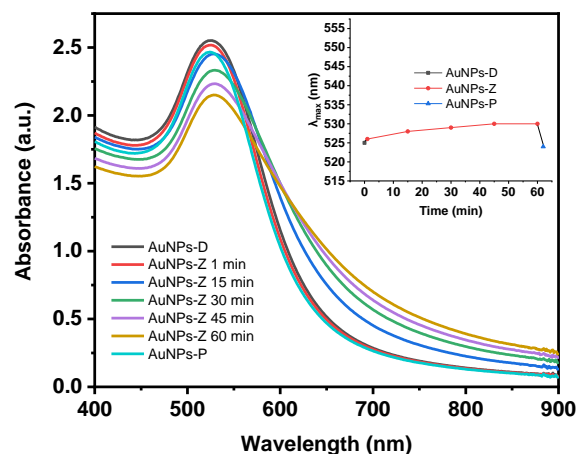


Figure 9.26: UV/Vis spectra of AuNPs-1-2 ($\theta = 0.18$) in the DMSO/water mixture ($C_w = 0.05$) at different protonated states, inset: changes in the wavelength maximum for increasing time.

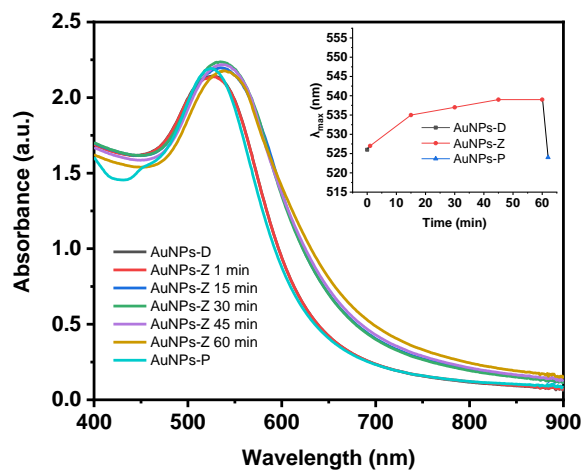


Figure 9.27: UV/Vis spectra of AuNPs-1-2 ($\theta = 0.33$) in the DMSO/water mixture ($C_w = 0.15$) at different protonated states, inset: changes in the wavelength maximum for increasing time.

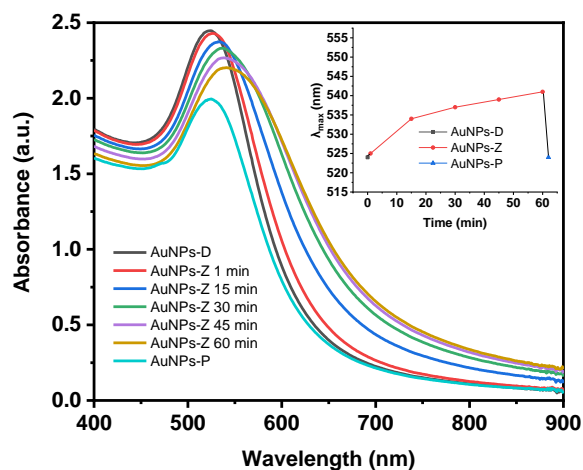


Figure 9.28: UV/Vis spectra of AuNPs-1-2 ($\theta = 0.39$) in the DMSO/water mixture ($C_w = 0.15$) at different protonated states, inset: changes in the wavelength maximum for increasing time.

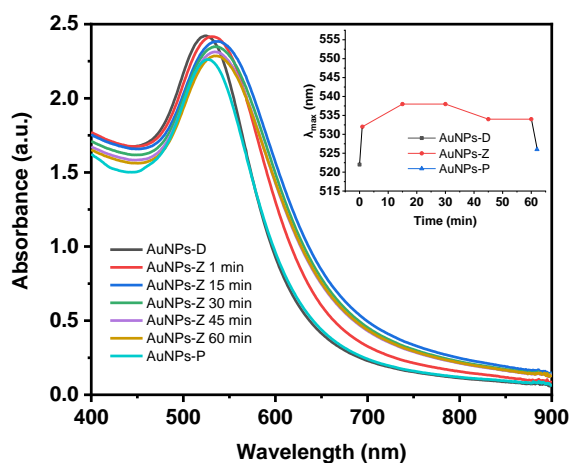


Figure 9.29: UV/Vis spectra of AuNPs-1-2 ($\theta = 0.44$) in the DMSO/water mixture ($C_w = 0.15$) at different protonated states, inset: changes in the wavelength maximum for increasing time.

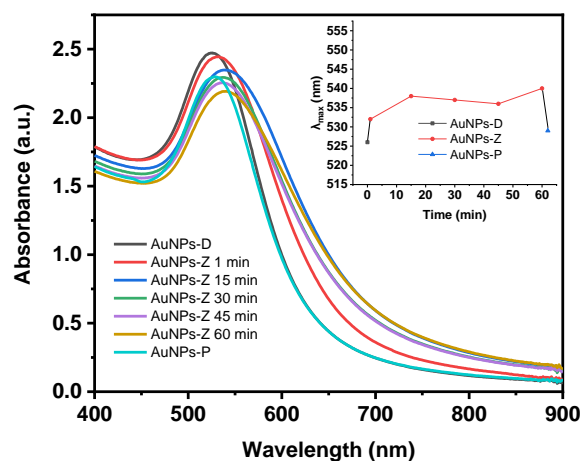


Figure 9.30: UV/Vis spectra of AuNPs-1-2 ($\theta = 0.49$) in the DMSO/water mixture ($C_w = 0.15$) at different protonated states, inset: changes in the wavelength maximum for increasing time.

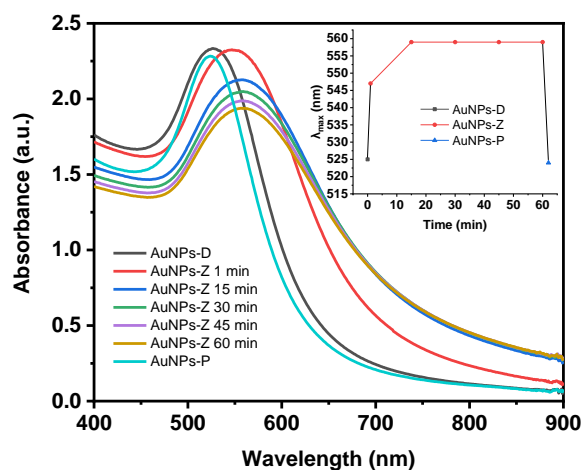


Figure 9.31: UV/Vis spectra of AuNPs-1-2 ($\theta = 0.66$) in the DMSO/water mixture ($C_w = 0.05$) at different protonated states, inset: changes in the wavelength maximum for increasing time.

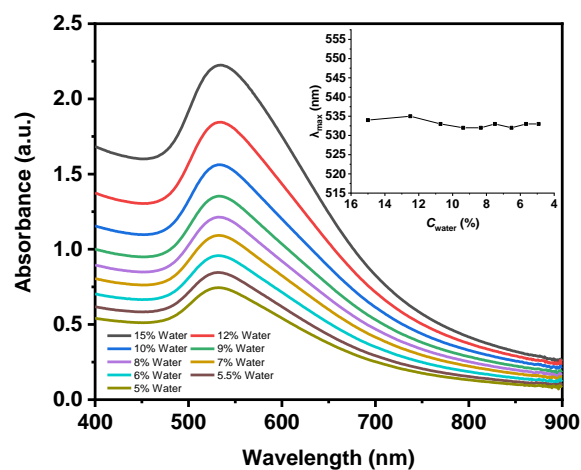


Figure 9.32: UV/Vis spectra of AuNPs-1-2-Z ($\theta = 0.15$) in the DMSO/water mixture with different C_w values, inset: changes in the wavelength maximum for decreasing C_w values.

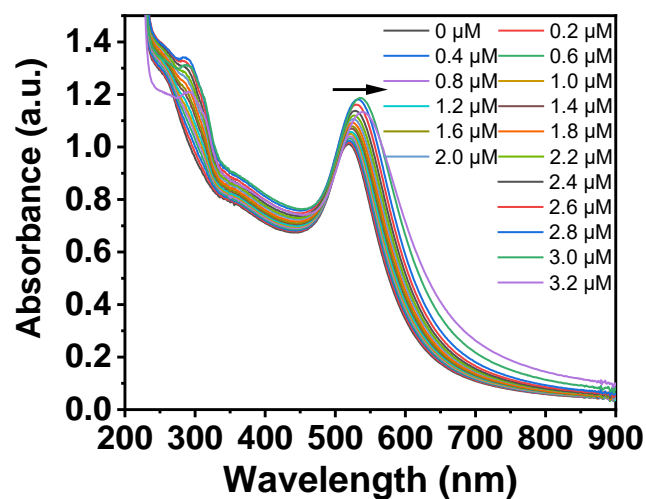


Figure 9.33: UV/Vis absorption of AuNPs-3 with the increasing concentration of ligand 5 (0.2 μM for each time).

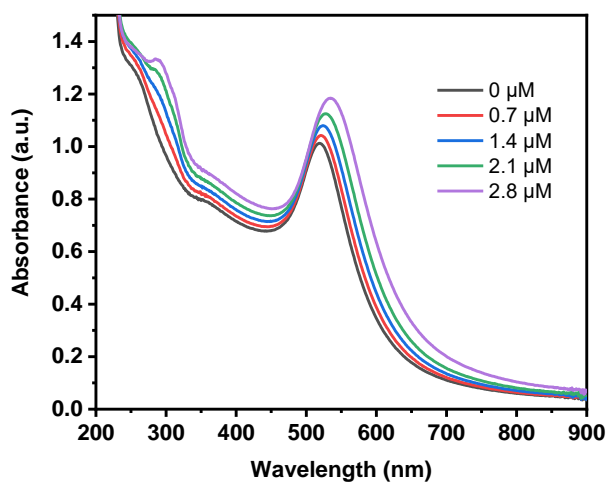


Figure 9.34: UV/Vis absorption of AuNPs-3 with the increasing concentration of ligand 5 (0.7 μM for each time).

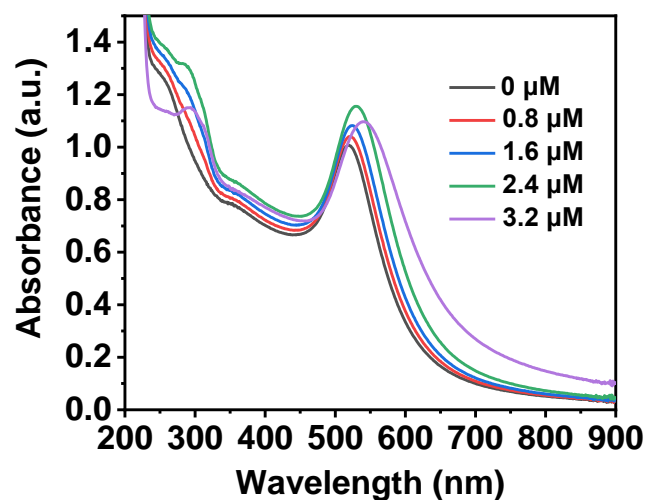


Figure 9.35: UV/Vis absorption of AuNPs-3 with the increasing concentration of ligand 5 (0.8 μM for each time).

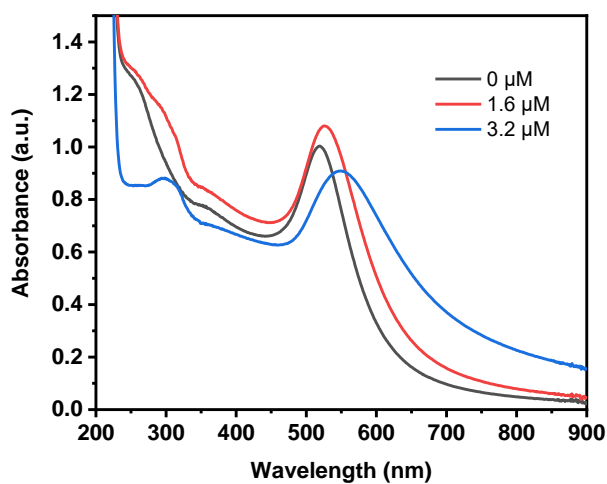


Figure 9.36: UV/Vis absorption of AuNPs-3 with the increasing concentration of ligand 5 (1.6 μM for each time).

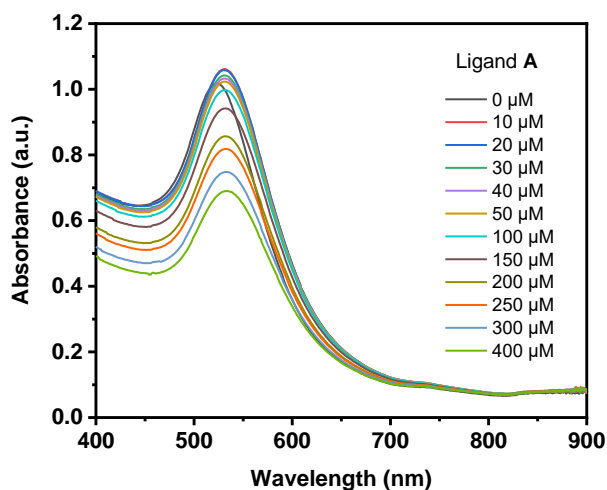


Figure 9.37: UV/Vis absorption of AuNPs-3 with high concentration of ligand 5.

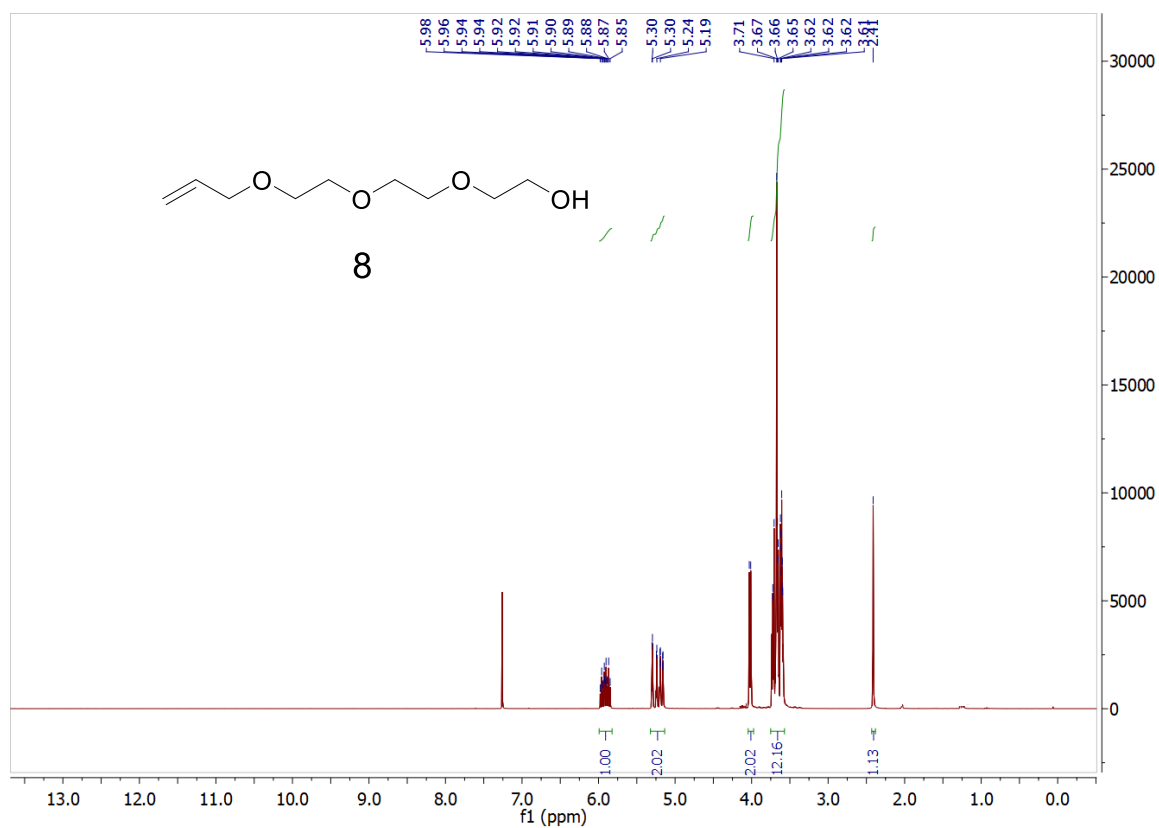
9.4 ^1H NMR and ^{13}C NMR

Figure 9.38: ^1H NMR spectrum of **8** (CDCl_3 , 300 MHz, 298 K).

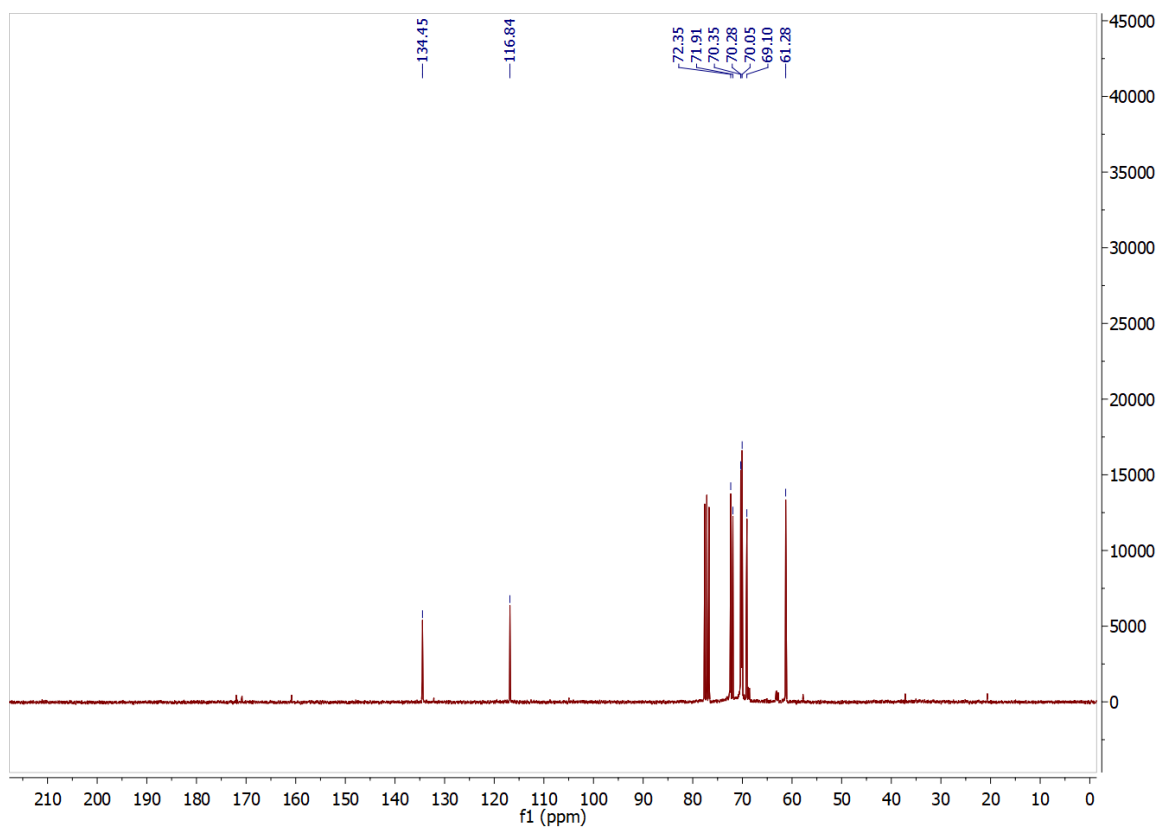


Figure 9.39: ^{13}C NMR spectrum of **8** (CDCl_3 , 75 MHz, 298 K).

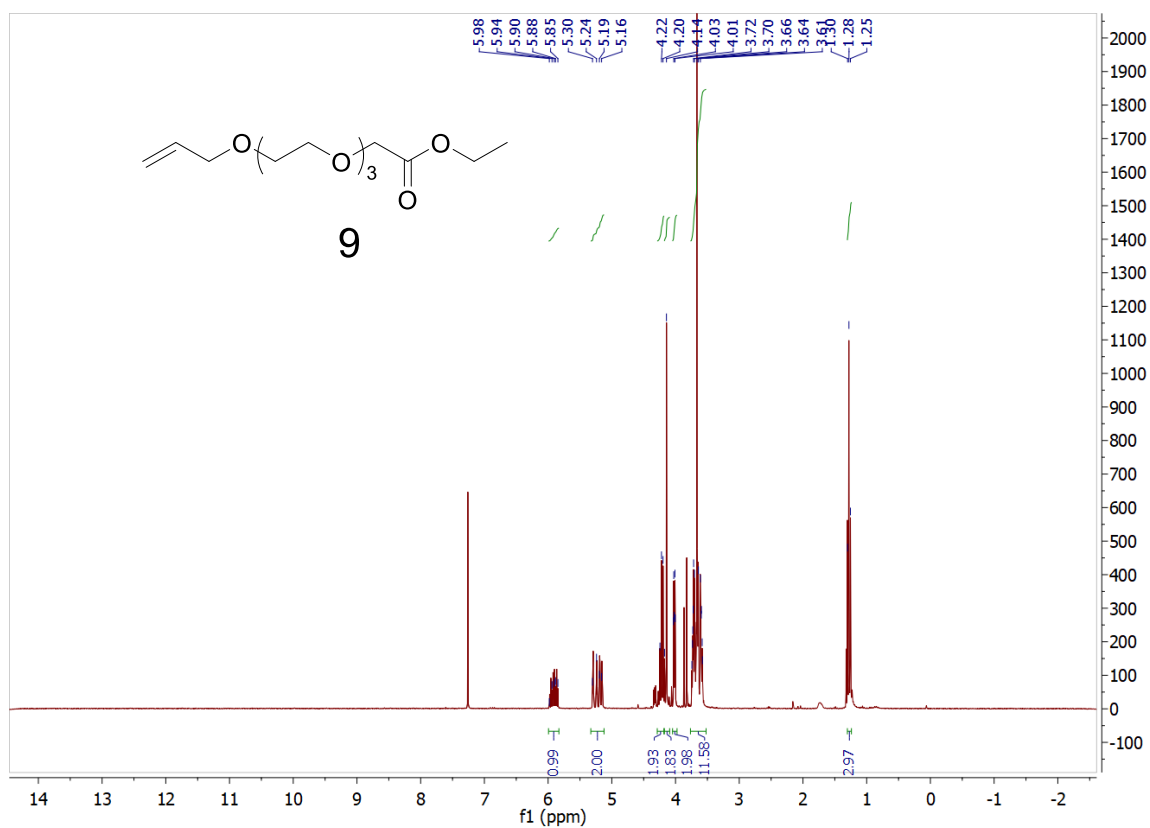


Figure 9.40: ¹H NMR spectrum of **9** (CDCl₃, 300 MHz, 298 K).

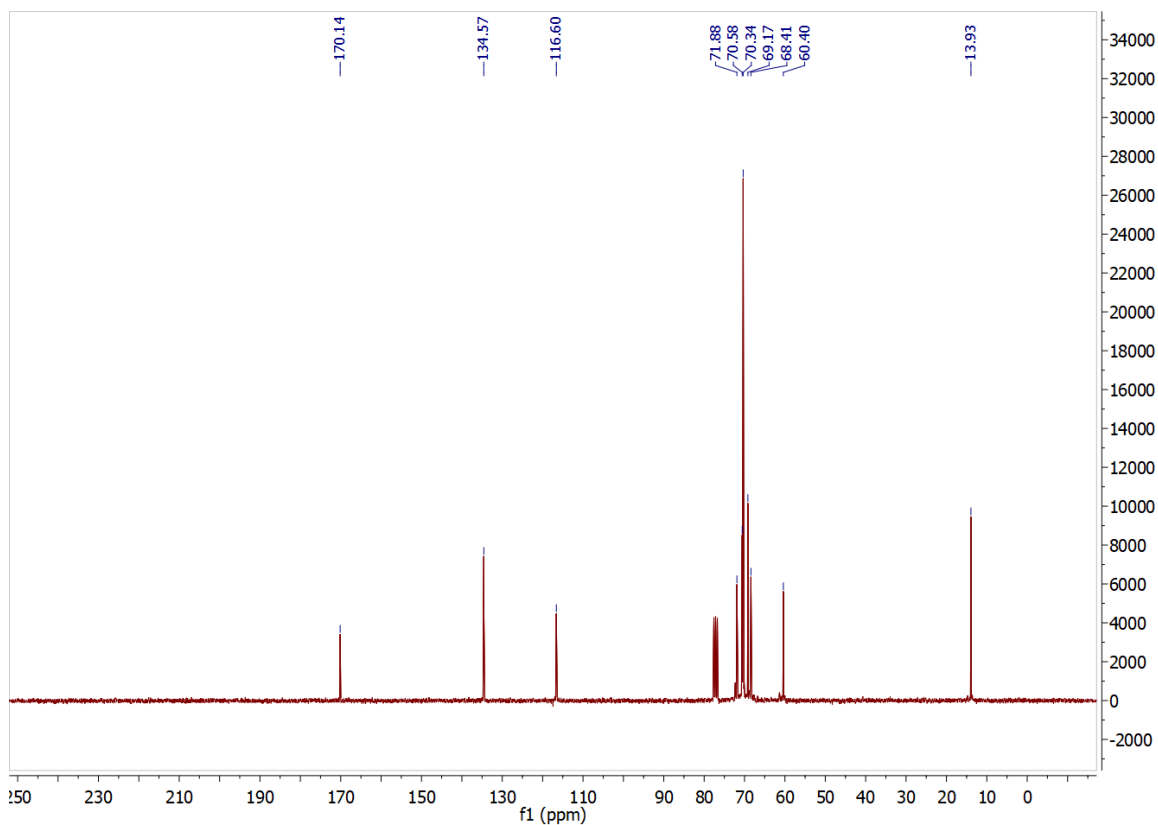


Figure 9.41: ¹³C NMR spectrum of **9** (CDCl₃, 75 MHz, 298 K).

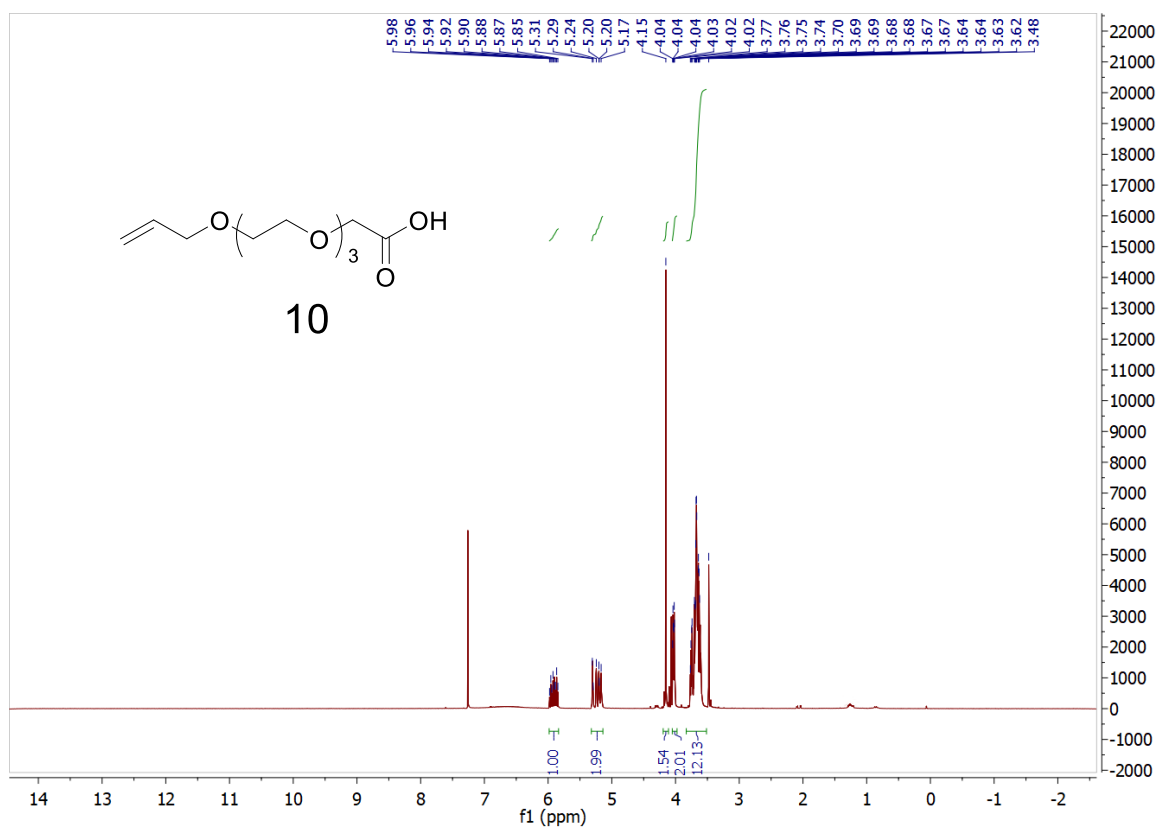


Figure 9.42: ¹H NMR spectrum of **10** (CDCl₃, 300 MHz, 298 K).

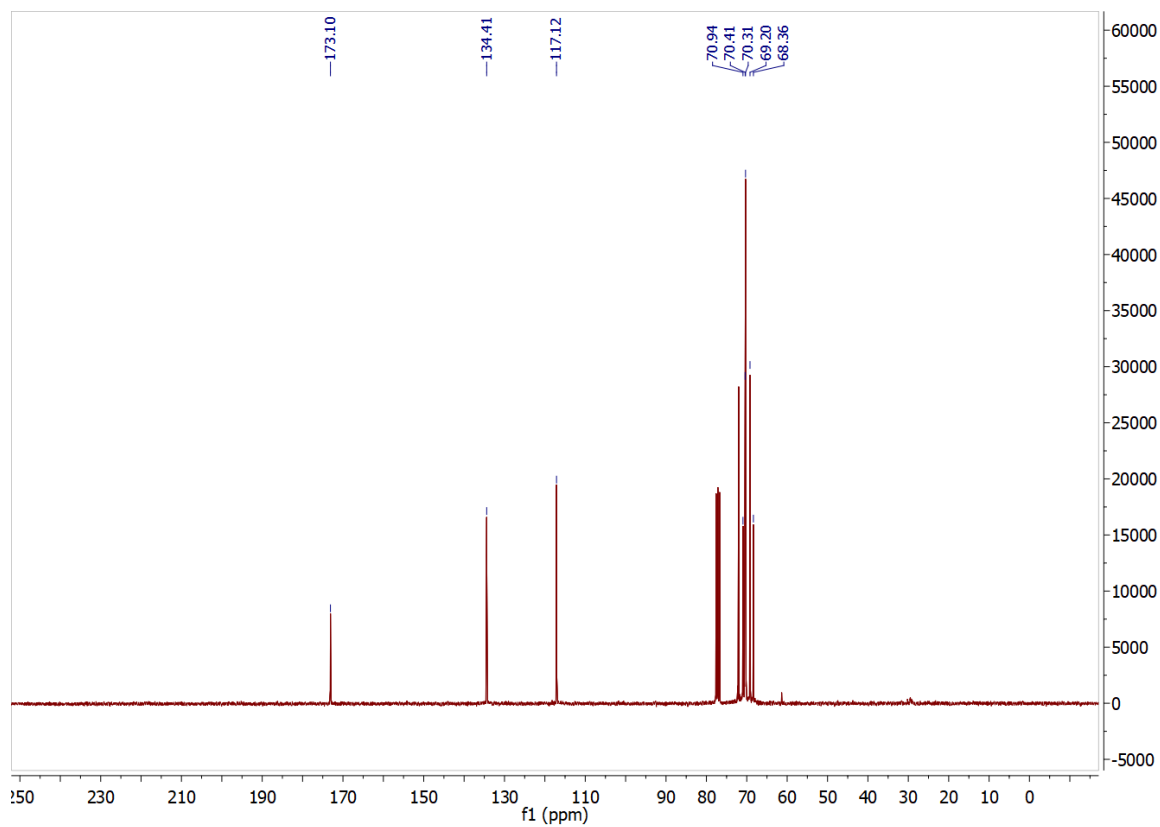


Figure 9.43: ¹³C NMR spectrum of **10** (CDCl₃, 75 MHz, 298 K).

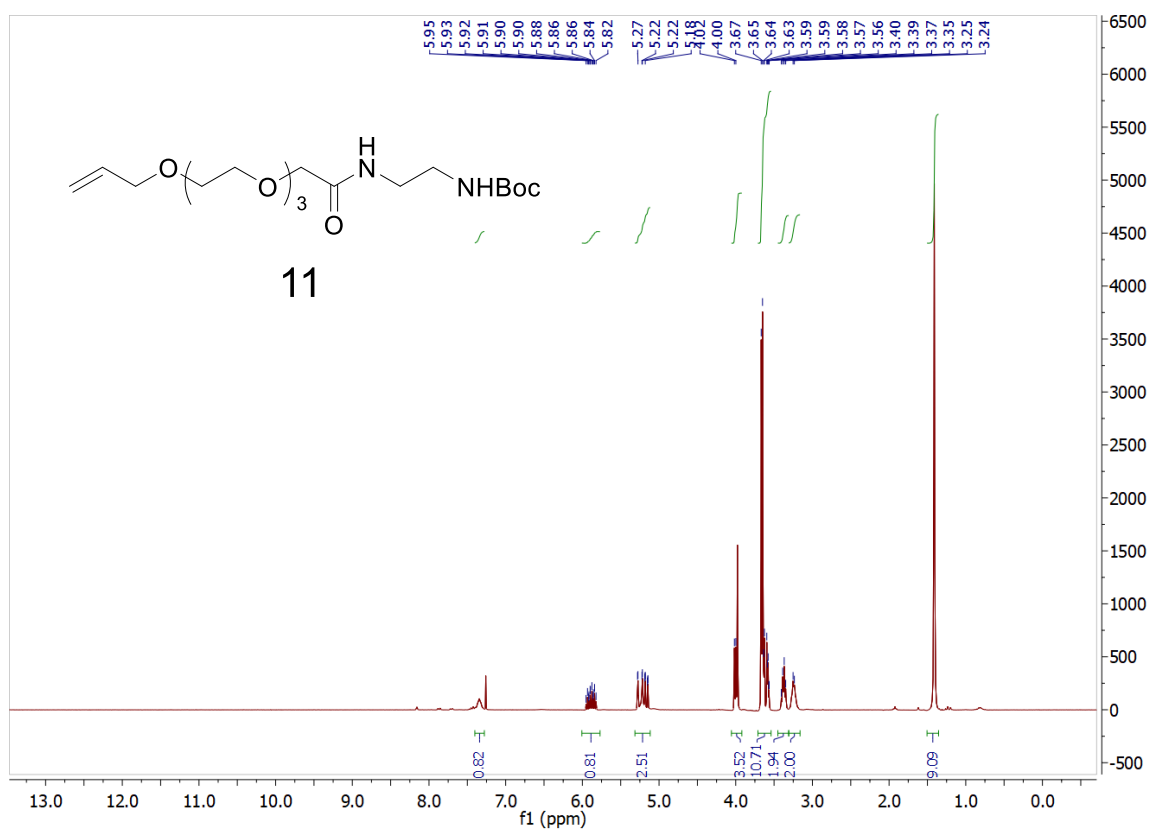


Figure 9.44: ¹H NMR spectrum of **11** (CDCl₃, 300 MHz, 298 K).

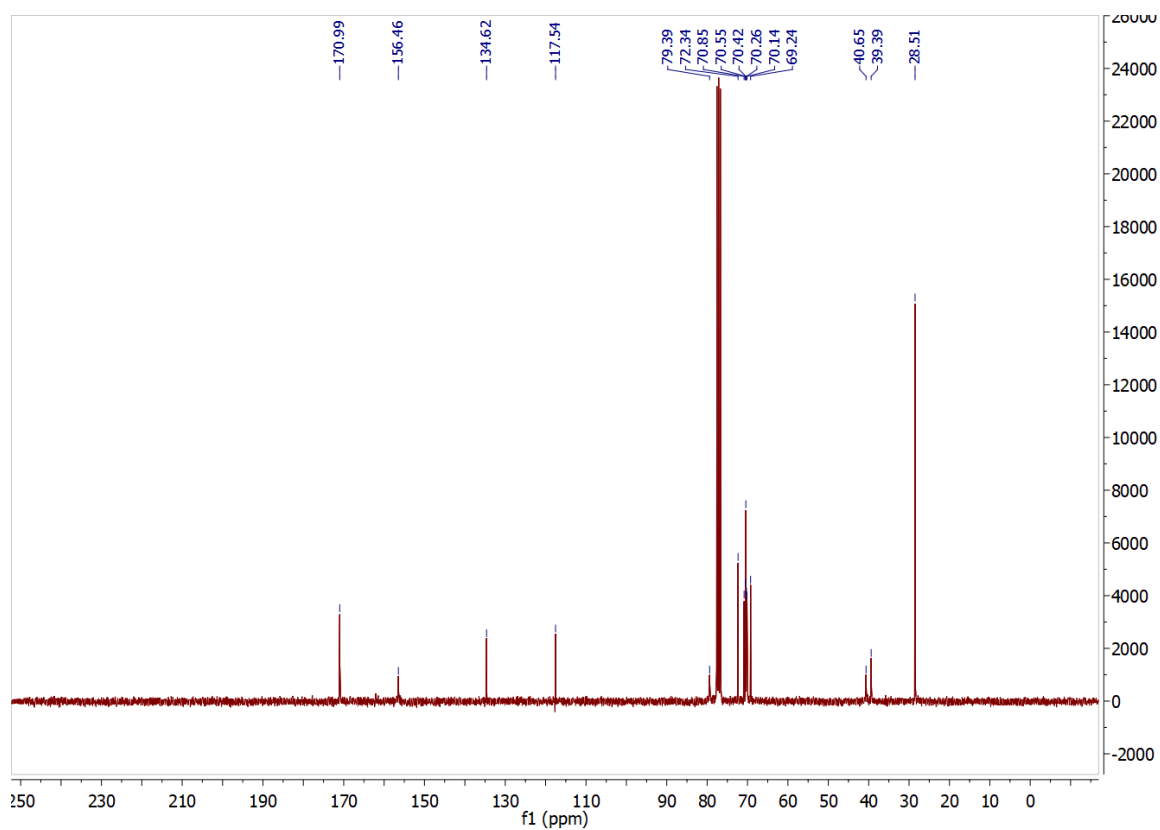


Figure 9.45: ¹³C NMR spectrum of **11** (CDCl₃, 75 MHz, 298 K).

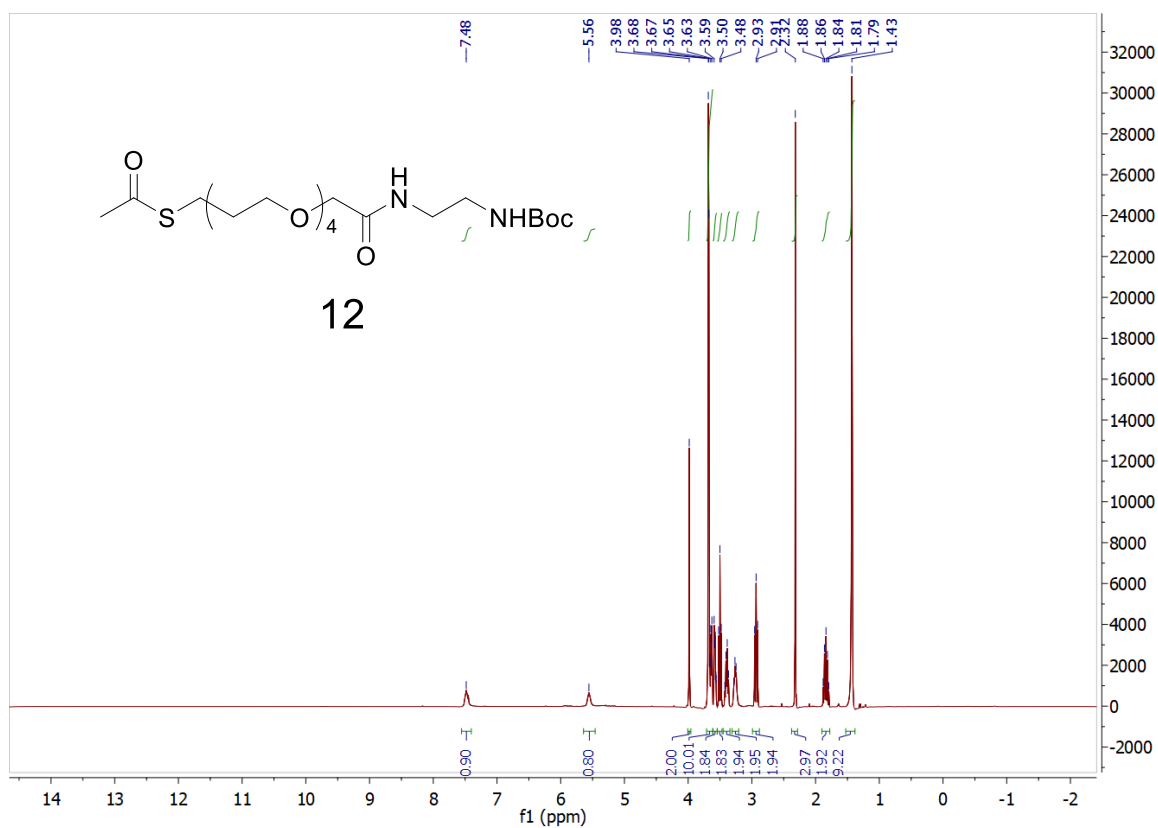


Figure 9.46: ^1H NMR spectrum of **12** (CDCl_3 , 300 MHz, 298 K).

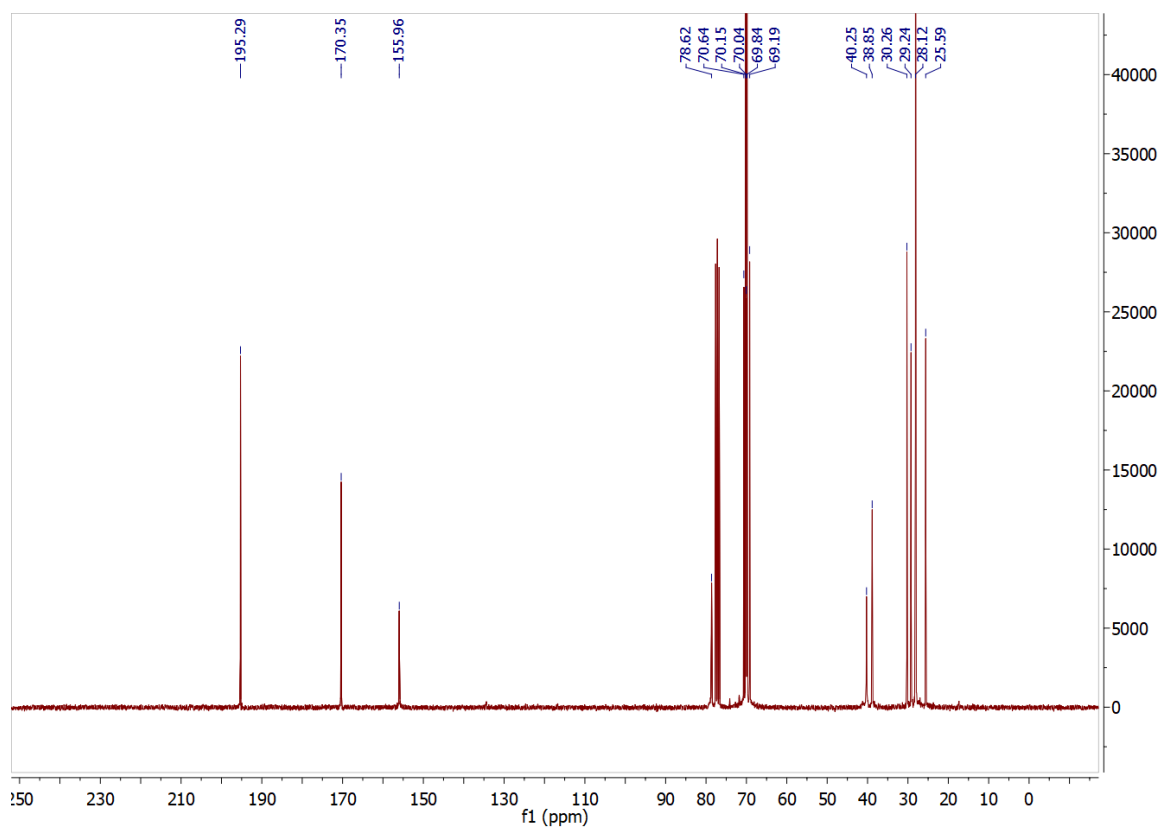


Figure 9.47: ^{13}C NMR spectrum of **12** (CDCl_3 , 75 MHz, 298 K).

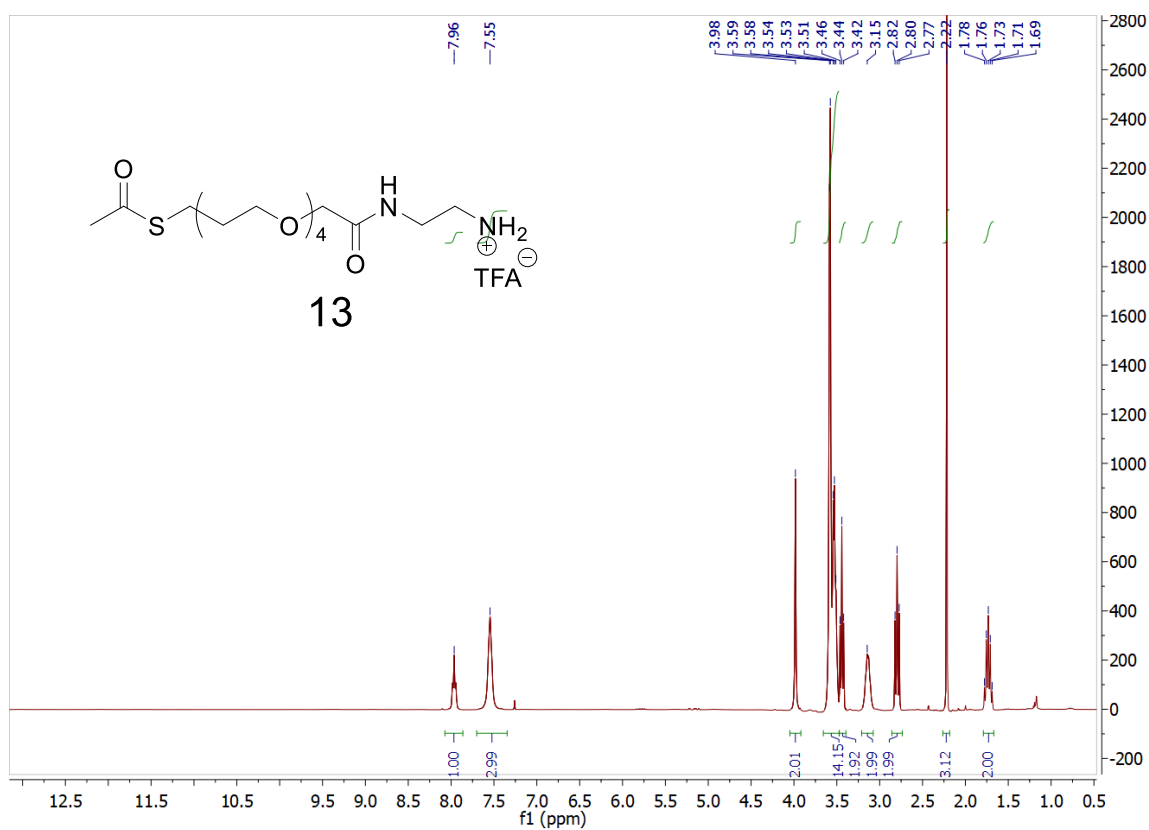


Figure 9.48: ¹H NMR spectrum of **13** (CDCl₃, 300 MHz, 298 K).

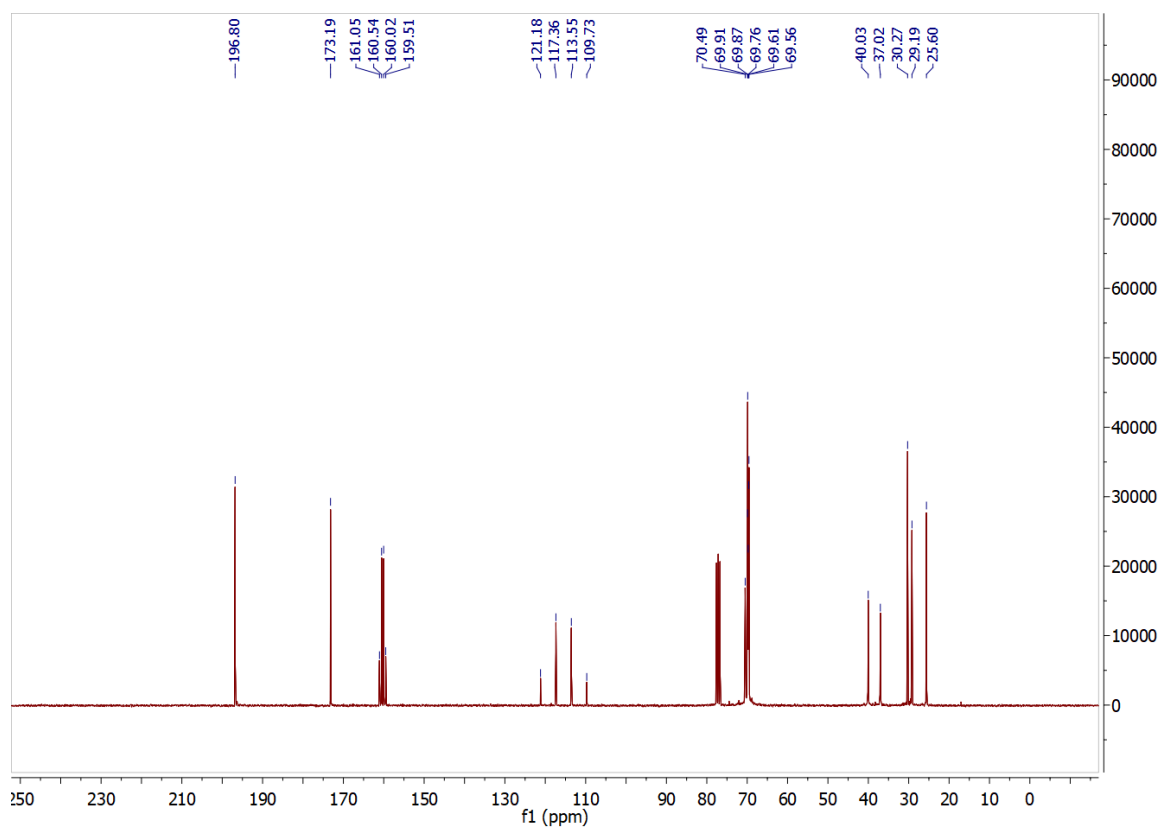


Figure 9.49: ¹³C NMR spectrum of **13** (CDCl₃, 75 MHz, 298 K).

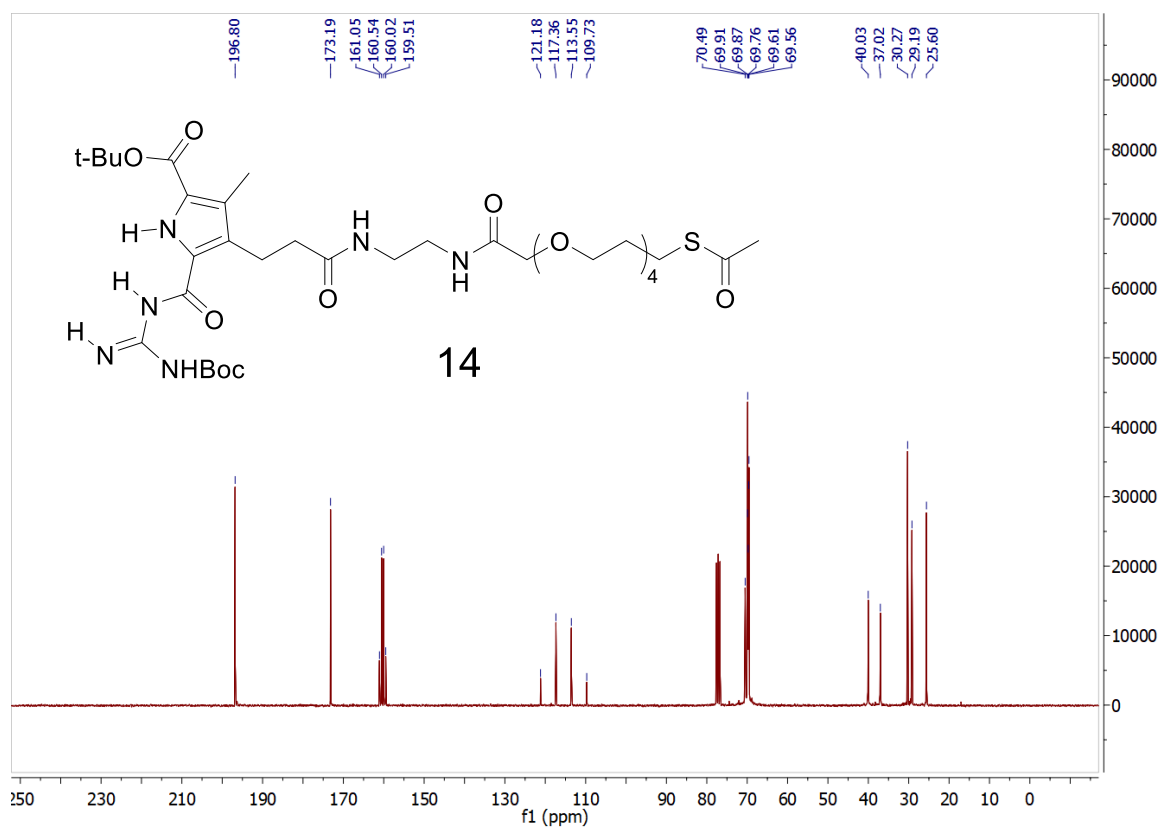


Figure 9.50: ^1H NMR spectrum of **14** (CDCl_3 , 300 MHz, 298 K).

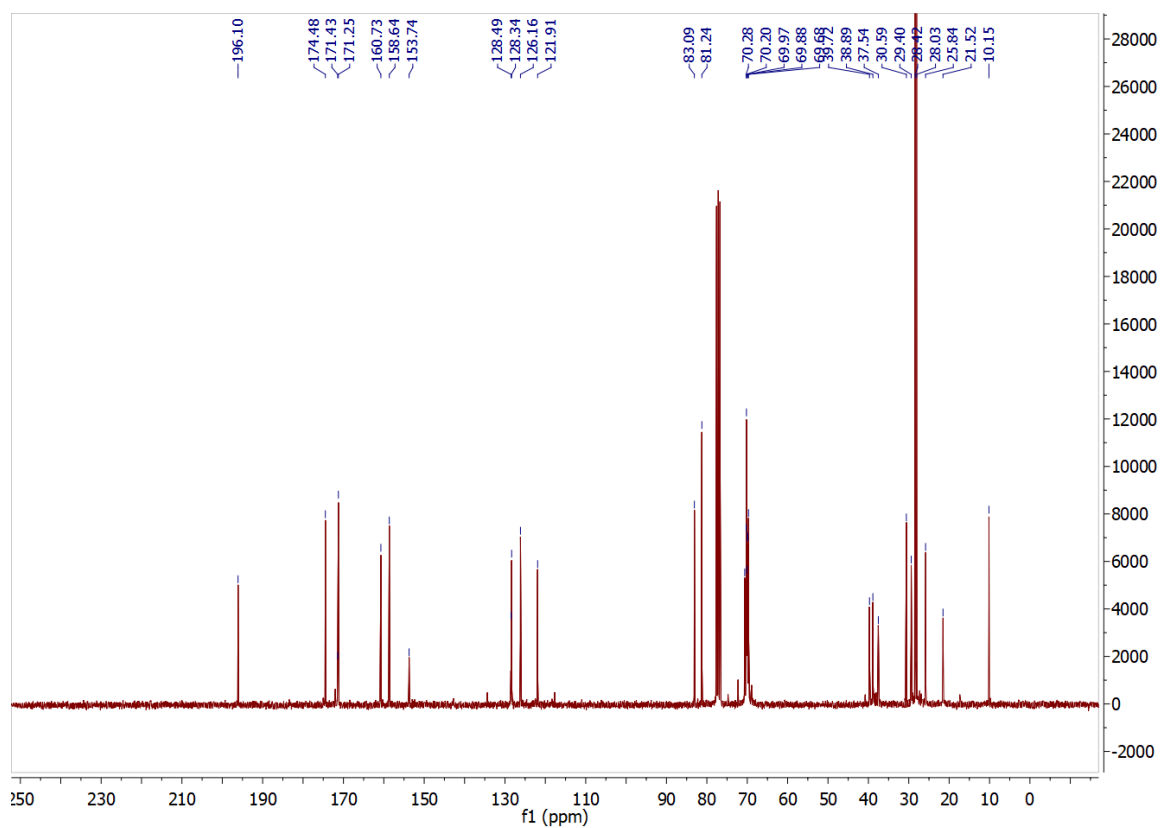


Figure 9.51: ^{13}C NMR spectrum of **13** (CDCl_3 , 75 MHz, 298 K).

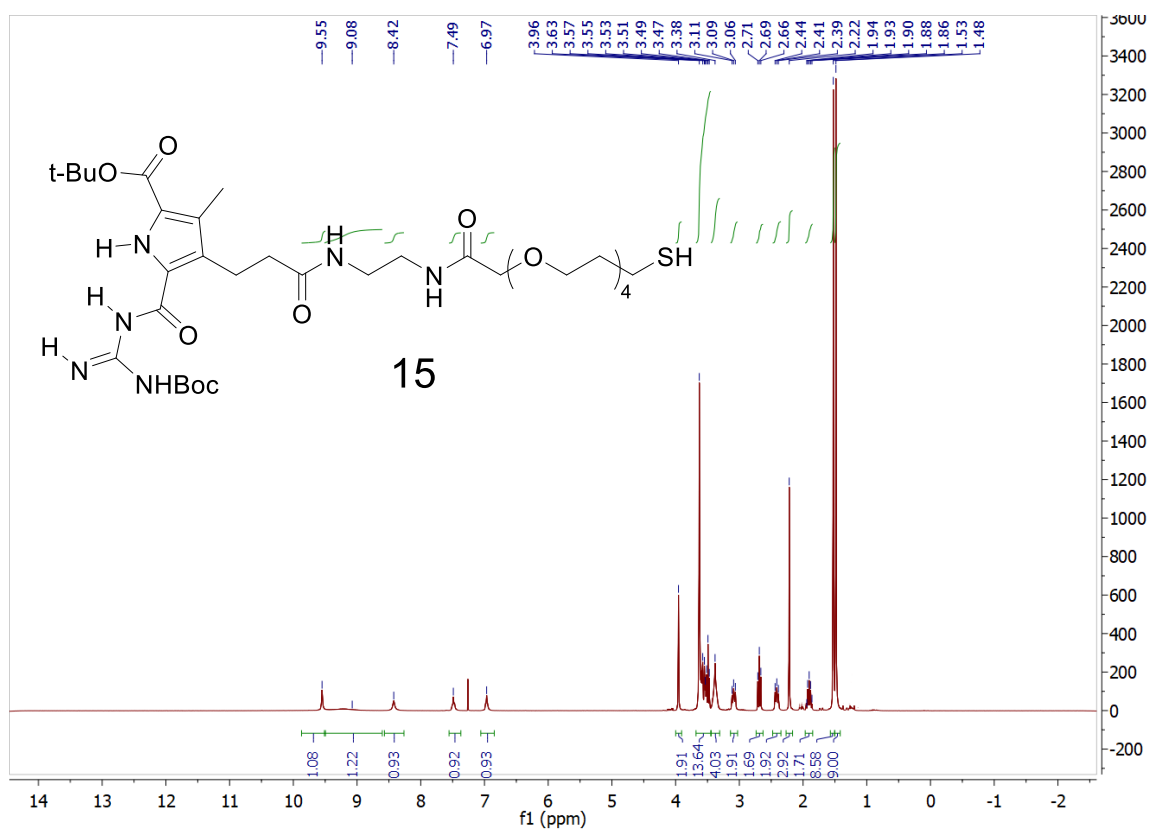


Figure 9.52: ^1H NMR spectrum of **15** (CDCl_3 , 300 MHz, 298 K).

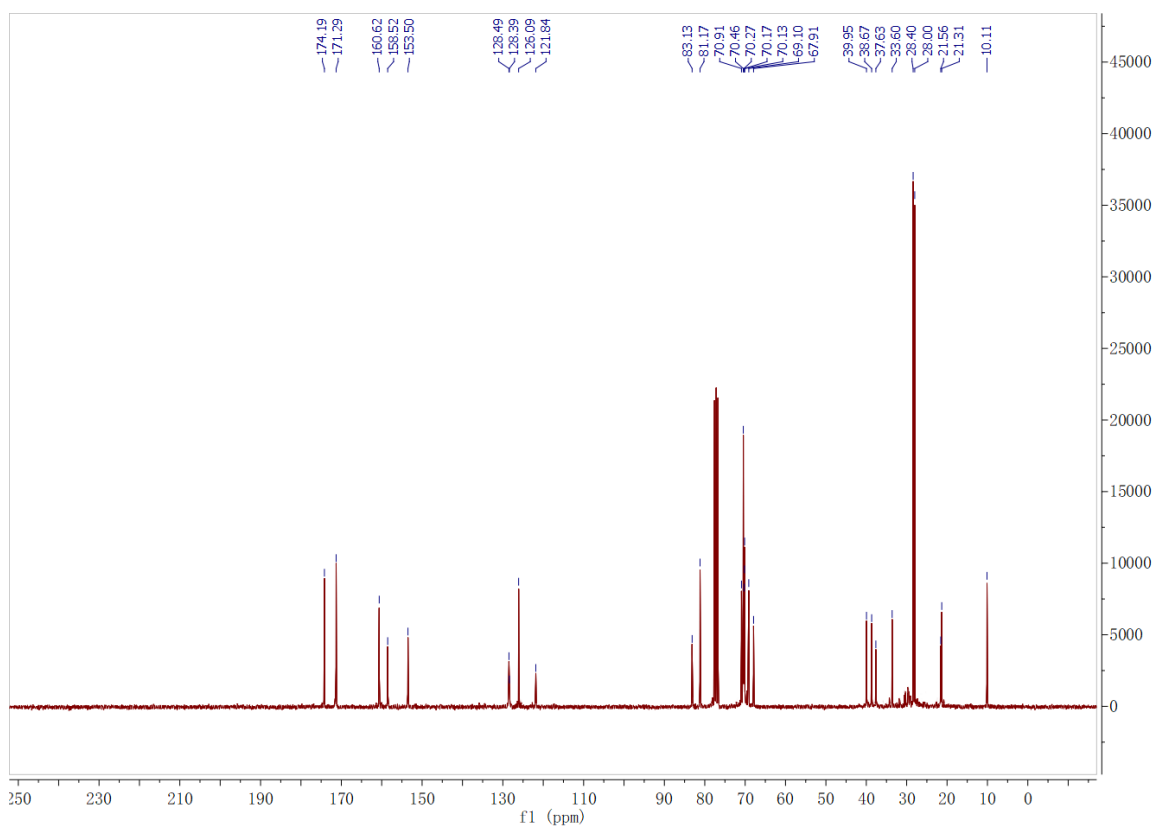


Figure 9.53: ^{13}C NMR spectrum of **15** (CDCl_3 , 75 MHz, 298 K).

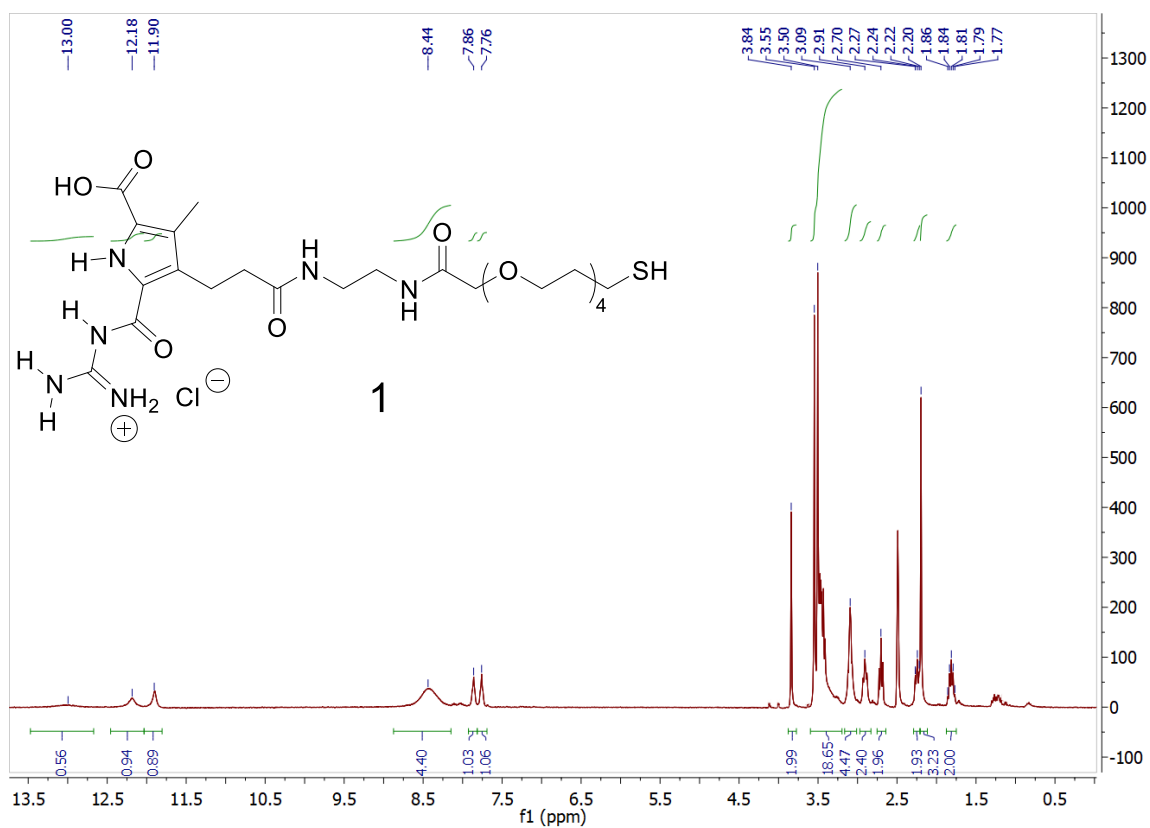


Figure 9.54: ^1H NMR spectrum of **1** (DMSO- d_6 , 300 MHz, 298 K).

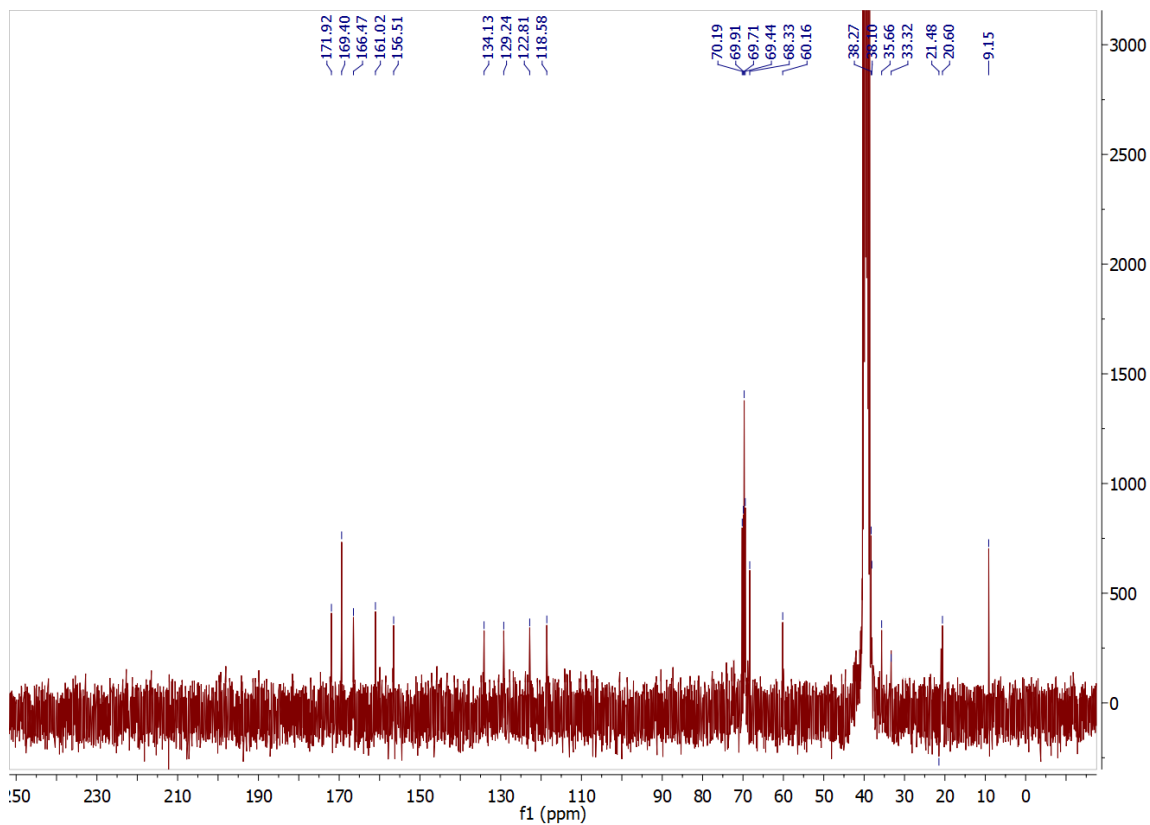


Figure 9.55: ^{13}C NMR spectrum of **1** (DMSO- d_6 , 75 MHz, 298 K).

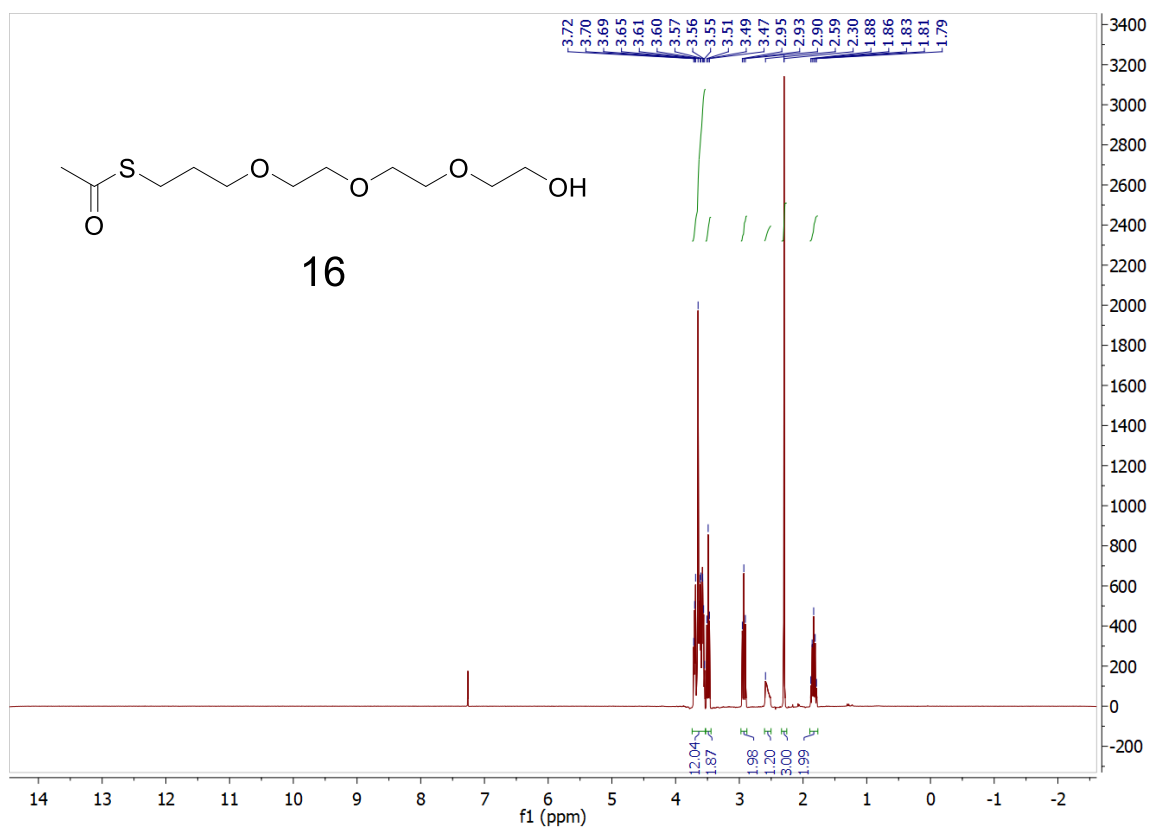


Figure 9.56: ¹H NMR spectrum of **16** (CDCl₃, 300 MHz, 298 K).

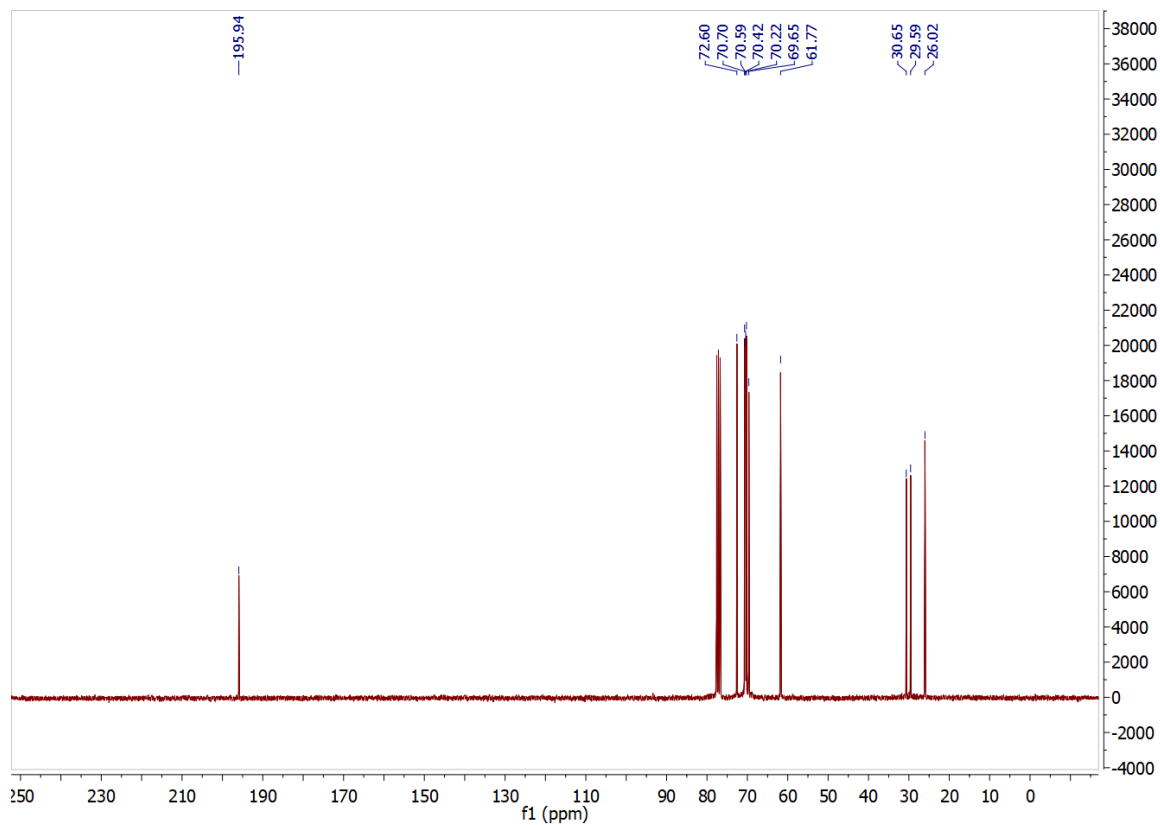


Figure 9.57: ¹³C NMR spectrum of **16** (CDCl₃, 75 MHz, 298 K).

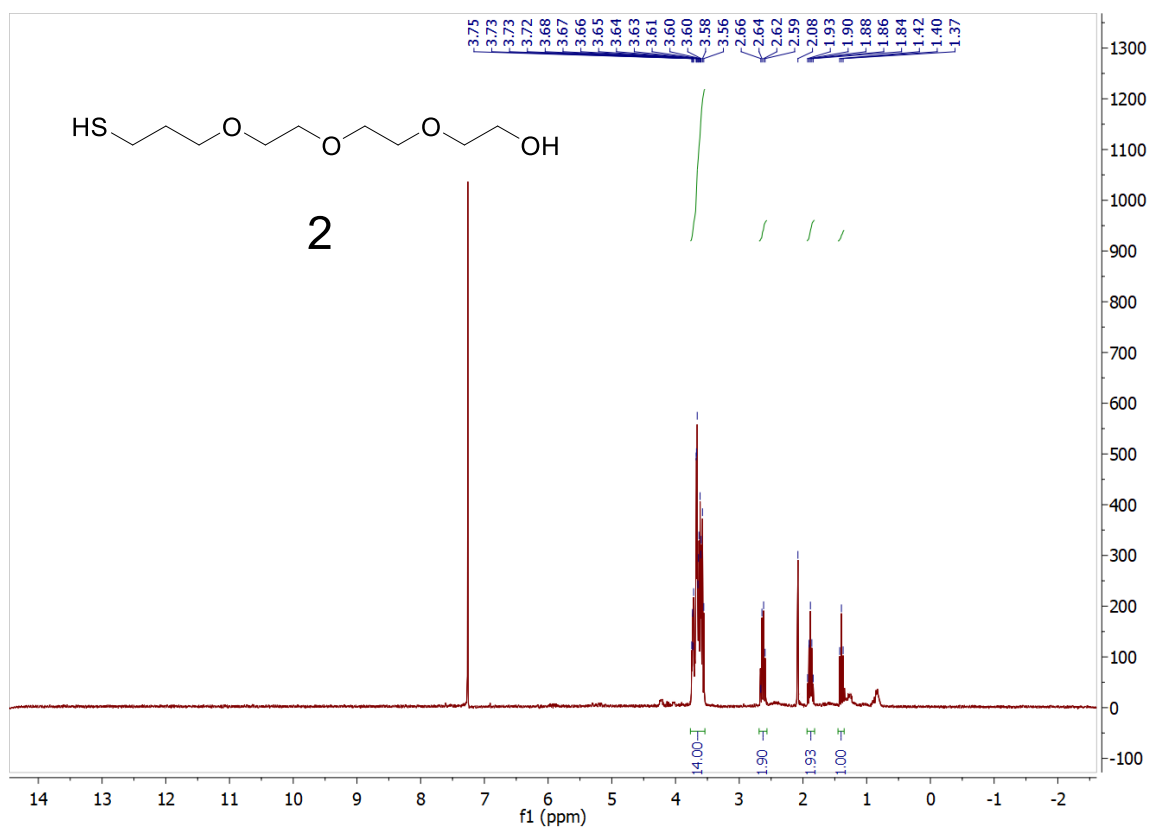


Figure 9.58: ^1H NMR spectrum of **2** (CDCl_3 , 300 MHz, 298 K).

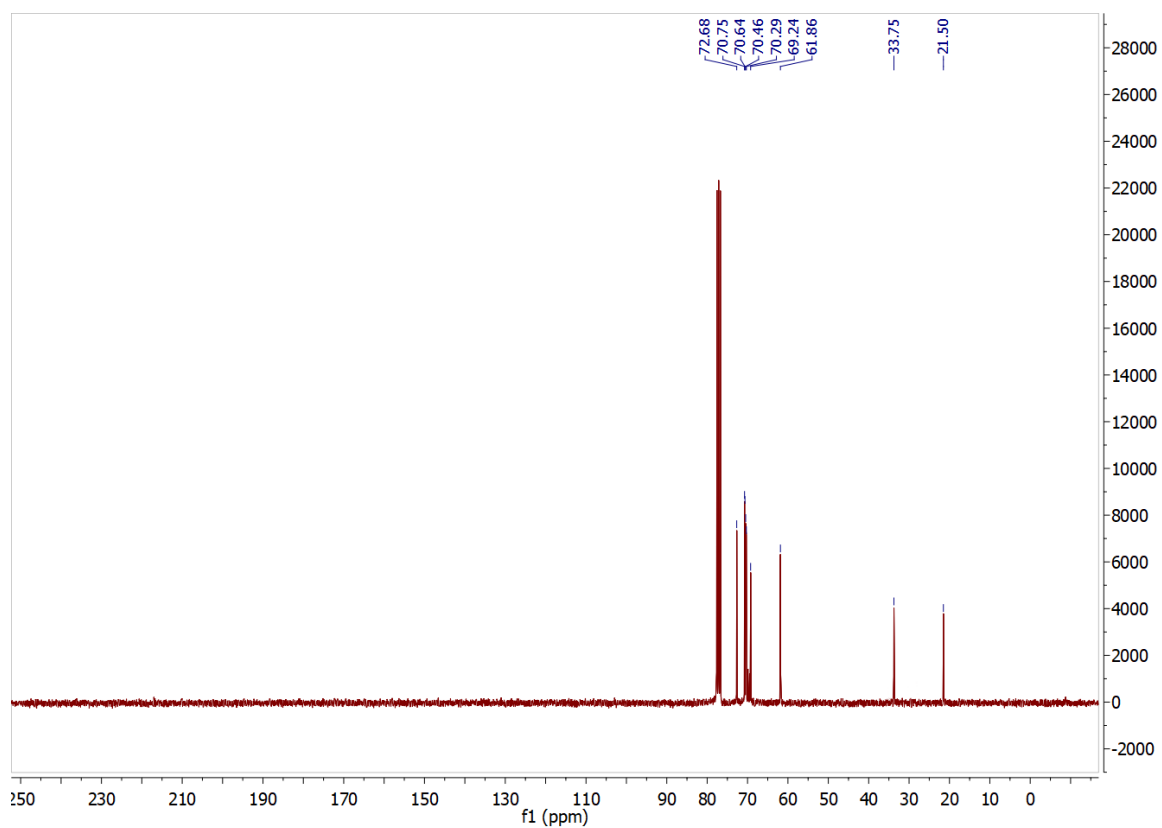


Figure 9.59: ^{13}C NMR spectrum of **2** (CDCl_3 , 75 MHz, 298 K).

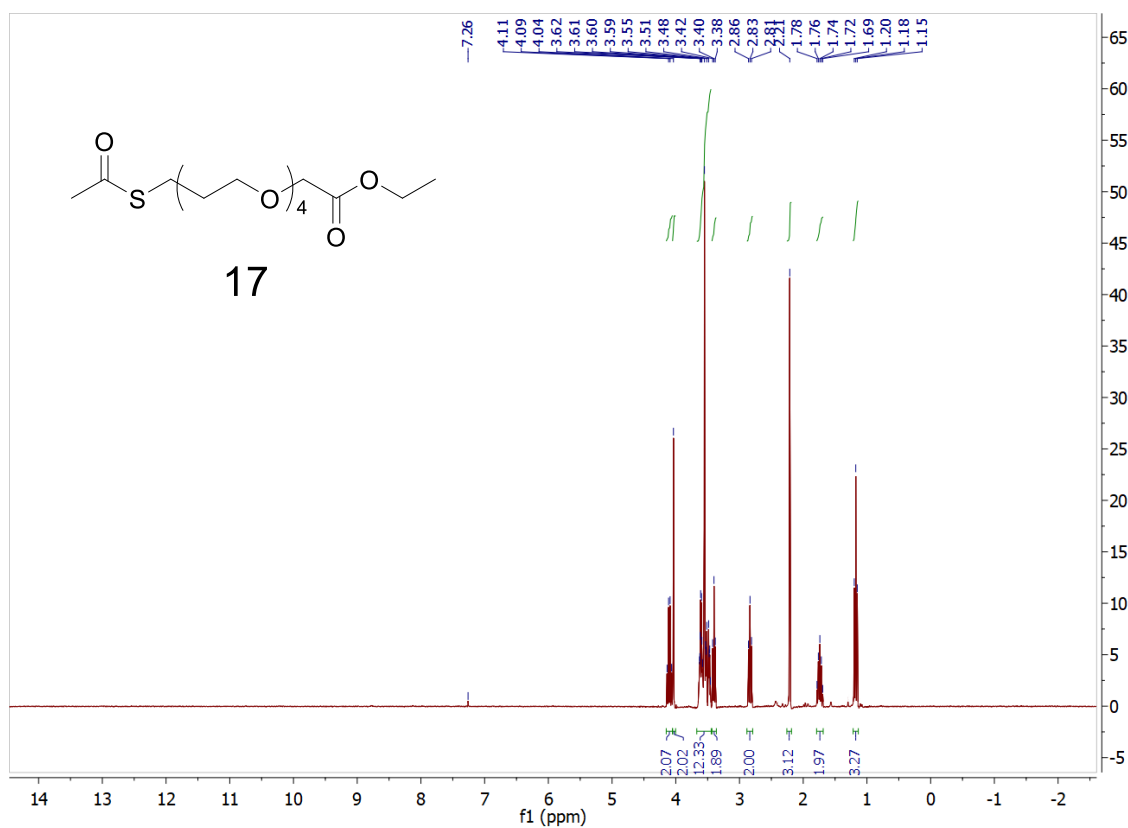


Figure 9.60: ^1H NMR spectrum of **17** (CDCl_3 , 300 MHz, 298 K).

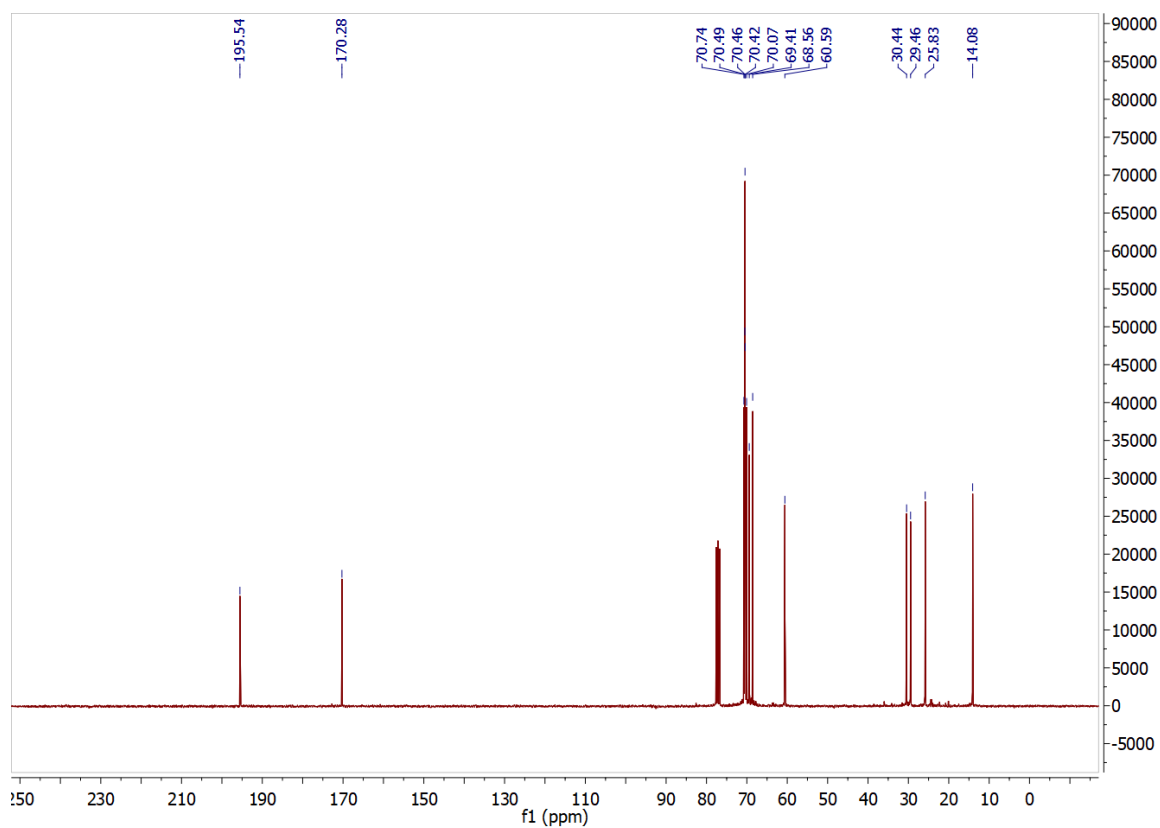


Figure 9.61: ^{13}C NMR spectrum of **17** (CDCl_3 , 75 MHz, 298 K).

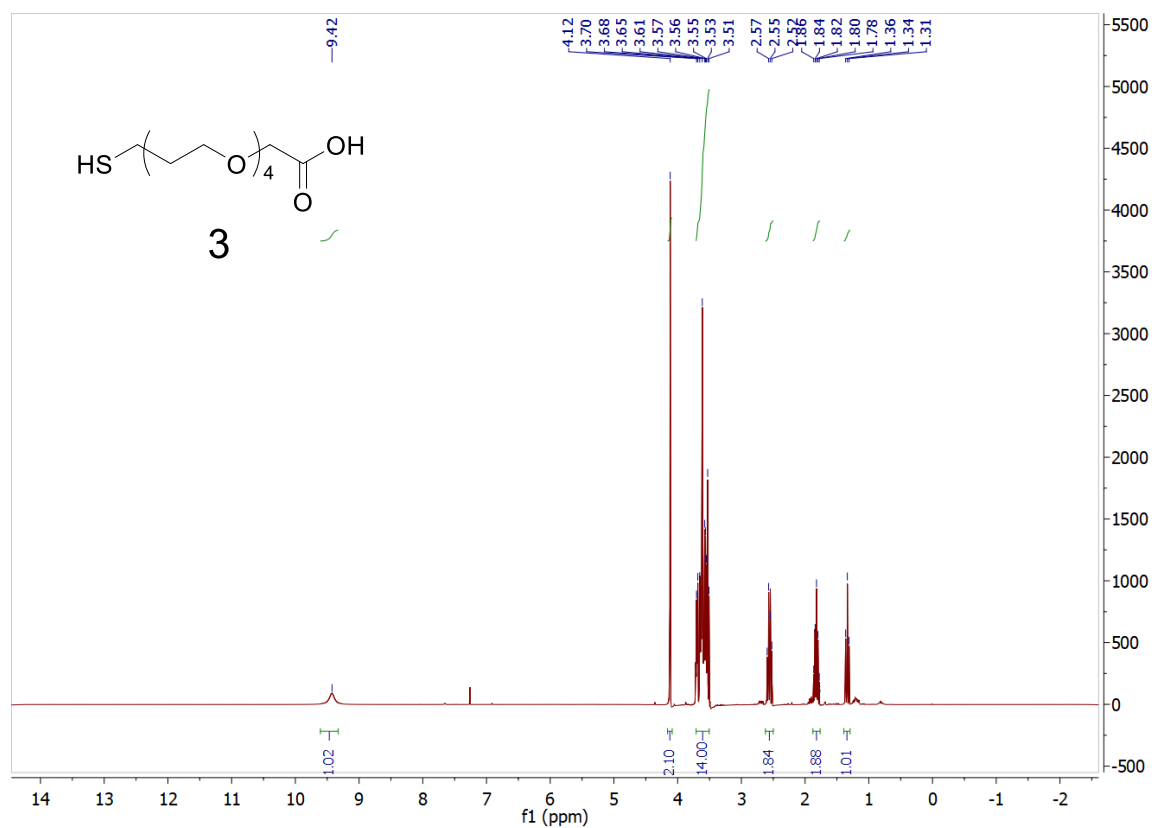


Figure 9.62: ^1H NMR spectrum of **3** (CDCl_3 , 300 MHz, 298 K).

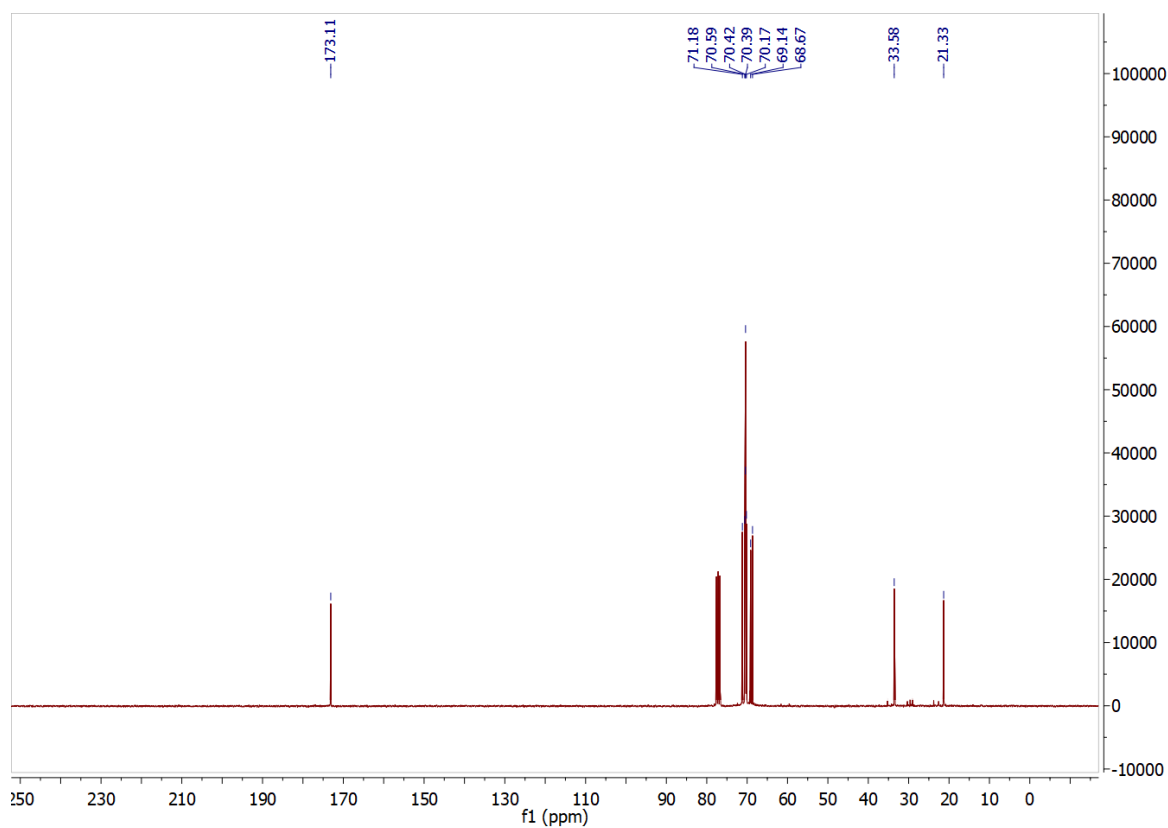


Figure 9.63: ^{13}C NMR spectrum of **3** (CDCl_3 , 75 MHz, 298 K).

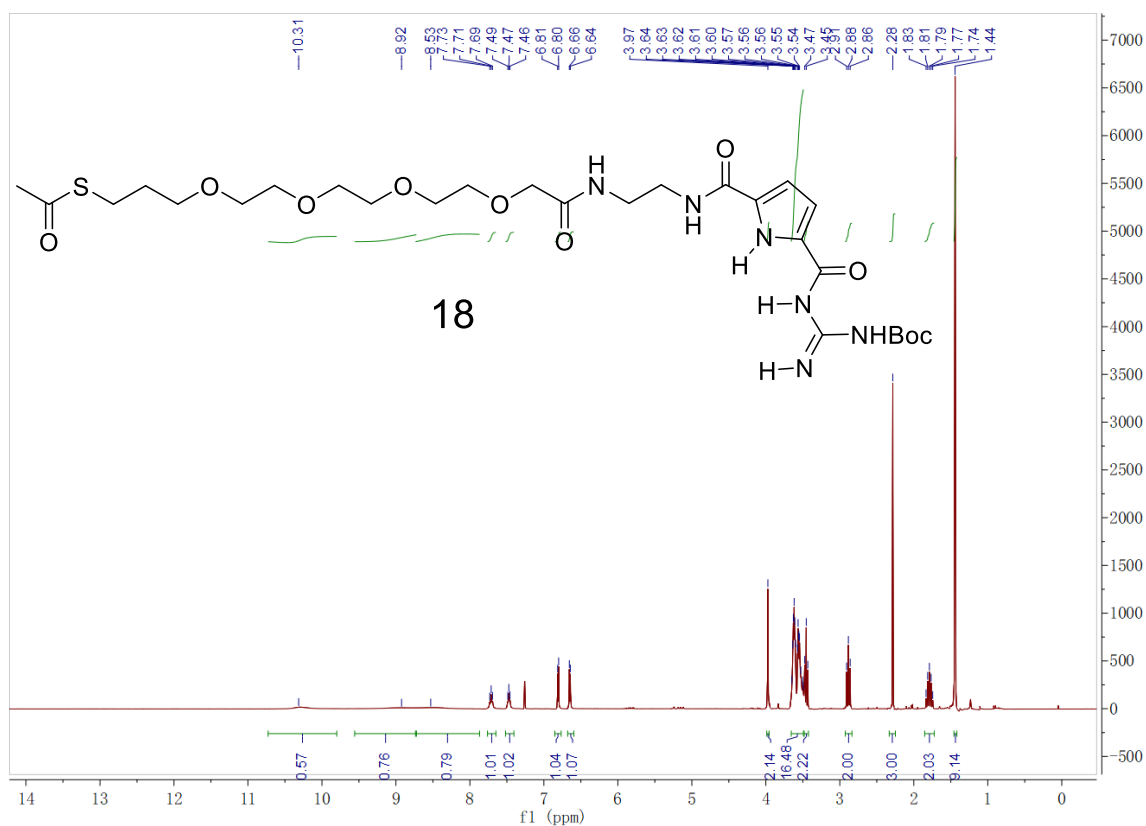


Figure 9.64: ^1H NMR spectrum of **18** (CDCl_3 , 300 MHz, 298 K).

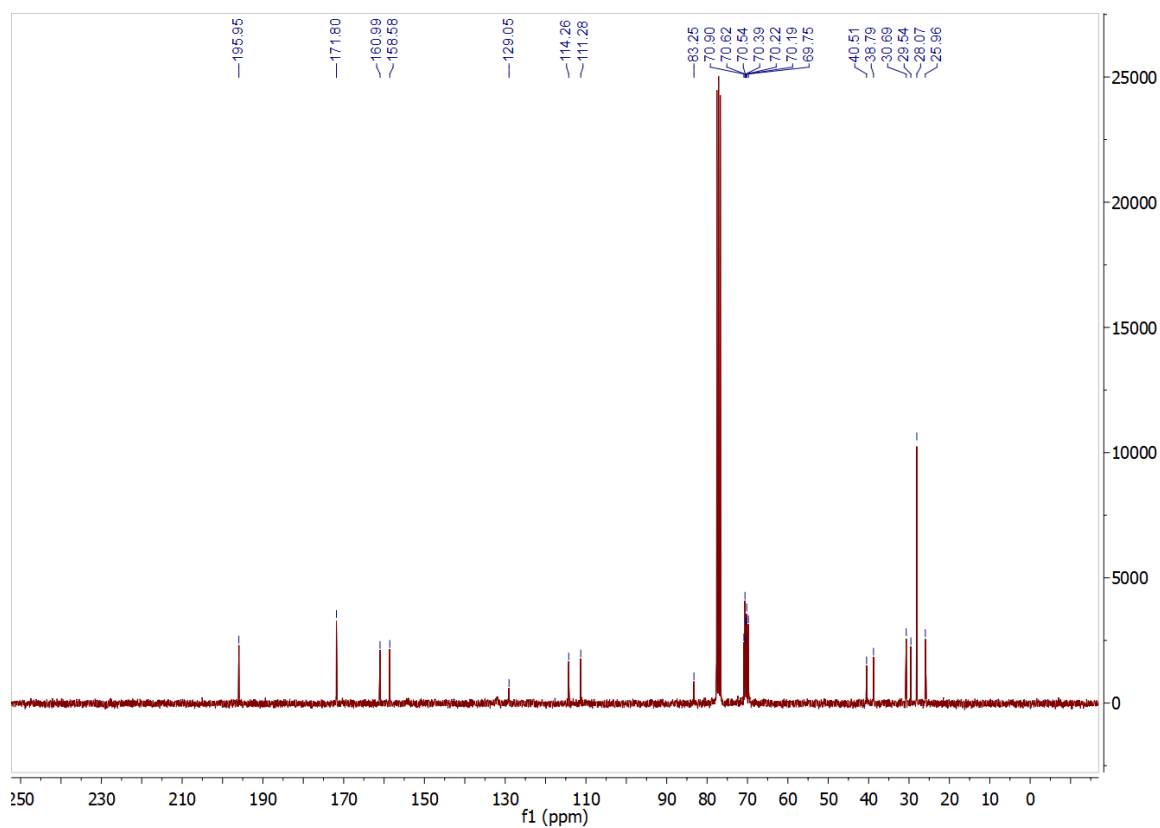


Figure 9.65: ^{13}C NMR spectrum of **18** (CDCl_3 , 75 MHz, 298 K).

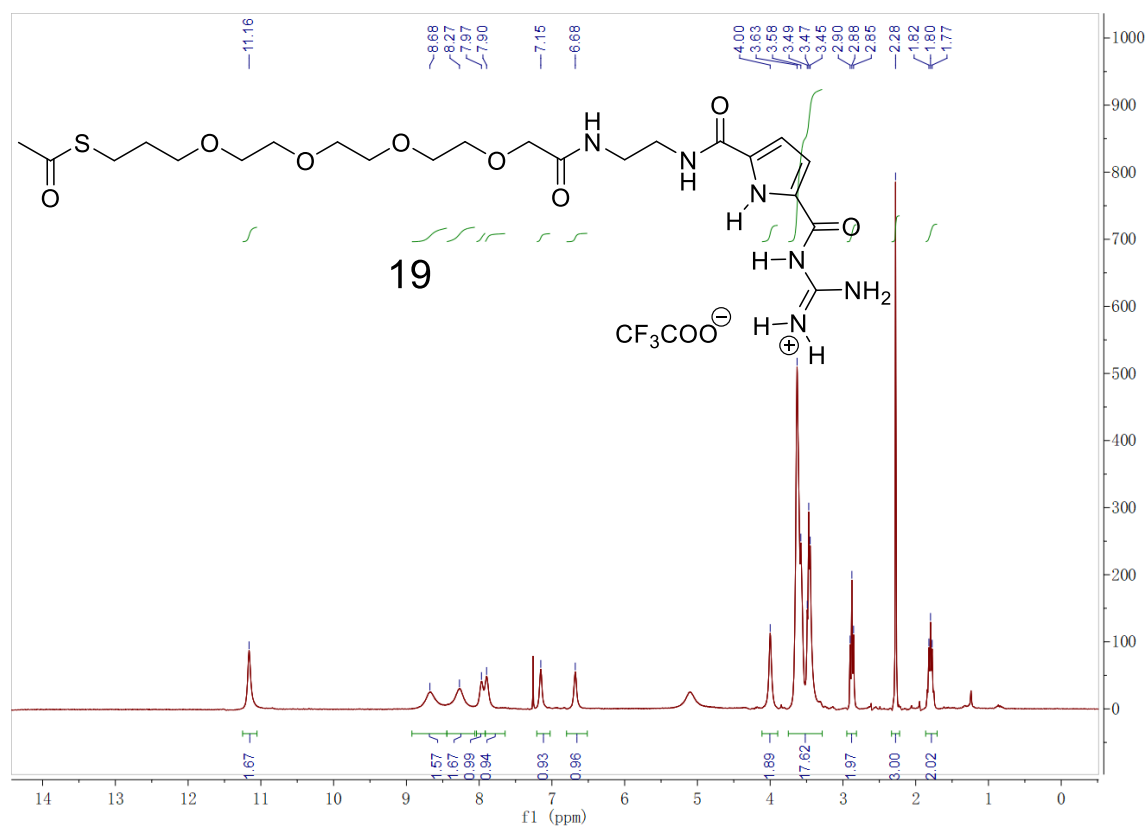


Figure 9.66: ^1H NMR spectrum of **19** (CDCl_3 , 300 MHz, 298 K).

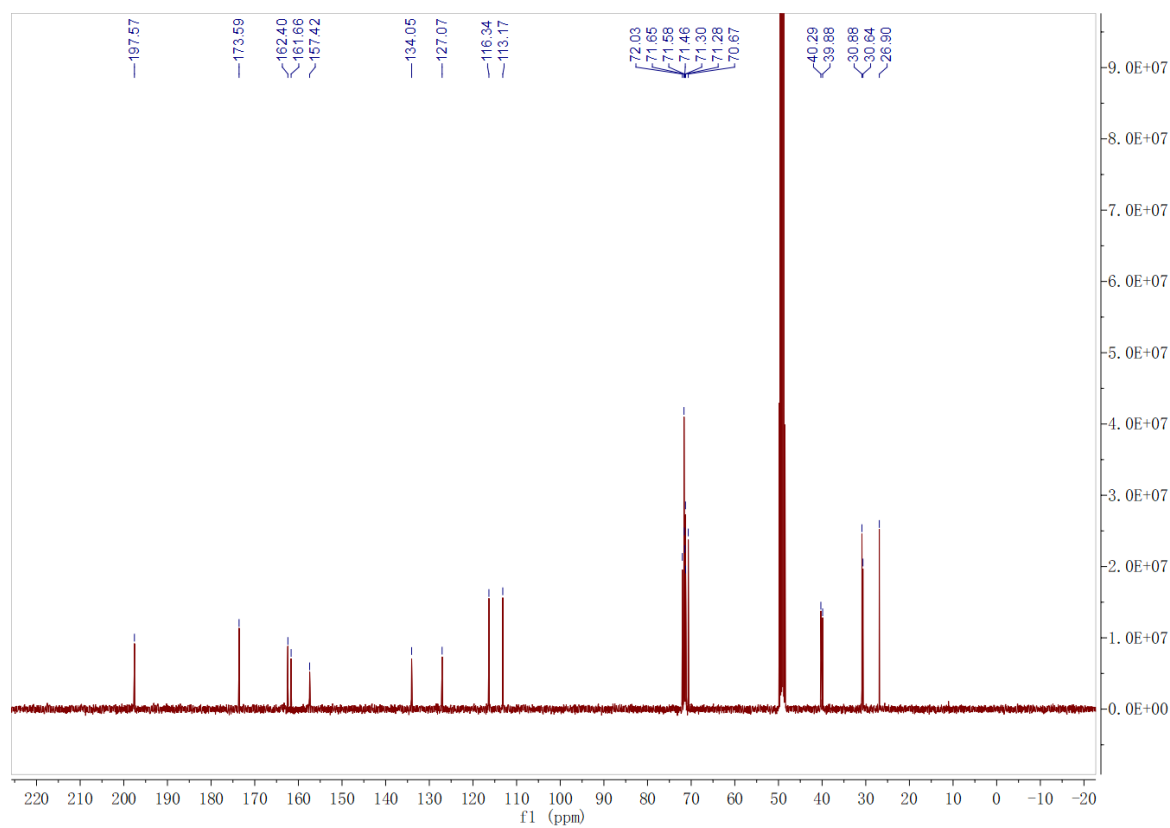


Figure 9.67: ^{13}C NMR spectrum of **19** (MeOD , 101 MHz, 298 K).

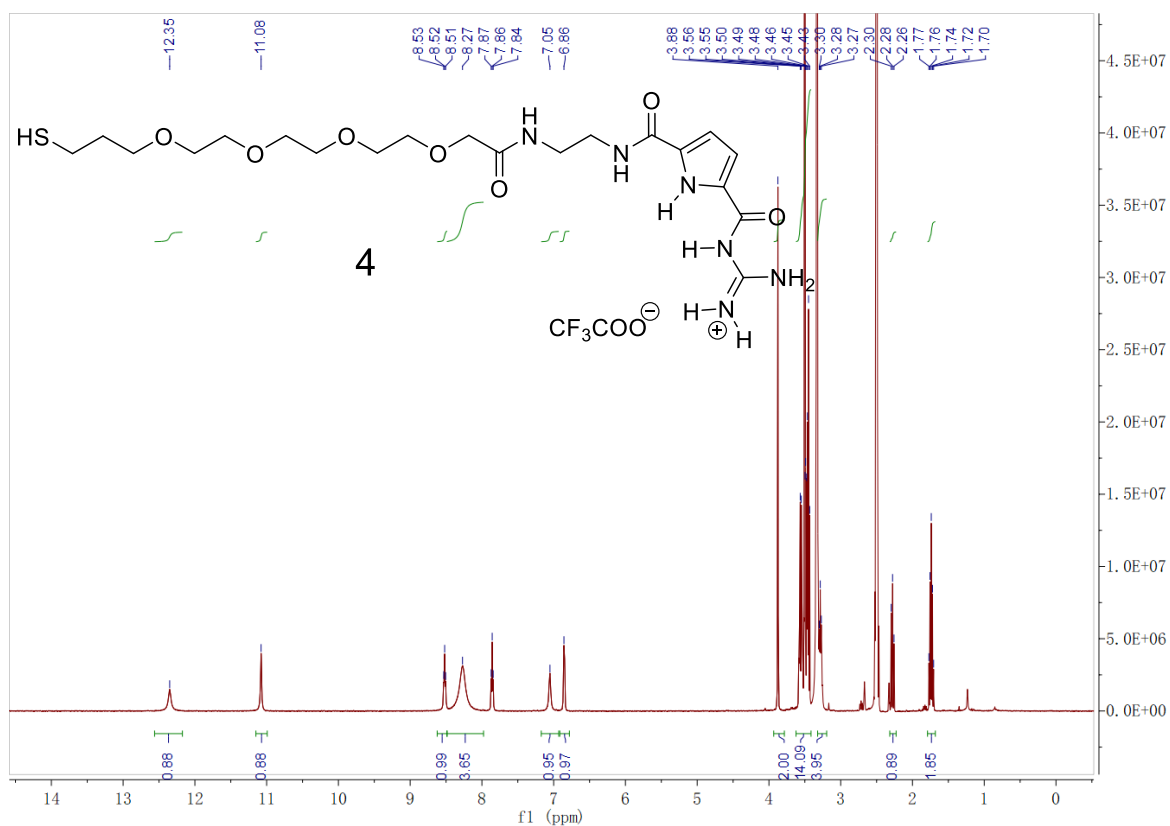


Figure 9.68: ^1H NMR spectrum of **4** (DMSO- d_6 , 400 MHz, 298 K).

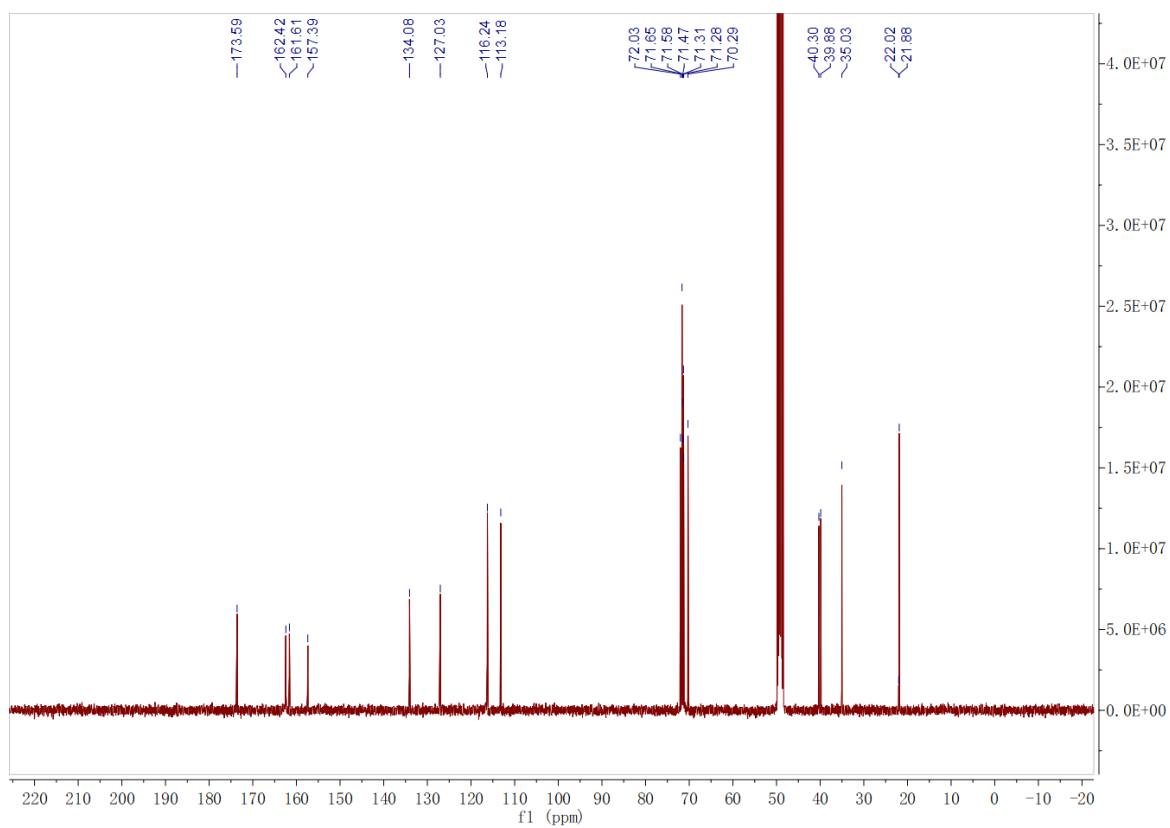


Figure 9.69: ^{13}C NMR spectrum of **4** (MeOD, 101 MHz, 298 K).

9.5 Curriculum vitae

The biography is not included in the online version for reasons of data protection.

9.6 List of Publications

Journal

Huibin He*, Jan-Erik Ostwaldt, Christoph Hirschhäuser, Carsten Schmuck, Jochen Niemeyer*;

Dual pH-Induced Reversible Self-Assembly of Gold Nanoparticles by Surface-Functionalization with Zwitterionic Ligands;

Small, **2020**, 16. 2001044

Poster Presentation

Huibin He, Carsten Schmuck;

The pH-switched self-assembly of gold nanorods functionalized with guanidiniocarbonyl pyrrole carboxylate zwitterion ligands;

ORCHEM 2018, Berlin, Germany, 10th -12th Sep **2018**.